

Magnetic Tunnel Junctions based on spinel $\text{Zn}_x\text{Fe}_{3-x}\text{O}_4$

Von der Fakultät für Physik und Geowissenschaften
der Universität Leipzig
genehmigte

Dissertation

zur Erlangung des akademischen Grades
Doctor rerum naturalium
Dr. rer. nat.

vorgelegt von
M.Sc. Michael Bonholzer
geboren am 30.04.1986 in Landshut

Gutachter: Prof. Dr. Marius Grundmann
Prof. Dr. Georg Schmidt

Tag der Verleihung: 24.10.2016

Bibliographische Beschreibung:

Bonholzer, Michael

Magnetic Tunnel Junctions based on spinel $\text{Zn}_x\text{Fe}_{3-x}\text{O}_4$

Universität Leipzig , Dissertation

257 Seiten¹, 345 Zitate², 83 Abbildungen, 7 Tabellen,

Referat:

Die vorliegende Arbeit befasst sich mit magnetischen Tunnelkontakten (magnetic tunnel junctions, MTJs) auf Basis des Oxids Zinkferrit ($\text{Zn}_x\text{Fe}_{3-x}\text{O}_4$). Dabei soll das Potential dieses Materials durch die Demonstration des Tunnelmagnetowiderstandes (tunnel magnetoresistance, TMR) in zinkferritbasierten Tunnelkontakten gezeigt werden. Dazu wurde ein Probendesign für MTJs auf Basis der „pseudo spin valve“-Geometrie entwickelt. Die Basis für diese Strukturen ist ein Dünnschichtstapel aus MgO (Substrat) / TiN / $\text{Zn}_x\text{Fe}_{3-x}\text{O}_4$ / MgO / Co. Dieser ist mittels gepulster Laserabscheidung (pulsed laser deposition, PLD) hergestellt. Im Rahmen dieser Arbeit wurden die strukturellen, elektrischen und magnetischen Eigenschaften der Dünnschichten untersucht. Des Weiteren wurden die fertig prozessierten MTJ-Bauelemente an einem im Rahmen dieser Arbeit entwickelten und aufgebauten TMR-Messplatz vermessen. Dabei ist es gelungen einen TMR-Effekt von 0.5% in $\text{Zn}_x\text{Fe}_{3-x}\text{O}_4$ -basierten MTJs nachzuweisen.

Das erste Kapitel der Arbeit gibt eine Einführung in die spintronischen Effekte Riesenmagnetowiderstand (giant magnetoresistance, GMR) und Tunnelmagnetowiderstand (TMR). Deren technologische Anwendungen sowie die grundlegenden physikalischen Effekte und Modelle werden diskutiert. Das zweite Kapitel gibt eine Übersicht über die Materialklasse der spinellartigen Ferrite. Der Fokus liegt auf den Materialien Magnetit (Fe_3O_4) sowie Zinkferrit ($\text{Zn}_x\text{Fe}_{3-x}\text{O}_4$). Die physikalischen Modelle zur Beschreibung der strukturellen, magnetischen und elektrischen Eigenschaften dieser Materialien werden dargestellt sowie ein Literaturüberblick über experimentelle und theoretische Arbeiten gegeben. Im dritten Kapitel werden die im Rahmen dieser Arbeit verwendeten Probenpräparations- und Charakterisierungsmethoden vorgestellt und technische Details sowie physikalische Grundlagen erläutert. Die Entwicklung eines neuen Probendesigns zum Nachweis des TMR-Effekts in $\text{Zn}_x\text{Fe}_{3-x}\text{O}_4$ -basierten MTJs ist Gegenstand des vierten Kapitels. Die Entwicklung des Probenaufbaus sowie die daraus resultierende Probenprozessierung werden beschrieben. Die beiden letzten Kapitel befassen sich mit der strukturellen, elektrischen und magnetischen Charakterisierung der mittels PLD abgeschiedenen Dünnschichten sowie der Tunnelkontaktstrukturen.

¹Seitenzahl insgesamt

²Anzahl der im Literaturverzeichnis ausgewiesenen Literaturangaben



Gefördert aus Mitteln
der Europäischen Union

Europa fördert Sachsen.



Funded by the European Union and the Free State of Saxony.

Contents

Introduction	1
1 Spintronics	5
1.1 Introduction to magnetoresistive effects and spintronics	5
1.1.1 Spintronic based data storage	5
1.1.2 Two current model of spintronics	8
1.1.3 Giant Magnetoresistance GMR	10
1.1.4 Tunnel Magnetoresistance TMR	13
1.1.5 Oxide Based spintronics	16
1.1.6 Further materials for spintronics	19
1.2 Theory of Tunnel Magnetoresistance (TMR)	22
1.2.1 Quantum tunneling and tunnel currents	22
1.2.2 Simmons-Model	26
1.2.3 Brinkman-Dynes-Rowell-Model (BDR-Model)	29
1.2.4 Expansion of Both basic Models	31
1.2.5 Spin-dependent Tunneling and TMR	37
2 The spinel Oxides Magnetite and Zinc ferrite	59
2.1 The spinel structure	59
2.1.1 Electrical conduction in spinel materials	64
2.1.2 Magnetism in spinel materials	65
2.1.3 Spin polarization in Fe_3O_4 and ZnFe_2O_4	71
2.2 Magnetite Fe_3O_4	72
2.2.1 Fe_3O_4 thin films	73
2.2.2 Fe_3O_4 at temperatures below 120 K: the Verwey transition	78
2.2.3 Fe_3O_4 in spintronics	80
2.3 Zinc ferrite ZnFe_2O_4	84
2.3.1 Nanocrystalline ZnFe_2O_4	84
2.3.2 Epitaxial ZnFe_2O_4 thin films	87
2.4 $\text{Zn}_x\text{Fe}_{3-x}\text{O}_4$ thin films	94
2.5 Summary: Fe_3O_4 , $\text{Zn}_x\text{Fe}_{3-x}\text{O}_4$ and ZnFe_2O_4 thin films	99

3	Sample preparation and characterization techniques	103
3.1	Thin film growth and <i>in-situ</i> characterization	103
3.1.1	Pulsed laser deposition (PLD)	103
3.1.2	Reflection high-energy electron diffraction (RHEED) . . .	105
3.1.3	Thin film growth modes	109
3.1.4	B-Chamber: PLD chamber with CO ₂ -laser heater and <i>in-situ</i> RHEED	115
3.2	X-ray diffraction	121
3.3	X-ray reflectivity	126
3.4	Atomic force microscopy	131
3.5	SQUID	135
3.6	Dual beam microscope: SEM, EDX and FIB	136
3.7	Sputter Deposition	138
3.8	Photolithography	139
3.9	Plasma Cleaning	140
3.10	Argon Ion Etching inside a SNMS machine	140
3.11	Laser scanning microscope	141
3.12	Plasma Enhanced Chemical Vapor Deposition (PECVD)	142
3.13	Wire Bonder	144
3.14	Electrical Characterization	144
3.14.1	Resistivity of thin films	144
3.14.2	I-V measurements at room temperature	145
3.14.3	TMR measurements: R(B,T), I-V(B,T)	145
4	Development of the MTJ-sample layout	149
4.1	First sample layout	149
4.2	Problems and evolution of the sample design	152
4.3	The final sample design	156
5	Growth and properties of thin films	165
5.1	MgO-substrate preparation	165
5.2	TiN-thin films	168
5.3	Zn _x Fe _{3-x} O ₄ thin films	172
5.3.1	Composition x of Zn _x Fe _{3-x} O ₄ thin films	173
5.3.2	Structural properties of Zn _x Fe _{3-x} O ₄ thin films	174
5.3.3	Electrical properties of Zn _x Fe _{3-x} O ₄ thin films	177
5.3.4	Magnetic properties of Zn _x Fe _{3-x} O ₄ thin films	179
5.4	MgO barrier	183
5.4.1	Growth and structural properties	184
5.4.2	I-V-measurements and barrier parameter	185
5.5	Co thin films	192
6	Magnetic properties and TMR of Zn_xFe_{3-x}O₄-based MTJs	195
	Summary	199

Bibliography	I
List of Figures	XXX
List of Tables	XXXIV
List of own and contributed Articles	XXXVI
List of own and contributed Conference Talks and Posters	XXXIX
Danksagung	XLII
Selbstständigkeitserklärung	XLV
Erklärung über die Anerkennung der Promotionsordnung	XLVI

Introduction

Spintronic (spin transfer electronic) is a new technology for electrical data storage and processing. It uses not only the charge of electrons but also their spin degree of freedom. Information is stored in the magnetization of thin layers and read out by spin polarized currents. This provides the possibility to build fast, non-volatile memories.

The intense research on spintronics started with the discovery of the giant magnetoresistance (GMR) in 1988 by Albert Fert [1] and Peter Grünberg [2]. The application of the GMR-effect in read heads of hard disc drives (HDDs) increased their storage density significantly. Due to the technological relevance of the GMR, the Nobel prize was given to Albert Fert [3] and Peter Grünberg [4] in 2007.

The second technologically relevant effect in spintronics is the tunnel magnetoresistance (TMR). Read heads based on the TMR achieve a higher magnetoresistance ratio ($MR = \Delta R/R$) and allow a smaller head size compared to GMR-based ones. Thus, the application of TMR-based read heads further increased the storage density of HDDs. Read heads based on the TMR-effect began to replace the GMR-based read heads in 2005 [5]. A second promising application of the TMR are magnetic random access memories (MRAMs). This type of memory has the capability to replace today's memory technologies since it is fast, less power consuming and non-volatile [6–9]. Spin logic devices for data processing based on the TMR-effect are also possible [10].

The TMR is based on a change of the resistance of a ferromagnet / insulator / ferromagnet tunnel structure due to the alignment of the magnetization directions of the ferromagnetic electrodes. The tunneling probability of electrons, and therefore the resistance of the device, depends on the density of spin-states at the Fermi level in the two ferromagnetic electrodes. The key parameter of the TMR is the spin polarization P of the tunnel current. The spin polarization is the difference between the amount of spin up and spin down conduction electrons. According to Julliere [11], the TMR-ratio is determined by the spin polarizations P_1 and P_2 of conduction electrons in the two electrodes. It is

$$\text{TMR} = \frac{R_{\uparrow\downarrow} - R_{\uparrow\uparrow}}{R_{\uparrow\uparrow}} = \frac{2P_1P_2}{1 - P_1P_2}. \quad (1)$$

$R_{\uparrow\downarrow}$ and $R_{\uparrow\uparrow}$ is the device resistance in the antiparallel and parallel alignment of layer magnetization, respectively.

In order to achieve high TMR-ratios it is important to use magnetic electrodes with a high spin polarization. Promising materials are so called half metals. Half metals show insulating behavior in one spin channel and semiconducting or even metallic behavior in the other spin channel. This results in a complete spin polarization of conduction electrons and a high TMR-ratio since the tunnel current is completely blocked in the antiparallel magnetization alignment. Promising half metals are the spinel oxides magnetite Fe_3O_4 and zinc ferrite $\text{Zn}_x\text{Fe}_{3-x}\text{O}_4$ ($0 < x \leq 1$). Fe_3O_4 is reported to be a ferrimagnetic, half metallic semiconductor at room temperature with a high Curie temperature of 860 K [12–14]. The magnetic and electric properties of Fe_3O_4 can be tuned by substituting a certain amount of iron by zinc. The resulting $\text{Zn}_x\text{Fe}_{3-x}\text{O}_4$ is reported to be ferrimagnetic, half metallic and semiconducting, too [15–17]. The half metallic nature of these materials is based on the conduction mechanism which is electron hopping between Fe^{2+} and Fe^{3+} -cations. The hopping electrons can only exhibit one spin direction due to the magnetic structure of the material. This leads to a complete spin polarization of the current.

The half-metallic nature of Fe_3O_4 and $\text{Zn}_x\text{Fe}_{3-x}\text{O}_4$ makes these materials promising candidates for spintronic applications. Few publications report on magnetic tunnel junctions based on Fe_3O_4 (see Section 2.2.3). The obtained TMR-ratios are far below the high values expected from the half-metallic nature of Fe_3O_4 . This is assigned to the properties of the interface between Fe_3O_4 and the tunneling barrier.

The objective of the present thesis is the preparation of magnetic tunnel junctions (MTJs) based on the spinel oxide $\text{Zn}_x\text{Fe}_{3-x}\text{O}_4$ to demonstrate the potential of this material for spintronic applications. For this purpose, a MTJ-sample design based on the pseudo spin valve geometry was developed in order to demonstrate the TMR-effect in $\text{Zn}_x\text{Fe}_{3-x}\text{O}_4$ -based MTJs. The design is based on thin film stacks of MgO (substrate) / TiN / $\text{Zn}_x\text{Fe}_{3-x}\text{O}_4$ / MgO / Co grown by pulsed laser deposition (PLD). The thin MgO -layer with a thickness of 2.8 nm forms the barrier layer, whereas Co is used as magnetic counter electrode. Since a high crystalline quality and smooth barrier interfaces are a prerequisite for working MTJ-devices, the PLD-parameters were adjusted in order to obtain a two-dimensional growth of the thin films. *In-situ* annealing of the MgO -substrate results in smooth, monolayer stepped surfaces, providing perfect conditions for two-dimensional thin film growth [A1]. The thin films are investigated for their structural, electrical and magnetic properties in order to show the suitability of the single layers for the application in MTJ-elements. A TMR-measurement setup was developed and assembled in the framework of this thesis in order to measure the desired TMR. A TMR-ratio of 0.5% was observed on our MTJ-samples.

The first chapter of the thesis gives an overview on spintronics and tunnel magnetoresistance. Theoretical models as well as reported experimental results are discussed. The second chapter describes the properties of the spinel oxides magnetite (Fe_3O_4) and zinc ferrite ($\text{Zn}_x\text{Fe}_{3-x}\text{O}_4$). The basic concepts for the description of the magnetic and electrical properties of these materials are presented. Experimental results on Fe_3O_4 and ZnFe_2O_4 reported in literature are discussed. Topic of the third chapter are the sample preparation and characterization methods used in the framework of this thesis. Technical details as well as physical principles of the methods are presented. The fourth chapter presents the magnetic tunnel junction sample design developed in the framework of this thesis. The structural requirements for MTJ-elements and the resulting sample design are discussed. Different preparation problems as well as their solutions are pointed out. The focus of the fifth chapter is on the growth and the properties (structural, magnetic and electric) of the thin PLD-grown films used to produce the magnetic tunnel junctions. The sixth chapter presents the results of TMR-measurements on $\text{Zn}_x\text{Fe}_{3-x}\text{O}_4$ -based magnetic tunnel junctions.

1 Spintronics

1.1 Introduction to magnetoresistive effects and spintronics

1.1.1 Spintronic based data storage

Spintronics (spin transfer electronics, also called magnetoelectronics or spin-based electronics) is a novel branch of electrical data storage and processing technologies. In spintronics, not only the electrical charge of an electron, but also its spin is used for data storage and processing. This gives an advantage over conventional electronics, where data is stored as charge on a capacitor (e.g. SRAM, DRAM, Flash-EEPROM). There are two major drawbacks in those conventional electronics: In SRAM and DRAM, volatility of the stored charges leads to a continuous power consumption in order to maintain the stored information, and in Flash-memories (USB-sticks and Solid State Discs, SSDs) the wearout process during every writing step, which is a voltage pulse of 12V over a SiO_2 -barrier to charge the capacitor, limits the lifetime of these devices [18].

Today, spintronic devices are mainly used in two sorts of data storage applications. Read heads in hard disc drives (HDDs) and storage units in MRAMs (magnetic random access memories).

Read heads in hard discs are sensing devices probing the magnetic field of the storage discs where digital information is coded as magnetic domains. The head is guided over the storage disk with a flight height of only a few nm. Stray fields above the disc lead to a change of resistance in the read head (magnetoresistance, Figure 1.1 b). Due to their higher magnetoresistance ratio, spintronic devices based on the GMR (giant magnetoresistance) or TMR (tunnel magnetoresistance) effect lead to a minimization of these devices, resulting in a much higher storage capacity of hard disc drives (Figure 1.1 a).

A typical structure of spintronic read heads is the spin valve. It consists of two magnetic layers, separated by a non magnetic metal (GMR) or an insulating (TMR) layer. One of the magnetic layers is exchange biased to an antiferromagnet. The magnetization of this layer is fixed and stays unchanged under applied fields. The magnetization of the second, the free layer, is rotated in the stray field of the recording media. The magnetic alignment relative to the

exchange biased reference layer gives a change in resistance of the device. This change in resistance is interpreted by the computer logic as the "0" and "1" of digital data. Therefore, the key value of magnetoresistive ratio (MR, can be either GMR or TMR ratio) can be defined as

$$\text{MR} = \frac{\Delta R}{R} = \frac{R_{\uparrow\downarrow} - R_{\uparrow\uparrow}}{R_{\uparrow\uparrow}} \quad (1.1)$$

Where $R_{\uparrow\downarrow}$ and $R_{\uparrow\uparrow}$ are the resistance of the device in antiparallel and parallel alignment of the layer magnetization, respectively. The higher this value is, the smaller can be the size of the read head without reaching a critical Bit Error Rate [19]. This leads to an increase of storage density in HDDs due to a minimization of the used read heads, based on an increase of their MR value. There are two typical spin valve designs used in magnetoresistive read heads. GMR read heads are usually CIP (current in sensor plane)-spin valves whereas TMR-based ones are CPP (current perpendicular to sensor plane)-type devices (Figure 1.1 b) [20].

Magnetic random access memories (MRAMs) are solid state memories based on the GMR [6, 23] or TMR [5, 20] effect. Nowadays, TMR is more important for MRAM application because TMR-based spin valves (also called magnetic tunnel junctions, MTJs) are natural CPP-devices. It makes arrangement and control of the device much easier, allows a higher storage density and achieves much higher speeds due to the better available signal [6, 20]. A MRAM-cell consists of an array of TMR spin valves (Figure 1.1 d). Every element can be set in parallel (low resistance, logic "0") or anti-parallel (high resistance, logic "1") alignment of magnetization directions. These states are stable due to the remanence of the free layer. Switching is done by currents through the word (write) and bit line. These lines are metallic stripes arranged in a cross grid on top and bottom of the TMR spin valves. In order to address single elements, a current is sent through the word and bit lines crossing at the position of the specific spin valve. The vector combination of the Oersted-fields of both currents switches the magnetization of the free layer. This requires the magnetization of the TMR-elements to be stable against disturbance by fields from a single current and to switch reliably in the combined fields [6]. A solution to this problem is the so called "toggle MRAM" design [7, 24].

For read out of a specific memory cell, a voltage is applied to the appropriate read word line and bit line. The read word line is the gate terminal of a field effect transistor with its source connected to the MTJ. The voltage opens the transistor and allows a current flow through the MTJ driven by the voltage applied to the bit line. The measured resistance is assigned to the two states of the MTJ [10, 20]. This geometry is chosen to suppress leakage currents through non-addressed cells during read processes and through all cells during writing processes.

A major drawback of spintronic-based MRAM technology is the need of high switching currents to achieve the required Oersted-fields [7]. But there are

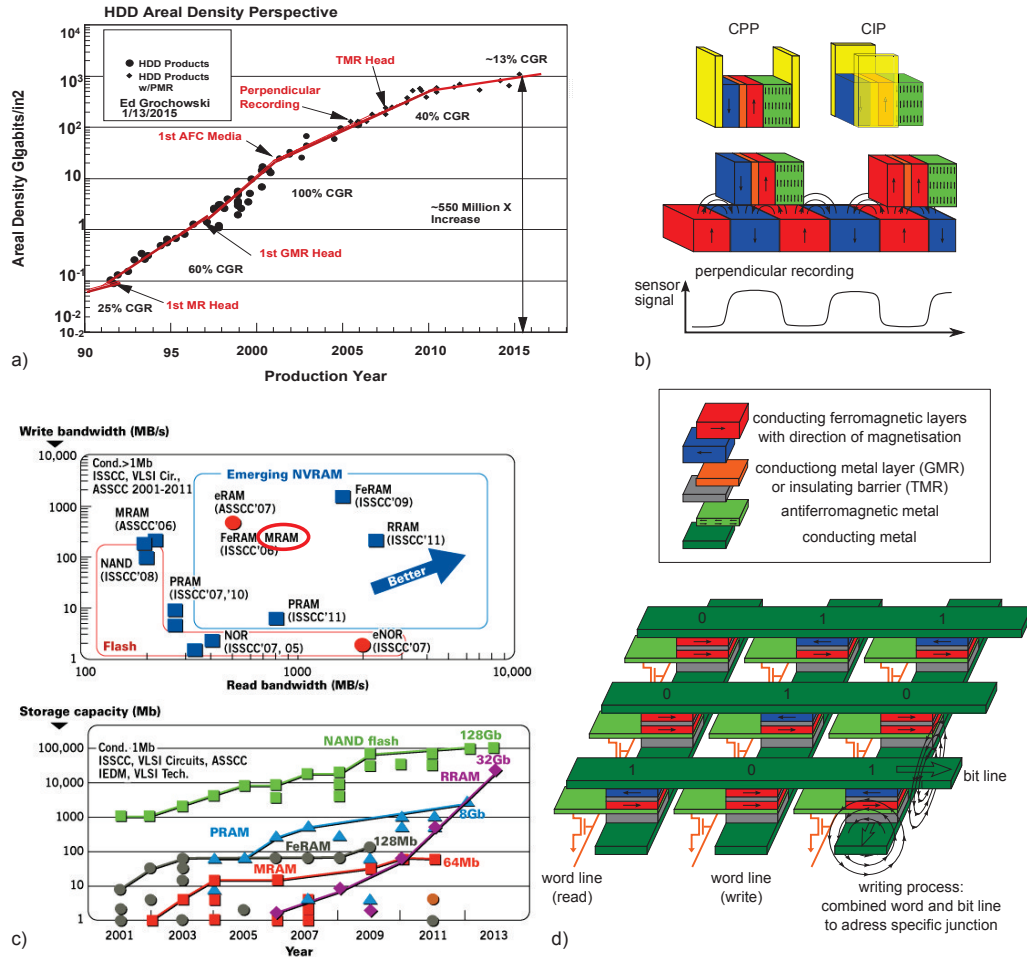


Figure 1.1: a) The development of storage density per square inch of hard disc drives during the last 20 years. The impact of spintronic devices (GMR and TMR read heads) can be clearly seen [21]. b) Sketch of the function principle of spintronic read heads. Shown here is the commonly used spin valve structure in the CPP (current perpendicular to sensor plane) and CIP (current in sensor plane) geometry. c) Top: Comparison of write and read bandwidth of different non-volatile memories. The MRAM technology seems to be appropriate to compete with today's FLASH-based devices. Bottom: The development of storage capacity of different non-volatile memories during the last 15 years [22]. d) Sketch of a TMR-based MRAM-array.

many overwhelming advantages in using spintronic-based MRAM technologies. MRAM is a non volatile memory with lifetimes of more than 10 [24] or even 20 years [25]. This is due to the storage of information in the long term stable magnetization of the free layer (like on HDD storage discs) [7]. MRAMs have short and symmetrical read and write times (≈ 35 ns) and therefore the potential to rival and replace SRAM and DRAM [6–9]. MRAM needs zero static power (non volatile) and provides instant wakeup if it replaces SRAM (no boot required) [10]. Its non-destructive read out eliminates the need of rewriting single bits after a read out process (compared to DRAM) [6]. And unlike today's Flash memories, MRAMs have no wear out mechanism and therefore unlimited endurance [18, 25].

A second generation of MRAM systems can overcome the main drawback of high writing currents. Spin transfer torque MRAMs (STT-MRAMs) utilize the effect of spin transfer torque to switch the magnetization of the free layer using a spin-polarized current [26]. The current needed for switching by spin transfer torque is orders of magnitude smaller compared to the current using the Oersted-field to switch the magnetization [10]. The effect of STT was proposed by Slonczewski in 1996 [27], verified experimentally by various groups (a great overview is given in [26]) and is well on the way to be used in customer electronics [28]. Nowadays, STT-MRAMs are used in special applications requiring reliability in harsh conditions, fast read and write speeds and non-volatility even in unexpected power-off situations. An example is the EVERSPIN MR2A16B Parallel Interface 4Mb MRAM used for live data recording in the superbike BMW 1000RR [29].

Due to their advantages, spintronic-based memories can be a candidate for replacing every single level in memory hierarchy (SRAM-DRAM-Flash-HDD) by one fast, reliable, enduring, high capacitance and low power consuming memory module [5, 7, 9, 30].

1.1.2 Two current model of spintronics

The principle of today's spintronic devices are spin-polarized currents. Due to exchange splitting in magnetic materials, the spin up and spin down electrons have different density of states at the Fermi-level and therefore a different amount in the flowing current. In simple magnetic metals (Fe, Ni, Co) the effect of exchange splitting can be described by the Heisenberg model. Exchange energy between spins is given by:

$$\Delta E = -\frac{1}{2} \sum_{i,j} J_{ij} S_i S_j \quad (1.2)$$

Here J_{ij} is the coupling constant (results from the correlation between mean coulomb energy and spin interaction [31]), and $S_{i,j} = \pm \frac{1}{2}$ are the electron spins. Due to minimization of energy, $J > 0$ favors parallel spin alignment and leads

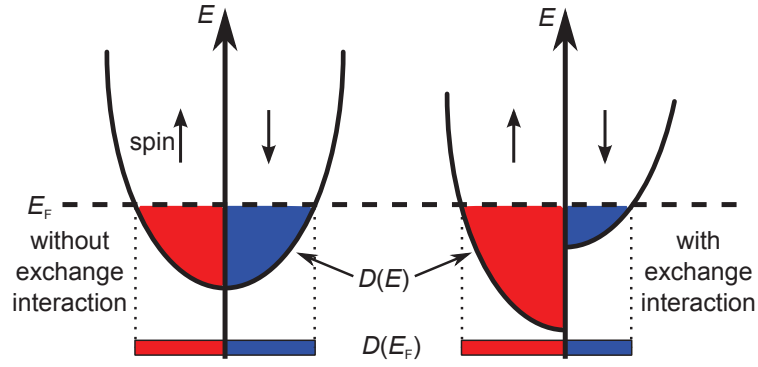


Figure 1.2: Exchange interaction in Metals, shift of the density of states due to the exchange interaction and resulting imbalance of $D_{\uparrow}(E_F)$ and $D_{\downarrow}(E_F)$

to ferromagnetism.

A second approach to describe the exchange interaction is the molecular field \mathbf{h} . Exchange energy is given by $\Delta E = \mathbf{h} \cdot \boldsymbol{\sigma}$. $\sigma = 2\mathbf{s}$ ($= \pm 1$) is the conventional Pauli spin operator [32].

The Pauli exclusion principle forces the growing number of parallel spins to occupy higher energy levels in the majority spin band. A steady state is reached when the energy cost of occupying higher energy levels equals the energy gain due to parallel alignment of spins. The Fermi energy E_F aligns for both spin directions, leading to a shift in the density of states and therefore different density of states at the Fermi level for spin up and down electrons (Figure 1.2).

In simple magnetic metals (Fe, Ni, Co), this effect leads to an energetic splitting of the d-band.

In magnetic complex alloys (e.g. Heusler alloys [33]) and oxides, the situation is more complicated. Band structure calculations predict different densities of states for spin up and spin down electrons. These differences are based on binding geometries and magnetic interactions within the material. The resulting difference at the Fermi level leads to a spin polarization of the current [12, 13].

Generally, the spin polarization P is defined as the difference between the density of states of spin up ($D_{\uparrow}(E_F)$) and spin down ($D_{\downarrow}(E_F)$) electrons at the Fermi level.

$$P = \frac{D_{\uparrow}(E_F) - D_{\downarrow}(E_F)}{D_{\uparrow}(E_F) + D_{\downarrow}(E_F)} \quad (1.3)$$

The keynote for describing spintronic effects is the assumption of two independent currents of spin up and spin down electrons getting added up in parallel ($\frac{1}{R} = \frac{1}{R_{\uparrow}} + \frac{1}{R_{\downarrow}}$) [20]. In order not to mix the spin channels, it is important that spin flip processes are very unlikely and can be neglected [3, 34]. Both spin currents show different transport properties in dependence of the magnetic state of the system, leading to large magnetoresistive effects.

This idea of two independent spin currents with different transport characteristics (scattering and tunneling probabilities) was first proposed by Mott in 1935 [35] and describes the spintronic-based magnetoresistance effects very well.

1.1.3 Giant Magnetoresistance GMR

There are two main magnetoresistive effects described in literature and used in technologies nowadays.

First is the giant magnetoresistance (GMR), discovered independently by the two groups of Albert Fert [1] and Peter Grünberg [2] in 1988. The effect of GMR can be observed in multilayers of magnetic metal films separated by non-magnetic ones (Figure 1.3). First observations were made on the Co/Cu [1] and Fe/Cr systems [2]. Usually, sandwich layers of Co/Cu are used for GMR-devices nowadays [3]. The dominant mechanism for the GMR effect is spin-dependent scattering, both in the bulk and at the interfaces. First ideas on resistance change due to spin-dependent scattering were made in the early 1970s. Albert Fert showed spin-dependent scattering in metals doped with different impurities. Co impurities in Ni scatter strongly the spin down electrons whereas Rh in Ni scatters strongly the spin up electrons. In the ternary alloy Ni(Co+Rh), this leads to a rise in resistivity due to the strong scattering of both spin channels. If one replaces now one type of impurities (Co or Rh) for example by Au, this particular spin channel is opened leading to a decrease in resistivity [3]. This idea was transferred to the above mentioned superlattices containing magnetic layers separated by non-magnetic ones. Now the magnetic layers play the role of impurities and the electrons flowing through have spin-dependent scattering rates.

This effect is known as Mott scattering [34]. In transition metals, scattering into d-states is a major contribution to resistivity. Since the scattering into this bands is proportional to the density of d-states at the Fermi level $D^d(E_F)$, scattering rates of spin up and spin down electrons differ due to the band splitting. Therefore, the resistivity for the spin up and spin down currents are different [36]. This is the so called bulk spin-dependent scattering.

The reason for spin-dependent scattering at the interfaces is the change of band structures of spin up and spin down electrons in the magnetic layer due to exchange splitting [34]. In order to obtain large differences in the scattering probability, the band structure of the non-magnetic metal should fit perfectly to the band structure of one spin channel in the magnetic layers (low scattering probability, low resistivity) and should have a large mismatch to the other one (high scattering probability, high resistivity) [34].

There are two different geometries for GMR-elements: CIP (current in plane) and CPP (current perpendicular to plane, see Figure 1.1 b).

Theoretical descriptions of CIP elements neglect the influence of spin-dependent interface scattering [4, 34, 37]. The numerical solution of the Boltzmann equa-

tion reproduces the main features of CIP-GMR by only taking bulk scattering into account [37]. Nevertheless, interface scattering at rough interfaces adds its contribution to the bulk scattering and gives rise to the GMR-effect [3].

A simple picture for getting an idea on what happens is the so called resistor network theory of GMR [34].

In case of a CIP-GMR element, the current flows parallel to the layers. Now one can argue that the layers simply are resistors in parallel and we have to add up the resistances ($\frac{1}{R} = \sum \frac{1}{R_i}$). This picture is true if the layer thickness of every single layer is large compared to the mean free path of the electrons. In this case the electrons stay confined in their starting layer and the resistances can be added up in parallel (layers and spin channels). But this gives no difference in the resistance of parallel and antiparallel alignments and therefore no GMR.

If the thickness of every single layer is smaller than the mean free path of electrons inside this layer (which is usually in the order of some tens of nm), the current is spread out equally over the whole layer stack. In this limit of a complete intermixing, electrons see a mean value of all single layer resistivities. The resistivity of the layer stack (magnetic unit cell, Figure 1.3 c) in this case is given by

$$\bar{\rho} = \frac{\sum_i d_i \rho_i}{\sum_i d_i} \quad (1.4)$$

with i the layer number in the magnetic unit cell, d_i the thickness and ρ_i the resistivity of layer i . In antiparallel alignment, both spin channels have contributions of large resistivities, giving rise to the overall resistance. In parallel, one spin channel is only affected by small resistivities (low scattering probabilities). This spin channel opens up and contributes to a comparatively low overall resistance of the device in parallel configuration (Figure 1.3 c).

This picture is also the start in finding a description of GMR by solving the Boltzmann equation numerically for the intermediate case between complete separation and complete intermixing of the single layer currents [34, 37].

Understanding of GMR in CPP geometry is much easier. Here the resistivities of single layers and interfaces simply add up.

$$\frac{1}{R} = \frac{1}{R_{\uparrow}} + \frac{1}{R_{\downarrow}} = \frac{1}{\sum R_{\uparrow i}} + \frac{1}{\sum R_{\downarrow i}} \quad (1.5)$$

Therefore, in ferromagnetic (parallel) configuration one spin channel opens up and has a low resistivity, whereas in antiferromagnetic (antiparallel) configuration both spin channels have a rather high resistivity (Figure 1.3 c) [34]. Measurements on CPP devices give the opportunity to determine the contribution of bulk and interface scattering individually [3].

It did not take much time from the first discovery of the principle physical effect to its implementation in technology and consumer products. A milestone was the development of the spin valve structure in 1991 by IBM [38] which

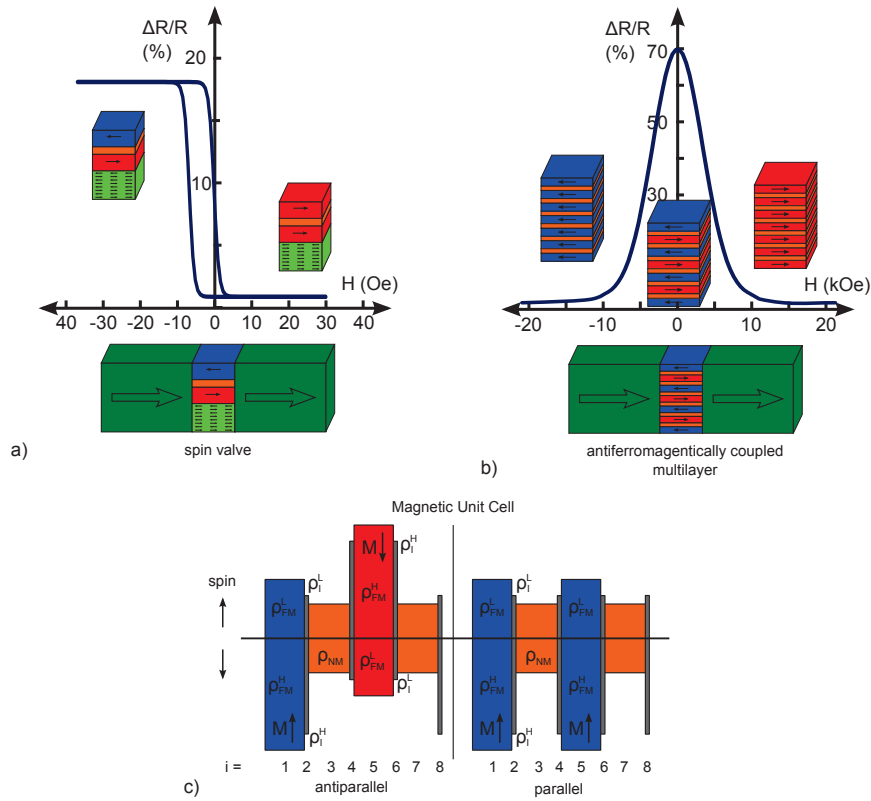


Figure 1.3: a) GMR spin valve with corresponding $R(H)$ -curve. b) Antiferromagnetically coupled multilayer with corresponding $R(H)$ -curve. Note the small switching fields of the spin valve compared to the multilayer. c) Distribution of local resistivities in a magnetic unit cell as basis for the resistor network theory of GMR [20, 23, 34, 38]

allows the use of GMR-based magnetic field sensors in hard disc drives due to its small switching field [3] (see also Figure 1.3). In 1997, IBM developed first GMR-based read heads for hard disc drives and put it on the market [39]. These type of read heads can be found virtually in all hard disc drives on the market until 2005. This emphasizes the technological relevance of spintronic devices. Also the Nobel prize, given to Albert Fert and Peter Grünberg in 2007 for their discovery of the GMR, points out the significance of spintronics. A good overview on the effect and history of GMR provide the Nobel lectures given by Albert Fert [3] and Peter Grünberg [4].

The success of GMR-based read heads originates in the higher magnetoresistive ratios compared to the priorly used AMR (anisotropic magneto resistance, reaches 2% of MR [19]) based heads leading to a higher possible storage density in HDDs (Figure 1.1 a) [20]. Based on antiferromagnetically coupled multilayers, an effect of up to 65% at room temperature (110% at 4.2K) can be achieved [40]. But these components are not suitable for use in read heads due to the high fields that are required to induce the effect (Figure 1.3). With the

commercially used spin valve geometry, an effect of usually 16-18% is achieved at very small applied fields of a few Oersted [20]. The record is 23.4% [41]. The main limiting factor for GMR-based read heads is the low resistance of the layer stack. This means that high currents are needed to produce a sufficient voltage signal for read out [20].

1.1.4 Tunnel Magnetoresistance TMR

Second spintronics-based magnetoresistive effect described in literature and used in technologies nowadays is the tunnel magnetoresistance (TMR). This effect can be observed on samples consisting of two ferromagnetic layers separated by a thin insulating barrier (Figure 1.4). The current through these devices originates from quantum mechanical tunneling of electrons through the thin barrier, which is only a few nanometers thick.

The effect of TMR is based on the dependence of electron tunnel probabilities on the densities of states at the Fermi level ($D(E_F)$) on both sides of the barrier. Due to exchange splitting, the density of states of spin up and spin down electrons are different. This leads to different tunnel probabilities, depending on spin direction and alignment of layer magnetization, and therefore to the observed magnetoresistive effect (see also Section 1.2.5).

Preliminary studies in the beginning of the 1970s on superconductor / insulator / metal layer systems show a spin dependency of the tunnel conductance ($G(V)$) due to magnetic field splitting of quasiparticle states in the superconductor. Tedrow and Meservey measured a symmetric splitting of the $G(V)$ -maximum at the edge of the superconducting gap in dependence on the applied magnetic field [42]. The spin dependency of the tunnel current was confirmed by $G(V)$ -measurements on superconductor / insulator / ferromagnet systems. This measurements show a deviation in the $G(V)$ -curves compared to systems with non-magnetic metals. These deviations, manifesting in differing heights of the split maxima, are related to the spin polarization of the ferromagnet [43] (see also Section 1.2.5). This asymmetry can now be used to derive spin polarizations of different metals below the critical temperature of the used superconductor (superconducting tunneling spectroscopy, STS) [20, 44, 45].

The idea of conductance change in spin-dependent tunneling due to a change in tunnel probability caused by spin polarization was the basis for the discovery of TMR in ferromagnet / insulator / ferromagnet systems. In 1975, Julliere performed conductance measurements on Fe / GeO / Co and found a conductivity change of 14% at low temperatures (4.2 K) between the parallel and antiparallel magnetization state of the ferromagnetic films [11]. He used the formalism of Tedrov and Meservey [43] to describe the measured effect. The combination of spin polarization in ferromagnets, dependence of tunnel probability on the density of states and the magnetization alignment (and therefore the change of "majority" and "minority" spins between the ferromagnetic films in antiparallel

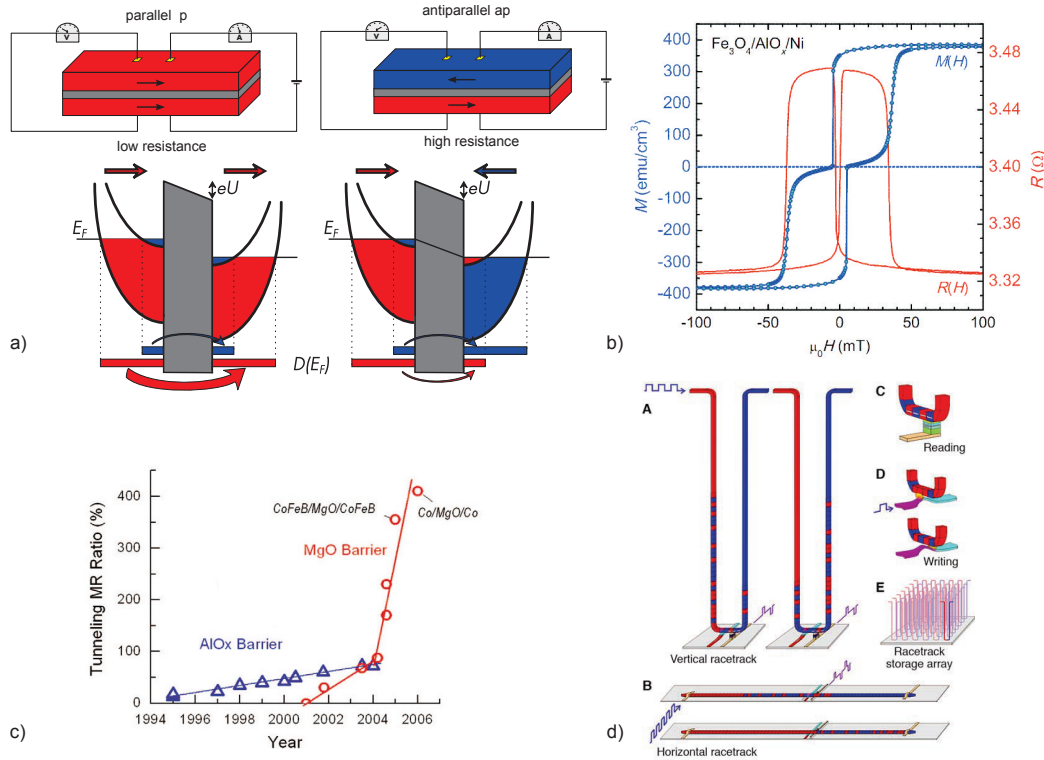


Figure 1.4: a) Sketch of a MTJ (TMR pseudo spin valve) in parallel (low resistance) and antiparallel (high resistance) alignment of magnetizations. The lower part shows the density of states of spin up (red) and spin down (blue) electrons and the resulting tunnel currents. b) resulting $R(H)$, $M(H)$ curves of a TMR pseudo spin valve. Switching from parallel to antiparallel and back is due to the different coercive fields [46]. c) Reported room temperature TMR ratios of Al_2O_3 and MgO -based MTJs. Reprinted from [5], with permission from Elsevier. d) Racetrack Memories. From [47], reprinted with permission from AAAS.

alignment) give a simple formula (see also Section 1.2.5). Julliere used the definition of junction magneto resistance JMR:

$$\text{JMR} = \frac{R_{\uparrow\downarrow} - R_{\uparrow\uparrow}}{R_{\uparrow\downarrow}} = \frac{G_{\uparrow\uparrow} - G_{\uparrow\downarrow}}{G_{\uparrow\uparrow}} = \frac{2P_1P_2}{1 + P_1P_2} \quad (1.6)$$

Today, the definition used to describe the effect is usually TMR, the tunnel magneto resistance. This value is often called "optimistic TMR-value" [48].

$$\text{TMR} = \frac{R_{\uparrow\downarrow} - R_{\uparrow\uparrow}}{R_{\uparrow\uparrow}} = \frac{G_{\uparrow\uparrow} - G_{\uparrow\downarrow}}{G_{\uparrow\downarrow}} = \frac{2P_1P_2}{1 - P_1P_2} \quad (1.7)$$

P_1 and P_2 are the spin polarizations of ferromagnetic electrode one and two, defined in Equation (1.3). This means that a high spin polarization of the tunnel current is required to achieve high TM-ratios.

Due to the fact that TMR could only be found at low temperatures, or only small values at room temperature (2.8% at room temperature in 1991, [49]), there was only slight attention on this effect. The main reason for this small experimental values were immature growth methods to achieve the required interface quality.

The situation drastically changed in 1995 when the groups of Moodera and Miyazaki independently reached room temperature TMR-values above 10%. Moodera reached 12% in CoFe / Al₂O₃ / Co multilayers [50] and Miyazaki 18% in Fe / Al₂O₃ / Fe structures [51]. These values are comparable to GMR-values that are achieved in technological relevant spin valve structures (16-18% [20]). This sufficiently high MR values in combination with several other advantages of TMR over GMR lead to a high interest in the effect of TMR as physical basis for future storage applications. Advantages of TMR over GMR are the fact that TMR elements are natural CPP devices [20], have higher and easily tunable resistances (via barrier thickness [6]) and therefore a much simpler obtainable MR-signal (smaller current densities are needed in order to achieve a sufficient voltage signal for read out, leading to a better signal, less noise and lower power consumption).

As a consequence, TMR-values found in literature steadily increased over the next 15 years (see Figure 1.4 c and [5]) and made this technology interesting for applications.

For nearly ten years, amorphous AlO_x-based MTJs provide the state of the art TMR-values, steadily increasing to a value of 70% in 2004 [52]. During this time, a first MRAM prototype was build by IBM in 1999, utilizing AlO_x-based MTJs providing a TMR-value of 30% [6]. In 2001, theories on MTJs with crystalline MgO barriers predict a TMR up to 1000% due to symmetric spin filtering and coherent spin-polarized tunneling [48, 53, 54]. First experiments on Fe / MgO / Fe(001) reached 27% at room temperature [55]. The use of epitaxial MgO barriers in combination with different electrode materials (Fe, FeCo, CoFeB) and new preparation steps (mainly annealing) leads to a fast increase in TMR-ratios. In 2004, MgO-based MTJs reached TMR values of AlO_x-based ones, namely 88% in Fe / MgO / Fe [54]. The use of textured CoFeB-electrodes led to a value of 355% [56] whereas epitaxial bcc-Co reached 410% in 2006 [57]. A further increase to 500% [58] in 2007 and to 604% in 2008 [59] was achieved by proper annealing of CoFeB / MgO / CoFeB-multilayers resulting in fully epitaxial interfaces. All the TMR values presented here are at room temperature.

In 2005, Seagate brought a first TMR-based read head for HDDs on the market. Other companies followed and today nearly all HDDs are equipped with TMR-based read heads [5]. The first commercial TMR-based MRAM with 4Mb storage capacity was available in 2006 (developed at Everspin, produced and sold by Freescale) [5, 9, 24]. Today, MRAMs (mainly STT-MRAMs) are well established in niche applications requiring reliability in harsh conditions, fast read and write speeds and non-volatility even in unexpected power-off sit-

uations [29].

A new type of memory utilizing TMR is Stuart Parkin's Racetrack Memory (Figure 1.4 d) [9, 47]. Here, the top magnetic electrode of a MTJ is replaced by a ferromagnetic nanowire (racetrack). Digital data is stored on this wire as magnetic domains separated by domain walls. Spin transfer torque-driven domain wall motion is used to move these domains inside the stripe over the read MTJ and the write line. In dependence of the type of domain on top of the magnetic tunnel junction (parallel or antiparallel magnetized in respect to the magnetization direction of the pinned layer), the resistance changes. This allows the electronic read out of data stored on the magnetic nanowire. The advantage of this technology is a high storage density reached by a three dimensional arrangement of read MTJs, vertical racetracks, writing lines and spin-polarized current injection (control of domain wall motion). Compared to TMR-based MRAMs, racetrack memory is much denser, but slower. Therefore it may be considered as replacement of HDDs [9].

High TMR-ratios are not the only value of interest. There is no doubt that this key figure is essential, but other properties of TMR-based devices are also important for a successful commercial use. Device resistance (affecting speed), switching properties, sensitivity, reliability, stability and power consumption are under permanent improvement in order to fit the desired application [20]. These applications contain not only storage of digital data like read heads in HDDs or MRAMs. Also data processing (logic) can be based on spintronic systems utilizing TMR. Examples are ASL (all spin logic) [10] or spin-FETs (spin field effect transistors [60]). Another interesting field is the research on memristive devices and neuronal networks based on spintronics. These devices mimic a human brain and computers based on this technology might be very effective in picture analysis and face recognition [61].

1.1.5 Oxide Based spintronics

Transition metal oxides show interesting physical properties like (anti-)ferromagnetism or ferroelectricity. They can be dielectric, semiconducting or metallic. They also can be multifunctional in the sense that they combine different properties in one single phase material or in an artificial heteroepitaxial multilayer [46, 62]. Therefore, oxides have a large variety of possible applications in spintronics: Some magnetic oxides show large spin polarizations up to half-metallic behavior ($P = 100\%$) [13], others are antiferromagnetic multiferroics which can be used for voltage controlled exchange biasing [63]. Also spin filters based on magnetic insulators are a possible application of oxides [62].

Half metals

Half metals are materials showing metallic behavior for one spin channel and a semiconducting or even insulating behavior in the other spin channel. That means only one spin direction contributes to the charge transport in these

materials, resulting in a large spin polarization of the current (ideally $P = 100\%$) [64]. Therefore, the usage of half metals in spintronics is highly desired and results in high TMR values. Half metallic materials can mainly be found in the groups of Heusler alloys [33, 65] and oxides [13]. Heusler alloys have the drawback of surface oxidation when used in oxide-containing heterostructures (oxide barriers), resulting in a loss of spin polarization at the interface [66]. This problem is avoided by using oxide half metals in spintronic applications. Prominent examples of oxide half metals are manganites and spinel ferrites. Manganites crystallize in the simple perovskite structure. Perovskite materials show many interesting properties, depending on composition and growth conditions [67]. LSMO ($\text{La}_{1-x}\text{Sr}_x\text{MnO}_3$, $x = 0.3-0.4$) is ferromagnetic with a Curie temperature of 360 K and theoretically half-metallic. Measured spin polarizations reach 65 up to 95% (derived from TMR-measurements [13, 68, 69]). Magnetic tunnel junctions of LSMO / STO / LSMO reach a TMR of 1800% at 4.2 K [68]. The record in metal-based MTJs (CoFeB / MgO / CoFeB) is 1144% at 5 K [59].

The problem with LSMO-based MTJs is the temperature dependency of TMR. It disappears at 300 K [68]. This can be explained by the decrease of spin polarization at the LSMO / barrier interface with increasing temperature. Spin polarization vanishes at $T \approx 300$ K [13, 69]. Therefore, room temperature TMR is not possible in this kind of structures.

The spinel ferrite getting most attention in the last decade is magnetite (Fe_3O_4). Its crystal structure is inverse spinel, it is ferrimagnetic with a Curie temperature of 858 K and theory predicts half-metallic behaviour [13, 20, 46]. Fe_3O_4 will be further discussed in Section 2.2.

MTJs of Fe_3O_4 / Al_2O_3 / Co reach a TMR of 20% at room temperature [46], showing the capability of this material class.

Bulk nickel ferrite (NiFe_2O_4) is an insulating, ferrimagnetic inverse spinel [70]. Thin films grown in Ar-atmosphere nevertheless show conductivity, ferrimagnetism ($T_C = 850$ K) and a high spin polarisation of 45% up to room temperature. This is related to cationic inversion of Ni and Fe [70–72]. NiFe_2O_4 / SrTiO_3 / LSMO-MTJs show a TMR of 15-140% at 4 K. The TMR decreases with increasing temperature due to the decrease of spin polarization in LSMO discussed above [13, 71, 72].

Also thin films of zinc ferrite (ZnFe_2O_4) show promising properties for spintronic applications. ZnFe_2O_4 and its properties are discussed in Section 2.3.

Multiferroics

In some complex oxides and oxide heterostructures a coupling of ferroelectric and (anti-)ferromagnetic properties (magnetoelectric coupling) can be observed [46, 63, 73, 74]. These multiferroics show new functionalities and allow, for example, a switching of magnetization by reversing the electric polarization by using a simple voltage pulse [63].

Multiferroic oxides can be divided into two groups: intrinsic and extrinsic

multiferroics. Intrinsic multiferroics are single phase materials showing (anti-)ferromagnetic and ferroelectric order and a magnetoelectric coupling between them [13]. There are only a few examples of intrinsic multiferroics like BiFeO_3 [13, 73] and some hexaferrites like $\text{Ba}_{0.52}\text{Sr}_{2.48}\text{Co}_2\text{Fe}_{24}\text{O}_{41}$ [73], showing magnetoelectric coupling at room temperature.

More promising for room temperature applications are extrinsic multiferroics (artificial heterostructure multiferroics). Different coupling mechanisms at the interface between an (anti-)ferromagnet and a ferroelectric are utilized to achieve a crosscoupling between magnetism and polarization. These proximity effects are strain, spin exchange and charge mediated magnetoelectric coupling [73]. The aim of this heterostructures is to switch the magnetization of the magnetic layer by changing the polarization of the ferroelectric and vice versa.

Most multiferroics show antiferromagnetic ordering. The desired application for these materials is electric field control of exchange biasing and therefore a shifting of the ferromagnetic hysteresis loop of the ferromagnet in contact to the multiferroic antiferromagnet. This can be used to reverse the magnetization of the "free layer" in a MTJ and hence switch the resistance of the device by applying a voltage pulse to the multiferroic in order to switch its electric polarization [63, 73]. There are different experimental works, mainly on BiFeO_3 , that show the capability of this approach. Local control of ferromagnetism by an electric field at room temperature (CoFe/BFO) [75], the control of exchange bias with voltage pulses at low temperatures (LSMO/BFO) [76, 77] and a large exchange bias between BiFeO_3 and CoFeB at room temperature [78] are demonstrated. In 2012, Allibe *et al.* achieved a shift of exchange bias between BFO and CoFeB in a complete GMR spin valve structure by applying different voltage pulses [79]. The change in exchange bias with applied voltage is visible in $\text{GMR}(H)$ measurements of the whole device. Unfortunately, this effect is not reversible. So up to now, an electrically switchable spintronic device is not demonstrated yet.

Spin filters

Ferro- or ferrimagnetic dielectric oxides can be used as spin filters to produce spin-polarized currents. In these materials, the bottom of the conduction bands for spin up and spin down electrons are at different energy levels due to the exchange splitting. Using these materials as barrier layer gives different barrier heights for spin up and down electrons. The exponential dependence of tunneling probability on barrier thickness and -height (Section 1.2.2) leads to different conductivities for spin up and down electrons. This results in a spin polarization of the tunnel current (also called spin filter efficiency) [62]. This effect can be used for efficient injection of spin-polarized currents into semiconductors (overcoming the conductivity mismatch at metal/semiconductor interfaces [80]), for example in ASL (all spin logic) [10, 81] or spin-FETs [60, 82]). Another application are MTJs containing only one magnetic electrode (non-

magnetic, conductive layer / spin filter / magnetic, conductive layer). Examples are spin filters based on NiFe_2O_4 , reaching spin filter efficiencies of 20% at low temperatures [70, 71], and based on CoFe_2O_4 , reaching spin filter efficiencies of 70% at room temperature [83].

Further information on oxide-based spintronics are reviewed in [13, 14, 46].

1.1.6 Further materials for spintronics

Materials suitable for producing spin-polarized currents in spintronic applications like MTJs should fulfill the following requirements:

- a high spin polarization even at room temperature (large T^*)
- a Curie temperature far above room temperature
- a stable magnetization

Transition metals Co, Fe, Ni and their alloys

The three magnetic transition metals Co, Fe and Ni and their alloys are the "classic" electrode materials in spintronic applications. Calculated density of states predict a sufficient bulk spin polarization in these metals (Figure 1.5). Based on these calculations, Fe has a positive spin polarization, whereas Ni and Co show a negative value. Contrary to this results, all spin polarizations of Co, Fe and Ni are positive when measured by Spin Tunneling Spectroscopy (STS) using Al_2O_3 barriers (Table 1.1, [45, 65]). This is due to the influence of the electrode / barrier interface on the tunneling density of states. The spin polarization of the tunneling current depends not on the bulk properties, but on the interface properties (see also Section 1.2.5, page 47 and 49). Therefore, polarization values obtained by STS are the important ones in order to describe the TMR effect in Al_2O_3 -based MTJs. This point is further confirmed by the increase of measured spin polarization by increasing the barrier quality [65] as pointed out in Table 1.1. Barriers containing a large amount of defects give rise to spin flip scattering and therefore decrease the measured spin polarization. MTJs with epitaxial MgO barriers based on bcc Fe, Co, CoFe or CoFeB reach

Table 1.1: Spin polarization of transition metals and alloys derived by Superconducting Tunneling Spectroscopy (STS, tunneling through Al_2O_3 -barriers into a superconductor). The values in the first line are taken from [45]. Values in the second line are polarization values obtained on newer samples, containing cleaner Al_2O_3 barriers [65]. This shows the influence of barrier quality on spin-dependent tunneling. Values in the third row are the Curie temperatures in K [84].

Material:	Ni	Co	Fe	$\text{Ni}_{80}\text{Fe}_{20}$	$\text{Co}_{50}\text{Fe}_{50}$	$\text{Co}_{84}\text{Fe}_{16}$
Spin polarization:	23%	35%	40%	32%		
New values:	33%	42%	44%	48%	55%	55%
Curie temperature:	627	1388	1043			

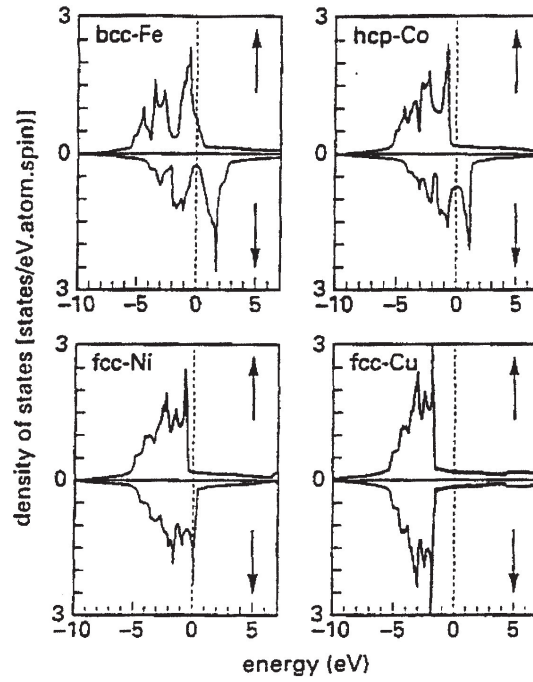


Figure 1.5: Calculated density of states of Fe, Co, Ni and Cu. Figure taken from [65]

much higher TMR values than predicted by the Julliere model using the spin polarization values from Table 1.1 (see Section 1.1.4). An example is CoFeB / MgO / CoFeB, reaching a TMR of 1144% at 5K and 604% at room temperature [59]. The reason for such high TMR values is the effective spin symmetry filtering in epitaxial MgO barriers (see Section 1.2.5, page 45).

Half-metallic Heusler alloys

Heusler alloys are ferromagnetic alloys with a theoretically predicted energy gap in the minority spin band. They therefore should be half-metallic with a spin polarization of 100% [65, 85, 86]. The chemical composition of Heusler alloys is X_2YZ (full Heusler) or XYZ (half-Heusler). X and Y are transition metal elements and Z is a s-p element [87]. Examples are NiMnSb [65], $\text{Co}_2(\text{Cr}_{0.4}\text{Fe}_{0.6})\text{Al}$ and Co_2FeSi [88].

Table 1.2 contains room temperature TMR values of Heusler-based MTJs with Al_2O_3 barriers. These are promising results for the use of Heusler alloys in TMR elements. Unfortunately, Heusler alloys have the drawback of surface oxidation when used in oxide containing heterostructures (oxide barriers), resulting in a loss of spin polarization at the interface [66]. Another problem is the large dependency of the spin polarization P on the crystalline structure and atomic site disorder. Only high quality thin films show a high spin polarization. Therefore, it is difficult to grow Heusler alloy thin films that show

Table 1.2: TMR values of MTJs based on different Heusler alloys. Barrier is amorphous Al_2O_3 in the first three cases and MgO in the last case.

Heusler alloy	counter electrode	TMR (at T)	TMR at RT	
NiMnSb	$\text{Ni}_{80}\text{Fe}_{20}$	7% (77 K)	2.4%	[65]
$\text{Co}_2(\text{Cr}_{0.4}\text{Fe}_{0.6})\text{Al}$	$\text{Co}_{75}\text{Fe}_{25}$	83% (5 K)	52%	[88]
Co_2FeSi	$\text{Co}_{75}\text{Fe}_{25}$	60% (5K)	41%	[88]
$\text{Co}_2\text{FeAl}_{0.5}\text{Si}_{0.5}$	$\text{Co}_2\text{FeAl}_{0.5}\text{Si}_{0.5}$	/	175%	[89]

real half-metallic behavior in MTJs [88]. A nice overview on Heusler-based spintronics is given in [90].

1.2 Theory of Tunnel Magnetoresistance (TMR)

The effect of TMR can be observed in MTJs, consisting of two ferromagnetic metal electrodes separated by a thin insulating barrier. This barrier cannot be crossed by electrons classically. In order to create a current flow through the MTJ, electrons have to tunnel quantum-mechanically through the barrier. The probability of tunneling through the barrier depends on the barrier parameters and the density of states at the Fermi level in both electrodes. Thus, TMR depends strongly on the spin polarization of the ferromagnetic electrodes.

In order to understand the effect of TMR, the effect of quantum tunneling is discussed (Section 1.2.1) and two theories, describing tunnel current in metal / insulator / metal systems, are introduced (Simmons, Section 1.2.2 and BDR, Section 1.2.3). Both models neglect the influence of band structure, and therefore the density of states, due to different assumptions. Unfortunately, there are no theories describing tunnel current in dependence on the band structure of the electrodes. Only numeric calculations on several specific systems exist. This means that the effects of tunnel current and TMR must be addressed separately in order to gain some basic understanding. Finally, the spin-dependent tunneling in ferromagnet / insulator / ferromagnet systems and the resulting magnetoresistance TMR will be discussed.

1.2.1 Quantum tunneling and tunnel currents

Theoretical description of quantum tunneling can be found in most books on quantum mechanics, e.g. in [91, 92].

Quantum mechanical tunneling describes the classically impossible transmission of a particle through a potential barrier. The macroscopic effect is described by the reflectivity (R , probability of being reflected) and the transmittance (C , probability of crossing the barrier). One has $C + R = 1$ which is the conservation of particle number. In case of a thick barrier, experiments give the classically expected result $C = 0$ and $R = 1$. Every particle is reflected. In case of a thin barrier, particles are observed to cross the barrier. Therefore $C > 0$ and $R < 1$. This non-zero probability of crossing the barrier can not be explained by classical mechanics.

In quantum mechanics, particles like electrons are treated as waves functions $\Psi(\mathbf{r}, t)$. $\Psi(\mathbf{r}, t)$ is the solution of the Schrödinger equation

$$i\hbar \frac{\partial}{\partial t} \Psi(\mathbf{r}, t) = \mathbf{H} \Psi(\mathbf{r}, t) \quad \mathbf{H}: \text{Hamiltonian} \quad (1.8)$$

for a particular problem. The square of the amplitude of Ψ ($|\Psi|^2$) is the probability density of presence of the particle. In case of a particle coming from the left and tunneling through a potential barrier $V(x)$ to the right, this probability decays exponentially with barrier thickness, leaving a non zero probability for the particle to cross the barrier (Figure 1.6 a).

In order to describe the tunneling problem mathematically, simply the one-dimensional, stationary Schrödinger equation for a single particle is used. In this case, the Hamiltonian is $\mathbf{H} = -\frac{\hbar^2}{2m} \frac{\partial^2}{\partial x^2} + V(x)$, with $V(x)$ the energy potential along the x-direction. This Hamiltonian is time independent, allowing to use a solution of the form $\Psi(\mathbf{r}, t) = \Psi(\mathbf{r}) \cdot \tau(t) = \Psi(\mathbf{r}) \exp\left(-i\frac{E}{\hbar}t\right)$. This transforms the problem into an eigenvalue equation for the Hamiltonian:

$$E \Psi(\mathbf{r}) = \mathbf{H} \Psi(\mathbf{r}) = \left(-\frac{\hbar^2}{2m} \frac{\partial^2}{\partial x^2} + V(x) \right) \Psi(\mathbf{r}) \quad (1.9)$$

With the potential describing one-dimensional tunneling through a rectangular barrier with height Φ and thickness d

$$V(x) = \begin{cases} 0 & \text{if } x < 0 \\ \Phi = \text{const.} & \text{if } 0 < x < d \\ 0 & \text{if } x > d \end{cases} \quad (1.10)$$

and $\Psi(\mathbf{r}) = \Psi(x)$, the Schrödinger equation has the form:

$$\begin{aligned} -\frac{\hbar^2}{2m} \frac{\partial^2 \Psi_{\text{I}}}{\partial x^2} &= E \Psi_{\text{I}} & (x < 0) \\ -\frac{\hbar^2}{2m} \frac{\partial^2 \Psi_{\text{II}}}{\partial x^2} + \Phi \Psi_{\text{II}} &= E \Psi_{\text{II}} & (0 < x < d) \\ -\frac{\hbar^2}{2m} \frac{\partial^2 \Psi_{\text{III}}}{\partial x^2} &= E \Psi_{\text{III}} & (x > d) \end{aligned} \quad (1.11)$$

The problem is solved by the following ansatz:

$$\begin{aligned} \Psi_{\text{I}} &= e^{ikx} + A e^{-ikx} & \text{mit } k^2 &= \frac{2mE}{\hbar^2} \\ \Psi_{\text{II}} &= B e^{-\kappa x} + C e^{\kappa x} & \text{mit } \kappa^2 &= \frac{2m(\Phi - E)}{\hbar^2} \\ \Psi_{\text{III}} &= D e^{ikx} \end{aligned} \quad (1.12)$$

This ansatz describes a particle coming to the barrier from the left (amplitude 1) with energy $E < \Phi$, getting partially reflected at the barrier (amplitude A) and partially transmitted through the barrier (amplitude D). This means

$$R = |A|^2 \quad \text{and} \quad C = |D|^2 \quad (1.13)$$

The prefactors A , B , C and D are determined by use of the continuity condition for Ψ and $\frac{\partial}{\partial x} \Psi$ at $x = 0$ and $x = d$.

The interesting value describing tunneling of electrons through a thin barrier

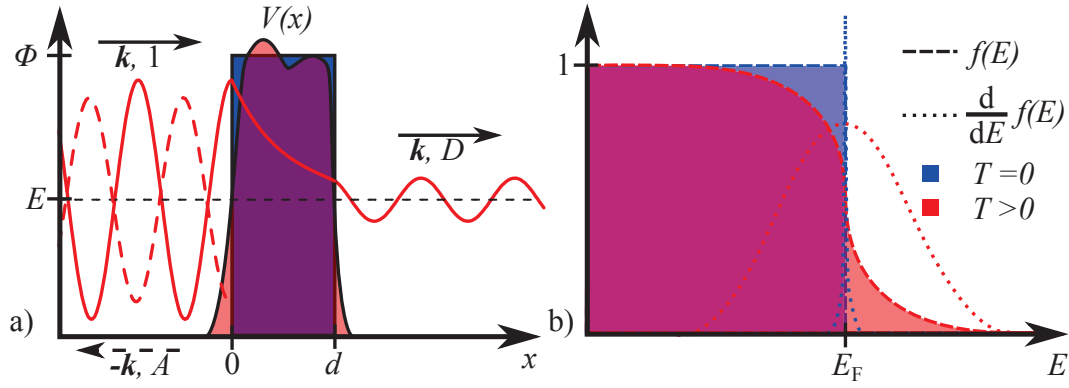


Figure 1.6: a) Potential landscape of a tunnel junction. b) Fermi function and derivatives at temperatures $T=0$ and $T>0$

is the transmission probability C . The determination of D gives

$$C(E) = \frac{1}{1 + \frac{(k^2 + \kappa^2)^2}{4k^2\kappa^2} \cdot \sinh^2(\kappa d)}. \quad (1.14)$$

In the case of $\kappa d \gg 1$, this simplifies to

$$C(E) = \left(\frac{4k\kappa}{k^2 + \kappa^2} \right)^2 e^{-2\kappa d}. \quad (1.15)$$

This formula for C provides the main features of quantum mechanical tunneling: The transmission probability decays exponentially with barrier thickness. Herein the inverse characteristic decay length κ depends on the effective barrier height ($\Phi - E > 0$). For typical barrier heights in the eV-range, $\frac{1}{\kappa} \approx 1\text{\AA}$.

In order to treat inhomogeneous barriers of the form $\Phi(x)$ (continuous, smooth function), the WKB-approximation (also called Asymptotic Approximation) [31, 93] is used in most descriptions of the tunnel effect [94, 95]. Here, a diffuse barrier is assumed where the band structure of the M/I/M system varies slowly compared to the electron wavelength [95]. This assumes no sharp edges in the potential at the interfaces and is maybe better suited than the exact solution because of a potential change (rounding) due to image forces [94]. The general solution of transmission probability C in quantum mechanical tunneling in the WKB approximation is [31, 93]:

$$C(E) = \exp \left(-\frac{2}{\hbar} \int_0^d \sqrt{2m(\Phi(x) - E)} dx \right) \quad (1.16)$$

For a rectangular barrier ($\Phi(x) = \Phi = \text{const.}$) we get:

$$C(E) = \exp\left(-\frac{2}{\hbar}\sqrt{2m(\Phi - E)} d\right) = e^{-2\kappa d} \quad (1.17)$$

In comparison to the exact solution for $\kappa d \gg 1$ (Equation (1.15)), the prefactor is missing. The difference in the theoretical description of tunnel current between the exact solution and the WKB approximation is discussed by Brinkman, Dynes and Rowels in [95] and Harrison in [96] (see also page 30).

In case of two solid state electrodes (metal, semiconductor) separated by an insulating barrier, electrons can only tunnel from a filled energy state in electrode 1 into an empty state in electrode 2 (Fermi's golden rule) [97]. The number of available states at a specific energy level is given by the density of states $D(E)$. Whether a state is empty or filled is described by the Fermi function:

$$f(E, T) = \frac{1}{\exp\left(\frac{E - E_F}{k_B T}\right) + 1} \quad (1.18)$$

At temperature $T = 0$, all energy states below E_F are filled, all above are empty and $f(E, T = 0)$ is a step function. For $T > 0$ the distribution changes gradually around E_F , allowing empty states below and filled states above E_F (Figure 1.6 b). In steady state ($V = 0$), Fermi energies of both electrodes are equal ($E_F^1 = E_F^2 = E_F$) (see Figure 1.7 and 1.8 in case of $V = 0$).

In the following calculations, the temperature is set to zero ($T = 0$). If we now apply a small voltage V between the two electrodes, electrons can tunnel into the opposing energy states ($D_1(E) \leftrightarrow D_2(E + eV)$, elastic tunneling, energy conservation). Filled energetic states in an electrode are given by $D(E)f(E)$, empty ones by $D(E)[1 - f(E)]$. If the golden rule is fulfilled, electrons can tunnel through the barrier with a probability of $C(E)$ (Equation (1.15) and (1.17), due to a small applied voltage, $C(E)$ is assumed to be independent of V).

Due to this considerations, the current from electrode 1 to 2 through the barrier can be written as

$$I_{1 \rightarrow 2} \approx \int_{-\infty}^{\infty} C(E) D_1(E) f(E) \cdot D_2(E + eV) [1 - f(E + eV)] dE \quad (1.19)$$

Using the same arguments, the current from electrode 2 to 1 is

$$I_{2 \rightarrow 1} \approx \int_{-\infty}^{\infty} C(E) D_1(E) [1 - f(E)] \cdot D_2(E + eV) f(E + eV) dE \quad (1.20)$$

This results in a total current of

$$I(V) = I_{1 \rightarrow 2} - I_{2 \rightarrow 1} \sim \int_{-\infty}^{\infty} C(E) D_1(E) D_2(E + eV) [f(E) - f(E + eV)] dE \quad (1.21)$$

In order to solve this integral, the Fermi function is analyzed more closely. Since V is small and the temperature is assumed to be zero ($T = 0$), we can rewrite $f(E) - f(E + eV)$ the following way:

$$f(E) - f(E + eV) = eV \frac{f(E) - f(E + eV)}{eV} \approx eV \frac{d}{dE} f(E) \quad (1.22)$$

The derivation of the Fermi function at low temperatures becomes the Dirac delta $\delta(E - E_F)$ (Figure 1.6 b)

$$\frac{d}{dE} f(E) \xrightarrow{T \rightarrow 0} \delta(E - E_F). \quad (1.23)$$

Therefore the total current through the barrier can be described as

$$I(V) \approx \int_{-\infty}^{\infty} C(E) D_1(E) D_2(E + eV) eV \delta(E - E_F) dE = C(E_F) D_1(E_F) D_2(E_F) eV. \quad (1.24)$$

This describes an ohmic I - V curve with conductance G

$$G(V) = \frac{dI}{dV} = eC(E_F) D_1(E_F) D_2(E_F) \quad (1.25)$$

From this formula, one can derive a few basic properties of the tunnel current through a tunnel junction. The I - V characteristic at small applied voltages V is ohmic. Conductance depends on barrier parameters ($C(E_F)$ depends on barrier height and thickness) and the density of states at the Fermi level $D(E_F)$ in both electrodes. Derivation after [98].

1.2.2 Simmons-Model

In 1963, Simmons described the current density of electrons tunneling through a thin potential barrier of arbitrary shape [94]. In order to neglect thermal currents over the barrier, low temperatures are assumed ($T \approx 0$). The starting point of his calculations was similar to Equation (1.21). He approximated the density of states in the electrodes ($D(E)$) by the expression of the free electron gas. To calculate the tunnel probability $C(E)$ of a single electron at energy E

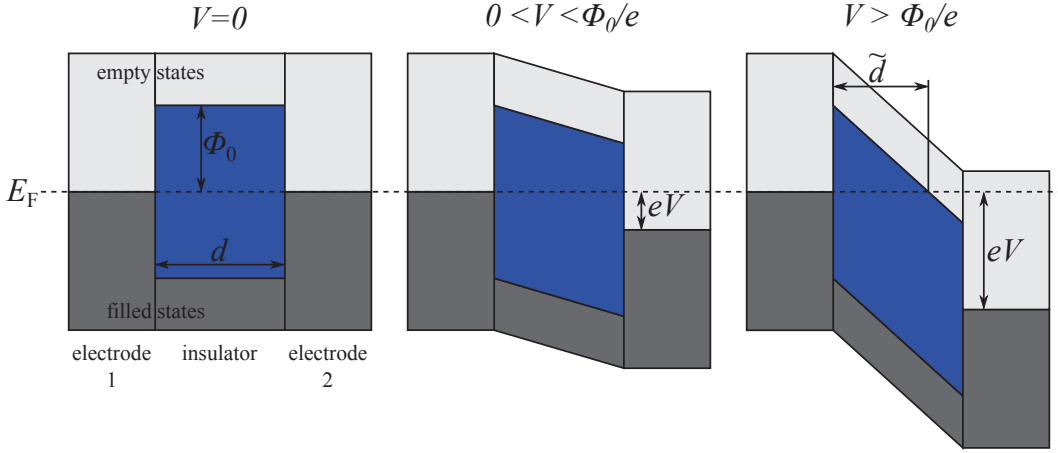


Figure 1.7: Barrier geometries for the Simmons-Model and its dependency on applied voltage. In case of $V > \Phi_0/e$ one has $\tilde{d} = d \cdot \frac{\Phi_0}{eV}$

he used the WKB formula (Equation (1.16)):

$$C(E) \approx \exp \left(-2 \int_0^d \kappa(x, E) dx \right) = \exp \left(-\frac{2}{\hbar} \int_0^d \sqrt{2m(\Phi(x) - E)} dx \right) \quad (1.26)$$

A key point in his description is the approximation of the arbitrary barrier shape $\Phi(x)$ by a mean barrier height $\bar{\Phi}$. This leads to the assumption of a symmetric, rectangular barrier (Figure 1.7).

$$\bar{\Phi} = \frac{1}{d} \int_0^d \Phi(x) dx \quad (= \Phi_0 \quad \text{at } V \approx 0) \quad (1.27)$$

Applying all these assumptions and calculating the integrals leads to a general formula for the current density through a potential barrier:

$$j(V) = \frac{e}{4\pi^2 \hbar d^2} \left\{ \bar{\Phi} \cdot \exp \left(-\frac{2\sqrt{2m}}{\hbar} \sqrt{\bar{\Phi}} d \right) - (\bar{\Phi} + eV) \cdot \exp \left(-\frac{2\sqrt{2m}}{\hbar} \sqrt{\bar{\Phi} + eV} d \right) \right\} \quad (1.28)$$

For low voltages ($0 \approx V \ll \Phi_0/e$), we can assume the potential to be independent of the applied voltage V . In this case the formula for the tunnel current density simplifies to

$$j(V) = \frac{e^2 \sqrt{2m}}{4\pi^2 \hbar^2} \cdot \frac{\sqrt{\Phi_0}}{d} \cdot \exp \left(-\frac{2\sqrt{2m}}{\hbar} \sqrt{\Phi_0} d \right) \cdot V \quad (1.29)$$

This describes an ohmic j - V -curve at small applied voltages, like Equation (1.24).

For higher voltages V , we have to take the voltage dependency of the barrier shape into account. Simmons introduced a linear deformation of the potential with applied voltage V :

$$\tilde{\Phi}(x) = \Phi(x) - \frac{x}{d}eV \quad (1.30)$$

This leads to a mean barrier height depending linearly on the applied voltage V

$$\bar{\Phi} = \Phi_0 - \frac{eV}{2} \quad (1.31)$$

Plugging this expression for the mean barrier height $\bar{\Phi}$ into Equation (1.28) leads to:

$$j(V) = \frac{e}{4\pi^2\hbar d^2} \left\{ \left(\Phi_0 - \frac{eV}{2} \right) \cdot \exp \left[-\frac{2\sqrt{2m}}{\hbar} \cdot \sqrt{\left(\Phi_0 - \frac{eV}{2} \right) d} \right] - \left(\Phi_0 + \frac{eV}{2} \right) \cdot \exp \left[-\frac{2\sqrt{2m}}{\hbar} \cdot \sqrt{\left(\Phi_0 + \frac{eV}{2} \right) d} \right] \right\} \quad (1.32)$$

This expression is valid for $0 < V < \Phi_0$. Figure 1.10 shows calculated j - V -curves of the Simmons model for different parameters. They show the typical S-shape for tunnel current j - V -curves with a linear part around $V = 0$. The linear part is described by Equation (1.29), which can also be derived by differentiation of Equation (1.32) at $V \approx 0$. The $G(V)$ curves in Figure 1.10 are calculated by numerical differentiation of Equation (1.32).

Voltages larger than the mean barrier height ($V > \bar{\Phi}_0$) lead to a change in the potential landscape. The barrier thickness changes due to the fact that parts of the potential fall below E_F of the first electrode. Electrons are now able to tunnel into the conduction band of the insulator. This changes the effective barrier thickness (see Figure 1.7). In this case, the formula for $j(V)$ derived by Simmons is:

$$j(V) = \frac{2.2e^3V^2}{16\pi^2\hbar\Phi_0d^2} \left\{ \exp \left[-\frac{2d}{2.96\hbar eV} \sqrt{2m\Phi_0^3} \right] - \left(1 + \frac{2eV}{\Phi_0} \right) \cdot \exp \left[-\frac{2d}{2.96\hbar eV} \sqrt{2m\Phi_0^3} \sqrt{1 + \frac{2eV}{\Phi_0}} \right] \right\} \quad (1.33)$$

For even higher voltages the second term in Equation (1.33) vanishes. The resulting formula is similar to the Fowler-Nordheim-Equation [31, 99–101],

describing field emission.

$$j(V) = \frac{2.2e^3V^2}{16\pi^2\hbar\Phi_0d^2} \exp \left[-\frac{2d}{2.96\hbar eV} \sqrt{2m\Phi_0^3} \right] \quad (1.34)$$

1.2.3 Brinkman-Dynes-Rowell-Model (BDR-Model)

In 1970, Brinkman, Dynes and Rowell expanded the theory of tunneling through a thin symmetric (rectangular) barrier to an asymmetric (trapezoidal) one [95]. They used the WKB-approximation and the independent particle model as starting point. In order to describe the asymmetry of the barrier, they assumed a trapezoidal shape of the potential Φ .

$$\Phi(x, V) = \Phi_1 + \frac{x}{d}(\Phi_1 - \Phi_2 - eV) = \Phi_1 - \frac{x}{d}(\Delta\Phi + eV) \quad (1.35)$$

Here, $\Delta\Phi = \Phi_2 - \Phi_1$ is the asymmetry parameter and Φ_1 and Φ_2 the left and right barrier heights, respectively. These two values differ due to the different work functions of the electrode materials. Other used barrier parameters are the mean barrier height $\bar{\Phi} = \frac{1}{2}(\Phi_1 + \Phi_2)$ and barrier thickness d (Figure 1.8). These assumptions were put together into a basic equation for the current density similar to Equation (1.21). The resulting current density $j(V)$ was calculated numerically by computer, assuming $T = 0$ K. From this result, Brinkman *et al.* derived an expression for the conductance by numerical differentiation ($G(V) = \frac{\partial j}{\partial V}(V)$). The next step was to expand the expression for the conductance in powers of voltage to obtain an approximated expressions for the linear and quadratic terms. The resulting formula is roughly accurate to 10% if $d > 10 \text{ \AA}$ and $\frac{\Delta\Phi}{\bar{\Phi}} < 1$.

After Brinkman *et al.* [95], the conductance $G(V)$ of an asymmetric barrier is given by:

$$\frac{G(V)}{G(0)} = 1 - \left(\frac{\sqrt{2m} d \Delta\Phi}{12\hbar \bar{\Phi}^{\frac{3}{2}}} \right) eV + \left(\frac{m d^2}{4\hbar^2 \bar{\Phi}} \right) (eV)^2 \quad (1.36)$$

with the conductance at $V = 0$:

$$G(0) = \frac{e^2 \sqrt{2m} \sqrt{\bar{\Phi}}}{4\pi^2 \hbar^2 d} \cdot \exp \left(-\frac{2\sqrt{2m}}{\hbar} d \sqrt{\bar{\Phi}} \right). \quad (1.37)$$

We note that it is the same formula as the approximation for small applied voltages V in the Simmons model (Equation (1.29)). Also in this model, the j - V -characteristic is linear for small applied voltages $V \approx 0$. Integrating Equation (1.36) over the applied voltage V and assuming the integration constant

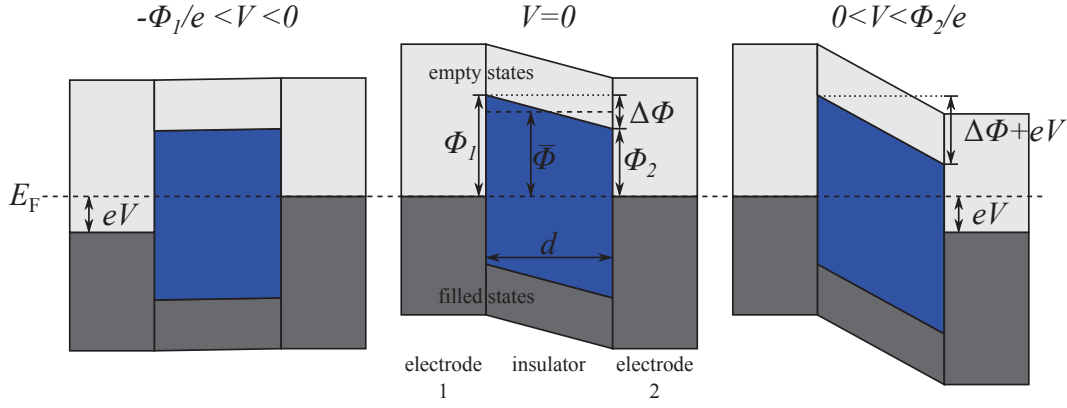


Figure 1.8: Barrier geometries for the BDR-Model, comparison of $\pm V$ displays the voltage asymmetry in $G(V)$

equal to zero (no current at zero voltage), results in the tunnel current density:

$$\begin{aligned}
 j(V) &= \int_{j(0)=0} G(V) dV = \\
 &= G(0) \left[V - \left(\frac{e\sqrt{2m}}{24\hbar} \frac{d\Delta\Phi}{\bar{\Phi}^{\frac{3}{2}}} \right) \cdot V^2 + \left(\frac{e^2 m d^2}{12\hbar^2 \bar{\Phi}} \right) \cdot V^3 \right] \quad (1.38)
 \end{aligned}$$

This j - V -characteristic shows also the typical S-shape of tunnel current and has a ohmic part around $V \approx 0$ (see Figure 1.10).

The $G(V)$ curve shows a "roughly" parabolic shape ("roughly " parabolic means that a simple parabola fits the data within an error of 5% at low voltages) with a characteristic shift of the minimum away from $V = 0$. The minimum of $G(V)$ occurs at

$$V_{\min} = \frac{\hbar}{3e\sqrt{2m}} \cdot \frac{\Delta\Phi}{d\sqrt{\bar{\Phi}}} \quad (1.39)$$

This asymmetry is originated in the exponential weighting factor of the WKB approximation. Therefore, changes in the model of the barrier should not affect the shape of the $G(V)$ curve. Brinkman *et al.* showed this fact by including image forces into the model. Compared to the trapezoidal potential shape (Equation (1.35)), image forces round off the corners of the potential. This leads to an overall increase of the conductance, but doesn't change the shape of the $G(V)$ curve.

If the formula of the tunnel current is derived using the WKB approximation, the energy dependent terms cancel out [96]. This is a result of the applied independent particle model. Therefore, the result is independent of the Fermi energy E_F and the density of states $D(E_F)$ [95].

Harrison [96] and Brinkman *et al.* [95] state that the use of the exact transmission probability (sharp boundary at barrier interfaces) leads to a tunnel current depending on the density of states. Therefore, Harrison points out

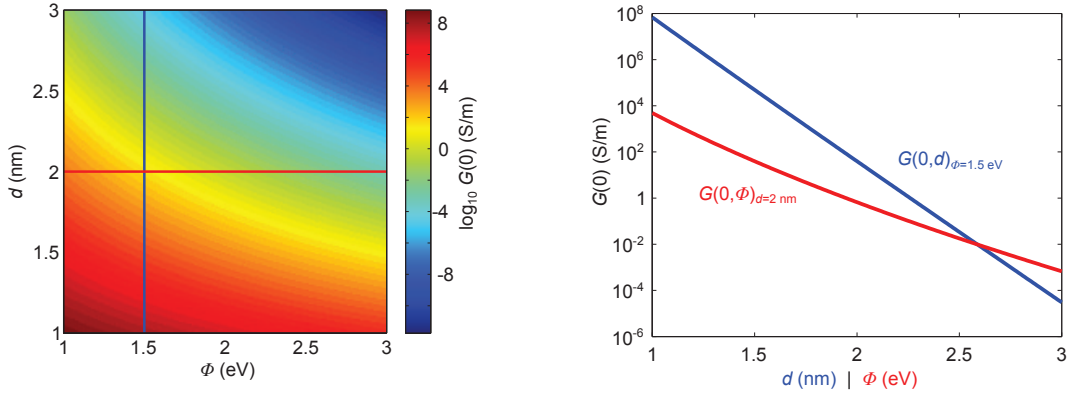


Figure 1.9: The zero conductance $G(0)$ in dependence of barrier thickness d and barrier height Φ (Equation (1.29) and (1.37)). $G(0)$ decays exponentially with d and $\sqrt{\Phi}$.

the possibility of an "interesting behavior with [...] transition metals" in 1961, probably predicting the effect of TMR [96]. In the same publication he also mentions that the independent particle model fails in the case of sharp boundaries and the WKB approximation gives good results for a barrier thickness large compared to a single electron wavelength. Therefore, the model based on the WKB approximation is used to describe the tunnel currents in this work (Equation (1.36) and (1.38)).

1.2.4 Expansion of Both basic Models

Simmons model with asymmetric barriers

In a second publication, Simmons also expanded his model to asymmetric barriers [102]. In this case, it is $\Delta\Phi = \Phi_1 - \Phi_2 \neq 0$, and the tunnel current density is generally described by Equation (1.28). Simmons found a symmetric behavior of the $j(V)$ characteristic at applied voltages $V < \min(\Phi_1, \Phi_2)/e$. The reason is his definition of the mean barrier height $\bar{\Phi}$ and effective thickness Δd (instead of d in Equation (1.28)). In case of $V < \Phi_1/e$ or $V < \Phi_2/e$ in the forward- or reverse-biased case, respectively, it is

$$\bar{\Phi} = \frac{\Phi_1 + \Phi_2 - eV}{2} \quad \Delta d = d \quad (1.40)$$

in both cases. Therefore, the $j(V)$ characteristic is symmetric and can be described as

$$j(V) = \theta(V + \gamma V^3) \quad (1.41)$$

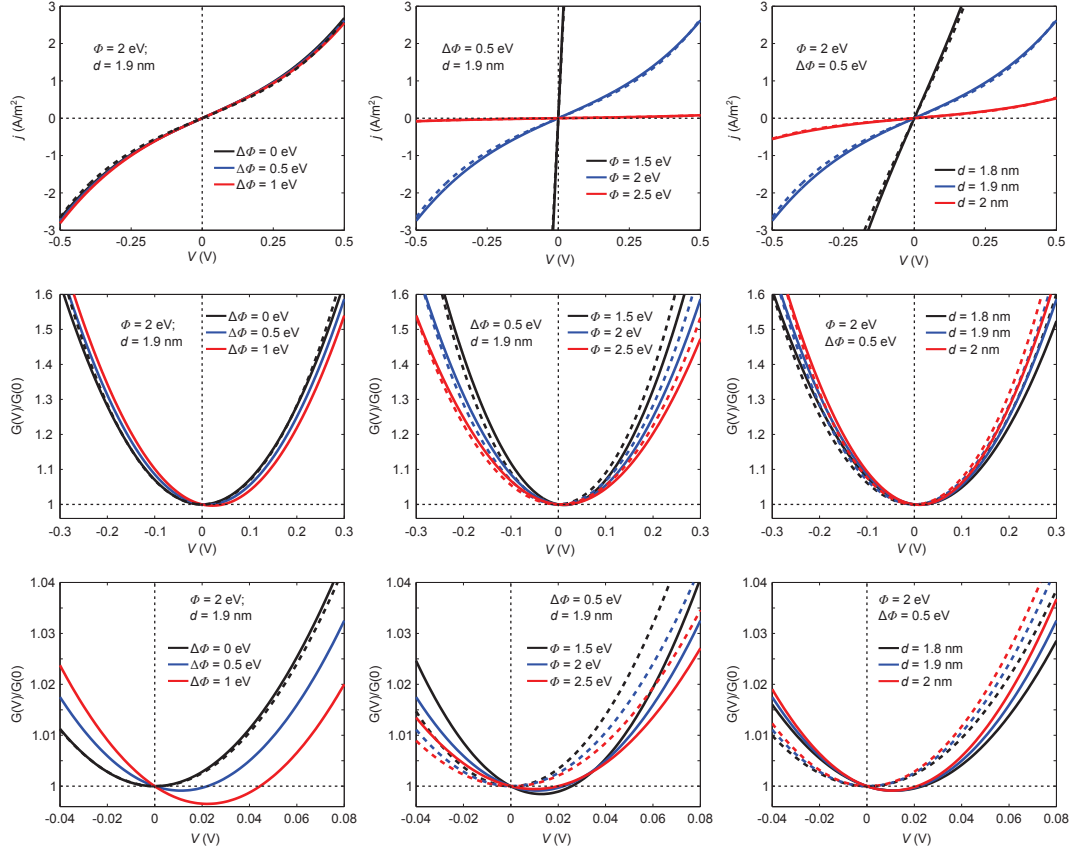


Figure 1.10: $j(V)$ and $G(V)$ curves calculated by the Simmons model (---, Equation (1.32) and numerical differentiation) and the BDR model (—, Equation (1.36) and (1.38)) for different barrier parameters. Here $\Phi = \Phi_0 = \bar{\Phi}$. $G(V)/G(0)$ is displayed for clarity due to the strong dependence of $G(0)$ on barrier thickness d and barrier height Φ (Figure 1.9).

$j(V)$ curves show the typical S-shape of tunnel current characteristics and ohmic behavior around $V = 0$. The strong dependence on barrier thickness d and barrier height Φ can be seen clearly. The difference in both models due to the asymmetry parameter $\Delta\Phi$ is weak in the $j(V)$ depiction.

The influence of barrier asymmetry gets clear if one compares the $G(V)$ curves calculated by the two different models. If calculated by the BDR model, $G(V)$ curves show a characteristic shift of the minimum away from $V = 0$. The asymmetry also can be recognized at higher voltages as deviation from the symmetric Simmons model. In order to illustrate the shift of $G(V)$ around $V = 0$ due to barrier asymmetry (Equation (1.39)), the bottom row shows enlarged views of the curves.

Regardless of the model used to calculate them, all $G(V)$ curves show a "roughly" parabolic shape.

with

$$\begin{aligned}\theta &= \left(\frac{e}{2\pi\hbar}\right)^2 \frac{\sqrt{m(\Phi_1 + \Phi_2)}}{d} \exp\left(-D\sqrt{\frac{\Phi_1 + \Phi_2}{2}}\right) \\ \gamma &= \frac{D^2 e^2}{48(\Phi_1 + \Phi_2)} - \frac{De^2}{32} \left[\frac{2}{\Phi_1 + \Phi_2}\right]^{\frac{3}{2}} \\ D &= \frac{2\sqrt{2m}d}{\hbar}\end{aligned}\tag{1.42}$$

It only depends on the mean barrier height $\bar{\Phi} = (\Phi_1 + \Phi_2)/2$ and barrier thickness d . This formula reduces to an ohmic characteristic at $V \approx 0$ equal to Equation (1.29).

Asymmetries in the $j(V)$ characteristics are obtained in the high voltage range. These asymmetries are assigned to the differences in barrier height and effective thickness due to a large distortion of the barrier as shown in Figure 1.7. In case of reverse-biased electrodes and an applied voltage $V > \Phi_2/e$, the mean barrier height and effective thickness are

$$\bar{\Phi} = \frac{\Phi_1}{2} \quad \Delta d = d \cdot \frac{\Phi_1}{eV - \Delta\Phi}\tag{1.43}$$

In contrast, if the electrodes are forward-biased and the applied voltage is larger than Φ_1/e , mean barrier height and effective thickness are given by:

$$\bar{\Phi} = \frac{\Phi_2}{2} \quad \Delta d = d \cdot \frac{\Phi_2}{eV - \Delta\Phi}\tag{1.44}$$

If these different expressions for Δd and $\bar{\Phi}$ are put into Equation (1.28), the asymmetry between forward- and reverse-bias becomes apparent. In contrast to the BDR-model [95], the asymmetric Simmons model does not include the characteristic shift of the conductance minimum nor the asymmetry at small voltages. In Equation (1.41), the factor θ is equal to $G(0)$ in the BDR model and γ shows similarities to the prefactors (V^2 and V^3) in Equation (1.38).

One year after the publication of Simmons, Hartman pointed out an error in the approximations done by Simmons. This approximations lead to the neglect of asymmetries at small voltages [103].

Temperature dependence of tunnel current

In the original derivation of the Simmons model, low temperatures ($T \approx 0$) are assumed. Therefore, Equation (1.21) can be simplified by using the Dirac δ distribution (Equation (1.22) and (1.23)). If the tunnel current at finite temperatures $T > 0$ and its temperature dependence is of interest, one has to calculate the integral of $f(E, T) - f(E + eV, T)$ over E . $f(E, T)$, the Fermi function, is temperature dependent and given by Equation (1.18). The term

$f(E, T) - f(E + eV, T)$ describes the amount of facing states involved in the tunnel process (see Figure 1.13). With increasing temperature and applied voltage, this bell-shaped curve becomes wider.

The step of calculating the tunnel current at finite temperatures was done by Stratton [104] numerically, resulting in rather complicated expressions. In his description, physical quantities of the barrier hide inside integrals, that can only be solved numerically. This makes it hardly possible to describe the effect of barrier parameter on the temperature dependence of tunnel current [105] and also makes it rather uncomfortable for data evaluation [106]. Only qualitative correlation with experiments is given.

The main finding of Strattons calculations was

$$j(T) \propto \frac{\pi c_1 k_B T}{\sin(\pi c_1 k_B T)} \quad (1.45)$$

with

$$c_1 = \frac{\sqrt{2m}}{\hbar} \int_0^d \frac{1}{\sqrt{\Phi(x, V) - E_F}} dx, \quad (1.46)$$

describing the main temperature dependence of tunnel current.

Simmons calculated this expression in terms of the generalized theory and included the physical constants explicitly [105]. The temperature dependence at a given voltage is determined as:

$$\frac{j(V, T)}{j(V, 0)} = \frac{\frac{\pi\sqrt{2m}}{\hbar} \frac{\Delta d}{\sqrt{\Phi}} k_B T}{\sin\left(\frac{\pi\sqrt{2m}}{\hbar} \frac{\Delta d}{\sqrt{\Phi}} k_B T\right)} = \frac{A \frac{\Delta d}{\sqrt{\Phi}} k_B T}{\sin\left(A \frac{\Delta d}{\sqrt{\Phi}} k_B T\right)} \quad (1.47)$$

This can be expressed as

$$\begin{aligned} j(V, T) &= j(V, 0) \left(1 + \frac{1}{6} \left(A \frac{\Delta d}{\sqrt{\Phi}} k_B T \right)^2 + \dots \right) = \\ &= j(V, 0) \left(1 + \frac{1}{6} A^2 \frac{\Delta d^2}{\Phi} k_B^2 T^2 \right) \end{aligned} \quad (1.48)$$

This formula is valid for symmetric ($\bar{\Phi}_0 = \Phi_0$) and asymmetric ($\bar{\Phi}_0 = (\Phi_1 + \Phi_2)/2$) barriers at intermediate voltages $V < \min(\Phi_1, \Phi_2)$. At high voltages, d and $\bar{\Phi}$ are given by Equation (1.43) and (1.44) leading to a difference in reverse and forward high voltage temperature characteristics in the case of an asymmetric barrier.

In order to understand these differences, the relative changes in current are further investigated:

$$\hat{j} = \frac{j(V, T) - j(V, 0)}{j(V, 0)} \quad (1.49)$$

For a symmetric barrier and in case of $eV < \Phi_0$, $\bar{\Phi}$ and Δd are:

$$\bar{\Phi} = \Phi_0 - \frac{eV}{2} \quad \Delta d = d \quad (1.50)$$

and in case of $eV > \Phi_0$, it is

$$\bar{\Phi} = \frac{\Phi_0}{2} \quad \Delta d = d \cdot \frac{\Phi_0}{eV} \quad (1.51)$$

This results in the following expressions for the relative current change in case of a symmetric barrier:

$$\hat{j} = \begin{cases} \frac{1}{6} A^2 \frac{d^2}{\Phi_0 - \frac{eV}{2}} k_B^2 T^2 & \text{if } eV < \Phi_0 \\ \frac{1}{3} A^2 \Phi_0 \frac{d^2}{(eV)^2} k_B^2 T^2 & \text{if } eV > \Phi_0 \end{cases} \quad (1.52)$$

Regarding an asymmetric barrier at reverse bias, $\bar{\Phi}$ and Δd are given by Equation (1.40) ($eV < \Phi_2$) and Equation (1.43) ($eV > \Phi_2$). The relative current change with temperature now is described by

$$\hat{j}_1 = \begin{cases} \frac{1}{3} A^2 \frac{d^2}{(\Phi_1 + \Phi_2 - eV)} k_B^2 T^2 & \text{if } eV < \Phi_2 \\ \frac{1}{3} A^2 \Phi_1 \frac{d^2}{(eV - \Delta\Phi)^2} k_B^2 T^2 & \text{if } eV > \Phi_2 \end{cases} \quad (1.53)$$

At forward bias, we have a slightly different symmetry and $\bar{\Phi}$ and Δd are defined as in Equation (1.40) ($eV < \Phi_1$) and Equation (1.44) ($eV > \Phi_1$). Therefore the relative change in current in case of forward bias is:

$$\hat{j}_2 = \begin{cases} \frac{1}{3} A^2 \frac{d^2}{(\Phi_1 + \Phi_2 - eV)} k_B^2 T^2 & \text{if } eV < \Phi_1 \\ \frac{1}{3} A^2 \Phi_2 \frac{d^2}{(eV - \Delta\Phi)^2} k_B^2 T^2 & \text{if } eV > \Phi_1 \end{cases} \quad (1.54)$$

Figure 1.11 a) shows the relative current change at 300 K for barrier heights $\Phi_1 = 1 \text{ eV}$ and $\Phi_2 = 1.5 \text{ eV}$ and $d = 20 \text{ \AA}$. One can clearly see a bunch of characteristic features:

At intermediate voltages, \hat{j}_1 is equal to \hat{j}_2 and both follow a $1/(1 - (eV/\bar{\Phi}))$ -law. As the voltage exceeds Φ_1/e , \hat{j}_2 decreases and \hat{j}_1 increases further until $V = \Phi_2/e$. The decrease is described by a $1/V$ -law.

Therefore, the change of the tunnel current with temperature (\hat{j}) has a maximum at $eV = \Phi_0$, or $eV = \Phi_1$ and Φ_2 , respectively. This can be used to determine the barrier heights of symmetric and asymmetric barriers.

Figure 1.11 b) shows an experimental result on $\text{Al}/\text{Al}_2\text{O}_3/\text{Al}$ [106]. The obtained change of tunnel current with temperature at a fixed applied voltage $V = 0.5 \text{ V}$ is shown in a $\log(\Delta j)$ - $\log(T)$ -plot ($\Delta j = j(T) - j(0)$). The obtained slope is 2.04, which is in accordance to Simmons' result (Equation (1.48)), and $\Delta j \propto T^2$. In Figure 1.11 b), a second fit is shown. It includes the terms

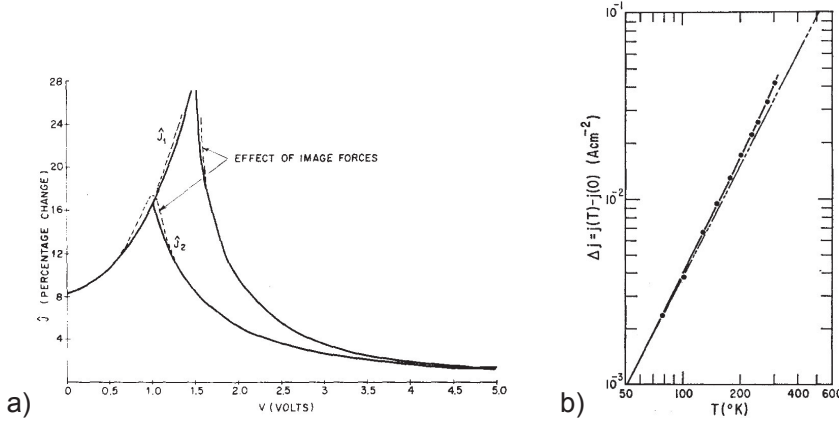


Figure 1.11: a) Relative current change \hat{j}_1 and \hat{j}_2 at 300 K in dependence of the applied voltage for barrier heights $\Phi_1 = 1$ V and $\Phi_2 = 1.5$ V and $d=20$ Å. Reprinted with permission from [105]. Copyright 1964, AIP Publishing LLC. b) Current density change in dependence of temperature at 0.5 V of an Al / Al₂O₃ / Al junction. The dashed line is the T^2 approximation (Equation (1.48)), the solid one corresponds to Equation (1.55) and includes the T^4 term. Figure taken from [106]. Copyright 1964 by the American Physical Society.

proportional to T^4 and fits the experimental data at higher temperatures up to room temperature much better than the pure T^2 -term. Hartman [106] therefore proposes to include the T^4 -term which leads to:

$$j(V, T) = j(V, 0) \left(1 + \frac{1}{6} A^2 \frac{\Delta d^2}{\Phi} k_B^2 T^2 + \frac{7}{360} A^4 \frac{\Delta d^4}{\Phi^2} k_B^4 T^4 \right) \quad (1.55)$$

Influence of image force potentials on tunnel current

Electrons flowing through the barrier lead to image charges at the interfaces. These charges induce the so called image force potential which rounds the corners of the potential. This leads to a reduction of the mean barrier height as well as the effective barrier thickness. Both, Simmons [94, 102] and Brinkman *et al.* [95] used an approximation based on the description of image forces derived by image force methods [94].

According to Equation (1.30), the potential landscape under an applied voltage is given by

$$\tilde{\Phi}(x) = \Phi(x) - \frac{x}{d} eV - V_i(x). \quad (1.56)$$

The new term, V_i , is the approximated image potential [94]

$$V_i(x) = -1.15\lambda \frac{d^2}{x(d-x)}, \quad \lambda = \frac{e^2 \ln 2}{8\pi\epsilon_r\epsilon_0 d} \quad (1.57)$$

with ϵ_r and ϵ_0 being the relative and vacuum permittivity, respectively. Concerning the changes to the barrier shape by the image force potential, the major

effects on the barrier are a rounding of the corners, a reduction of maximal barrier height and a narrower width.

The key parameters in the description of tunnel currents by Simmons and Brinkman *et al.* are the mean barrier height

$$\bar{\Phi} = \frac{1}{d} \int_{x_1}^{x_2} \Phi(x) dx, \quad (1.58)$$

and the barrier thickness $d = x_2 - x_1$. These two parameter change due to the influence of the image force potential. The change in the barrier shape leads to a reduction of the mean barrier height as well as the effective barrier thickness. x_1 and x_2 are defined as the points with $\Phi(x) - E_F = 0$ (the limits of the trapezoidal barrier defined by Equation (1.58)).

The effect of the image force potential on I - V characteristics of tunnel junctions is linked to the change of barrier height and thickness. It mainly changes the zero conductance $G(0)$ and leaves the overall shape of the $G(V)$ curves unchanged [95].

1.2.5 Spin-dependent Tunneling and TMR

The two models mentioned above (Simmons and BDR) describe tunneling in the free electron picture and therefore do not take the band structure of the electrodes into account. This also means that spin-dependent tunneling is not covered by these models. This problem was addressed by several theoreticians and experimentalists starting in the early 1970s. The following chapter will provide an overview on theories, thoughts and experiments on spin-dependent tunneling.

In the early 1970s, Tedrow and Meservey investigated spin-dependent tunneling from magnetic metals into a superconductor [43, 44] (Section 1.1.4). They recognized an asymmetry in the conductance-voltage curves measured in an applied magnetic field due to the spin polarization of conduction electrons in the magnetic metal (see Figure 1.12).

Tunneling conductivity in solid state physics is described by independent tunneling of electrons from filled into empty states and is therefore linked to the density of states and the Fermi distribution in both electrodes (Equation (1.21)). Tunneling between a metal and a superconductor therefore can be understood by means of the density of states of quasi particles given by the BCS-theory, D_{BCS} [107] (Figure 1.12 a) left). Following the calculation in Section 1.2.1 and setting $E_F = 0$, we obtain the voltage dependency of

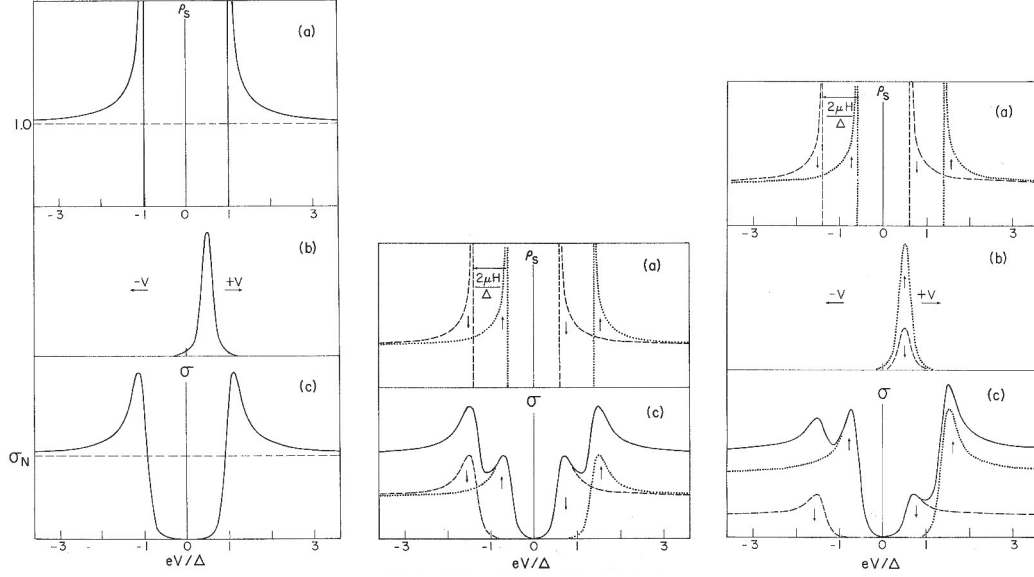


Figure 1.12: Spin-dependent tunneling into a superconductor:

left: normal metal - superconductor tunneling without magnetic field.

middle: normal metal - superconductor tunneling with magnetic field $\mu_0 H$.

right: tunneling from a magnetic metal into a superconductor with applied magnetic field $\mu_0 H$.

a) Density of states for quasi particles in the superconductor, $D_{\text{BCS}}(E)$ (BCS-theory, [107]). The gap is $E_{\text{gap}} = 2\Delta$. The states of different spin directions split up in an applied magnetic field (dotted and dashed lines). Splitting is $\Delta E = 2\mu H$

b) Differentiation of Fermi function times the density of states in the metal $D_{\text{m}} \cdot \frac{d}{dE} f(E + eV)$, representing the electronic states around $E_{\text{F}} = 0$ contributing to the current ($= D_{\text{m}} \cdot \delta(E - E_{\text{F}})$ for $T \rightarrow 0$). Due to spin polarization $P > 0$, the contributions of spin up and down electrons differ in a magnetic metal. The applied voltage shifts the metal density of states with respect to the superconducting density of states D_{BCS} .

c) Resulting conductance $G(V)$. In terms of math, this is a convolution of $D_{\text{BCS}}(E)$ and $D_{\text{m}} \cdot \frac{d}{dE} f(E)$. Total conductance $G(V)$ (solid line) is a sum of the contributions from spin up (dotted) and spin down (dashed) channels. The asymmetry due to the spin polarization P can clearly be seen by comparing the case of non-magnetic and magnetic metal electrodes.

Figures taken from [44]. Copyright 1973 by the American Physical Society.

conductivity in metal / insulator / superconductor tunneling:

$$\begin{aligned}
 G(V) &\propto \int_{-\infty}^{\infty} D_{\text{BCS}}(E) \cdot D_{\text{metal}}(E + eV) \cdot \frac{d}{dE} f(E + eV) dE = \\
 &= D_m \cdot \int_{-\infty}^{\infty} D_{\text{BCS}}(E) \cdot \frac{d}{dE} f(E + eV) dE
 \end{aligned} \tag{1.59}$$

The term $\frac{d}{dE} f(E + eV)$ describes a bell-shaped curve around $E_F + eV = eV$ (E_F is assumed to be zero). Due to this term, only states near the Fermi energy contribute to the tunnel current and the Fermi energy of the metal shifts by $\Delta E = eV$ in respect to the one inside the superconductor. The density of states in the metal is assumed to be constant near the Fermi energy, and thus $D_{\text{metal}}(E) = D_m = \text{const.}$

For $T \rightarrow 0$ the term $\frac{d}{dE} f(E + eV)$ is $\delta(E + eV)$ and $G(V) \propto D_m \cdot D_{\text{BCS}}(eV)$. Therefore, the measured conductivity $G(V)$ at $T = 0$ is a direct image of the superconducting density of states $D_{\text{BCS}}(E)$.

In terms of math, $G(V)$ is a convolution of $D_{\text{BCS}}(E)$ with $D_m \cdot \frac{d}{dE} f(E)$. The contributing parts and the resulting $G(V)$ curve are shown on the left of Figure 1.12. Descriptively, this picture tells you that only electronic states in the metal with energies $E \approx E_F$ are involved in the tunneling process. They can be used in $G(V)$ measurements as probe for the superconducting density of quasi particle states. In these measurements, E_F is shifted with respect to the superconducting density of states due to the applied voltage V ($\Delta E = eV$). The resulting value of $G(V)$ is the overlap of $D_{\text{BCS}}(E)$ with $D_m \cdot \frac{d}{dE} f(E)$ at a specific voltage V .

If a magnetic field is applied to the superconductor, spin up and down quasi particle states at the edge of the superconducting gap split up and are shifted by $\pm \mu_e \mu_0 H = \pm \mu H$ (Figure 1.12 a) middle). This results in a symmetric splitting of the $G(V)$ curve around the original peak positions without field. Due to spin conservation and the Mott model (Section 1.1.2), $G(V)$ is now described as a sum of the contributions of spin up and down channels.

If a normal metal is used as electrode, both spin contributions are equal ($P = 0$, Figure 1.12 c) middle) and $G(V)$ is given by:

$$G(V) \propto D_m \int_{-\infty}^{\infty} \left(D_{\text{BCS}}^{\uparrow}(E + \mu H) + D_{\text{BCS}}^{\downarrow}(E - \mu H) \right) \frac{d}{dE} f(E + eV) dE \tag{1.60}$$

This leads to a symmetric splitting of the maxima in the $G(V)$ curve as observed in experiments.

In case of a magnetic metal, the density of states of spin up and down are different, $D_m^{\uparrow} \neq D_m^{\downarrow}$, and therefore give different contributions to $G(V)$ ($P > 0$,

Figure 1.12 c) right).

$$G(V) \propto D_m^\uparrow \cdot \int_{-\infty}^{\infty} D_{\text{BCS}}^\uparrow(E + \mu H) \cdot \frac{d}{dE} f(E + eV) dE + \\ + D_m^\downarrow \cdot \int_{-\infty}^{\infty} D_{\text{BCS}}^\downarrow(E - \mu H) \cdot \frac{d}{dE} f(E + eV) dE \quad (1.61)$$

This formula describes the observed asymmetric splitting of the maxima in the $G(V)$ curve very well. This means that the spin polarization of conduction electrons (different densities of states at the Fermi level $D(E_F)$ in magnetic metals) and the Mott two current picture explain the observed difference in tunneling between superconductor and non-magnetic or magnetic metal visible in the $G(V)$ curves measured in a magnetic field. This is a proof of the validity of these assumptions made to describe tunnel currents, resulting in Equation (1.25).

Julliere model

In 1975, Julliere expanded the idea of spin-dependent tunneling to a system of ferromagnetic metal layers separated by a thin insulating film. He found a change in conductivity due to the alignment of magnetization in an Fe / GeO / Co system. He measured a high conductance in parallel alignment of layer magnetizations and a low conductance in antiparallel. The junction magnetoresistance (JMR) and tunnel magnetoresistance (TMR) therefore are defined as

$$\text{JMR} = \frac{G_p - G_{\text{ap}}}{G_p}, \quad \text{TMR} = \frac{G_p - G_{\text{ap}}}{G_{\text{ap}}} \quad (1.62)$$

with G_p and G_{ap} being the conductance in parallel and antiparallel magnetic state, respectively.

Julliere linked this effect to the spin polarization of conduction electrons in magnetic materials [11]. Following the formalism of Tedrow and Meservey [44], the fraction of majority electrons (spin parallel to layer magnetization) at the Fermi level is given by:

$$a = \frac{D_\uparrow(E_F)}{D_\uparrow(E_F) + D_\downarrow(E_F)} \quad (1.63)$$

Deductively, the fraction of minority spins (spin antiparallel to layer magnetization) is

$$1 - a = \frac{D_\downarrow(E_F)}{D_\uparrow(E_F) + D_\downarrow(E_F)} \quad (1.64)$$

and the spin polarization P can be written as

$$P = \frac{D_{\uparrow}(E_F) - D_{\downarrow}(E_F)}{D_{\uparrow}(E_F) + D_{\downarrow}(E_F)} = 2a - 1 \quad (1.65)$$

Due to the two current picture proposed by Mott (Section 1.1.2), the overall conductance G is the sum of conductance in the spin up and down channel. According to Equation (1.25), it is directly proportional to the density of states at the Fermi level of the appropriate spin direction. In parallel state, this leads to:

$$\begin{aligned} G_p &= G_{p(\uparrow 1 \rightarrow \uparrow 2)} + G_{p(\downarrow 1 \rightarrow \downarrow 2)} \propto \\ &\propto D_{\uparrow 1}(E_F)D_{\uparrow 2}(E_F) + D_{\downarrow 1}(E_F)D_{\downarrow 2}(E_F) = \\ &= a_1 a_2 + (1 - a_1)(1 - a_2) = \\ &= \frac{1}{2}(1 + P_1 P_2) \end{aligned} \quad (1.66)$$

And in antiparallel:

$$\begin{aligned} G_{ap} &= G_{ap(\uparrow 1 \rightarrow \downarrow 2)} + G_{ap(\downarrow 1 \rightarrow \uparrow 2)} \propto \\ &\propto D_{\uparrow 1}(E_F)D_{\downarrow 2}(E_F) + D_{\downarrow 1}(E_F)D_{\uparrow 2}(E_F) = \\ &= a_1(1 - a_2) + (1 - a_1)a_2 = \\ &= \frac{1}{2}(1 - P_1 P_2) \end{aligned} \quad (1.67)$$

$D_{\uparrow \downarrow 1 2}(E_F)$ are the density of states at the Fermi level of majority (\uparrow) and minority (\downarrow) spins in electrode 1 and 2, respectively.

Plugging G_p and G_{ap} as results of this considerations into the definition of JMR and TMR (Equation (1.62)) leads to the well known Julliere formula [11]:

$$\text{JMR} = \frac{G_p - G_{ap}}{G_p} = \frac{2P_1 P_2}{1 + P_1 P_2} \quad , \quad \text{TMR} = \frac{G_p - G_{ap}}{G_{ap}} = \frac{2P_1 P_2}{1 - P_1 P_2} \quad (1.68)$$

In 1975, Julliere used the definition of JMR to describe the effect. Today the usually used definition is TMR, often called "optimistic TMR value"[43].

In the model of Julliere, the effect depends only on the spin polarization of the electrodes, P_1 and P_2 . An illustrative description of this model addresses the tunneling of electrons from occupied states in electrode 1 to empty states in electrode 2 with the same spin direction (Figure 1.13). It is forbidden to tunnel into states with another spin direction. Neglection of spin flips in the tunneling process leads to the two current Mott model and to two independent conduction channels of spin up and down electrons.

In case of a parallel alignment of electrode magnetization, majority spins in both electrodes have the same spin direction. So do minority ones. Therefore,

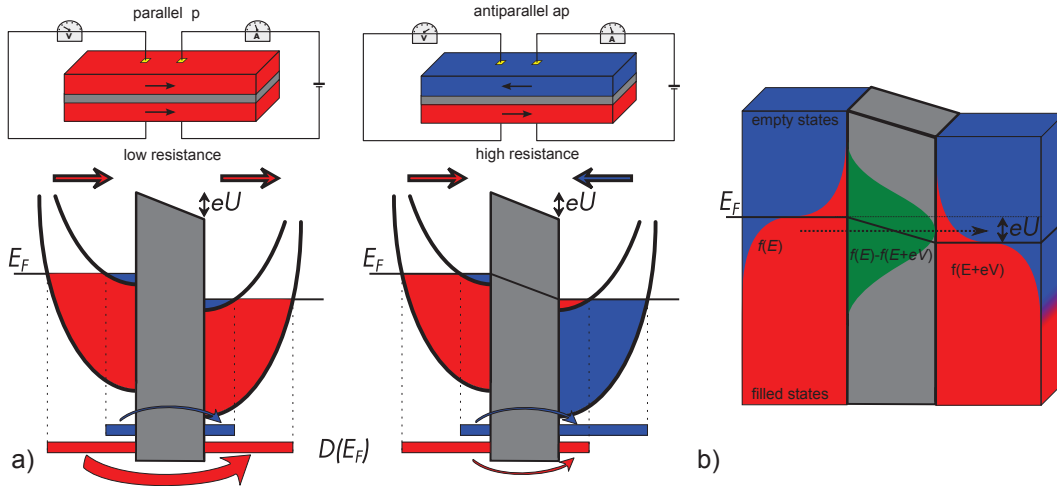


Figure 1.13: a) Illustrative presentation of the Julliere model. On top, a sketch of MTJs in parallel and antiparallel state of magnetization alignment is shown. Below, the density of states of majority (same color as magnetization) and minority (different color as magnetization) spin electrons and their density of states at the Fermi level $D(E_F)$ in both electrodes are depicted. The arrows indicate the tunnel current while their thickness illustrates the amount of flowing current. b) Illustration of the descriptive principle of tunneling from filled into empty states. Red color marks the filled states, blue the empty ones, and green the amount of facing empty and filled states $f(E) - f(E + eV)$.

a large amount of filled majority spin states at the Fermi energy in electrode 1 ($D_{\uparrow 1}(E_F)$) faces a large amount of empty states in electrode 2 ($D_{\uparrow 2}(E_F)$) (Figure 1.13). This means, many electrons have many possibilities to tunnel into, which leads to a high conductivity in the majority spin channel. We have the opposite situation in the minority channel. Only few filled states in electrode 1 ($D_{\downarrow 1}(E_F)$) and few empty states in electrode 2 ($D_{\downarrow 2}(E_F)$) are available. This leads to a small conductivity in the minority channel compared to the one of the majority channel. All in all, conductivity in parallel state (G_p), which is the sum of majority (high G) and minority (small G) channel conductivity, is high.

In antiparallel alignment of electrode magnetization, the role of spin changes between electrodes. Majority spins in electrode 1 ($D_{\uparrow 1}(E_F)$) have to conserve their spin direction and must tunnel into minority states in electrode 2 ($D_{\downarrow 2}(E_F)$). Consequently, minority spins in electrode 1 ($D_{\downarrow 1}(E_F)$) have to tunnel into majority states in electrode 2 ($D_{\uparrow 2}(E_F)$). This means that the large amount of majority spin electrons out of electrode 1 have to tunnel into a few minority states in electrode 2. For minority spin electrons out of electrode 1, it is the other way around: There are only few of them available to tunnel into the large amount of majority states in electrode 2 (Figure 1.13). This results in a low conductivity in both channels and therefore in a small overall conductivity in antiparallel alignment of magnetization ($G_{ap} < G_p$).

Influence of barrier parameter and band structure on electron tunneling

In 1989, Slonczewski used a different approach to determine the conductivity of a tunnel junction with magnetic electrodes [32]. Starting point was a modified Hamiltonian. He introduced the internal exchange energy $\mathbf{h}(x) \cdot \sigma$ describing the exchange interaction in ferromagnets. $\mathbf{h}(x)$ is the molecular field and $\sigma = 2\mathbf{s}$ the conventional Pauli spin operator. The Hamiltonian for this problem is:

$$\mathbf{H} = -\frac{\hbar^2}{2m} \frac{\partial^2}{\partial x^2} + V(x) + \mathbf{h}(x) \cdot \sigma, \quad (1.69)$$

$V(x)$ is the usual barrier potential (Equation (1.10)). $\mathbf{h}(x)$ depends on the electrode material and is zero in the non magnetic barrier.

$$\mathbf{h}(x) = \begin{cases} \mathbf{h}_1 = \text{const.} & \text{if } x < 0 \\ 0 & \text{if } 0 < x < d \\ \mathbf{h}_2 = \text{const.} & \text{if } x > d \end{cases} \quad (1.70)$$

Considering only a single free electron and assuming bands to be parabolic one obtains the wave vectors k^σ in the electrodes:

$$k^\sigma = \frac{\sqrt{2m(E + \sigma\mathbf{h})}}{\hbar}, \quad \sigma = \pm 1 \quad (1.71)$$

The inverse characteristic decay length κ remains unchanged.

$$\kappa = \frac{\sqrt{2m(\Phi - E)}}{\hbar} \quad (1.72)$$

Due to two spin channels ($\sigma = \pm 1$) and according to Equation (1.12), one has to determine eight pre-factors. This is done by using the continuity condition for Ψ and $\frac{\partial}{\partial x}\Psi$ at $x = 0$ and $x = d$. The relative orientation of the electrode magnetizations (angle ϕ) results in four more equations. The change in quantization axis at $x = d$ needs the spinor transformation for Ψ and $\frac{\partial}{\partial x}\Psi$:

$$\Psi_{\uparrow 2} = \Psi_{\uparrow 3} \cos\left(\frac{\phi}{2}\right) + \Psi_{\downarrow 3} \sin\left(\frac{\phi}{2}\right) \quad \Psi_{\downarrow 2} = -\Psi_{\uparrow 3} \sin\left(\frac{\phi}{2}\right) + \Psi_{\downarrow 3} \cos\left(\frac{\phi}{2}\right) \quad (1.73)$$

Due to this consideration, we get a transmission coefficient $C = C_\uparrow + C_\downarrow$ that is a function of κ , k^\uparrow , k^\downarrow and ϕ . The conductance is given by the Landauer-Büttiker formula [108]:

$$G = \frac{e^2}{(2\pi)^2 \hbar} \int C(k_\parallel) d^2 k_\parallel \quad (1.74)$$

Integrating over k_{\parallel} and taking only the leading terms in $1/d$ gives

$$G = \frac{e^2}{8\pi\hbar} \frac{\kappa}{d} C \quad (1.75)$$

for the tunnel conductance. Due to the spin and angle (ϕ) dependency of C , this can be expressed as

$$G = G_0(1 + P_{\text{eff},1}P_{\text{eff},2}\cos(\phi)) \quad (1.76)$$

with the effective spin polarization at the barrier-electrode interface:

$$P_{\text{eff},i} = \frac{(k^{\uparrow} - k^{\downarrow})(\kappa^2 - k^{\uparrow}k^{\downarrow})}{(k^{\uparrow} + k^{\downarrow})(\kappa^2 + k^{\uparrow}k^{\downarrow})} = P \cdot A_{\text{interface}} \quad (1.77)$$

At $\phi = \pi$, the Julliere-model (Equation (1.68)) is reproduced with $P_i = P_{\text{eff},i}$. In case of free electrons, k^{σ} is proportional to $D_{\sigma}(E_F)$ and the first term in Equation (1.77),

$$P = \frac{(k^{\uparrow} - k^{\downarrow})}{(k^{\uparrow} + k^{\downarrow})} \quad (1.78)$$

is the usual spin polarization of the electrodes (Equation (1.3)). The second factor,

$$A_{\text{interface}} = \frac{(\kappa^2 - k^{\uparrow}k^{\downarrow})}{(\kappa^2 + k^{\uparrow}k^{\downarrow})} \quad (1.79)$$

is related to the interface and describes the polarization at the electrode-barrier interface. It depends on the barrier height Φ and covers the range $-1 < A_{\text{interface}} < 1$. This is based on the different penetration depths of wave functions Ψ_{σ} , which depend on k^{σ} . Apparently, it changes sign and a sufficiently low barrier height Φ results in a negative spin polarization of the interface and might result in a negative TMR-value.

Bratkovsky extended the formula of Slonczewski and added the influence of the effective mass m^* of electrons inside the barrier [109]. This takes into account the band structure inside the barrier.

$$P_{\text{eff},i} = \frac{(k^{\uparrow} - k^{\downarrow})(\kappa^2 - m^{*2}k^{\uparrow}k^{\downarrow})}{(k^{\uparrow} + k^{\downarrow})(\kappa^2 + m^{*2}k^{\uparrow}k^{\downarrow})} \quad (1.80)$$

In 1997, MacLaren *et al.* [108] calculated the tunnel conductance in the free electron model numerically and compared it to the results of Julliere and Slonczewski. Figure 1.15 shows the calculated conductance ratio ($\Delta G/G$) in dependence on the electrode spin polarization for various barrier height and thickness values. The results of Julliere's formula and Slonczewski's approximation are drawn for comparison. Apparently, Julliere's model is not capable to reproduce the influence of barrier parameters on the TMR effect. Slonczewski's formula gives a relatively good approximation for thick barriers, but fails in

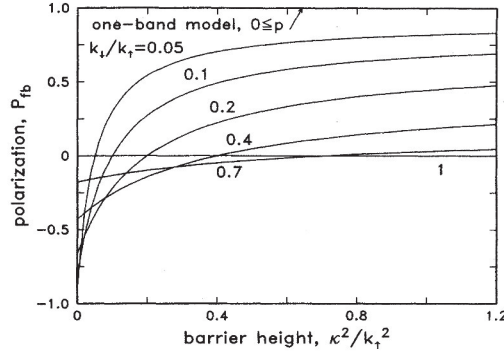


Figure 1.14: Effective spin polarization P_{eff} in dependence of barrier height and spin polarization of the bulk electrode ($k_{\downarrow}/k_{\uparrow} = 2/(1 + P) - 1$) after Slonczewski (Equation (1.77)). Usual barrier heights are approximately 5 times κ^2/k_{\uparrow}^2 . Figure taken from [32]. Copyright 1989 by the American Physical Society.

case of thin ones.

MacLaren *et al.* further calculated the conduction ratio $\Delta G/G$ for the case of a real band structure in the electrodes. In this work, they depict Fe-electrodes separated by a rectangular barrier. The barrier material was not further specified. They found a strong dependence of $\Delta G/G$ on the band structure of iron and pointed this fact out by calculating the dependency of tunnel conductance on the wave vector (k_x, k_y), which is quite different from the one derived by the free electron model. The dependence on barrier parameter in this case is strong for the barrier height, but only weak for the barrier thickness.

MacLaren *et al.* concluded, that the Julliere model (only based on considerations regarding spin polarization, neglecting barrier parameter) and the free electron model (neglecting band structure) are not appropriate to describe tunneling between real solid state electrodes.

Nevertheless, Julliere's model gives appropriate TMR values if spin polarization is defined the right way. In this case, the right way is to use spin polarization values derived by STS (spin tunnel spectroscopy, see Section 1.1.4). Now, the Julliere model gives reasonable upper boundaries for TMR-values [108, 110] (see Figure 1.16).

This states the important role of the barrier and the barrier/electrode interface in spin-dependent electron tunneling.

Tunneling through amorphous and crystalline barriers

The importance of barrier properties in electron tunneling becomes more obvious by comparing amorphous and crystalline (epitaxial) barriers.

In case of dielectric, diamagnetic and amorphous barriers like Al_2O_3 (often labeled as AlO_x), the tunneling probability $T(E)$ only depends on the basic barrier parameter height Φ and thickness d . In this case, the tunnel probab-

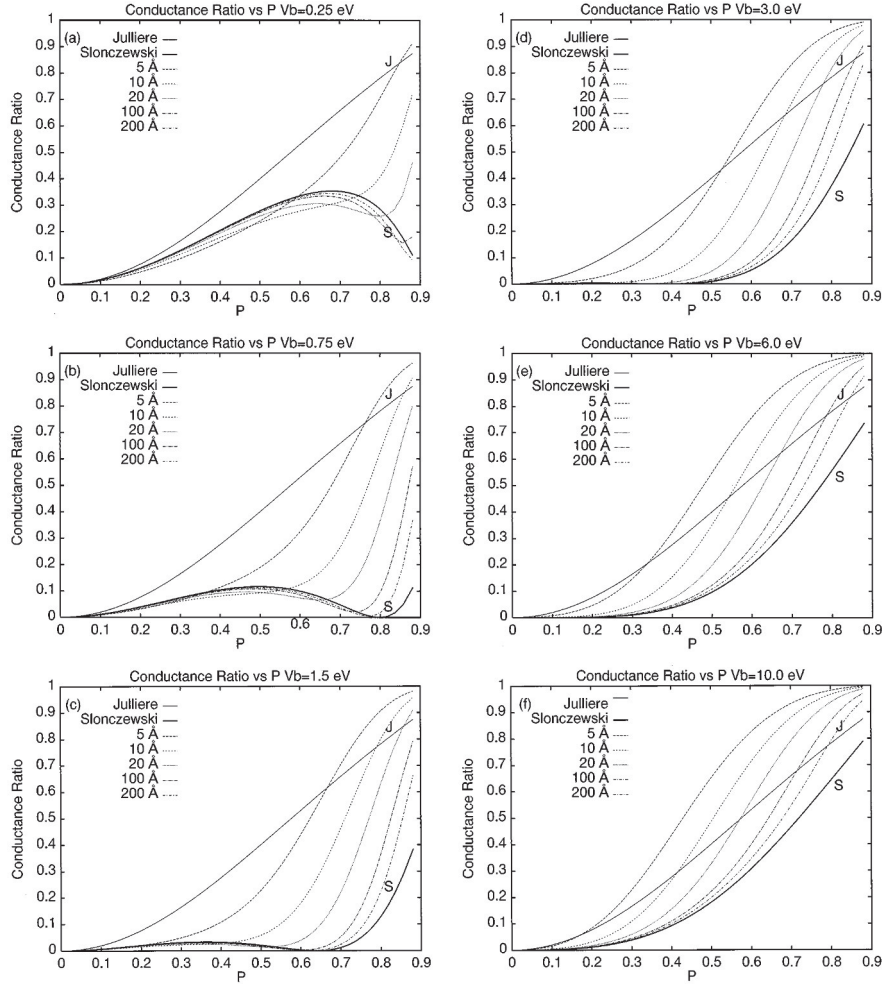


Figure 1.15: Conductance ratio ($\Delta G/G$) calculated by MacLaren *et al.* [108] for free electron spin-dependent tunneling for various barrier heights (a) 0.25 eV, (b) 0.75 eV, (c) 1.5 eV, (d) 3.0 eV, (e) 6.0 eV, and (f) 10.0 eV. In each panel, barrier widths of 5, 10, 20, 100, and 200 Å are shown along with the Julliere and Slonczewski results labeled by (J) and (S) respectively. Figures taken from [108]. Copyright 1997 by the American Physical Society.

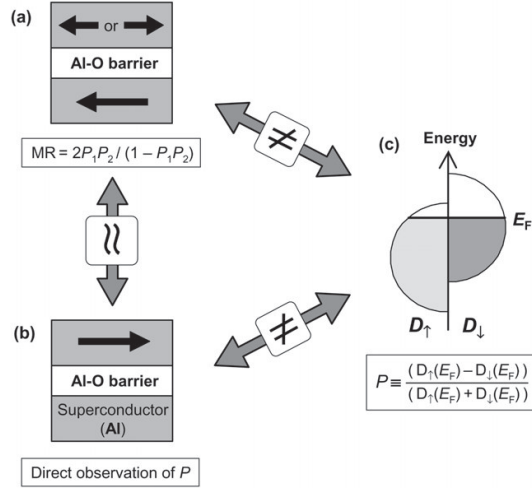


Figure 1.16: Correlation between the TMR effect (a), the polarization of tunnel current obtained by STS measurements (b) and the spin polarization in the bulk of an electrode (c). Bulk spin polarizations obtained by band structure calculations do not agree with those measured in tunneling experiments. This is due to the influence of the barrier on tunnel current, namely symmetry filtering in epitaxial barriers and the electronic properties of the interface between barrier and electrode. Figure taken from [110].

ity for all electrons can be described by $T(E) \propto \exp(-2\kappa d)$ (Equation (1.15) and (1.16)) [62].

Considering a crystalline barrier, the situation is different. It is expected that the crystalline structure and the resulting symmetries influence the tunneling probabilities. Electrons, traveling through a crystal along a given crystallographic direction, occupy several states with different symmetries. At the interface to a crystalline barrier, the wave functions penetrate the barrier and decay with different decay lengths depending on their symmetry and the crystal structure of the barrier [48, 53]. Therefore, the transmission coefficient depends on symmetry-specific inverse decay lengths κ_i and $T_i(E) \propto \exp(-2\kappa_i d)$ for different possible wave-function symmetries i [62]. In case of a (001)-oriented MgO barrier between two (001) bcc-Fe electrodes, mainly Δ_1 (spd-like), Δ_2 (pd) and Δ_5 (d) Bloch states contribute to the tunnel current.

In k-space, the Γ -H direction is the propagation direction of electrons moving perpendicular to the interface plane (k_\perp). The band structure of bcc Fe in this direction shows contributions of Δ_1 , Δ_2 and Δ_5 states at the Fermi energy in the majority spin band (Figure 1.17) [48, 53, 57]. The minority spin bands only contain contributions of Δ_2 and Δ_5 states at the Fermi energy. Δ_1 symmetry is absent. All these different symmetries Δ have different decay lengths inside the MgO barrier. The decay of Δ_1 is much smaller than that of Δ_2 and Δ_5 [53]. Therefore, Δ_1 states mainly contribute to the high conductivity in parallel state. In antiparallel alignment of magnetization, the injected major-

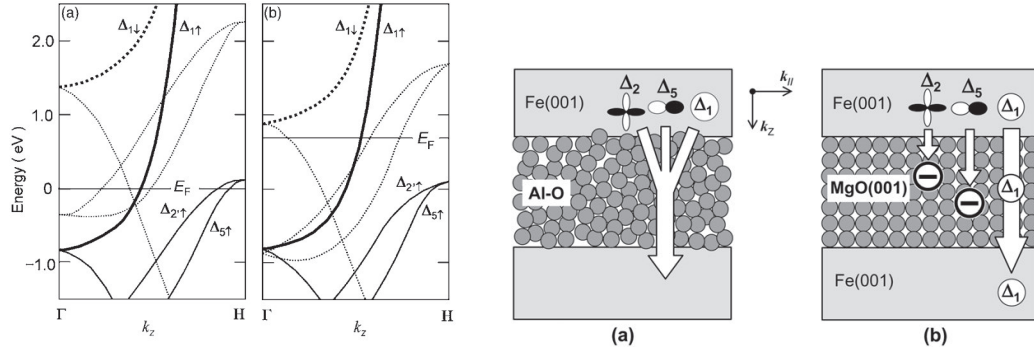


Figure 1.17: Left: Band dispersion of bcc-Fe (a) and bcc-Co (b) in the [001]-direction (Γ -H). The absence of the minority Δ_1 spin band (thick dotted lines) at the Fermi energy E_F is clearly visible. This absence and the preferred transmission of Δ_1 Bloch states lead to the huge TMR observed in MTJs based on epitaxial MgO barriers due to an half-metallic character of Δ_1 states. The different energies of the onset of Δ_1 states above E_F (1.3 eV for iron and 0.2 eV for Co) explain the differences in TMR(V) between Fe- and Co-based MTJs. See also Figure 1.18. Reprinted with permission from [57]. Copyright 2006, AIP Publishing LLC.

Right: Schematic illustration of symmetry filtering in tunnel junctions. In case of an amorphous barrier (e.g. Al_2O_3 , a), all symmetries tunnel equally. In case of an epitaxial MgO barrier (b), the decay of evanescent states of Δ_2 and Δ_5 symmetry is fast compared to that of Δ_1 . Therefore, states of Δ_1 symmetry mainly contribute to the tunnel current. Figures taken from [110].

ity Δ_1 electrons face no Bloch state with matching symmetry in the collecting electrode and the current is only due to the fast decaying Δ_2 and Δ_5 states. This results in a low conductivity in antiparallel alignment. This very effective symmetry filtering leads to high TMR-ratios.

Also other bcc metals and alloys (Co, CoFe, CoFeB) show this symmetry filtering and therefore reach high TMR values in combination with (001)-oriented MgO barriers (Section 1.1.4) [62, 110, 111].

Another crystalline and epitaxial barrier used in MTJs is SrTiO_3 . It is usually used in combination with perovskite electrodes, e.g. half-metallic LSMO, allowing epitaxial growth [68, 112–115]. Theoretic calculations [116, 117] also predict different decay lengths for different Bloch state symmetries inside the SrTiO_3 barrier. The situation is more complicated than in MgO and decay rates depend strongly on energy. Δ_2 states decay very fast inside the SrTiO_3 barrier, but two symmetries (Δ_1 and Δ_5) have rather slow and comparable decay rates near the Fermi level. This is the experimentally accessible energy range and therefore, these two contribute mainly to the tunnel current.

Influence of electrode band structure on electron tunneling

The band structure of the electrodes is an important point to consider. Not only the k_{\parallel} dependency of tunnel conductance, as pointed out by MacLaren *et al.* [108], but also the band structure in one particular direction, like Γ -H (k_{\perp}), effects the tunnel current. This can be pointed out clearly on the simple example of Fe / MgO / Fe and Co / MgO / Co. These systems show clear differences in the voltage dependency of TMR [57]. Yuasa *et al.* found a larger dependence of TMR on applied voltages in Co-based structures than in Fe-based. The difference is apparent at voltages larger 0.2 V. Yuasa *et al.* [57] explain this behavior by the different energies of the onset of the minority Δ_1 band. In Fe, the minority Δ_1 band is located 1.3 eV above the Fermi level and is not involved in tunneling as long as the applied voltage is smaller than 1.3 V. In Co, this band is only 0.2 eV above the Fermi level. Therefore, it is involved in tunneling at voltages larger 0.2 V. This leads to an opening of the Δ_1 channel in antiparallel alignment which means that the effective spin polarization of tunneling Δ_1 states is considerably reduced for voltages larger than 0.2 V. This leads to an enhanced conductivity in antiparallel alignment of magnetization and therefore to a reduction of TMR.

These features can also be found in the second derivative tunnel spectrum ($\frac{d^2I}{dV^2}$). Here, the abrupt onset of conductivity at 1.3 and 0.2 eV for Fe and Co, respectively, gives peaks in the $\frac{d^2I}{dV^2}$ spectrum at the assigned voltages (Figure 1.18) [110, 118].

The influence of the band structure on the tunnel current was also investigated by De Teresa *et al.* on LSMO / STO / Co junctions [119–121]. They observed a large dependency of TMR on the applied voltage V (Figure 1.20 A). For negative and small positive voltages, this structures show an inverse TMR effect, $\text{TMR} < 0$ ($P_{\text{Co}} < 0$). At voltages $V > 0.8$ V, the sign of TMR changes. De Teresa *et al.* linked this observation to the structure of the density of Co d-states [119, 120]. Due to the shift of facing states by the applied voltage, energy levels with $P_{\text{Co}} > 0$ contribute to the tunneling and change the spin polarization of Co. The maximal normal and inverse TMR at $V = +1.15$ V and $V = -0.4$ V are assigned to maxima in density of states of spin up and down 3d band at this particular energies, respectively [120]. Although this result is six years older than the measurements of Yuasa *et al.* [57], it can further explain the measured voltage dependency of TMR and the differences in Co- and Fe-based MTJs with MgO barrier due to the differences in band structures.

Influence of the interface between barrier and electrode on electron tunneling

Also the chemical structure at the interface has an influence on the TMR effect. As stated before, the theoretical description of the TMR effect depends

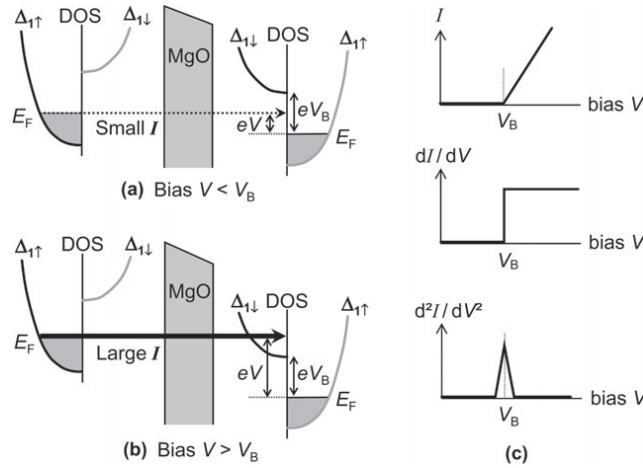


Figure 1.18: (a) (b) Tunneling process of Δ_1 electrons in (001)bcc Fe- or Co-based MTJs with an epitaxial MgO(001) barrier. Magnetization is aligned antiparallel. For applied voltages V smaller V_B , minority Δ_1 states do not contribute to the tunnel current. If the voltage V exceeds V_B , the shift between density of states is large enough and minority Δ_1 states face incoming majority ones. This allows the electrons to tunnel and therefore increases the current in antiparallel alignment, leading to a decrease of TMR. (c) Expected features in the I - V curves and derivatives in antiparallel alignment of magnetization. The onset of current is at $V_B = 1.3$ eV (Fe) or 0.2 eV (Co). This is due to the band structure of minority Δ_1 states (see Figure 1.17). Figures taken from [110]

strongly on the definition of the spin polarization (Figure 1.16). Spin polarizations of the bulk material (derived by theoretical calculations or bulk-sensitive measurements) are not suitable to describe the TMR effect. Spin polarization responsible for TMR tends to be the interface spin polarization depending on the structure and bonding chemistry of the electrode / barrier interface.

One theoretical example is a thin layer of FeO at the Fe / MgO interface in an Fe / FeO / MgO / Fe structure. It reduces the coupling between Δ_2^{Fe} Bloch states and the evanescent states of the same symmetry in the MgO barrier. This effect reduces the conductivity of Δ_2^{Fe} Bloch states in the parallel configuration and therefore the observed TMR [122]. This results in small, for thin barrier layers even negative, TMR values [123].

In contrast, describing a symmetric structure, consisting of Fe / FeO / MgO / FeO / Fe, Tuschke *et al.* predict huge TMR values. Symmetrization of the tunnel junction due to the two FeO interface layers results in a fully coherent MTJ, which leads to giant TMR values [123].

An experimental proof of the interface dependence of the spin polarization is given by De Teresa *et al.* [119–121]. They investigated LSMO and Co-based tunnel junctions with different barrier materials, namely epitaxial SrTiO₃ and amorphous Al₂O₃ (Figure 1.19 and Figure 1.20).

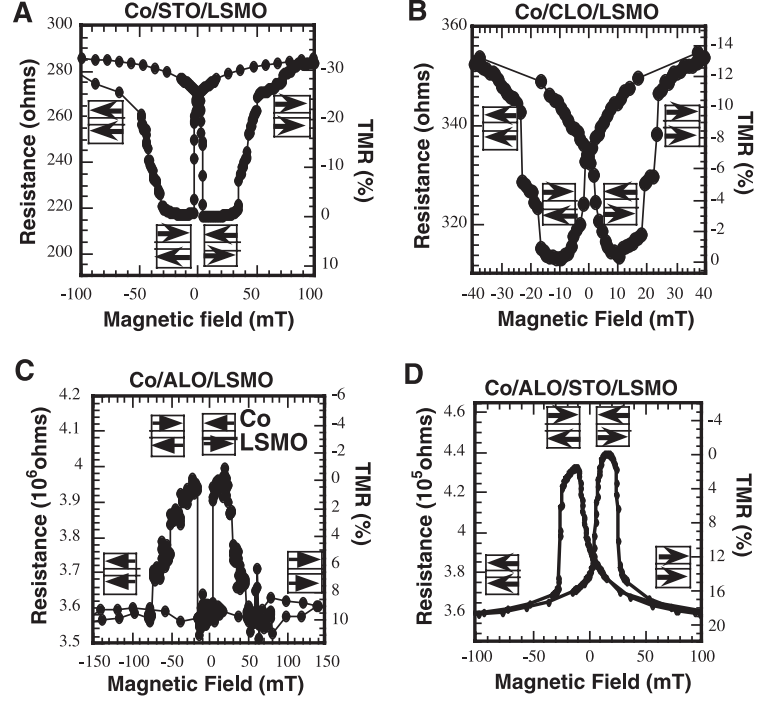


Figure 1.19: Influence of the barrier material on the TMR in LSMO ($\text{La}_{0.7}\text{Sr}_{0.3}\text{MnO}_3$) and Co-based tunnel junctions. A,B) inverse TMR with STO (SrTiO_3) and CLO ($\text{Ce}_{0.69}\text{La}_{0.31}\text{O}_{1.845}$) barriers. C) normal TMR with Al_2O_3 barrier. D) normal TMR with an Al_2O_3 /STO double barrier. All TMR curves are taken at an applied voltage of $V = -10$ mV, with electrons tunneling from LSMO into Co. In case of a STO or CLO barrier, the negative TMR indicates a negative spin polarization at the Co/STO or Co/CLO interface. In contrast, the spin polarization at the Co/ Al_2O_3 interface is positive due to the observed normal TMR. The dominating influence of interface spin polarization is demonstrated by inserting an Al_2O_3 barrier between Co and STO. This reverses the TMR from inverse (STO case) to normal (Al_2O_3 case), indicating the Co/barrier interface being responsible for the effect of changing TMR sign, and not the symmetry filtering inside the epitaxial STO barrier. From [119]. Reprinted with permission from AAAS.

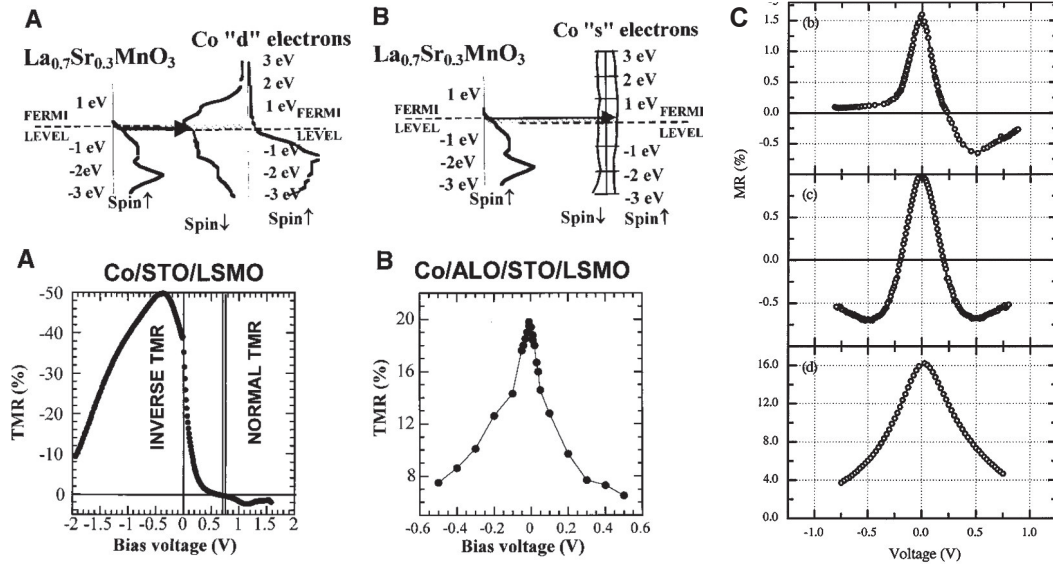


Figure 1.20: A) Density of states in LSMO and Co and the measured TMR(V) curve of a Co/STO/LSMO junction. For Co in combination with a STO barrier, the density of d-states is shown, which is responsible for the observed negative TMR at small voltages and the measured TMR(V) curve. B) Density of states in LSMO and Co and the measured TMR(V) curve of a Co/ Al_2O_3 /STO/LSMO junction. Here, the Co s-states are shown. They seem to be responsible for tunneling in Co/ Al_2O_3 /LSMO or Co/ Al_2O_3 /STO/LSMO junctions. Figures A and B are from [119]. Reprinted with permission from AAAS.

C) TMR(V) curves of b) NiFe/ Al_2O_3 /Ta $_2$ O $_5$ /NiFe, c) NiFe/Ta $_2$ O $_5$ /NiFe and d) NiFe/ Al_2O_3 /NiFe MTJs. The TMR(V) curves show characteristic forms that can be explained by the different density of states contributing to the tunnel current at the different interfaces. At the NiFe/ Al_2O_3 interface, s-states contribute to the tunnel current. In contrast, d-states contribute at the NiFe/Ta $_2$ O $_5$ interface. This is similar to the Co/barrier interfaces in A and B. The measured TMR(V) curves of the different structures display the interface density of states at both sides of the particular barrier. Figure C taken from [124]. Copyright 1999 by the American Physical Society.

MTJs with an Al_2O_3 barrier show normal TMR ($\text{TMR} > 0$) indicating a positive spin polarization at the Co interface. This is in agreement with STS (superconducting tunneling spectroscopy) results on transition metal electrodes combined with Al_2O_3 barriers [45], but in contrast to density of states calculations, predicting a negative spin polarization in Ni and Co [34, 45]. In contrast, an inverse TMR is reported in case of a SrTiO_3 barrier, which is due to a negative spin polarization at the Co interface.

This behavior is assigned to the preferred transmission of s-like electrons in case of an Al_2O_3 barrier and of d-like electrons in case of a SrTiO_3 barrier due to the electronic structure at the interface [62, 119]. In case of the Co- Al_2O_3 interface, density of states calculations predict a positive spin polarization due to a sp-d bonding mechanism between Al and Co [119]. The positive spin polarization is the result of a preferred transmission of positive spin-polarized s-like electrons through this interface layer.

Therefore, the voltage dependency of TMR on samples with an SrTiO_3 barrier shows a clear dependence on the density of p-states in Co (see page 49). This influence is completely absent in the case of an Al_2O_3 barrier. In this case, the voltage dependency is assigned to the energy dependence of surface density of states [119] or to excitation of spin waves [125].

The influence of symmetry filtering as origin of this effect was precluded by measurements on Co / Al_2O_3 / SrTiO_3 / LSMO structures. They show a positive TMR similar to a single Al_2O_3 barrier and therefore suggest that the positive spin polarization is originated in the Co- Al_2O_3 interface and not in symmetry filtering, resulting in a rapid decay of minority states inside the barrier [119].

Similar results were obtained by Sharma *et al.* on NiFe / Ta_2O_5 / Al_2O_3 / NiFe structures [124]. The spin polarization at the NiFe / Ta_2O_5 interface shows an inversion near the Fermi surface. This means, it changes its sign near the Fermi energy and switches from positive to negative. This is similar to the picture of the Co/LSMO interface (Figure 1.20 A). In NiFe / Ta_2O_5 / Al_2O_3 / NiFe structures, the rather unstructured density of s-states at the NiFe / Al_2O_3 interface faces the inverting density of d-states at the NiFe / Ta_2O_5 interface. Therefore, the $\text{TMR}(V)$ curve displays the spin polarization of the NiFe / Ta_2O_5 interface (Figure 1.20 C-b). The change of sign of TMR in NiFe / Ta_2O_5 / NiFe structures can also be explained by the facing density of states, inverting with applied voltage. At small voltages, densities of states with the same sign of spin polarization are facing. At a certain voltage, the spin polarization of one electrode shifts so far that first the spin polarization vanishes ($\text{TMR} = 0$) and then, by further increasing the voltage, changes its sign. This leads to the negative TMR at high applied voltages shown in Figure 1.20 C-c. For NiFe / Al_2O_3 / NiFe structures, the situation is equal to Co / Al_2O_3 / LSMO structures (Figure 1.20 C-d).

These interface states, leading to the observed different spin polarizations, are

often assigned to metal-induced gap states. They are assigned to be the reason for a non-zero density of states at the barrier interface, which is different to the one inside the bulk magnetic electrodes. This density of states strongly depends on barrier material and interface structure [62, 126–128].

Temperature dependence of surface spin polarization

Spin polarization as reason for the TMR effect is an interface effect and strongly depends on the properties of the electrode / barrier interface. The temperature dependency of spin polarization can be described by a Bloch law [13, 129]:

$$P(T) = P_0(1 - \gamma T^{\frac{3}{2}}) \quad (1.81)$$

P_0 is the interface polarization at $T = 0$, usually derived by STS experiments, and γ is a material parameter, dependent on the interface. This temperature dependency is a consequence of the thermal excitation of spin waves. The parameter γ and the interface spin polarization P_0 strongly depend on surface contamination [65] and therefore are sensitive to interface structure and quality.

The Co / Al₂O₃ interface has a very small γ of $\gamma_{\text{Co} / \text{Al}_2\text{O}_3} = 1 \text{ to } 6 \cdot 10^{-6} \text{ K}^{-3/2}$ [129] and can be neglected in most cases when using oxide counter electrodes. Measurements on LSMO / oxide barrier / LSMO junctions show a clear dependence of the temperature coefficient γ of LSMO surface polarization [69]. Used barriers are STO, LAO and TiO₂. The resulting temperature coefficient γ of these interfaces are:

$$\begin{aligned} \gamma_{\text{LSMO} / \text{LAO}} &= 5.1 \cdot 10^{-5} \text{ K}^{-3/2} \\ \gamma_{\text{LSMO} / \text{TiO}_2} &= 15.8 \cdot 10^{-5} \text{ K}^{-3/2} \\ \gamma_{\text{LSMO} / \text{STO}} &= 19.0 \cdot 10^{-5} \text{ K}^{-3/2} \end{aligned}$$

These coefficients are one order of magnitude larger than those of transition metal / barrier interface and therefore are responsible for the temperature dependence of TMR in mixed junctions (oxide / barrier / transition metal).

Influence of Barrier defects on TMR

Real barriers are never perfect and contain defects (e.g. oxygen vacancies) which form localized states inside the barrier. Tunnel conduction of electrons in these barriers is a sum of direct tunneling (elastic) and tunneling including several steps over localized states (inelastic). Conduction paths including localized states also give rise to spin flips, decreasing the spin polarization of the tunnel current and therefore the TMR. We can assume two currents in parallel, the spin-dependent one (direct tunneling, Mott-picture) and the spin-independent one (spin flip scattering). The TMR in this case is reduced to

$$\text{TMR} = \frac{2P_1P_2}{1 + P_1P_2} \left(1 - \frac{I_{\text{ap}}^{\text{spinflip}}}{I_{\text{ap}}^{\text{total}}} \right). \quad (1.82)$$

Here, $I_{\text{ap}}^{\text{spinflip}}$ is the amount of tunneling current involving spin flip processes and $I_{\text{ap}}^{\text{total}}$ is the total tunneling current, both in the antiparallel (ap) state [46, 130].

Glazman and Matveev [131] developed a theory for electrons tunneling through imperfect barriers. An interesting point in the theory of Glazman and Matveev [131] is the temperature dependency of the tunnel conductance. It is the sum over all paths including n localized states weighted by the probability of the particular path:

$$G(T) = G_0 + \sum_{n=1}^{\infty} c_n \cdot T^{n - \frac{2}{n+1}} \quad eV \ll k_B T \quad (1.83)$$

According to Glazman and Matveev, $n = 0$ (direct tunneling) and $n = 1$ (tunneling via a single localized state) gives the elastic tunnel current and $n \geq 2$ describes the inelastic tunnel current [130]. For thin barriers, the $n = 2$ case is the most probable and gives a major contribution to the inelastic tunnel conductivity. Therefore, $G(T) \propto T^{4/3}$ is a good approximation for most barriers.

Experimental proof of this theory is given by Shang *et al.* [129] on Al_2O_3 barriers. They investigated the spin-independent part of the tunnel current and linked it to imperfections and localized states inside the barrier. The main point is the spin scattering during conduction over localized states, leading to a loss of spin polarization. The spin independent conductivity $G_{\text{in}}(T)$ is proportional to $T^{4/3}$. This means, according to Glazman and Matveev [131], that the $n = 2$ channel dominates the spin independent current.

Taking the spin-dependent (elastic, G_{el}) and the spin-independent (inelastic, G_{in} , multiple scattering inside the barrier) current into account, the Julliere model can be written as:

$$\text{TMR} = \frac{2P_1P_2}{1 + P_1P_2} \frac{G_{\text{el}}}{G_{\text{el}} + G_{\text{in}}} \quad (1.84)$$

The new factor describes the decrease of the TMR-ratio due to the spin flip scattered, and therefore spin independent, current I_{in} .

Assuming a major contribution of the $n = 2$ channel to the inelastically scattered current ($G(T) \propto T^{4/3}$), one gets the following temperature dependency of the TMR [132]:

$$\text{TMR}(T) \propto (1 - \alpha T^{\frac{4}{3}}) \quad (1.85)$$

This dependency considers only the fact of a spin-independent current in parallel to the spin-dependent one, caused by multiple scattering and random spin flips inside the barrier. This spin-independent current is one more reason for

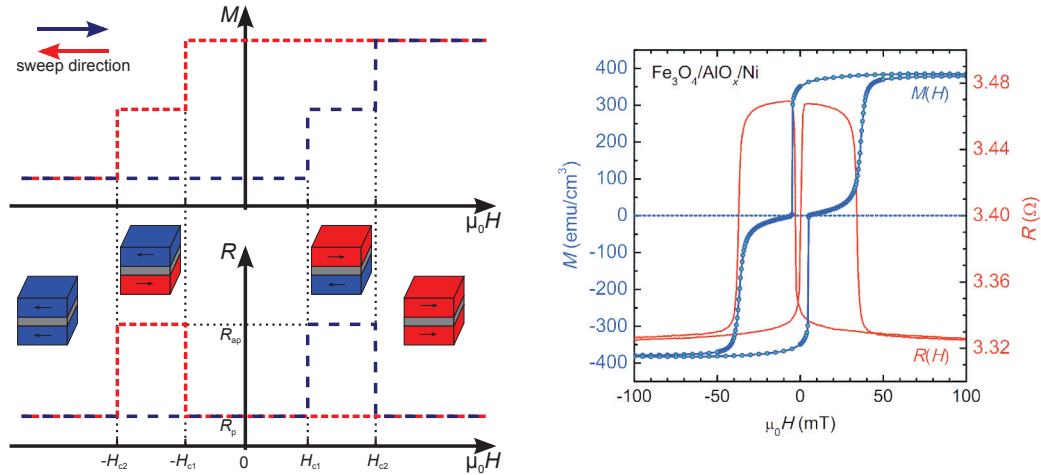


Figure 1.21: Magnetization (M) and corresponding resistance (R) of a pseudo spin valve TMR element in dependence of the applied in plane magnetic field. Measurement graph taken from [46]

TMR-values smaller than the predicted value by the Julliere model. Also a faster decay of TMR than predicted by the decrease of interface spin polarization with temperature can be explained by this model [129].

Pseudo spin valve

The structure Julliere used in his experiments is a so called pseudo spin valve (Figure 1.21). It consists of two magnetic layers with different coercive fields separated by a thin insulating barrier. Compared to a spin valve, the exchange bias layer is missing. Parallel and antiparallel alignment of magnetization is achieved due to the different coercive fields of the layers. A magnetic field sweep from negative to positive fields and back is used to set the different alignments during resistance measurements. Large negative magnetic fields align the magnetization in the parallel, low resistive state (R_p). Once the field exceeds the coercive field of one layer, the corresponding magnetization reverses (is now parallel to the applied field), resulting in the antiparallel state. The resistance increases to R_{ap} . A further increase of field strength above the coercive field of the second layer switches its magnetization parallel to the applied field and the magnetization of the other electrode. Thus the resistance value lowers back to R_p . This rather simple geometry is widely used to investigate new materials for spintronics paired with well known ones like Fe, Ni or Co (see e.g. [12, 14, 62]).

Summary: Spin-dependent tunneling

As pointed out in this chapter, it is not an easy task to describe spin-dependent tunnel currents between magnetic electrodes. It depends on electrode and bar-

rier material as well as the quality of the interfaces and the barrier. Thus, it is a complicated process, that is not yet completely understood. A lot of future theoretical and experimental work is needed to be done in order to be able to fully understand and describe the effect of TMR.

A conclusion from this chapter is, that spin dependent tunnel current and TMR depend mainly on two factors. First, the electronic structure of the barrier and the resulting symmetry filtering, and second, the electronic properties of the interface. The interface properties determine the density of states and therefore the spin polarization due to bonding effects at the electrode-barrier interfaces.

Interesting chapters and reviews on the influence of the barrier and the barrier/electrode interface can be found in [3, 62, 110, 133, 134].

2 The spinel Oxides Magnetite and Zinc ferrite

Magnetite (Fe_3O_4) and zinc ferrite (ZnFe_2O_4) are members of the mineral class of spinel [135]. This material class received a lot of attention in material science due to the wide range of different properties and the tuneability of these properties by growth conditions.

Fe_3O_4 is reported to be a ferrimagnetic, half metallic semiconductor at room temperature with a high potential in spintronic applications [12–14]. Its properties, magnetic as well as electric, can be tuned by substituting a certain amount of iron by zinc. The resulting $\text{Zn}_x\text{Fe}_{3-x}\text{O}_4$ is reported to be half metallic, semiconducting and ferrimagnetic, too [15–17]. Also ZnFe_2O_4 , reported to be an antiferromagnetic insulator in its bulk form [136, 137], shows interesting magnetic and electric properties when deposited as thin film [137–142] or synthesized as nanoparticles [143–145]. Its properties can be tuned between a ferrimagnetic semiconductor and an antiferromagnetic insulator.

These different and tunable properties make Fe_3O_4 , ZnFe_2O_4 and $\text{Zn}_x\text{Fe}_{3-x}\text{O}_4$ thin films an interesting material class for application in spintronic devices. Therefore, an overview on the reported properties as well as on theories, describing these materials, will be given in this chapter.

2.1 The spinel structure

Fe_3O_4 and ZnFe_2O_4 crystallize in the spinel structure, which is named after the mineral MgAl_2O_4 (Figure 2.1). This structure belongs to the space group $\text{Fd}3\text{m}$ (No. 227) [146]. The stoichiometry of this compounds is AB_2O_4 with A a divalent (A^{2+}) and B a trivalent (B^{3+}) metal ion [147]. A unit cell contains eight formula units, resulting in 56 atoms per unit cell. The oxygen atoms form a cubic closed packed (fcc) lattice with a lattice constant $a_{\text{O}} = 1/2 \cdot a_{\text{spinel}}$. This lattice contains 96 interstitial sites, 64 tetrahedral and 32 octahedral coordinated ones, that can be occupied by the cations. The energetic minimum, and therefore a stable structure, is reached when the metal cations occupy $1/8$ of the tetrahedral sites (labeled as **A**) and half of the octahedral sites (labeled as **B**) [147]. In this configuration, the tetrahedral coordinated cations form a cubic diamond sublattice ($a_{\text{tet.}} = a_{\text{spinel}}$). The overall cation sublattice

tice, containing all occupied tetrahedral and octahedral sites, forms a MgCu_2 -type Laves phase structure with a lattice parameter equal to the spinel one ($a_{\text{cation}} = a_{\text{spinel}}$) [146].

In this structure, **A**-site tetrahedra are isolated from each other. They only share corner anions with **B**-site octahedra, and no edges with other occupied sites. **B**-site octahedra further share six of their 12 edges (O-O) with occupied nearest neighbor **B**-sites, and the remaining six with empty octahedra. The occupied **B**-sites and their shared O-O edges form chains along the $\langle 110 \rangle$ directions of the spinel lattice [146]. This configuration of **A** and **B**-site cations will be of interest in the discussion of magnetic and electric properties of spinel materials.

We can distinguish three cases of cation distribution in this structure: In normal spinel, all A-cations occupy tetrahedral sites, whereas all B-type cations sit in octahedral sites. This case is described as

$$(\text{A})_{\text{tet.}}[\text{B}_2]_{\text{oct.}}\text{O}_4 \quad (\text{normal spinel}). \quad (2.1)$$

Examples for normal spinel are MgAl_2O_4 , ZnFe_2O_4 and ZnCo_2O_4 [135].

Second case is the inverse spinel structure. Here all A-cations and half of the B-cations occupy octahedral sites. The other half of the B-cations sits in tetrahedral sites. It can be written as

$$(\text{B})_{\text{tet.}}[\text{AB}]_{\text{oct.}}\text{O}_4 \quad (\text{inverse spinel}). \quad (2.2)$$

A prominent example for an inverse spinel is magnetite Fe_3O_4 . Other examples are NiFe_2O_4 and CoFe_2O_4 [135].

Third case is the partially inverse or mixed spinel. In this case, the A and B cations both occupy tetrahedral and octahedral sites. The degree of distribution is described by the inversion parameter δ ($0 < \delta < 1$). The case of $\delta = 0$ describes the normal spinel, $\delta = 1$ the inverse spinel and $\delta = 2/3$ a completely random distribution of cations on the tetrahedral and octahedral sites [148, 149]. The mixed spinel can be described as

$$(\text{A}_{1-\delta}\text{B}_\delta)_{\text{tet.}}[\text{A}_\delta\text{B}_{2-\delta}]_{\text{oct.}}\text{O}_4 \quad (\text{mixed spinel}). \quad (2.3)$$

Examples are MgFe_2O_4 ($\delta = 0.45$) and CuAl_2O_4 ($\delta = 0.2$) [135]. Also ZnFe_2O_4 [150, 151] and NiFe_2O_4 [71, 72] can occur in mixed spinel form. The inversion parameter δ strongly depends on growth conditions. We will see later, that the electric and magnetic properties of spinel are related to the cation structure and therefore the degree of inversion.

All three cases (normal, inverse and mixed spinel) occur in nature. In the following section, the physical reasons for the formation of the different types of spinel will be discussed.

The normal spinel structure is preferred due to electrostatic reasons [147].

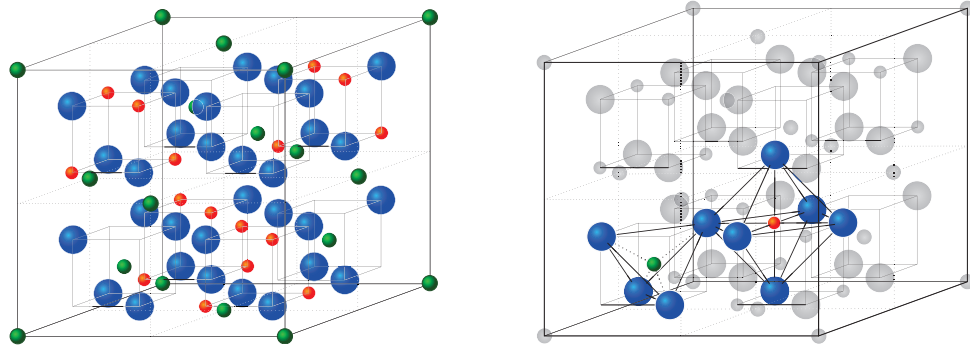


Figure 2.1: Sketch of the spinel structure. Left: Complete structure of one cubic unit cell. The oxygen atoms (blue) form a cubic closed packed fcc lattice. Right: Examples of a tetrahedrally coordinated **A**-site (green) and an octahedrally coordinated **B**-site (red).

First consideration is upon the Madelung constant. This constant describes the electrostatic binding energy inside the lattice. It is higher in case of a normal spinel structure, making the normal spinel configuration more stable compared to the inverse one [146]. Second consideration addresses the cationic charge. A higher charged cation prefers large coordination numbers in order to be neutralized effectively. Therefore, B^{3+} -cations prefer octahedral sites, leading to a stabilization of the normal spinel structure [146].

The occurrence of inverse or mixed spinel can be explained by the crystal field theory (also called ligand field theory) [135, 147]. The crystal field theory describes the energetic splitting of d-orbitals due to the geometry of these orbitals and the surrounding ligands. This splitting leads to a decrease in energy, depending on the electronic configuration of the cation (number of d-electrons). The energy gain, called crystal field stabilization energy (CFSE), is larger in an octahedral ligand field than in a tetrahedral one. The difference between the CFSE in the octahedral and the tetrahedral ligand field is called octahedral site preference energy (OSPE). The OSPE describes the energy gain of the system by putting the cation on an octahedral place instead of a tetrahedral one. The larger the OSPE, the larger the tendency of cations to occupy octahedral places. If we now compare the OSPE of A and B cations, the one with a larger OSPE will occupy the octahedral sites in the oxygen fcc lattice.

The crystal field stabilization energy (CFSE) is defined as the difference between the energy of the electron configuration in the ligand field and the energy of the electron configuration in an isotropic field, thus

$$CFSE = E_{\text{ligand field}} - E_{\text{isotropic field}}. \quad (2.4)$$

The CFSE depends on ligand geometry, number of d-electrons, spin pairing energy and the ligand character (see Table 2.1). In case of ferrites, ligands are always oxygen atoms. So we can neglect the influence of the ligand character.

d^n	d^1	d^2	d^3	d^4	d^5	d^6	d^7	d^8	d^9	d^{10}
CFSE _{tet.}	e^1 2.67	e^2 5.34	$e^2t_2^1$ 3.56	$e^2t_2^2$ 1.78	$e^2t_2^3$ 0	$e^3t_2^3$ 2.67	$e^4t_2^3$ 5.34	$e^4t_2^4$ 3.56	$e^4t_2^5$ 1.78	$e^4t_2^6$ 0
CFSE _{oct.}	t_{2g}^1 4	t_{2g}^2 8	t_{2g}^3 12	$t_{2g}^3e_g^1$ 6	$t_{2g}^3e_g^2$ 0	$t_{2g}^4e_g^2$ 4	$t_{2g}^5e_g^2$ 8	$t_{2g}^6e_g^2$ 12	$t_{2g}^6e_g^3$ 6	$t_{2g}^6e_g^4$ 0
OSPE	1.33	2.66	8.44	4.22	0	1.33	2.66	8.44	4.22	0

Table 2.1: Crystal field stabilization energy (CFSE) for tetrahedral (tet.) and octahedral (oct.) ligand field geometry and the resulting octahedral site preference energy (OSPE). All values are in Dq. The case of a weak field is displayed, thus spin pairing plays no role and all values describe the high spin configuration. The modulus of energies is shown, but all energies are negative due to the stabilizing nature of the CFSE. All values are 0 for the d^0 configuration. The rows above the energy values show the orbital filling. [135, 147]

Also the spin pairing energy plays no role in ferrites. The high spin configuration is always preferred due to the fact that the energy splitting caused by the oxygen atoms is small compared to the spin pairing energy. The only example of a low spin configuration in spinel is Co^{3+} in Co_3O_4 [135].

The influence of ligand geometry on the energy of the electronic system is depicted in Figure 2.2. The d-orbitals are labeled by the expressions t_{2g} , t_2 , e_g and e . These labels originate from the group theory and describe the different types of orbitals. The term t_2 describes the energetically threefold degenerated orbitals (d_{xy} , d_{yz} and d_{xz}), whereas e describes the twofold ones ($d_{x^2-y^2}$ and d_{z^2}). The g indicates a symmetry center which is present in the case of octahedral symmetry and is missing in the tetrahedral one. The energy splitting between the different types of d-orbitals is expressed in values of Dq (due to historic reasons) and the splitting in the octahedral ligand geometry is defined as $\Delta_O = 10 Dq \approx 100 - 500 \text{ kJ/mol} \approx 1 - 5 \text{ eV}$ [147].

In case of an octahedral ligand symmetry, the maximum electron density of e_g -orbitals ($d_{x^2-y^2}$ and d_{z^2}) points in the direction of the negatively charged ligand atoms. The electrostatic repulsion increases the energy of this orbitals by $0.6 \Delta_O = 6 Dq$ compared to an isotropic ligand field. The t_{2g} -orbitals (d_{xy} , d_{yz} , d_{xz}) arrange in between the ligand atoms, resulting in a lowering of their energy levels by $0.4 \Delta_O = 4 Dq$. A filling of the orbitals following Hund's rule (no spin pairing unless the energy gain Δ_O is higher than the spin pairing energy) gives the CFSE_{oct.} values listed in Table 2.1. These values describe a lowering of the total energy of a d-electron configuration due to the octahedral ligand field geometry.

The energy splitting in the tetrahedral geometry is smaller than in the octahedral case. It is $\Delta_T = 4/9 \Delta_O$ [147]. In a tetrahedral ligand field geometry, the ligand atoms arrange in the direction of the t_2 -orbitals, raising the energy of

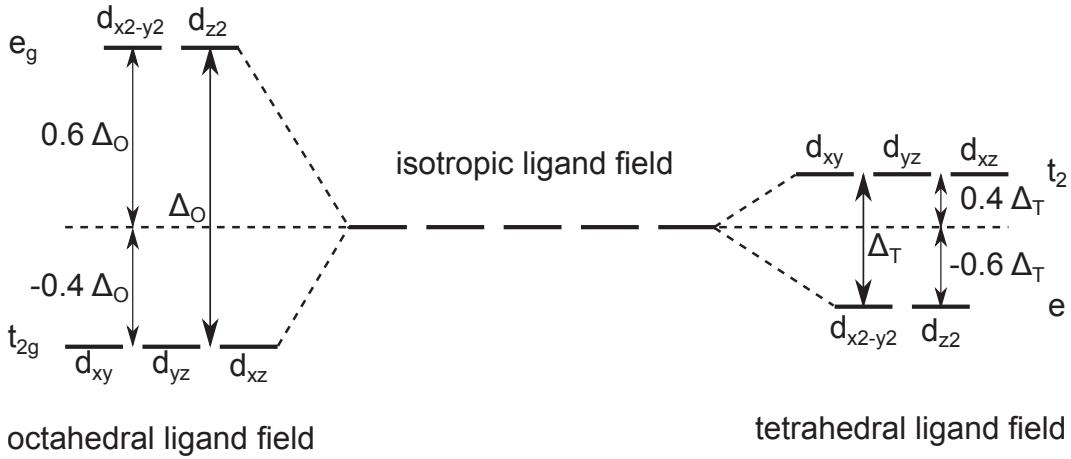


Figure 2.2: Energetic splitting of the 3d-orbitals in an octahedral (left) and a tetrahedral (right) coordinated ligand field. Degeneracy of d-orbitals is lifted due to the geometry of the ligand field. The splitting energies are $\Delta_O = 10 Dq$ in the case of an octahedral field and $\Delta_T = 4/9 \Delta_O$ in a tetrahedral field.

the d_{xy} , d_{yz} and d_{xz} orbitals by $0.4 \Delta_T = 0.4 \cdot 4/9 \Delta_O = 1.78 Dq$. The e-orbitals ($d_{x^2-y^2}$ and d_{z^2}) arrange in between the ligand atoms, lowering there energy by $0.6 \Delta_T = 0.6 \cdot 4/9 \Delta_O = 2.67 Dq$. The orbital filling results in the CFSE_{tet.} values in Table 2.1, describing the energy gain in tetrahedral ligand geometry compared to an isotropic ligand field.

The amount of lowering or raising the energy level of the orbitals is calculated by the "energy barycenter principle" [147]. The total splitting is defined as Δ ($= \Delta_O$ or Δ_T). Now the principle implies, that the barycenter of the energy remains constant. This leads to an energy shift of $3/5 \Delta = 0.6 \Delta$ for the two $e_{(g)}$ orbitals and a shift of $2/5 \Delta = 0.4 \Delta$ for the three $t_{2(g)}$ -orbitals [147].

As pointed out before, the cations form a $MgCu_2$ -type Laves phase structure in spinel, occupying half of the octahedral and one eighth of the tetrahedral coordinated sites inside the fcc-lattice of the oxygen atoms. Electrostatic interactions stabilize the normal spinel structure, where A^{2+} cations occupy the tetrahedral sites and B^{3+} ones the octahedral sites. Nevertheless, the inverse spinel structure can be the stable one due to the different CFSEs of cations on tetrahedral and octahedral sites.

The key value is the octahedral site preference energy (OSPE). It is the difference between the CFSE of a cation in an octahedral ligand field and in a tetrahedral one.

$$OSPE = \Delta CFSE = CFSE_{oct.} - CFSE_{tet.} \quad (2.5)$$

Table 2.1 summarizes the OSPE-values for different electron configurations d^n . In case of a d^0 , d^5 or d^{10} electron configuration, the OSPE is zero. These ions are called spheric. If both cations are spheric, no prediction on cation distribution based on the crystal field theory can be made. In this case, the A^{2+}

will occupy tetrahedral sites and the B^{3+} octahedral ones and form a normal spinel structure, due to the considerations on electrostatic reasons made in the beginning of this chapter.

In order to swap the A and B cations, one needs to spend some energy. This electrostatic energy is small compared to the OSPE of non spheric cations, which is the energy gained by the ligand field if we change from tetrahedral to octahedral sites. Therefore, the cation with the higher OSPE will occupy the octahedral sites. If the OSPE of the A^{2+} cation is the larger one, the structure will be inverse spinel. If the OSPE of the B^{3+} cation is larger, it will be normal spinel.

We now can apply these considerations to the two materials Fe_3O_4 and $ZnFe_2O_4$. In Fe_3O_4 , the A^{2+} cations are Fe^{2+} and the B^{3+} cations are Fe^{3+} . Fe^{2+} has an OSPE of

$$OSPE(Fe^{2+}) = -1.33 Dq \quad (2.6)$$

and Fe^{3+} is spheric due to its d^5 configuration and has an OSPE of

$$OSPE(Fe^{3+}) = 0 Dq. \quad (2.7)$$

Therefore, the A-cations (Fe^{2+}) will occupy half of the octahedral sites, whereas half of the B-cations (Fe^{3+}) occupy the remaining octahedral sites and the tetrahedral sites. This means, Fe_3O_4 crystallizes in the inverse spinel structure, and therefore

$$Fe_3O_4 = (Fe^{3+})[Fe^{2+}Fe^{3+}]O_4. \quad (2.8)$$

In $ZnFe_2O_4$, we have Zn^{2+} (A) and Fe^{3+} (B) cations. Both of them are spheric (Zn^{2+} has d^{10} and Fe^{3+} has d^5 configuration), and therefore

$$OSPE(Zn^{2+}) = OSPE(Fe^{3+}) = 0 Dq. \quad (2.9)$$

Thus, we end up in normal spinel structure and Zn^{2+} occupies tetrahedral sites and Fe^{3+} octahedral ones due to electrostatic reasons.

The formation of mixed spinel $ZnFe_2O_4$ can be explained by cation disorder, formed by the growth process. Both cations (Zn^{2+} and Fe^{3+}) are spheric and therefore, the energy needed to change positions is rather small. This allows to stabilize the "metastable" disordered structure by choosing an appropriate growth method (see Section 2.3).

2.1.1 Electrical conduction in spinel materials

In the following, tetrahedral cation sites will be labeled as **A**-sites, whereas octahedral ones will be labeled as **B**-sites.

Spinel materials can occur as electrical insulator or conductor. Electrical conductivity in spinel is attributed to an electron hopping mechanism between

cations of different valences, occupying **B**-sites. A requirement for this conduction mechanism are cations being able to have different valence states and have the ability to add or release an electron easily, like Fe^{2+} and Fe^{3+} (Figure 2.4). As mentioned earlier, **B**-site cations share six of twelve edges (O-O) of their octahedra with their nearest neighbor **B**-site cation. This arrangement forms chains along the $\langle 110 \rangle$ directions. In this chains, the **B-B** distances are short and no intervening oxygen anions are between the **B**-site cations. Therefore, electrons can jump between the divalent cations and contribute to a non zero conductivity [146, 152]. This hopping mechanism is often also assigned to double exchange interaction between the Fe^{2+} and Fe^{3+} -cations located on the **B**-site lattice [12, 14, 153]. This interaction allows electrons to jump between the Fe atoms, mediated by the surrounding oxygen atoms (see also Section 2.1.2).

Due to the hopping mechanism along the chains in the $\langle 110 \rangle$ directions, conductivity in spinel is linked to the degree of inversion, or at least the occurrence of mixed valent cations on the octahedral sites [14, 15, 134]. The occurrence of divalent cations on **B**-sites in normal spinel is related to oxygen vacancies. Their presence leads to a chemical reduction of trivalent **B**-site cations [137, 138]. In normal spinel ferrite (e.g. ZnFe_2O_4), this divalent cations are Fe^{2+} , located at the octahedral sites due to their non-zero OSPE. Another reason for the formation of Fe^{2+} -cations on **B**-sites in ZnFe_2O_4 is iron surplus. Fe^{3+} on **A**-sites cause the formation of Fe^{2+} on **B**-sites due to charge neutrality [15].

The density of itinerant charge carriers is determined by the amount of Fe^{2+} on **B**-sites [15]. Following this considerations, bulk Fe_3O_4 is a rather good conductor (inverse spinel, Fe^{2+} and Fe^{3+} on **B**-site) [134] whereas bulk ZnFe_2O_4 is an insulator (normal spinel, only Fe^{3+} on **B**-site) [137]. Nevertheless, thin films of ZnFe_2O_4 , grown at low oxygen partial pressures, are conducting due to the occurrence of Fe^{2+} on **B**-sites [137, 139, 140] (see Figure 2.4).

2.1.2 Magnetism in spinel materials

Magnetism in transition metal oxides is based on the magnetic moments of the atoms and the interactions between these moments. The magnetic moment of a transition metal ion depends on the electron configuration in the 3d-shell. Due to Hund's rules, the orbitals are occupied by single electrons of parallel spin, until all orbitals are half filled. If the number of electrons exceeds the number of orbitals, spin pairing occurs and the remaining electrons align their spin antiparallel to the first ones. The spin and magnetic moments of the shell electrons sum up, resulting in a total spin of $s = n/2$ in case of an up to half filled 3d-shell and $s = (10 - n)/2$ for a more than half filled 3d-shell, with n the number of electrons (spin $s_e = 1/2$) in the 3d-shell. According to the magnetic moment of a single electron, the magnetic moment μ of a transition

metal cation is approximately

$$\mu = g_e s \mu_B \quad (2.10)$$

with the electron spin g-factor $g_e \approx 2$ and the Bohr magneton μ_B . In case of Fe_3O_4 and ZnFe_2O_4 , we get the following magnetic moments for zinc and iron cations [14, 15, 154].

$$\begin{aligned} \text{Zn}^{2+} : (\mathbf{d}^{10}) &\rightarrow s = 0 &\rightarrow \mu = 0\mu_B \\ \text{Fe}^{2+} : (\mathbf{d}^6) &\rightarrow s = \frac{4}{2} = 2 &\rightarrow \mu = 4\mu_B \\ \text{Fe}^{3+} : (\mathbf{d}^5) &\rightarrow s = \frac{5}{2} &\rightarrow \mu = 5\mu_B \end{aligned}$$

The interaction between the transition metal ions in oxide spinels are oxygen mediated superexchange and double exchange. The interaction strength is described by the coupling constant J . Due to the nature of the exchange interactions, only nearest neighbors must be taken into account. The energy shift due to the magnetic interactions can be described by the Heisenberg model

$$\Delta E = -\frac{1}{2} \sum_{i,j} J_{ij} S_i S_j. \quad (2.11)$$

with $S_{i,j} = \pm s_{i,j}$ the total spin of cations i and j , and J_{ij} the interaction between cation i and j . Due to the minimization of the energy, a coupling constant $J < 0$ favors antiferromagnetic coupling, whereas a positive coupling constant causes ferromagnetic coupling. Also the strength of the coupling is responsible for the magnetic response of the material. A large negative value of J causes antiferromagnetism, a large positive value causes ferromagnetism and a small interaction results in paramagnetism. A detailed overview, describing the different types of magnetic phenomena, is given in [155].

Spinel materials show a broad range of magnetic properties, ranging from antiferromagnetic to ferrimagnetic. These different properties are caused by the magnetic interactions within and between the two sublattices **A** and **B**. This principle of treating the magnetization in spinels is called Néel-model and was developed by Néel in 1948 [156, 157]. The model describes the magnetic response of a lattice consisting of two magnetic sublattices interacting with each other. Therefore, the occupation of **A** and **B** sites with different cation species and the degree of inversion play a major role in the description of magnetic properties in spinel materials. The focus in this section will be on the ferrites Fe_3O_4 and ZnFe_2O_4 . The dominant interactions in these materials are listed in Table 2.2. The interaction inside the sublattice **A** is the weakest, due to the fact that occupied **A**-site tetrahedra do not share any edge atoms (oxygen) that can mediate the interaction [146].

The magnetic interactions in oxides are usually indirect magnetic exchange

interactions between transition metal ions separated by an O^{2-} ion [14]. These interactions are based on a virtual electron transfer (superexchange interaction) or a real electron transfer (double exchange interaction) between the cations, mediated by the oxygen atoms (see Figure 2.3). The transition metal cations and the oxygen anions are covalently bound with a strong ionic character. Nevertheless, there is an overlap of the binding orbitals between cations (3d-orbitals) and oxygen (2p-orbitals), allowing an exchange of electrons between them. This exchange is responsible for the magnetic coupling of the transition metal cations. These interactions depend strongly on the orbital structure of the involved ions. Both, the sign and the strength are influenced by the degeneracy and occupancy of the 3d orbitals of the transition metal ions, and their overlap with the O-2p orbitals [14]. In 1955, Goodenough and Loeb [159] applied this idea of "semicovalent exchange" to spinel materials in order to describe their magnetic properties. The discussion is rather complex and the following section will only give a brief overview on this topic.

Superexchange interaction

The theory of superexchange was developed by Anderson [160], Goodenough [161, 162] and Kanamori [163] in the 1950s. The superexchange interaction is described by the Goodenough-Kanamori rule. This rule states, that superexchange interactions are antiferromagnetic when the virtual electron transfer is between overlapping, half-filled orbitals. In case of a virtual electron transfer from a half-filled to an empty orbital or from a filled to a half-filled orbital, the interaction is ferromagnetic [164]. This rule is based on [164]:

1. The conservation of the spin angular momentum in an electron transfer (no matter if it is virtual or real).
2. The restrictions on electron transfer from a half-filled to a half-filled orbital or two-electron transfer from the same anion-p orbital due to the Pauli exclusion principle.

Table 2.2: Magnetic interactions in spinel ferrite. It is $|J_{AA}| < |J_{BB}| \ll |J_{AB}|$ [14, 15, 138, 158].

participating sites	interaction type	strength
<hr/>		
$Fe^{3+}-O-Fe^{3+}$		
A-O-A	antiferromagnetic superexchange	weak
B-O-B	antiferromagnetic superexchange	weak
A-O-B	antiferromagnetic superexchange	strong
<hr/>		
$Fe^{2+}-O-Fe^{3+}$		
B-O-B	ferromagnetic double exchange	weak

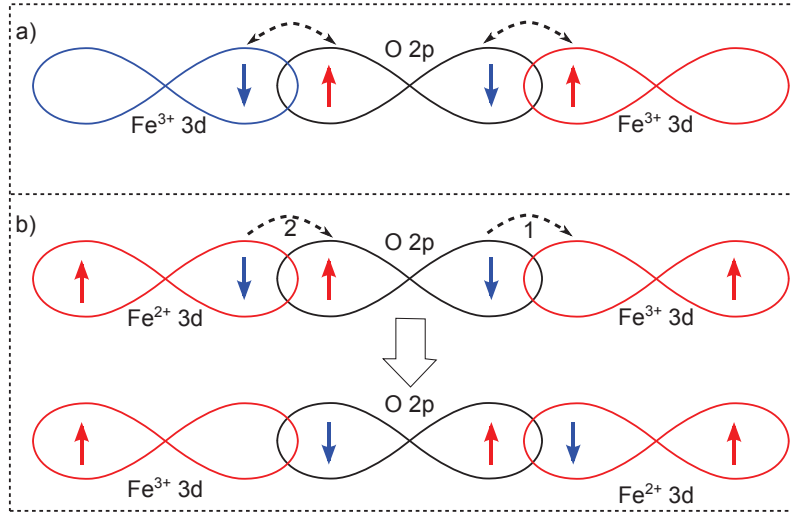


Figure 2.3: a) Antiferromagnetic superexchange interaction between two Fe^{3+} -cations ($3d^5$), mediated by an oxygen atom (O^{2-} , $2p^6$). Electron exchange is per virtual electron hopping between Fe^{3+} and O^{2-} . b) Ferromagnetic double exchange between Fe^{2+} and Fe^{3+} . In contrast to the virtual hopping in superexcahnge, the electron transfer trough double exchange is real and the minority electron is transferred from one iron atom to another.

3. The angular dependence of the expectation value t_{ij} for an electron transfer due to the quantization of the electron spins:

$$t_{ij}^{\uparrow\uparrow} = b_{ij} \sin\left(\frac{\theta}{2}\right) \quad (2.12)$$

Figure 2.3 a) shows a sketch of the superexchange interaction between two Fe^{3+} -cations separated by an O^{2-} -anion in 180° -configuration. Only overlapping 3d and 2p orbitals are shown. The electrons in the filled oxygen-2p orbital are aligned antiparallel (paired spins). All 3d-orbitals in Fe^{3+} are half filled and the electron spins are aligned in parallel (d^5 high spin configuration). Due to the overlap of the orbitals, the electrons of the oxygen can virtually transfer to an iron-3d orbital. This leads to a virtually excited state that can reduce the total energy of the system when both spins are aligned antiparallel as it is calculated by higher order perturbation theory [14]. Therefore, each oxygen-2p spin aligns antiparallel to the iron-3d spin inside the overlapping orbital. This forces the two iron moments into the antiparallel state. These considerations are based on the points 1 and 2 of the Goodenough-Kanamori rule. The third point results in a strong interaction at 180° , decreasing with decreasing bond angle to a rather weak interaction at 90° .

In conclusion, the superexchange interaction is an antiferromagnetic interaction, that weakens with decreasing binding angle. Thus, the interaction between Fe^{3+} -cations on the two sublattices **A** and **B** with a binding an-

gle of approximately 125° [162] is strong compared to the interactions inside the sublattices, where the binding angle is close to 90° . Therefore it is $|J_{AA}| < |J_{BB}| \ll |J_{AB}|$ [14, 15, 138, 158].

Double exchange interaction

In contrast to the superexchange interaction, the interaction between Fe^{3+} and Fe^{2+} , mediated by an oxygen atom, is based on a real electron exchange between divalent and trivalent Fe-atoms. It is called double exchange and was theoretically described by Zener [165], Anderson and Hasegawa [166] as well as de Gennes [167]. Although it is a complicated quantum mechanical process, the principle of double exchange can be understood by applying the Goodenough-Kanamori rule to the Fe^{2+} -O- Fe^{3+} coupling. Figure 2.3 b) shows a sketch of the orbitals involved in the double exchange interaction and the resulting charge transfer between the two iron atoms. All 3d orbitals of Fe^{3+} are half filled. In Fe^{2+} , one t_{2g} orbital is completely filled. According to the Goodenough-Kanamori rule, the interaction between these two iron atoms is ferromagnetic. This can be explained by the exchange of the minority spin electron. The oxygen gives one 2p electron to the Fe^{3+} . The spin of this electron must be antiparallel to the magnetic moment of the accepting Fe atom. Thus, the paired minority spin of the Fe^{2+} can occupy the half filled O-2p orbital, because its spin is antiparallel to the one of the remaining O-2p electron. The situation is now mirror symmetric to the initial one. The resulting delocalization, and thus the hopping of the electron, reduces the energy of the system. This exchange, and therefore the lowering of energy, is only possible in the parallel alignment of the magnetic moments of the divalent iron atoms. This leads to the predicted ferromagnetic alignment of Fe^{2+} and Fe^{3+} on **B**-sites. The expectation value t_{ij} for an electron transfer in case of double exchange is

$$t_{ij}^{\uparrow\uparrow} = b_{ij} \cos\left(\frac{\theta}{2}\right). \quad (2.13)$$

The double exchange interaction and the resulting hopping mechanism between the Fe^{3+} and Fe^{2+} on **B**-sites is responsible for electron conduction in ferrites [12, 14]. The conductivity in these materials can be reduced by a finite spin canting angle due to the angular dependence of the hopping probability [14, 15].

Magnetism in Fe_3O_4 and ZnFe_2O_4

In bulk ZnFe_2O_4 , Zn^{2+} -cations (resulting spin $s = 0$) occupy **A**-sites, consequently showing no magnetic interactions. **B**-sites are occupied by Fe^{3+} ($s = 5/2$), coupled by antiferromagnetic superexchange interactions mediated by the oxygen atoms. The weak antiferromagnetic superexchange aligns the magnetic moments of Fe^{3+} -cations on **B**-sites antiparallel, causing the antiferromagnetism in ZnFe_2O_4 . This interaction is rather weak, resulting in a low

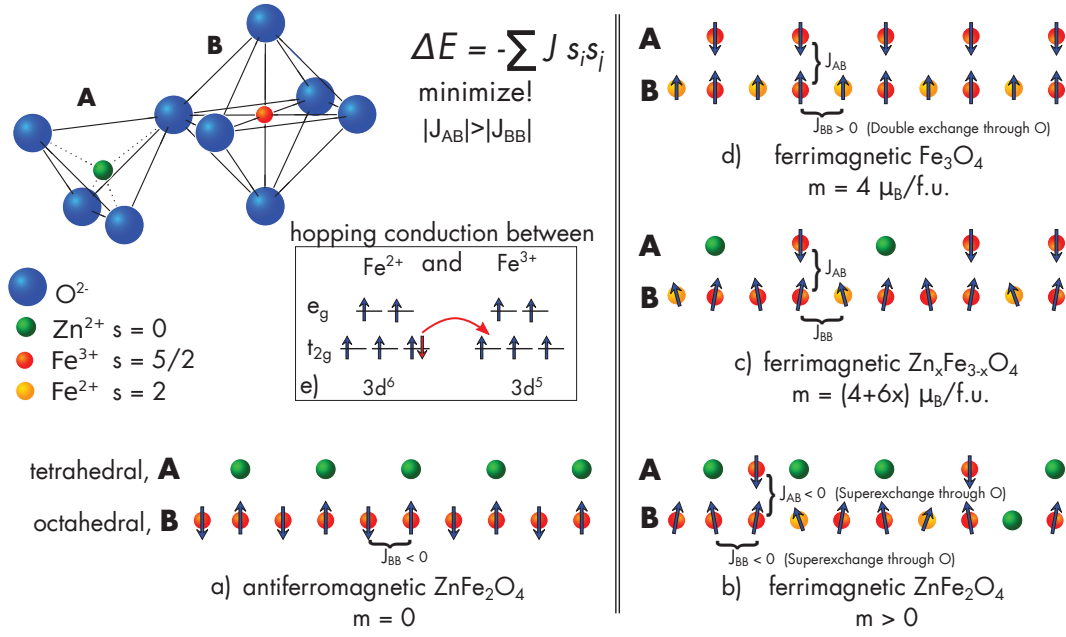


Figure 2.4: Sketch of the spin configuration in a) bulk ZnFe_2O_4 (insulating, antiferromagnetic), b) ZnFe_2O_4 thin films (conducting, ferrimagnetic), c) $\text{Zn}_x\text{Fe}_{3-x}\text{O}_4$ (conducting, ferrimagnetic) and d) Fe_3O_4 (conducting, ferrimagnetic). The resulting magnetization is given in $\mu_B/\text{f.u.}$ (Bohr magneton per formula unit). The inset e) shows the spin states of Fe^{2+} and Fe^{3+} and the hopping of the minority spin electron due to double exchange.

Néel temperature of $T_N = 10 \text{ K}$ [138]. Above this temperature, ZnFe_2O_4 is paramagnetic.

The magnetic response in Fe_3O_4 is described by the Néel-model [156, 157]. The Fe^{3+} -cations occupy the **A**-sites and half of the **B**-sites in Fe_3O_4 . The other half is filled with Fe^{2+} -cations ($s = 2$). This cation distribution (inverse spinel), leads to magnetic interactions inside the sublattices **A** and **B**, but also in between these two sublattices. All these interactions are antiferromagnetic superexchange. The interaction inside the lattices (**A**–O–**A** and **B**–O–**B**) are rather weak, as indicated by the small Néel temperature in ZnFe_2O_4 . The interaction between the two sublattices (**A**–O–**B**) is strong due to the binding angle of 125° [162]. It is $|J_{AA}| < |J_{BB}| \ll |J_{AB}|$ [14, 15, 138, 158]. Therefore, the magnetic moments inside the sublattices are forced to align in parallel, whereas the magnetic moments of the two sublattices get aligned antiparallel (see Figure 2.4). The ferromagnetic double exchange between the Fe^{2+} - and Fe^{3+} -cations on the **B**-site lattice aligns the magnetic moment of the Fe^{2+} -cations in parallel to the Fe^{3+} -cations. This overall configuration of magnetic moments causes the ferrimagnetic nature of magnetism in Fe_3O_4 . The Fe^{3+} moments, sitting on the **A** and **B** sublattice in an equal amount, cancel out each other. The remaining magnetic moment is caused by the moments of Fe^{2+} -cations located on the **B**-sites. This leads to an overall magnetization

of $4\mu_B/\text{f.u.}$ (Bohr magneton per formula unit) [14, 15]. The ferromagnetic double exchange between **B**-site Fe^{2+} and Fe^{3+} is usually not taken into account in the Néel-model. A more recent work by Loos and Novák [168] shows the importance of this interaction. If the double exchange is not considered, fitting the magnetization curves of Fe_3O_4 requires a positive J_{BB} , which is in contradiction to the negative J_{BB} in ZnFe_2O_4 [168].

The situation in ZnFe_2O_4 thin films is rather similar to the one in Fe_3O_4 . Fe^{3+} occupies **A**-sites due to iron surplus. The resulting magnetic interactions force the moments located on the **B**-site sublattice in the parallel alignment, resulting in a ferrimagnetic order and a high overall magnetic moment [138, 158]. According to the Néel-model, the magnetic moment in ferrimagnetic ZnFe_2O_4 should be larger than that in Fe_3O_4 . This is due to the small amount of Fe^{3+} on **A**-sites that no longer compensates the moments of **B**-site Fe^{3+} . Due to oxygen vacancies and charge neutrality issues caused by the Fe^{3+} -cations on **A**-sites, Fe^{2+} is formed on **B**-sites, leading to conductivity in ZnFe_2O_4 thin films [15, 137, 138]. All three cases (Fe_3O_4 , bulk ZnFe_2O_4 and ZnFe_2O_4 thin films) are summarized in Figure 2.4.

An additional effect in $\text{Zn}_x\text{Fe}_{3-x}\text{O}_4$ ($0 < x < 1$) influences the magnetic response of thin films. Due to the increasing amount of Zn^{2+} and the resulting decrease of Fe^{3+} on **A**-sites compared to pure Fe_3O_4 , the **A**-O-**B** interaction weakens (J_{AB} is decreased). Also the ferromagnetic double exchange interaction between **B**-site Fe^{2+} and Fe^{3+} weakens due to the decreasing amount of Fe^{2+} , caused by charge neutrality. This allows the antiferromagnetic **B**-O-**B** interaction to compete with the interaction between the two sublattices. Therefore, the **B**-lattice spins are no longer aligned strictly in parallel, but show a finite canting angle, the Yafet-Kittel angle [169]. Yafet and Kittel described this situation by introducing two **B**-site sublattices with a finite canting angle between the magnetization of these two lattices. This angle results in a decrease of the overall magnetization of the system. Also conductivity decreases due to a smaller amount of Fe^{2+} , decreasing the amount of free charge carriers, as well as due to the spin canting, that reduces the hopping amplitude between Fe^{2+} and Fe^{3+} [14, 15]. Similar effects can be observed in ferrimagnetic ZnFe_2O_4 thin films (Figure 2.4).

2.1.3 Spin polarization in Fe_3O_4 and ZnFe_2O_4

A combination of the pictures of magnetism and conduction in spinel materials results in a high spin polarization of charge carriers. Spin polarization in Fe_3O_4 and conducting, ferrimagnetic ZnFe_2O_4 is $P = -100\%$ in theory. The magnetic moments of the **B**-site Fe^{2+} and Fe^{3+} cations originate from the localized electron spins ($s = 5/2$, high spin configuration) and are aligned in parallel. Due to Hund's rule, the conduction electron is the spin down electron in the t_{2g} -state of Fe^{2+} (see Figure 2.4). This spin is antiferromagnetically coupled to the resulting magnetic moment and thus, the flowing current only

consists of minority spin electrons (electrons with a spin antiparallel to the layer magnetization). Therefore, Fe_3O_4 and conducting, ferrimagnetic ZnFe_2O_4 are promising candidates for spintronic applications.

2.2 Magnetite Fe_3O_4

Magnetite (Fe_3O_4) is a ferrimagnetic iron oxide and gained interests in the spintronic community due to its predicted half metallic character [12–14]. Fe_3O_4 crystallizes in the inverse spinel structure with a lattice parameter of $a = 0.8367 \text{ nm}$ [12]. Ferrimagnetism originates from the strong antiferromagnetic superexchange interaction between the **A**- and **B**-site sublattice. This interaction forces the magnetic moments located at the two sublattices to align antiparallel. Therefore, the magnetic moments of the **A**- and **B**-site Fe^{3+} cations cancel out each other. The remaining moments of the Fe^{2+} , located at **B**-sites, result in a magnetization of $4 \mu_{\text{B}}/\text{f.u.}$ (Bohr magneton per formula unit). The Curie temperature of Fe_3O_4 is $T_{\text{C}} \approx 860 \text{ K}$ and therefore far above room temperature [12–14].

Conductivity in Fe_3O_4 is assigned to electron hopping between Fe^{2+} and Fe^{3+} on **B**-sites, mediated by double exchange [12, 14, 15, 134]. Charge transport is therefore due to the transfer of the minority spin electron in the t_{2g} -orbital from Fe^{2+} to Fe^{3+} (see Figure 2.4). This transport mechanism results in the predicted half metallic nature of Fe_3O_4 . Also band structure calculations confirm the half metallic nature of magnetite. Self-consistent APW (augmented plane wave) calculations by Yanase and Siratori [170] show an energy gap in the majority spin band and metallic behavior in the spin down band, predicting half metallicity in Fe_3O_4 . LSDA calculations by Zhang and Satpathy [154] confirmed this results (see Figure 2.5). The calculations further show, that the minority spin band at the Fermi level consists of t_{2g} -orbitals of **B**-site cations. This result confirms both, the hopping conduction by itinerant Fe - t_{2g} minority electrons and the half metallicity of bulk Fe_3O_4 . More recent works by Fonin *et al.* [171], Zhu *et al.* [172] and Yu *et al.* [173] focus on the surface of Fe_3O_4 thin films. They also predicted half metallicity in the bulk material, but a reduced spin polarization at the surface. According to these works, surface spin polarization depends strongly on the surface plane and the termination. Most scenarios lead to a metallic state at (111)-oriented surfaces, and therefore the loss of half metallicity at the surface. Yu *et al.* [173] predicted half metallicity at (100)-surfaces, whereas Fonin *et al.* [171] calculated a spin polarization of $P = -40\%$. This result was confirmed by spin-polarized photo electron spectroscopy (SP-PES) measurements on (100) surfaces, yielding $-(55 \pm 10)\%$ of spin polarization at the Fermi level [171, 174]. Also Huang *et al.* [175] measured -55% on (100)-surfaces of PLD-grown Fe_3O_4 by SP-PES. Measurements on (111)-surfaces yield $-(80 \pm 5)\%$ [174, 176]. In contrast, Tobin *et al.* [177] report a spin polarization of -30 to -40% on (100)-surfaces and -65% in the bulk. This results are subject to intense discussions on the measurement techniques

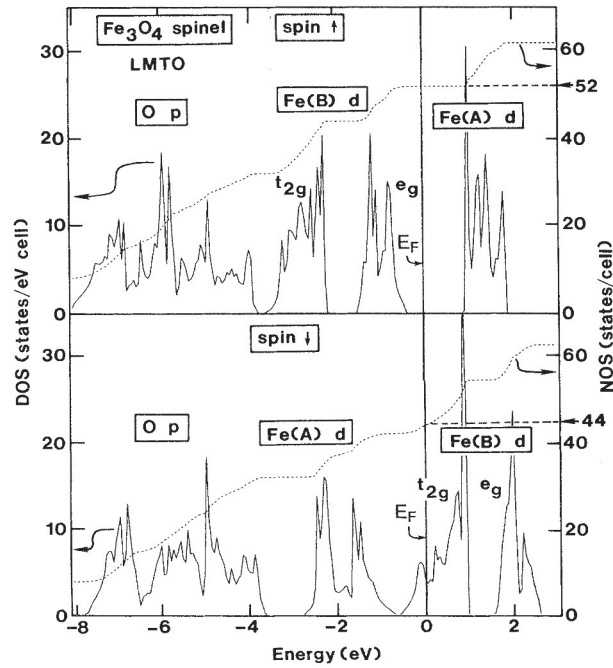


Figure 2.5: Calculated density of states (DOS) for Fe_3O_4 . The majority spin states show a gap at the Fermi level. The minority spin band is formed by t_{2g} -orbitals of B-site iron. From [154]. Copyright 1991 by the American Physical Society.

and the origin of spin polarization in SP-PES measurements [174, 177, 178]. In summary, all the SP-PES measurements do not reach the predicted spin polarization of -100%. Nevertheless, the obtained spin polarization is large enough for utilizing Fe_3O_4 in spintronic applications.

2.2.1 Fe_3O_4 thin films

Applications usually require thin films of the functional material. Fe_3O_4 thin films were grown by sputtering [179], MOCVD [180, 181], oxygen assisted MBE [12, 182–185] and PLD [134, 186–191] on different substrates. The cation distribution in the spinel structure of these films was determined by XAS (X-ray absorption spectroscopy) and XMCD (x-ray magnetic circular dichroism) measurements [12, 192]. The results indicate an inverse spinel structure of Fe_3O_4 , containing mainly Fe^{2+} on B-sites and Fe^{3+} equally distributed on A and B-sites. This is in a good agreement with the expected inverse spinel structure of Fe_3O_4 .

Nevertheless, all these thin films show deviations from the properties of Fe_3O_4 single crystals. Saturation magnetization values are lowered compared to these in single crystals. Thin films with a thickness between 5nm and 50 nm reach 50% up to 73% of the value obtained in single crystals, respectively [12]. Also the ratio of remanent magnetization M_R and magnetization at 1.2 T,

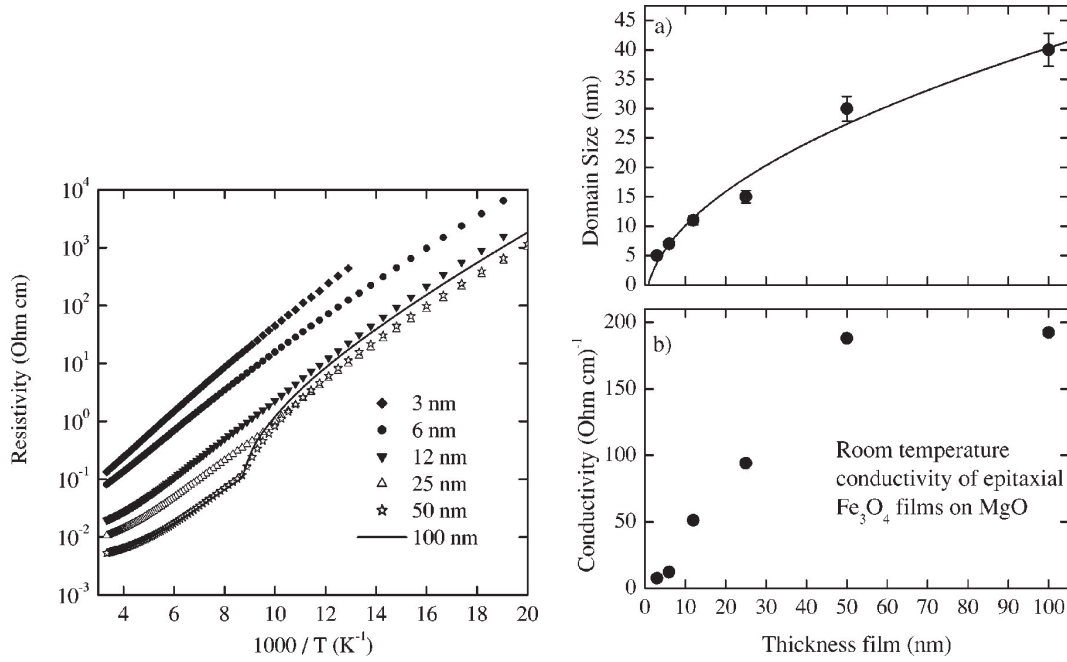


Figure 2.6: Left: Resistivity over $1/T$ of epitaxial Fe_3O_4 thin films on MgO grown by MBE. The Verwey transition is visible in thick films. Right: a) Domain size of anti phase boundaries in dependence of film thickness. The solid line is a fit $D \propto \sqrt{d}$. b) Room temperature conductivity of Fe_3O_4 thin films in dependence of layer thickness. Figure taken from [197]. Copyright 2002 by the American Physical Society.

$M_R/M(1.2\text{ T})$, lowers and varies between 30% in thin layers (5 nm) and 69% in thicker layers (50 nm) [12]. Another difference in the magnetization of thin films and single crystals is the approach of saturation. Saturation is reached quickly in single crystals. In contrast, thin films reach saturation slowly, showing a significant positive slope at high fields ($\mu_0 H > 1\text{ T}$) [12, 179, 193]. Single crystalline Fe_3O_4 shows no magnetoresistance at room temperature [194, 195]. In contrast, thin films exhibit a negative magnetoresistance of several percent [12, 194–196]. The negative slope in the magnetoresistance curves reflects the absence of saturation even up to high fields of 7 T [12, 196]. Room temperature resistivity is also increased in Fe_3O_4 thin films. It depends on film thickness and increases with decreasing film thickness (see Figure 2.6) [12, 197, 198]. For comparison, room temperature resistivity of bulk Fe_3O_4 is $4 \cdot 10^{-3}\ \Omega\text{cm}$. [197]. The temperature dependency (slope) of resistivity near room temperature is nearly the same for all samples and shows no dependence on film thickness.

The impact of antiphase boundaries (APBs)

All these differences between single crystals and thin films are assigned to a structural disorder of the thin films, called antiphase boundaries (APBs)

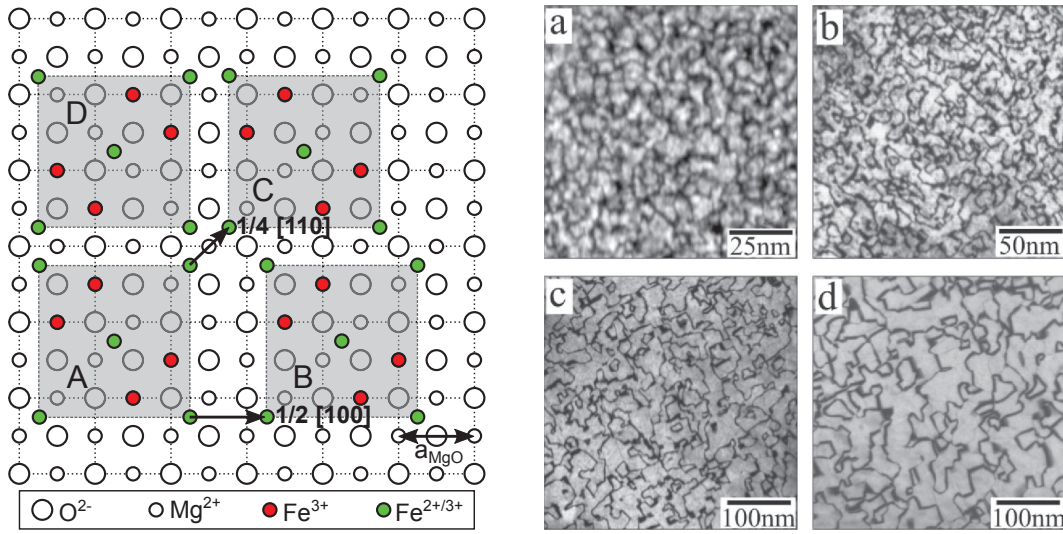


Figure 2.7: Left: Schematic illustration of the possible shifts and the rotation in respect to the MgO substrate, leading to APBs in Fe_3O_4 . B) $1/2 a$ along 100 C) $1/4 \sqrt{2}a$ along 110 and D) rotation by 90° (after [200]). Right: TEM dark field image of a) 3 nm b) 6 nm c) 12 nm and d) 25 nm thick Fe_3O_4 films on MgO , showing the increase of antiphase domain size with increasing film thickness. Figure B taken from [197]. Copyright 2002 by the American Physical Society.

[12, 14]. Antiphase boundaries are regions inside the Fe_3O_4 -crystal, where antiphase domains (APDs) meet and the cation lattice shows a displacement. They form during growth, because the lattice constant of Fe_3O_4 is approximately twice the lattice constant of commonly used substrates, e.g. MgO and SrTiO_3 . In the initial stage of thin film growth, different islands form on the substrate surface. When these islands meet and grow together, they might be shifted by $1/2 a$ along $\{100\}$ or $1/4 \sqrt{2}a$ along $\{110\}$ or be rotated by 90° with respect to each other [14]. The situation at the interface between substrate (MgO) and the Fe_3O_4 film and the resulting formation of APDs and APBs are shown in Figure 2.7. At APBs, the oxygen lattice is undistorted, but the cation lattice is displaced and shows stacking faults, resulting in a perturbation of the magnetic order on the **A** and **B**-sublattice [193, 199, 200]. Antiphase boundaries create a strong antiferromagnetic coupling between APDs [12]. This is the reason for the perturbation of the spin structure at the **B**-site lattice and results in the observed magnetoresistance as well as the decrease of magnetization and conductivity.

The decrease of magnetization is based on the antiferromagnetic coupling and the resulting alignment of **B**-site moments. It is described by a linear ferromagnetic chain model with an antiferromagnetic coupling at several places, describing the APBs (see Figure 2.8). In this model, the relative decrease of magnetization at a specific applied magnetic field depends only on the density of APBs [12, 189, 201].

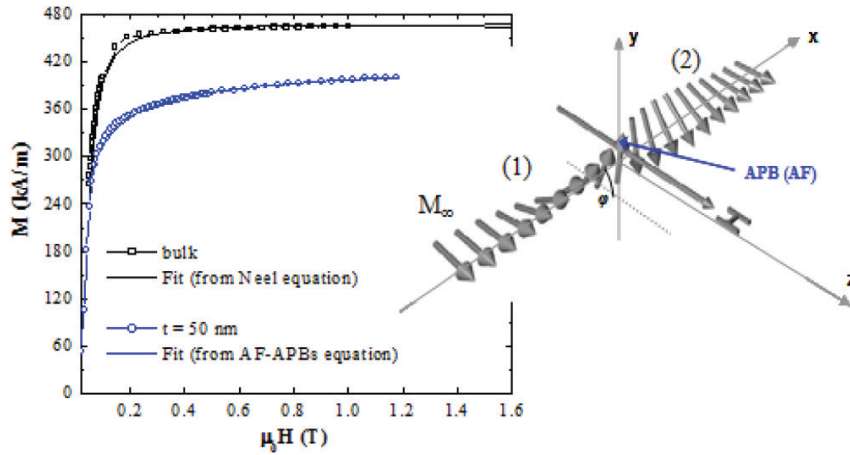


Figure 2.8: In plane virgin magnetization curves at $T=300 \text{ K}$ for a Fe_3O_4 single crystal and a 50 nm thick film. The blue line is the fit to the APB-based theory. The schematic on the right shows the linear chain model used to describe the influence of antiferromagnetic APBs on the properties of Fe_3O_4 thin films. The two ferromagnetic linear chains (1) and (2) are coupled antiferromagnetically at the APB. Figures taken from [12].

Magnetoresistance in Fe_3O_4 thin films is described by a rather similar model. A spin dependent transport model across an APB, based on two ferromagnetically coupled linear chains that are connected antiferromagnetically at the APB (see Figure 2.8), is used to describe the observed magnetoresistance [12, 202, 203]. According to this model, the magnetoresistive ratio depends on the ferromagnetic coupling strength inside the two chains, the antiferromagnetic coupling strength at the APB and the density of APBs.

Also the increase of room temperature resistivity with decreasing film thickness can be explained by the density of APBs. The antiferromagnetic coupling at a APB prevents the spin polarized charge transport. The spin polarized charge transport needs the ferromagnetic alignment between **B**-site magnetic moments. The antiferromagnetic coupling reduces the hopping amplitude, that is proportional to $\cos(\theta/2)$, with θ the angle between the spin of two neighboring **B**-site cations (Equation (2.13)). Therefore, APBs act as scattering centers and hinder the propagation of electrons in the Fe_3O_4 thin film. This leads to the observed decrease of conductivity in these films due to the density of APBs. Eerenstein *et al.* modeled the room temperature resistivity of Fe_3O_4 thin films by an effective media approximation [197], showing the impact of the density of APBs.

Concerning this picture of an APB, the observed negative magnetoresistance can be described vividly by an alignment of the antiferromagnetically coupled spins at an APB in direction of the applied magnetic field. The higher the applied field gets, the smaller the angle θ between these spins gets. This increases the hopping amplitude over an APB and lowers the resistivity of the

system.

A second approach to describe the magnetoresistance in Fe_3O_4 is based on the presence of magnetic disorder (spin canting) [15, 196]. The spins at the **B**-sublattice are not aligned perfectly in parallel. This reduces the hopping amplitude between iron cations, leading to an increased resistivity. Alignment of the spins due to an applied magnetic field increases the hopping amplitude and decreases the resistivity (see also page 78).

The size of antiphase domains between APBs increases with increased thickness d and is proportional to \sqrt{d} (see Figure 2.6) [12, 14, 197]. Therefore, the density of APBs decreases with increasing film thickness. This leads to the observed dependence of resistivity, magnetoresistance and magnetic properties on film thickness.

Conduction mechanisms in Fe_3O_4 at $T > 120$ K

Fe_3O_4 shows semiconducting behavior up to 320 K [12, 134, 195], which is in contrast to the predicted metallic state at the Fermi level in the spin down band. Only at temperatures above 320 K, Fe_3O_4 shows metallic behavior [134, 204]. This characteristic is due to the strong electron-phonon interaction in Fe_3O_4 . It leads to the formation of polarons, affecting the conduction mechanisms in magnetite [134]. In the temperature range between 120 and 320 K, there are three models describing conduction in Fe_3O_4 :

1. Charge transport by large polarons, described by Todo *et al.* [204].
2. Phonon assisted electron hopping in a small polaron band, suggested by Mott and experimentally supported by Boekema *et al.* [205].
3. Superposition of a small polaron band and hopping transport. This theory is known as Ihle-Lorenz model [206–208].

The variety of different theories on the conduction mechanism in Fe_3O_4 shows the complexity of this topic [134, 208, 209].

The semiconducting behavior of charge transport in Fe_3O_4 can also be described by the thermal activation of the electron hopping between the cations on the **B**-site lattice [12, 152]. Conductivity and resistivity in dependence of temperature are then modeled by

$$\sigma(T) = \sigma_0 \exp\left(-\frac{E_A}{k_B T}\right) \quad \text{and} \quad \rho(T) = \rho_0 \exp\left(\frac{E_A}{k_B T}\right), \quad (2.14)$$

respectively. σ_0 and $\rho_0 = 1/\sigma_0$ are the respective values of conductivity and resistivity at $T \rightarrow \infty$ ($1/T \rightarrow 0$) and E_A is the activation energy. According to literature, the activation energies in Fe_3O_4 -samples (thin films and bulk) vary between 50 and 90 meV [12, 195, 210].

The influence of non-stoichiometry: $\text{Fe}_{3(1-\delta)}\text{O}_4$

A decrease of magnetization and conductivity is reported in non-stoichiometric or iron deficient Fe_3O_4 samples [15]. This is related to iron vacancies. The presence of iron vacancies in Fe_3O_4 reduces the amount of Fe^{2+} due to charge neutrality. This reduces the amount of itinerant charge carriers. The resulting deviation from the 1:1 balance between Fe^{2+} and Fe^{3+} on the **B**-site sublattice towards Fe^{3+} weakens the ferromagnetic double-exchange interaction between Fe^{2+} and Fe^{3+} on **B**-sites. The competition between the antiferromagnetic superexchange and the weakening ferromagnetic double exchange tend to align the magnetic moments of **B**-site irons no longer strictly in parallel. The result is a spin canting angle (Yafet-Kittel angle) between the neighboring magnetic moments. This angle between the spins of **B**-site cations reduces the overall observed magnetization of the system. It further reduces the hopping amplitude of electrons between Fe^{2+} and Fe^{3+} -cations due to the angular dependence of the hopping probability in double exchange (Equation (2.13)).

This picture also explains the large negative magnetoresistance in Fe_3O_4 thin films without (or only a small amount) of antiphase boundaries [15] (see also page 77).

2.2.2 Fe_3O_4 at temperatures below 120 K: the Verwey transition

Fe_3O_4 undergoes a phase transition at $T_V \approx 123\text{ K}$, significantly changing its physical properties [12–14]. This phase transition, first described by Verwey in 1939 [211, 212], is known as Verwey-transition and occurs at the Verwey temperature T_V . Main modifications in the physical properties of Fe_3O_4 at T_V is a change of the crystallographic structure from the cubic room temperature phase to a monoclinic phase, associated with a loss of symmetry [213]. Also an anomaly in the specific heat is observed [214, 215]. Furthermore, a decrease of magnetization by a few per cent [190, 216] and a strong increase in resistivity [12, 216, 217] can be observed by cooling Fe_3O_4 below T_V .

The Verwey transition is strongly sensitive to stoichiometry [212, 215] and crystal quality (structural defects like APBs and residual stress) of thin films [12, 195, 216]. Therefore, the presence of a Verwey transition in a thin film of Fe_3O_4 is a evidence of the high structural and chemical quality of this layer [12].

Verwey described the transition as the change from a disordered to a charge ordered state of Fe^{2+} and Fe^{3+} cations at the **B**-site sublattice at T_V [152, 212]. In the high temperature phase above T_V , Fe^{2+} and Fe^{3+} are dynamically disordered in the lattice. The dynamical transformation of Fe^{2+} into Fe^{3+} allows the minority spin electrons to jump between the iron cations and move through the crystal. This mechanism is responsible for the high conductivity in Fe_3O_4 above T_V . Below T_V , Verwey proposed a long range spatial order of Fe^{2+} and Fe^{3+} cations. This periodic order localizes the electrons and decreases

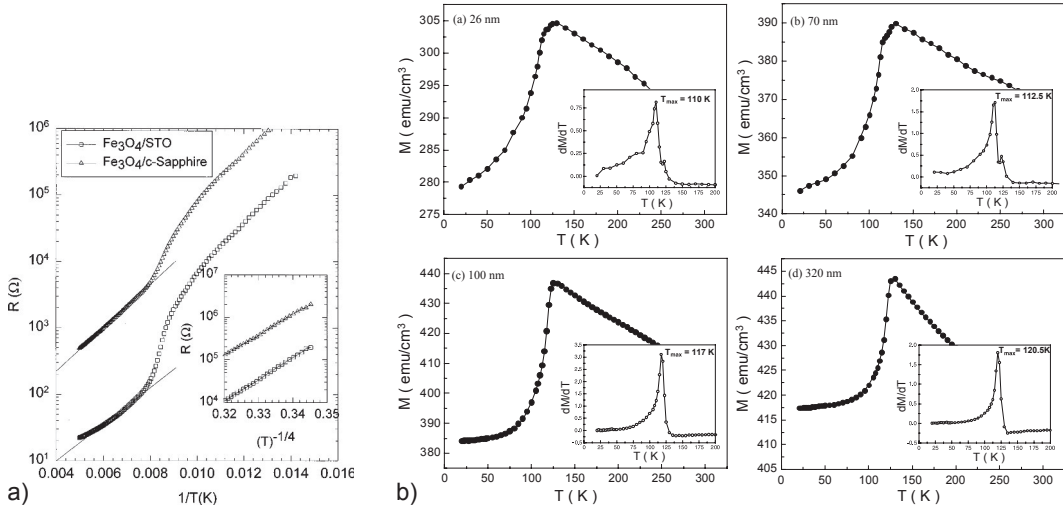


Figure 2.9: a) Temperature dependence of resistance of Fe_3O_4 thin films on different substrates (SrTiO_3 and c-sapphire). The high temperature part ($T_V < T < 320 \text{ K}$) is fitted to Equation (2.14) ($\ln(\rho) \propto 1/T$). The low temperature part ($T < T_V$) is fitted to Equation (2.15) ($\ln(\rho) \propto (1/T)^{1/4}$). From [210]. Copyright 1998 by the American Physical Society. b) Magnetisation in dependence of temperature for Fe_3O_4 thin films on MgAl_2O_4 with different thickness of a) 26 nm b) 70 nm c) 100 nm and d) 320 nm. Insets show the determination of the Verwey temperature. T_V increases with increasing film thickness (increasing crystal quality of thin films), approaching the ideal value of 123 K. Reprinted from [190], with permission from Elsevier.

the motion of charge carriers, leading to an increase of resistivity [12].

Temperature dependence of conductivity and resistivity in Fe_3O_4 below T_V can be modeled as

$$\sigma(T) = \sigma_0 \exp \left[- \left(\frac{E_A}{k_B T} \right)^{1/4} \right] \quad \text{and} \quad \rho(T) = \rho_0 \exp \left(\frac{E_A}{k_B T} \right)^{1/4} \quad (2.15)$$

[12, 186, 208, 210, 218]. The temperature dependency of conductivity proportional to $T^{-1/4}$ corresponds to the variable range hopping mechanism described by Mott [12, 208, 219, 220].

The existence of a charge ordered state below T_V as proposed by Verwey is not clear. Experiments show contradictory results. High-resolution neutron and synchrotron X-ray powder-diffraction confirms the existence of a charge ordered state [221]. In contrast, NMR [222] and X-ray resonant scattering experiments [223] show no evidence of a charge ordered state below the Verwey temperature.

As indicated by the large amount of theories and experimental results, the origin and mechanism of the Verwey transition and the conduction mechanism in Fe_3O_4 is still topic of a lively debate. Walz [208], as far as García and

Subías [209], give a good overview on the discussions on different theoretical descriptions of conductivity and the Verwey-transition in Fe_3O_4 .

2.2.3 Fe_3O_4 in spintronics

Table 2.3: TMR-values with assigned temperature (TMR (@ T)) and room temperature TMR-values of Fe_3O_4 based magnetic tunnel junctions

orientation	2 nd electrode	barrier	TMR (@ T)	TMR	
poly	Co	Al_2O_3	43% (4.2 K)	13%	[224]
(110)	CoFe	AlO_x	16% (120 K)	13%	[225]
(110)	CoFe	AlO_x		14%	[226]
poly	NiFe	AlO_x		7%	[227]
(111)	Co	$\gamma\text{-Al}_2\text{O}_3$	3% (150 K)	3%	[228]
(100)	Ni	AlO_x	5% (220 K)	3%	[229]
(100)	Co	AlO_x	16% (350 K)		[46]
poly	CoFe	AlO_x		11%	[230]
poly	NiFe	AlO_x		-0.3 to +15%	[231]
(110)	Fe	Al_2O_3		-12%	[232]
(111)	CoFe	MgO/AlO_x		-26 to +18%	[233]
(111)	CoFe	MgO		-8 to -2%	[233]
(111)	CoFe	MgO		-14 to +2%	[234]
(100)	Fe_3O_4	MgO	$\approx 1.5\%$ (150 K)	$\approx 0.5\%$	[235]
(100)	Fe_3O_4	MgO	$\approx 0.5\%$ (190 K)		[236]
(100)	Ni	MgO	$< 0.5\%$ (220 K)		[229]
(100)	Co	MgO	-22% (80 K)	-8.5%	[237]
			+5% (80 K)	0%	
(100)	CoFeB	MgO		-12 to +2%	[238]
(110)	LSMO	CoCr_2O_4	-25% (60 K)		[239]
(110)	LSMO	FeGa_2O_4	-11% (60 K)		[240]
(110)	LSMO	MgTi_2O_4	-26% (70 K)		[240]

Due to its physical properties (semiconducting, ferrimagnetic, high spin polarization, high Curie temperature), Fe_3O_4 is a promising material for spintronic applications. Many groups build (pseudo) spin valves or magnetic tunnel junctions (MTJs) based on Fe_3O_4 in order to show the capability of the material. Table 2.3 gives an overview on the achieved tunnel magnetoresistance (TMR) values in Fe_3O_4 -based MTJs. The following section will discuss the results of selected publications on Fe_3O_4 -based MTJs and point out the mechanisms that are responsible for the electrical properties of this junctions as suggested in these works.

Best room temperature TMR values are achieved in combination with amor-

phous AlO_x barriers. But these values are far below the values expected due to the half metallic nature of Fe_3O_4 . Assuming a spin polarization of +42% at the Co / AlO_x interface (see Section 1.1.6) and a TMR of 16% [46], one gets a spin polarization of +17% at the $\text{Fe}_3\text{O}_4 / \text{AlO}_x$ interface by applying Jullieres formula. This positive value is contradictory to the expected value of $P = -100\%$ and the measured spin polarization of -40% at the Al_2O_3 surface of an $\text{Fe}_3\text{O}_4 / \text{Al}_2\text{O}_3$ double layer by SP-PES by Bataille *et al.* [228, 241].

This discrepancy can be explained by the nature of the tunneling electrons [242]. The positive spin polarization of Ni and Co, derived by STS measurements with AlO_x -barriers, is in contrast to theoretical band structure calculations. These calculations predict a negative spin polarization at the Fermi level due to the contribution of d-states (Section 1.1.6) [242]. The positive sign of P in STS measurements is assigned to the high contribution of s-electrons to the tunnel current due to the high mobility of s-electrons compared to d-electrons [12]. There is no symmetry filtering in amorphous barriers. The assumption of a positive spin polarization at the Co / AlO_x -interface leads to a positive spin polarization of Fe_3O_4 in AlO_x -based tunnel junctions. This is in contrast to the expected negative values in theory and SP-PES measurements on $\text{Fe}_3\text{O}_4 / \text{Al}_2\text{O}_3$ double layers [228, 241].

According to theoretical band structure calculations, mainly d-states are responsible for the negative spin polarization in Ni and Co [14, 242]. The assumption of a dominant contribution of d-electrons to the tunnel current, and therefore a negative spin polarization at the Co / AlO_x -interface, results in a negative spin polarization at the Fe_3O_4 interface, as expected [14]. This assumption states, that not only the barrier, but also the electrode materials can act as symmetry filter. The conduction in Fe_3O_4 is due to t_{2g} d-states. This suppresses the tunnel probability of s-type electrons and favors d-type ones, leading to the observed positive TMR in $\text{Fe}_3\text{O}_4 / \text{AlO}_x / \text{Co}$ -MTJs due to the negative spin polarization at both interfaces. The result of Nagahama *et al.* [232] confirms this assumption. Fe_3O_4 -based tunnel junctions with an Fe counter-electrode and an Al_2O_3 barrier show a negative TMR of -12% at room temperature. This is in agreement with the positive total spin polarization (s and p electrons) in Fe (see Section 1.1.6) and the negative one of Fe_3O_4 . All these results are also in agreement with the SP-PES measurements on the Al_2O_3 surface of an $\text{Fe}_3\text{O}_4 / \text{Al}_2\text{O}_3$ double layer, resulting in a spin polarization of -40% [228, 241]. SP-PES sums up over all electrons, regardless of mobility, and therefore reproduces the theoretical DOS-calculations, in contrast to STS [242].

Park [231] achieves TMR-values between -0.3 and +15% in $\text{Fe}_3\text{O}_4 / \text{AlO}_x / \text{NiFe}$ -structures and proposes a different mechanism responsible for the different TMR-values. He assigned the different TMR-values to different iron oxide stoichiometries ($\text{Fe}_3\text{O}_{4-\delta}$) at the Fe_3O_4 -interface. Iron surplus at the interface leads to positive TMR-values, whereas a perfectly stoichiometric Fe_3O_4 -interface shows negative TMR. Park [231] also states the presence of a surface

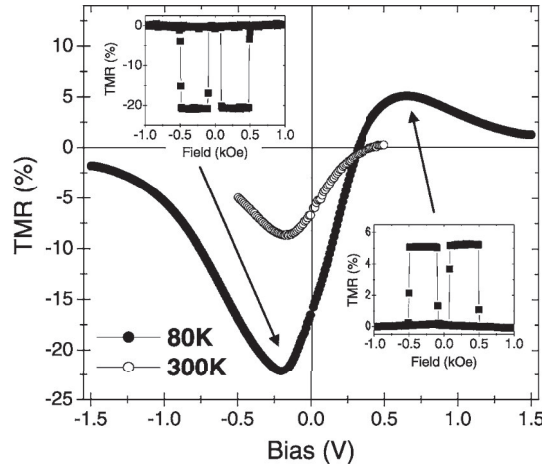


Figure 2.10: TMR(V) of a $\text{Fe}_3\text{O}_4/\text{MgO}/\text{Co}$ -MTJ at two different temperatures. The shape of the TMR(V)-curve represents the density of states, and therefore the spin polarization, of the $\text{Fe}_3\text{O}_4/\text{MgO}$ -interface (see Figure 2.5). Reprinted with permission from [237]. Copyright 2008 AIP Publishing LLC.

reaction while depositing Al on Fe_3O_4 . Al gets oxidized at the interface, extracting the oxygen from the Fe_3O_4 [243]. This may lead to the observed positive TMR-values in $\text{Fe}_3\text{O}_4/\text{AlO}_x$ -tunnel junctions. Also the negative TMR in LSMO ($P_{\text{LSMO}} > 0$ [119–121]) based tunnel junctions with a crystalline barrier (FeGa_2O_4 , MgTi_2O_4 [240] and CoCr_2O_4 [239]) confirms the negative spin polarization at the Fe_3O_4 -interface.

In MTJs with a sputtered, epitaxial MgO-barrier and a Co counter electrode, the TMR reported by Greullet *et al.* [237] is negative and shows a huge dependence on the applied voltage (see Figure 2.10) [237]. This can be explained by assuming a positive spin polarization at the Co interface, resulting in a main contribution of s-electrons and a constant DOS around the Fermi level (see Figure 1.20 B). The high contribution of s-electrons might be due to the high transmission of Δ_1 -states (spd-like) through the MgO-Barrier (symmetry filtering). The assumption of a positive spin polarization at the Co-interface gives the expected negative value at the Fe_3O_4 -interface. The voltage dependency of TMR (Figure 2.10) and the change in its sign can be explained by an overlay of the constant density of s-states at the Co-interface and the density of states in Fe_3O_4 (Figure 2.5). Spin polarization in Fe_3O_4 is negative at E_F and above. The applied negative voltage shifts the Fermi level E_F to higher energies with a higher DOS of spin down electrons. By applying a positive voltage, E_F shifts down and the spin polarization decreases and even shifts to positive values at a voltage of approximately 0.3 V due to the onset of the majority spin band. This situation is similar to the example in Figure 1.20 C,b).

Kado *et al.* [233, 234] prepared Fe_3O_4 -based MTJs with MgO and MgO/AlO_x barriers. They report room temperature TMR-values ranging from -26 to

+18% and -14 to +10% in junctions with MgO and MgO/ AlO_x barriers, respectively. The TMR-values depend strongly on the resistance-area product (RA) of nominally similar junctions. Kado *et al.* state, that the negative TMR is intrinsic in this junctions, and the positive values are a result of imperfections inside the barrier. The decrease of the RA -value is linked to barrier imperfections due to defect induced conductivity through the barrier. The dependency of TMR on barrier quality is confirmed by all negative TMR-values (-8 to -2% at RT) in MTJs containing improved MgO barriers [233]. The use of MgO / AlO_x -double barriers excludes the impact of the MgO / CoFe-interface on the transport properties. The voltage dependency shows a strong decrease of TMR with applied voltage without a sign change [234], in contrast to the result of Greullet *et al.* [237].

Actually, most MTJs based on Fe_3O_4 and MgO show positive TMR values of approximately 0.5%, most of them at temperatures of about 200 K. This behavior is assigned to a magnetically "dead" layer (thickness approximately 1 nm) at the interface between Fe_3O_4 and MgO [236, 244]. The mechanism of spin canting at the Fe_3O_4 -surface seems to be responsible for this effect [236, 244].

Marnitz *et al.* [238] suggested a diffusion of Mg from the barrier into the Fe_3O_4 . This assumption is based on annealing experiments. The TMR develops from a value of -12% in as prepared samples with pre-treated Fe_3O_4 -surface to a value of +2% in annealed samples. The TMR-values increase with increasing annealing temperature, suggesting a Mg diffusion at the Fe_3O_4 / MgO-interface which alters the electrical properties of the interface.

The incorporation of Mg into the Fe_3O_4 is also very likely to happen in samples with MgO-barriers grown by pulsed laser deposition (PLD). This is due to the large kinetic energy of the particles during the deposition of MgO.

Another point, that has to be considered in Fe_3O_4 -based tunnel junctions, is the impact of antiphase boundaries. Due to its spin structure, caused by the antiferromagnetic coupling (Figure 2.8), the presence of APBs prevents a clear antiferromagnetic alignment between the magnetization of the Fe_3O_4 -layer and the magnetization of the second electrode. This significantly reduces the observed TMR [12].

All these examples show, that the TMR and the spin polarization in Fe_3O_4 -based tunnel junctions strongly depend on the selection of materials, be it counter electrode or barrier, and the preparation methods used to build the junctions. Thus, the preparation methods used to build Fe_3O_4 -based MTJs have to be improved, as well as the understanding of the physical mechanisms causing the different properties of all these tunnel junctions. Therefore, the reproducible fabrication of Fe_3O_4 -based MTJs with high TMR-ratios is not an easy task.

2.3 Zinc ferrite ZnFe_2O_4

Bulk ZnFe_2O_4 crystallizes in the normal spinel structure with a lattice constant of $a = 0.84411 \text{ nm}$ [245]. It is known as an insulating oxide [137], that is paramagnetic at room temperature and antiferromagnetic below its Néel temperature of 10 K [136, 138, 141]. This behavior is due to its normal spinel structure. The Zn^{2+} -cations occupy tetrahedral **A**-sites and the Fe^{3+} -cations the octahedral **B**-sites. Fe^{2+} , usually responsible for electron conduction in ferrites, is absent in this structure, resulting in an insulating state [137]. The magnetic properties are linked to the weak antiferromagnetic superexchange between the Fe^{3+} -cations on **B**-sites (see Page 69).

2.3.1 Nanocrystalline ZnFe_2O_4

In contrast, nanocrystalline ZnFe_2O_4 is found to be ferrimagnetic at room temperature [143, 144]. Also superparamagnetism is reported in nanocrystalline samples [144, 246]. These properties make nanocrystalline ZnFe_2O_4 and other nanocrystalline ferrites technologically important materials, due to their high permeability, low core loss and soft magnetic nature [144, 247]. They find applications in biology and medicine as ferrofluids, hyperthermia for cancer treatment [248], for quantitative immunoassay and drug delivery. Also electrical components, memory devices, magnetostrictive devices, as well as electronic devices like transformers, choke coils, noise filters, multi layer chip inductors, and recording heads are possible applications of nanocrystalline ferrites (see [144, 247] and references within). Further applications are gas sensors [249] and humidity sensors [250]. Due to its wide range of possible applications, nanocrystalline ferrite powders, including zinc ferrite, have been intensively studied during the last decades [251, 252] and many different synthesis methods have been developed ([151] and references within). Nanocrystalline thin films, prepared by sputtering and pulsed laser deposition, show similar properties to powder samples [143, 246].

The reason behind the change in properties from bulk to nanocrystalline ZnFe_2O_4 is assigned to the non-equilibrium cationic order in the spinel structure of small crystallites. A partial inversion of the normal spinel structure takes place in nanosized ZnFe_2O_4 -particles [151, 245, 246, 253]. Zn^{2+} and Fe^{3+} are distributed over both sublattices **A** and **B**, resulting in a mixed spinel structure [151, 245] (see Section 2.1). The partially inverted cation distribution is described by the inversion parameter δ as

$$(\text{Zn}_{1-\delta}^{2+}\text{Fe}_{\delta}^{3+})_{\mathbf{A}}[\text{Zn}_{\delta}^{2+}\text{Fe}_{2-\delta}^{3+}]_{\mathbf{B}}\text{O}_4. \quad (2.16)$$

Due to the inversion, nanocrystalline ZnFe_2O_4 shows similar magnetic properties to Fe_3O_4 . The strong antiferromagnetic superexchange between Fe^{3+} on **A** and **B**-sites aligns the magnetic moments of the two sublattices antiparallel

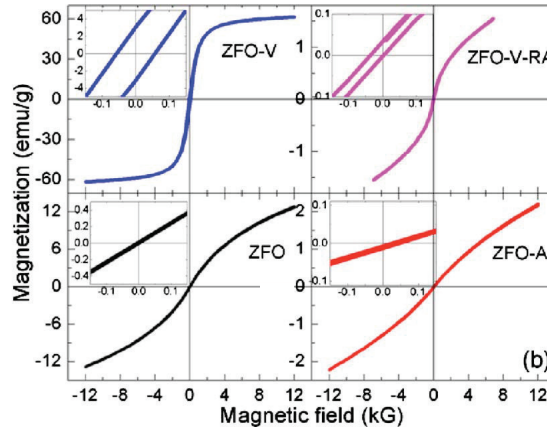


Figure 2.11: Room temperature magnetization measurements of nanocrystalline ZnFe_2O_4 . ZFO: as grown sample, ZFO-A: sample annealed in air, ZFO-V: annealed in vacuum and ZFO-V-RA: sample ZFO-V reannealed in air. As grown and air-annealed samples show bulk properties with paramagnetic behavior. Mössbauer measurements show normal spinel structure without inversion in these samples. The Vacuum annealed sample shows ferrimagnetic behavior, and consequently a non zero inversion. Reannealing in air reduces the ferrimagnetic properties and shifts it back to paramagnetic. Reprinted with permission from [253]. Copyright 2010, AIP Publishing LL.

to each other. This ferrimagnetic configuration results in a large magnetic moment due to the small amount of Fe^{3+} on **A**-sites, compensating the moments of the **B**-site Fe^{3+} -cations [151, 246] (see Figure 2.4). The combination of magnetic hysteresis measurements (large saturation magnetisation, small, but non zero remanence magnetization and coercive field) as well as Mössbauer spectroscopy, X-ray diffraction (XRD) and X-ray absorption near edge spectroscopy (XANES) (evidence of inversion) confirms this picture [151, 253]. Since both, Fe^{3+} and Zn^{2+} , are spheric cations with an OSPE of zero, the formation of a non-equilibrium, partially inverse cation distribution in ZnFe_2O_4 needs only a small increase in lattice energy. Therefore, the degree of inversion depends strongly on the synthesis method used to obtain the material [138, 151]. This behavior is confirmed by Mössbauer spectroscopy measurements on samples obtained by ball milling and sol-gel methods. The inversion parameter differs significantly between the samples grown by different methods [254].

The influence of sample preparation on inversion in ZnFe_2O_4 nanocrystals is further pointed out by annealing experiments performed by Ayyappan *et al.* [253]. Samples annealed in vacuum show ferrimagnetic behavior, whereas samples annealed in air are paramagnetic (see Figure 2.11 a). This magnetic properties can be switched between one another by the different annealing procedures. This behavior is assigned to the influence of oxygen vacancies, formed during annealing in vacuum, on the cationic order. Oxygen vacancies

seem to support the occupation of **A**-sites by Fe^{3+} , and thus the formation of an inverse spinel structure [253].

Gomes *et al.* [245] investigated the cationic structure in ZnFe_2O_4 nanoparticles by X-ray absorption near edge spectroscopy (XANES) and X-ray diffraction (XRD). The investigated particles show a large magnetic and magneto-optical response. The XANES results on this samples show a clear inversion. Zn^{2+} is found on **B**-sites and Fe^{3+} on **A**-sites. The amount of Fe^{3+} on **A**-sites varies between the amount in Fe_3O_4 ($\delta = 1$) and bulk ZnFe_2O_4 ($\delta = 0$). Also XRD measurements, analyzed by the Rietfeld method, confirm this result. Measurements on an antiferromagnetic reference bulk sample reveal no inversion at all, showing the dependency of magnetic properties and cationic inversion on sample preparation [245].

Also nanocrystalline ZnFe_2O_4 thin films, sputtered at room temperature, show a ferrimagnetic behavior. Nakashima *et al.* [246, 255, 256] assign this to the inversion of the spinel cationic order due to the growth method. The growth of ZnFe_2O_4 thin films by sputtering at room temperature involves a very rapid cooling of the energetic plasma particles at the sample surface. This leads to a non-equilibrium, partially inverse spinel structure [246, 255–257]. Annealing in air changes the cationic order to normal spinel with antiferromagnetic or paramagnetic properties, like in bulk samples [255, 256]. The cationic order in this samples was determined by XANES measurements, interpreted in terms of first principle calculations. As prepared samples show a high amount of Zn^{2+} on **B**-sites and Fe^{3+} on **A**-sites, indicating a large degree of inversion. Samples annealed in air show normal spinel structure, confirming the influence of sample preparation on oxygen vacancies and the cationic disorder in the spinel structure of ZnFe_2O_4 .

In ferrites, the occurrence of Fe^{2+} on **B**-sites is responsible for electrical conduction. In case of ZnFe_2O_4 , the formation of Fe^{2+} is assigned to oxygen vacancies and iron surplus [15, 137, 138]. Fe^{2+} will occupy octahedral **B**-sites because of its high OSPE. The spinel structure can then be described as [141]

$$(\text{Zn}_{1-\delta}^{2+}\text{Fe}_{\delta}^{3+})_{\text{A}}[\text{Zn}_{\delta}^{2+}\text{Fe}_{2-\delta-\epsilon}^{3+}\text{Fe}_{\epsilon}^{2+}]_{\text{B}}\text{O}_4. \quad (2.17)$$

Results of Mössbauer spectroscopy measurements on the occurrence of Fe^{2+} in ZnFe_2O_4 are contradictory. Chinnasamy *et al.* [258] report no evidence of Fe^{2+} in ZnFe_2O_4 nanoparticle powders obtained by high energy ball milling. In contrast, Goya *et al.* [259] report Fe^{2+} in nanoparticle powders also made by mechanosynthesis (ball milling).

Daruka Prasad *et al.* [144] as well as Ponpandian and Narayanasamy [145] report semiconducting behavior in nanocrystalline ZnFe_2O_4 compounds. AC conductivity and impedance measurements are interpreted in terms of small polaron assisted electron hopping. This conduction mechanism is linked to the charge exchange between Fe^{2+} and Fe^{3+} on **B**-sites and therefore a hint for the existence of divalent iron in ZnFe_2O_4 nanoparticles.

Zhang *et al.* [260] report a huge TMR of 150% at room temperature in two phase samples consisting of ZnFe_2O_4 and $\alpha\text{-Fe}_2\text{O}_3$. The zinc ferrite nanoparticles with a mean size of 150 nm are separated by approximately 7 nm of insulating $\alpha\text{-Fe}_2\text{O}_3$. I - V -curves, measured on sintered pellets, show a clear evidence of tunneling. The resistivity of the two phase material decreases with increasing applied magnetic field. This is due to the alignment of magnetization directions of the nanoparticles. Without magnetic field, they are aligned antiparallel, resulting in a high resistance. If a magnetic field is applied, the magnetizations of particles get aligned in parallel, which lowers the resistance. Also You-Wei *et al.* [261] report a huge TMR effect (158% at RT) in $\text{Zn}_{0.41}\text{Fe}_{2.59}\text{O}_4$ polycrystalline samples with grains separated by approximately 6 nm of $\alpha\text{-Fe}_2\text{O}_3$. The occurrence of such high MR-values, assigned to tunneling in two phase films, is a further hint on the nature of the conduction mechanism in ZnFe_2O_4 . The current is highly spin polarized due to the hopping of minority spin electrons between Fe^{2+} and Fe^{3+} , as it is the case in Fe_3O_4 .

To sum up, nanocrystalline ZnFe_2O_4 shows properties different to its bulk form. It is ferrimagnetic and semiconducting. It also shows a non zero spin polarization, as demonstrated by a large TMR in two phase samples. These properties are due to a non-equilibrium cation distribution in the spinel structure of ZnFe_2O_4 and can be achieved by the right choice of preparation methods. Therefore, this material is interesting for application in spintronic components. Today, most devices are based on planar technology and utilize epitaxial thin films of the functional material. Thus, also thin, epitaxial films of ZnFe_2O_4 were investigated during the last few years. Focus of these works is on structure as well as electric and magnetic properties of epitaxial ZnFe_2O_4 thin films. These films also show properties different from bulk, rather similar to these of nanocrystalline ZnFe_2O_4 .

2.3.2 Epitaxial ZnFe_2O_4 thin films

Epitaxial ZnFe_2O_4 thin films, grown on c-sapphire, SrTiO_3 , MgAl_2O_4 and MgO , also show ferrimagnetic and semiconducting behavior, in contrast to bulk samples [137–142]. All the mentioned works report the growth and characterization of phase clean films by pulsed laser deposition or sputtering.

Conductivity of ZnFe_2O_4 thin films

Room temperature conductivity of ZFO thin films strongly depends on substrate temperature T_S during growth and can be tuned from insulating to conducting over several orders of magnitude [139, 141]. ZnFe_2O_4 thin films grown at low substrate temperatures ($T_S < 500^\circ\text{C}$) are semiconducting, whereas films grown at higher temperatures are insulating (Figure 2.12 a). The transition

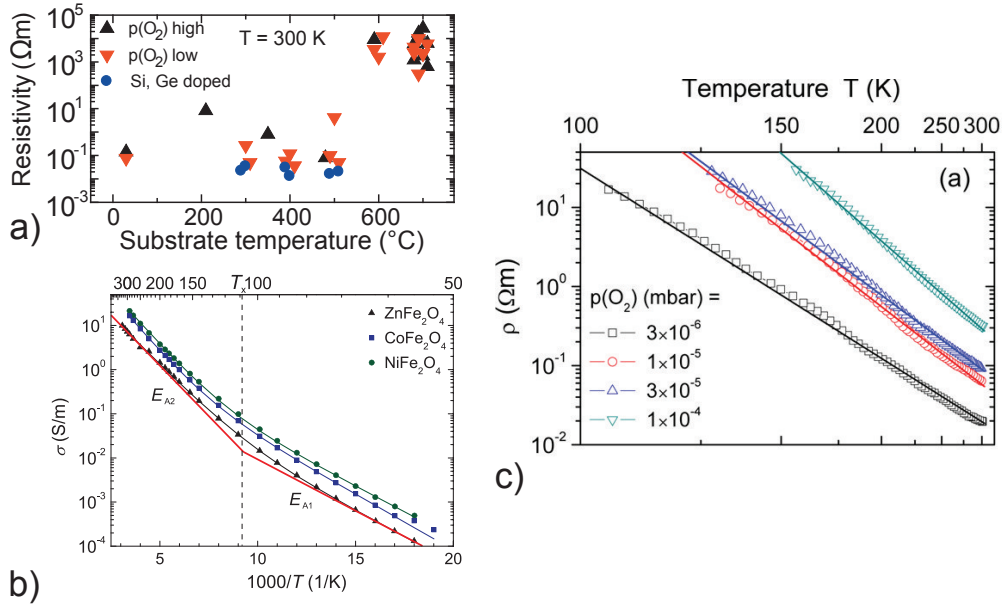


Figure 2.12: a) Dependence of resistivity of ZnFe_2O_4 thin films on the substrate temperature during growth. Figure taken from [139]. b) Conductivity of a ZnFe_2O_4 thin film in dependence of temperature. The fit is to the two energy activation formula (Equation (2.19)). Figure taken from [155]. c) Resistivity of ZnFe_2O_4 thin films in dependence of temperature. The data is fitted to the simple thermal activated nearest neighbor hopping formula (Equation (2.18)) Figure taken from [140]

always occurs, regardless of the oxygen pressure during growth. This behavior might state the importance of disorder for electrical conduction in ZnFe_2O_4 thin films. Samples grown at intermediate temperatures ($400 \leq T_s < 500^{\circ}\text{C}$) also show a dependency of conductivity on oxygen pressure during growth [137, 140]. Samples grown at low oxygen pressures are better conductors than samples grown at high pressures (Figure 2.12 c). This underlines the influence of oxygen vacancies on the transport properties of ZnFe_2O_4 thin films. Conductivity in thin film ZnFe_2O_4 samples is assigned to the formation of Fe^{2+} on **B**-sites and the resulting hopping of electrons between Fe^{2+} and Fe^{3+} on **B**-sites due to double exchange. The formation of Fe^{2+} in ZnFe_2O_4 is due to charge neutrality issues, caused by Fe^{3+} on **A**-sites (disorder in the cationic lattice or iron surplus) and oxygen vacancies. Due to the large OSPE, Fe^{2+} preferably occupies octahedral **B**-sites. X-ray Photoelectron Spectroscopy (XPS) [142] measurements clearly show the presence of Fe^{2+} in conducting samples.

Hall effect measurements in large magnetic fields indicate hopping between Fe^{2+} and Fe^{3+} on B-sites as dominant conduction mechanism [139]. Temperature dependent conductivity data obtained on ZnFe_2O_4 thin films can be fitted by assuming a simple thermal activated nearest neighbor hopping process [137, 140, 142] (Figure 2.12 c). This further underlines electron hopping

as dominant conduction mechanism. Temperature dependence of conductivity is therefore described as

$$\sigma(T) = \sigma_0 \exp\left(-\frac{E_A}{k_B T}\right). \quad (2.18)$$

The activation energy E_A is found to be between 50 and 130 meV and increases with increasing substrate temperature and oxygen pressure during growth [137, 140, 142].

Lorenz *et al.* [139] and Brachwitz *et al.* [141] report a second thermal activated process at low temperatures (Figure 2.12 b). They describe the temperature dependency of conductivity by a model with two contributions, involving different activation energies.

$$\sigma(T) = \sigma_1(T) + \sigma_2(T) = \sigma_{01} \exp\left(-\frac{E_{A1}}{k_B T}\right) + \sigma_{02} \exp\left(-\frac{E_{A2}}{k_B T}\right) \quad (2.19)$$

The activation energies assigned to the high temperature contribution are also in the former reported range of $65 < E_A < 130$ meV. Low temperature activation energies range from 40 to 55 meV. Brachwitz *et al.* [141] compared this behavior to the Verwey transition in Fe_3O_4 , as reported by Ziese and Blythe [195]. The crossing temperature T_x , where $\sigma_1(T) = \sigma_2(T)$, is found to be in the range between 107 and 125 K. This might be an indication of a change in the cationic order in ZnFe_2O_4 , similar to Fe_3O_4 . Lorenz *et al.* [139], and also Brachwitz *et al.* [141], further linked the appearance of two different conductivity contributions to different vacancy configurations, influencing the hopping transport. Brachwitz *et al.* [141] suggest an electron hopping over a single charged oxygen vacancy, $\text{Fe}^{2+}\text{-V}_{\text{O}}^{\bullet}\text{-Fe}^{3+}$. This transport mechanism shows a lower activation energy compared to hopping over an oxygen atom. A second approach to explain the curved $\log(\sigma) - 1/T$ -curves is the assumption of grain boundaries in the structure of ZnFe_2O_4 -thin films. Brachwitz [155] reports a linear curve in the $\log(\sigma) - (1/T)^{1/2}$ -representation, resulting in a best fit to the formula

$$\sigma(T) = \sigma_0 \exp\left[-\left(\frac{E_A}{k_B T}\right)^{\frac{1}{2}}\right], \quad (2.20)$$

describing conduction over grain boundaries in conducting, granular materials [262].

Magnetism in ZnFe_2O_4 thin films

In contrast to bulk ZnFe_2O_4 , thin films show a strong ferrimagnetic response with high saturation magnetization and coercive fields [138–140, 142, 263] (Figure 2.13 a). All these films show Curie temperatures far above 350 K, even

values up to 600 K are reported [140]. The formation of a ferrimagnetic order in normal spinel is assigned to the occupation of **A**-sites by Fe^{3+} -cations. XANES measurements by Rodríguez Torres *et al.* [138] show an occupation of both sites by Fe^{3+} -cations, confirming this theory. Due to the strong, antiferromagnetic superexchange between Fe^{3+} -cations on **A** and **B**-sites, the magnetic moments of these two sublattice align antiparallel. This forces the moments within every single lattice in parallel, overcoming the weak antiferromagnetic interaction inside each lattice.

The magnetic response of thin films is reported to depend on the oxygen pressure during growth. It decreases with increasing oxygen pressure, which is a hint to the influence of oxygen vacancies on the cationic disorder, being the reason for the magnetic properties of ZnFe_2O_4 thin films [138, 142]. Nevertheless, a rough estimation of the fraction of iron cations distributed on **A** (x_{A}) and **B**-sites (x_{B}), and contributing to the measured magnetic moment ($\propto x_{\text{B}} - x_{\text{A}}$), yields no dependence on oxygen partial pressure during growth. Chen *et al.* [140] conclude an intrinsic magnetic disorder in these samples, probably caused by the non-equilibrium growth by pulsed laser deposition.

A fast decrease of coercive field with increasing temperature was observed. This behavior is linked to the existence of magnetic clusters and a blocking mechanism in the ZnFe_2O_4 thin films [138–140].

Temperature dependent magnetization measurements on ZnFe_2O_4 thin films (Figure 2.13 b) show a linear decrease of magnetization with increasing temperature. Linear approximation to higher temperatures results in a Curie temperature of 600 K [140]. The linear dependence of magnetization on temperature might arise from spin glass behavior, or might be assigned to the ferrimagnetic nature of ZnFe_2O_4 thin films [140].

Measurements of ZFC (zero field cooled) and FC (field cooled) curves show a hysteresis in the temperature dependency [140, 142, 263] (Figure 2.13 c). This can be linked to spin glass behavior due to disorder in the magnetic system and competing interactions [140, 142]. Another explanation is the presence of domain walls, leading to a similar behavior [140, 263]. The domain wall scenario is supported by the similarity of the temperature dependence of the coercive field and the ZFC-peak fields [140] (inset in Figure 2.13 c).

Spin glass behavior is a possible scenario in ZnFe_2O_4 thin films due to the disordered cation lattice, causing the magnetic properties of the material. Also competing interaction between the iron cations occupying **A** and **B**-sites give rise to spin glass like properties [255]. The antiferromagnetic interaction between **A** and **B** sublattice strengthens with increasing amount of Fe^{3+} on **A**-sites. Therefore, the blocking or spin freezing temperature increases with increasing disorder in the cation system [142, 255]. Since this temperature should be far above room temperature for spintronic application of spin glass like materials [140], highly disordered ZnFe_2O_4 is a good candidate.

A further hint to a spin glass state in ZnFe_2O_4 thin films is the occurrence of a significant positive slope in the magnetization curve at high applied fields,

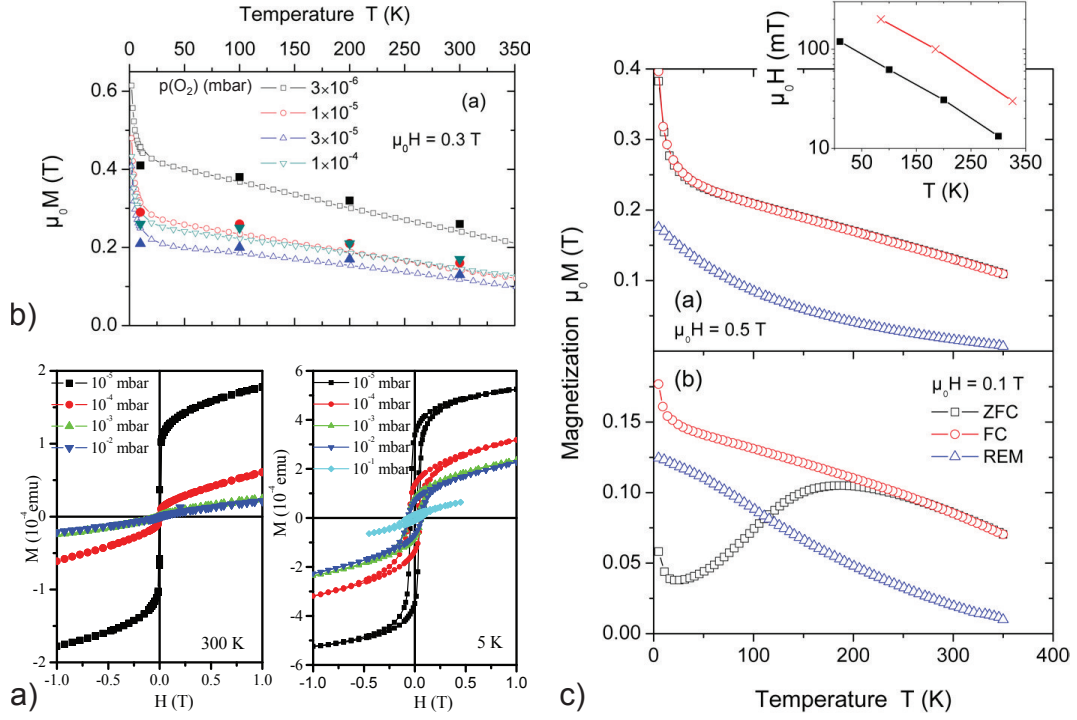


Figure 2.13: Magnetization in ZnFe_2O_4 thin films: a) Magnetic moment as function of the applied magnetic field at 300 K and 5 K. From [138]. Copyright 2011 by the American Physical Society. b) Magnetization in dependence of temperature at an applied magnetic field of 0.3 T. Solid symbols are saturation magnetization values. c) Field cooled (FC), zero field cooled (ZFC) and remanent magnetization (REM) measurements at 0.5 T and 0.1 T. The inset shows the temperature dependence of the coercive field (squares) and the ZFC-peak fields (crosses). Figure b) and c) taken from [140].

that indicates the presence of paramagnetic components [138, 140]. This was confirmed by temperature dependent magnetization measurements, where an upturn in magnetization was observed at low temperatures. Chen *et al.* [140] assigned this behavior to a fraction of Fe^{3+} -cations, which are magnetically uncoupled and couple at low temperatures, giving rise to the observed magnetic moment. Another reason for the positive slope in the magnetization curve might be the presence of antiphase boundaries (APBs), like in Fe_3O_4 thin films (see pages 74 ff.).

Magnetoresistance in ZnFe_2O_4 thin films

A large negative magnetoresistance is observed in ZnFe_2O_4 thin films [142] (Figure 2.14). This magnetoresistance is assigned to the presence of magnetic disorder [15, 142]. Due to the competing interactions inside the spinel lattice of ZnFe_2O_4 (the antiferromagnetic superexchange interactions $\text{Fe}_B^{3+}\text{-O-Fe}_B^{3+}$, $\text{Fe}_A^{3+}\text{-O-Fe}_B^{3+}$ and the ferromagnetic double exchange interaction $\text{Fe}_B^{2+}\text{-O-Fe}_B^{3+}$),

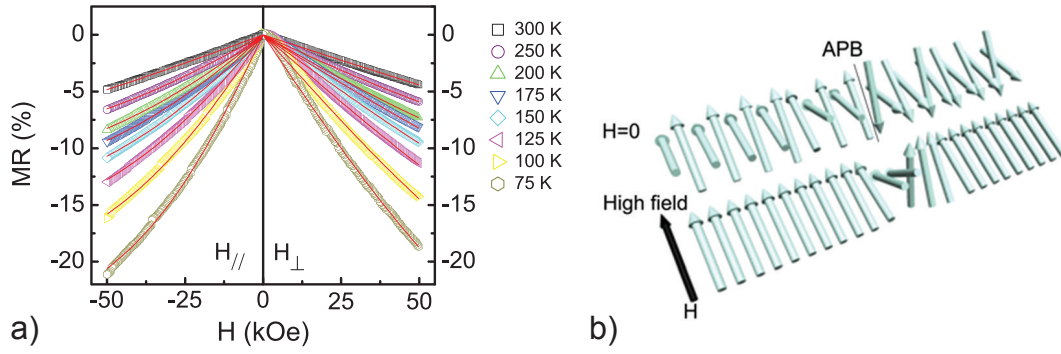


Figure 2.14: a) Magnetoresistance curves of an epitaxial ZnFe_2O_4 thin film. The magnetic field is applied parallel (left) and perpendicular (right) to the film plane. Red lines are fits to the spin canting model b) Spin canting in ZnFe_2O_4 . The angle decreases with increasing applied magnetic field, arranging the spins in parallel. Reprinted with permission from [142]. Copyright 2014, AIP Publishing LLC.

the spins at the **B**-site lattice are not aligned perfectly in parallel, but exhibit a finite canting angle (Yafet-Kittel angle [169]). The hopping amplitude of electrons between Fe^{2+} and Fe^{3+} depends on the angle θ between the spins of the iron cations and is proportional to $\cos(\theta/2)$ (Equation (2.13)). A large canting angle therefore induces a small conductivity in the system. The applied magnetic field aligns the magnetic moments more parallel to each other, reducing the spin canting angle (see Figure 2.14). This results in a higher hopping amplitude and a higher conductivity. Thus, the resistivity of ZnFe_2O_4 decreases with increasing applied magnetic field, giving the observed negative magnetoresistance [15, 142]. Also antiphase boundaries (APBs) can give rise to the observed magnetoresistance. Jin *et al.* [142] state, that the influence of APBs decreases under the influence of spin canting. The antiferromagnetic coupling is not longer 180° and the spins at the APB are aligned much easier along the direction of the magnetic field (see Figure 2.14 b).

Figure 2.14 a shows the magnetoresistance curves of epitaxial thin films. The red lines are a fit to the model based on spin canting and reproduce the curves really well [142]. This mechanism of magnetoresistance further confirms the picture of conduction in Fe_3O_4 and ZnFe_2O_4 due to spin polarized hopping of electrons between **B**-site iron cations.

Theoretical calculations on ZnFe_2O_4

Calculated density of states show, that antiferromagnetic normal spinel ZnFe_2O_4 is insulating [142, 264]. Calculations by Jin *et al.* [142] show, that introducing a certain degree of inversion switches the system to a ferrimagnetic, insulating state with a splitting of the conduction band minima of majority and minority states. The calculated band splitting is about 0.6 eV. This properties make partially inverse ZnFe_2O_4 interesting for the application as barrier in spin fil-

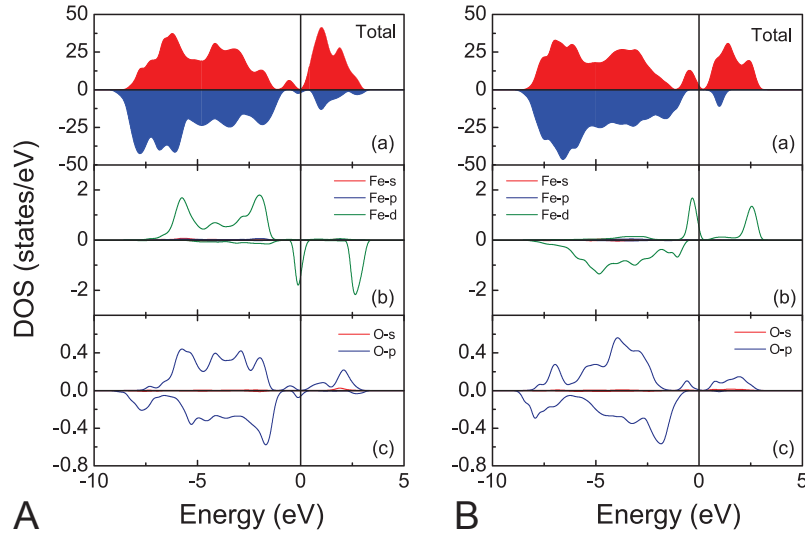


Figure 2.15: Calculated density of states for partial inverse ZnFe_2O_4 ($\delta = 1/8$), assuming a certain amount of oxygen vacancies. The amount of oxygen vacancies in the model system is A: $\sigma = 1/16$ and B: $\sigma = 1/8$. In both figures a) is the total density of states and b) and c) the density of states of Fe and O, respectively. Reprinted with permission from [142]. Copyright 2014, AIP Publishing LLC.

ter tunnel junctions [142]. Jin *et al.* report calculated magnetization values of $6.1 \mu_B/\text{f.u.}$ in case of $\delta = 1/8$ and $4.8 \mu_B/\text{f.u.}$ in case of $\delta = 1/4$, in accordance to the Néel-model. They explain the discrepancy between the lower experimentally observed values (0.75 to $3.2 \mu_B/\text{f.u.}$) and the theoretical values with the reduction of magnetization caused by spin canting [142].

In order to describe conducting, ferrimagnetic ZnFe_2O_4 , oxygen vacancies were inserted into the system. The insertion of oxygen vacancies into the partial inverted model system $((\text{A}_{1-\delta}\text{B}_\delta)_{\text{tet.}}[\text{A}_\delta\text{B}_{2-\delta}]_{\text{oct.}}\text{O}_{4-\sigma}, \delta = 1/8)$ gives rise to the contribution of iron-3d states at the Fermi level (Figure 2.15) and therefore to the conductivity of the system. At $\sigma = 1/16$, the system shows half metallic behavior with negative spin polarization (Figure 2.15 A). In contrast, calculations using a value of $\sigma = 1/8$ yield a half metallic behavior with positive spin polarization (Figure 2.15 B) [142]. The result of this calculations indicates the influence of oxygen vacancies on the conductivity of partially inverse ZnFe_2O_4 . Oxygen vacancies give rise to the conductivity, probably due to the formation of Fe^{2+} in **B**-sites. They also seem to change the sign of the spin polarization in dependency of their amount, which would be of great interest for spintronic applications. The calculated magnetization values of oxygen deficient ZnFe_2O_4 are similar to the values obtained without oxygen vacancies.

Cationic order and inversion in ZnFe_2O_4 thin films

The position of Zn^{2+} in ZnFe_2O_4 is discussed in literature and seems to depend on growth conditions (see page 86). XANES measurements on nanocrystalline ZnFe_2O_4 samples, exhibiting ferrimagnetic properties, show a clear partial inversion. Normal spinel structure is observed in antiferromagnetic or paramagnetic samples.

XANES measurements on stoichiometric ZnFe_2O_4 thin film samples grown at high oxygen partial pressures by PLD [138] show also Zn^{2+} in **A**- and **B**-sites and therefore usual inversion. In contrast, samples grown at low oxygen partial pressures exhibit only Zn^{2+} in **A**-sites. This can be explained by the high tetrahedral site preference of Zn^{2+} [265], probably supported by the high OSPE of Fe^{2+} -cations, occurring in oxygen deficient samples [266]. An amount of Fe^{2+} was detected in **B**-sites, confirming its octahedral preference.

Usual inversion seems not to be the main reason for ferrimagnetism in ZnFe_2O_4 thin films grown in oxygen deficient environments. Zn^{2+} was only found on tetrahedral places and Fe^{3+} in tetrahedral and octahedral sites. This cationic order is maybe not the result of inversion, but of superoccupation of former empty **A**-sites by Fe^{3+} , caused by oxygen vacancies [138] or iron surplus [14, 15]. XANES measurements were done on insulating ZnFe_2O_4 thin films grown at 500°C substrate temperature. Therefore, this measurements do not rule out the possibility of usual inversion in conducting ZnFe_2O_4 samples due to cationic disorder caused by the growth process at low temperatures.

Also optical measurements support this picture of magnetism and conductivity in ZnFe_2O_4 thin films. Spectroscopic ellipsometry measurements by Zviagin *et al.* [267] show clear features correlated to inter valence charge transfer (IVCT) between Fe^{2+} and Fe^{3+} in octahedral coordination, indicating the presence of Fe^{2+} on **B**-sites. Magneto-optical Kerr effect (MOKE) measurements on this samples show features related to Fe^{3+} on both sites, **A** and **B**, explaining the magnetic response of these samples. The strength of the features, linked to ferrimagnetism and conductivity, is related to the degree of disorder in the normal spinel structure of ZnFe_2O_4 thin films [267].

2.4 $\text{Zn}_x\text{Fe}_{3-x}\text{O}_4$ thin films

Zn substitution in Fe_3O_4 thin films gives the opportunity to alter the magnetic and electric properties of the material [15–17]. Also the presence of oxygen during growth plays a major role for the achieved properties of the thin films [15, 16]. The presence of oxygen during growth introduces iron vacancies into the inverse spinel structure of Fe_3O_4 , changing the properties of the films [15] (see page 78).

Electronic transport in $\text{Zn}_x\text{Fe}_{3-x}\text{O}_4$ films, as well as in iron deficient Fe_3O_4 ones, is described by electron hopping between Fe^{2+} and Fe^{3+} on **B**-sites, sim-

ilar to Fe_3O_4 . The temperature dependency of conductivity can be modeled with simple thermally activated hopping ($\sigma \propto \exp(-E/k_{\text{B}}T)$), like in Fe_3O_4 . The activation energies are in the range of 60 to 85 meV, confirming oxygen mediated hopping between divalent cations [15]. They show no major dependence on stoichiometry.

First, the influence of Zn substitution in stoichiometric Fe_3O_4 thin films will be discussed. The room temperature resistivity of samples grown in Ar atmosphere (no iron deficiency) increases with increasing Zn-content [15]. This behavior can be explained by the substitution of Fe^{3+} by Zn^{2+} on **A**-sites [15, 265], which reduces the amount of Fe^{2+} at **B**-sites due to charge neutrality. This has two effects on the conduction of electrons due to hopping between Fe^{2+} and Fe^{3+} on **B**-sites. First, the amount of itinerant charge carriers decreases with decreasing amount of Fe^{2+} . Second, the ferromagnetic double interaction inside the B-site lattice weakens ($\text{Fe}_{\text{B}}^{2+}\text{-O-Fe}_{\text{B}}^{3+}$), whereas the antiferromagnetic superexchange interaction ($\text{Fe}_{\text{B}}^{3+}\text{-O-Fe}_{\text{B}}^{3+}$) strengthens. Also the inter-sublattice interaction (antiferromagnetic superexchange, $\text{Fe}_{\text{A}}^{3+}\text{-O-Fe}_{\text{B}}^{3+}$) weakens with increasing amount of nonmagnetic Zn^{2+} in **A**-sites. Due to the competition between these interactions, the magnetic moments of **B**-site cations are no longer aligned strictly in parallel. They exhibit a non zero canting angle (spin canting or Yaffet-Kittel angle), that increases with increasing zinc content [15]. Based on the dependence of the amplitude of electron hopping by double exchange on the angle between the spins of **B**-site cations, the spin canting angle reduces the hopping probability, and therefore the conductivity of the system.

All samples reported by Venkateshvaran *et al.* [15], show a strong ferrimagnetic response at room temperature (Figure 2.16 a). A decrease of the saturation as well as the remanent magnetization with increasing zinc content is observed in samples grown in pure Ar (no iron deficiency). The finite canting angle between the magnetic moments on **B**-sites explains the observed decrease of saturation magnetization with increasing zinc content. This is in contrast to the descriptive Néel picture of two unequally strong ferromagnetic lattices aligned antiparallel. In this picture, the reduction of the magnetic moment of the **A**-site lattice M_{A} due to the incorporation of non magnetic Zn^{2+} results in an increase of overall magnetization ($M = |M_{\text{B}}| - |M_{\text{A}}|$) [17]. This increase gets compensated by the canting of the **B**-site magnetic moments [15], which reduces M_{B} and therefore explains the observed decrease in magnetization.

Iron deficiency has a similar influence on the magnetic and electric properties of Fe_3O_4 thin films (see page 78). Wang *et al.* [16] linked the changes in properties between stoichiometric Fe_3O_4 and iron-deficient $\text{Fe}_{3(1-\delta)}\text{O}_4$ or Zn substituted $\text{Zn}_x\text{Fe}_{3-x}\text{O}_4$, and therefore the influence of iron vacancies and Zn substitution of **A**-site iron. They stated a compositional correspondence between iron vacancies and Zn substitution in the form of $x \rightleftharpoons 3\delta$. This correspondence is pointed out by a simple calculation. Due to mass and charge

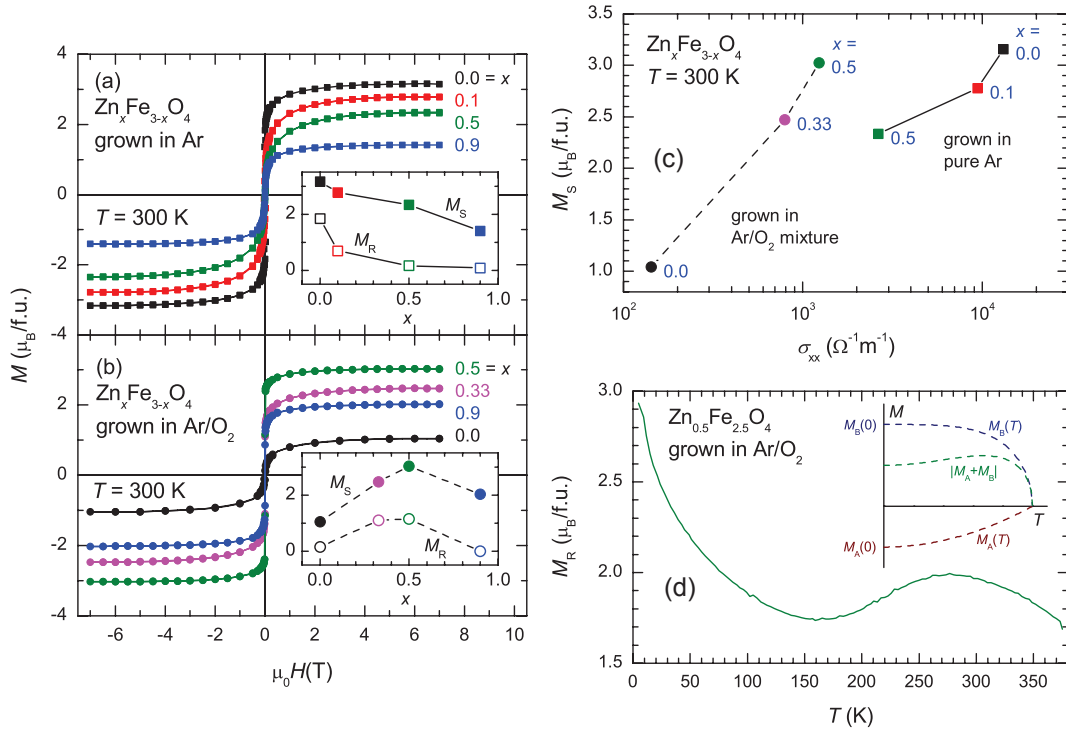


Figure 2.16: Magnetic moment of $\text{Zn}_x\text{Fe}_{3-x}\text{O}_4$ thin films a) grown in pure Ar atmosphere. b) grown in an Ar/ O_2 mixture. The insets show the saturation and remanent magnetisations in dependence of the zinc content c) Correlation between saturation magnetization and conductivity in different $\text{Zn}_x\text{Fe}_{3-x}\text{O}_4$ thin films. d) Temperature dependency of magnetization of a $\text{Zn}_x\text{Fe}_{3-x}\text{O}_4$ sample grown in Ar/ O_2 . The inset shows the impact of two sublattices with different temperature dependency of magnetization caused by the different strength of interaction within these lattices. From [15]. Copyright 2009 by the American Physical Society.

balance, it is

$$\text{Fe}_{3(1-\delta)}\text{O}_4 = \text{Fe}_{2+6\delta}^{3+}\text{Fe}_{1-9\delta}^{2+}\text{O}_4 \quad (2.21)$$

and therefore, there are 3δ less itinerant charge carriers per formula unit. Descriptively, one missing Fe^{3+} is equated by three Fe^{2+} changing to Fe^{3+} , in order to gain back charge neutrality. In $\text{Zn}_x\text{Fe}_{3-x}\text{O}_4$, x Zn^{2+} -cation replacing x Fe^{3+} -cations per formula unit on an **A**-site, also change x Fe^{2+} to Fe^{3+} . Therefore, the effect of both stoichiometric changes on the valence contribution is equal and $x \rightleftharpoons 3\delta$ [16].

Naively, one would think that both mechanisms sum up and zinc substitution in iron deficient $\text{Fe}_{3(1-\delta)}\text{O}_4$ thin film further decreases the magnetic response and the conductivity of the films. In contrast, Venkateshvaran *et al.* [15] report an increase of both, magnetism and conductivity, with increasing zinc content (Figure 2.16 b). The authors link this behavior to a compensating nature of the substituting Zn^{2+} -cations. Zn^{2+} does not only remove one Fe^{2+} by substituting Fe^{3+} on **A**-sites, but also reduces the amount of iron vacancies due

to an expansion of the lattice caused by the larger ionic radius of Zn^{2+} . Iron can be incorporated much easier into the expanded lattice, which reduces the amount of vacancies. The reduction of iron vacancies due to the amount of zinc is confirmed by X-ray diffraction measurements. Therefore, the incorporation of zinc into $\text{Fe}_{3(1-\delta)}\text{O}_4$ increases the amount of Fe^{2+} on **B**-sites and increases the amount of itinerant charge carriers, as well as the ferromagnetic double exchange interaction. This leads to a decrease in the spin canting angle and therefore an increase in the overall magnetic moment as well as the hopping amplitude and the conductivity. A maximum in magnetization is observed in zinc substituted iron deficient Fe_3O_4 samples. This is explained by the amount of iron vacancies. Only a limited amount of Zn is needed to compensate the effect of iron vacancies. More zinc has the same effect as in non iron deficient samples and reduces the magnetic moment (Figure 2.16 b). A similar behavior is reported by Tian *et al.* [268]. In contrast, the authors explain the increase in magnetization at low Zn contents in terms of the Néel-model (weakening of the **A**-site magnetization due to Zn incorporation). The decrease of magnetization at high Zn contents is also explained by spin canting.

Figure 2.16 c shows the correlation between saturation magnetization and conductivity at 300 K. This correlation further underlines the similarity of the main reason for the decrease in magnetization and conductivity, namely the spin canting angle, introduced by a change in the cationic structure.

The influence of the spin canting angle is further pointed out by magnetoresistance measurements. The temperature dependency as well as the dependence on the magnetic field is well reproduced by the model concerning the influence of spin canting on the hopping conduction in $\text{Zn}_x\text{Fe}_{3-x}\text{O}_4$ [15].

The mentioned weakening of the interaction inside the **A**-site sublattice due to substitution of iron by zinc can be observed in the temperature dependency of the magnetization of some samples [15] (Figure 2.16 d). The magnetization first decreases with increasing temperature. After a minimum at 150 K, the magnetization increases to a maximum at 275 K and decreases again. Venkateshvaran *et al.* [15] assigned this behavior to the ferrimagnetic nature of magnetism in $\text{Zn}_x\text{Fe}_{3-x}\text{O}_4$. The occurrence of the maximum is due to two different temperature dependencies of the magnetization of the two sublattices **A** and **B**. In result of the partial substitution of iron by zinc, the effective molecular field of the **A**-sites is small compared to that of the **B**-sites, resulting in a stronger temperature dependence in $M_{\mathbf{A}}(T)$ [15]. The result of the different temperature dependencies on the magnetization ($M(T) = M_{\mathbf{A}}(T) + M_{\mathbf{B}}(T)$) is shown schematically in the inset of Figure 2.16 d. Venkateshvaran *et al.* state that the occurrence of the observed maximum is a direct experimental evidence for **A**-site substitution of Zn^{2+} in the inverse spinel structure.

Theoretical calculations on the $\text{Zn}_x\text{Fe}_{3-x}\text{O}_4$ -system by Cheng *et al.* [269] show a decrease in conductivity with increasing zinc content. The saturation magnetization increases linearly up to $x = 0.75$. Above, it decreases fast to zero

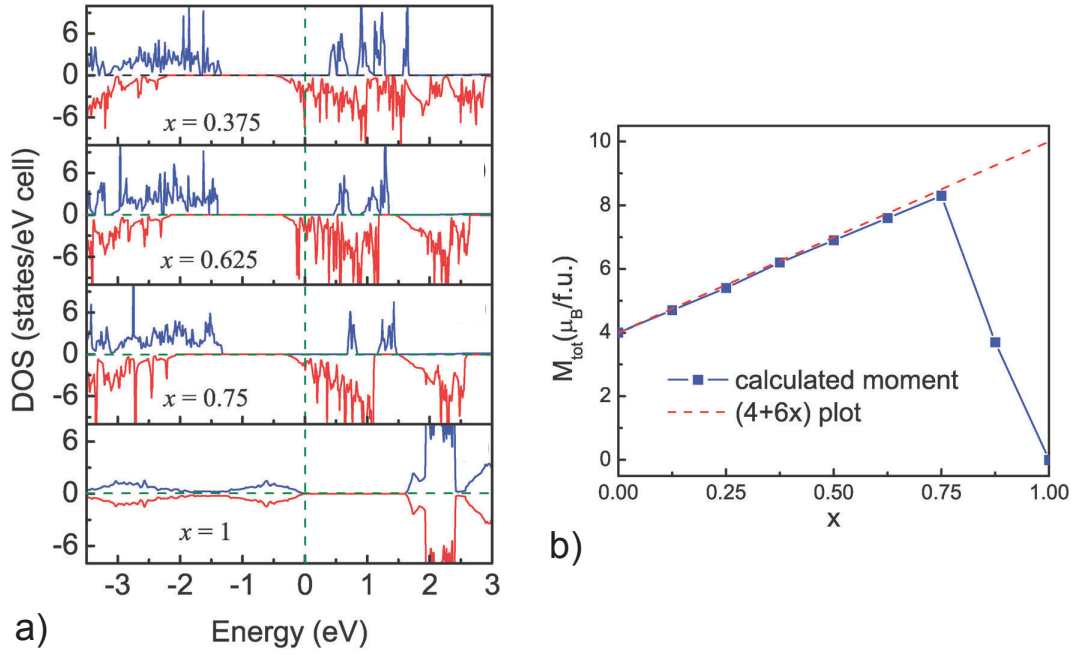


Figure 2.17: a) Calculated density of states of $\text{Zn}_x\text{Fe}_{3-x}\text{O}_4$ at different zinc concentrations x . The density of states show clear half metallicity with negative spin polarization for values of $x \leq 0.75$. At $x = 1$, the well known insulating state of antiferromagnetic ZnFe_2O_4 is reproduced. b) Calculated magnetic moment of $\text{Zn}_x\text{Fe}_{3-x}\text{O}_4$ in dependence of the zinc content x . Also shown is the $(4 + 6x)$ -plot, describing the expected magnetization as a result of the simple Néel model. Reproduced from [269] with permission of the PCCP Owner Societies.

at $x = 1$. Calculations were done under the assumption, that Zn^{2+} only substitutes **A**-site Fe^{3+} . The results explain the decrease in resistivity with increasing zinc content by the decreasing amount of Fe^{2+} , and therefore the decreasing amount of free charge carriers. The model does not consider the effect of spin canting. Magnetic moments are by definition either parallel or antiparallel aligned (two state system, either up or down). The calculated densities of states show a clear half metallic character for zinc concentrations of $0 \leq x \leq 0.75$, similar to pure Fe_3O_4 (Figure 2.17 a). The states at the Fermi level in the minority spin band are assigned to t_{2g} -states of **B**-site iron. This result confirms the conduction mechanism of electron hopping in $\text{Zn}_x\text{Fe}_{3-x}\text{O}_4$. At zinc concentrations larger $x = 0.75$, the spin down t_{2g} -states at the Fermi level vanish and a gap opens up. The spin down t_{2g} -states are shifted above the Fermi level, because their filling decreases with decreasing amount of Fe^{2+} . At $x = 1$, the well known insulating state of antiferromagnetic ZnFe_2O_4 is reproduced (Figure 2.17 a).

The calculated increase in magnetization in the range of $0 \leq x \leq 0.75$ fits well to the findings of the simple Néel-model (Figure 2.17 b). The so called $(4 + 6x)$ -law is the result of the weakened **A**-site magnetization due to the sub-

stitution of magnetic Fe^{3+} ($s = 5/2, \mu = 5\mu_B$) by nonmagnetic Zn^{2+} ($s = 0$). The decreasing amount of Fe^{3+} on **A**-sites reduces the compensating magnetic moment $M_{\mathbf{A}}$ by $5x$. The magnetic moment of the **B**-site lattice increases by $1x$ due to the change of Fe^{2+} ($s = 2, \mu = 4\mu_B$) to Fe^{3+} ($s = 5/2, \mu = 5\mu_B$), caused by charge neutrality. In sum, the total magnetization is enhanced by $6x$, resulting in a total value of $(4 + 6x)\mu_B/\text{f.u.}$ This is in contrast to the results of Venkateshvaran *et al.* [15], showing a decrease of magnetization with increasing zinc content. The discrepancy can be explained by the spin canting angle, which significantly reduces the overall magnetization of the system. The model of Cheng *et al.* [269] defines the spins of the single atoms either aligned in parallel or antiparallel. This definition excludes the possibility of spin canting. Nevertheless, at high zinc concentrations (calculated is $x=0.875$), the system shows a significant decrease of the magnetic moment. This is assigned to a decrease of the magnetization values per iron atom in **B**-sites. This decrease is due to the changes in interaction strengths, which usually lead to spin canting. In the two-state model (spins either up or down), this causes some spins on the **B**-sites to align in antiparallel, reducing the mean magnetization of the **B**-site lattice. This results in the observed reduction of the mean magnetic moment of the **B**-site iron atoms. In the extreme case of $x = 1$, the antiferromagnetic state of normal spinel ZnFe_2O_4 is reproduced with zero magnetic moment. This fast decrease in the calculated magnetization for zinc contents of $0.75 \leq x \leq 1$, and its explanation in the two state system, points out the importance of spin canting in $\text{Zn}_x\text{Fe}_{3-x}\text{O}_4$. Therefore, it confirms the picture of Venkateshvaran *et al.* [15].

2.5 Summary:

Fe_3O_4 , $\text{Zn}_x\text{Fe}_{3-x}\text{O}_4$ and ZnFe_2O_4 thin films

The magnetic and electric properties of Fe_3O_4 , ZnFe_2O_4 and $\text{Zn}_x\text{Fe}_{3-x}\text{O}_4$ thin films are related to the order (or disorder) in the cationic system. Conduction in all these materials is due to electron hopping, either small polaron assisted or simple thermally activated, between Fe^{2+} and Fe^{3+} -cations on **B**-sites [12, 14, 15, 134].

Fe_3O_4 is a ferrimagnetic conductor at room temperature and shows semiconducting behavior [12, 13]. Its curie temperature is approximately 860 K and therefore far above room temperature [12, 14]. Theoretical calculations suggest Fe_3O_4 to be half metallic due to the conduction mechanism of electron hopping [154, 170]. In contrast, measurements of the spin polarization by SP-PES [171, 174, 177, 178] or tunneling experiments (Table 2.3) do not show the expected -100% spin polarization.

The ferrimagnetic nature of Fe_3O_4 is due to the inverse spinel cation order

caused by the high OSPE of Fe^{2+} [135]. The magnetic properties are determined by the antiferromagnetic superinteractions (strong $\text{Fe}_\text{A}^{3+}\text{-O-Fe}_\text{B}^{3+}$, weak $\text{Fe}_\text{B}^{3+}\text{-O-Fe}_\text{B}^{3+}$, weak $\text{Fe}_\text{A}^{3+}\text{-O-Fe}_\text{A}^{3+}$) and the ferromagnetic double interaction ($\text{Fe}_\text{B}^{2+}\text{-O-Fe}_\text{B}^{3+}$), leading to the observed ferrimagnetic state [12, 14, 15].

The properties of Fe_3O_4 thin films strongly depend on stoichiometry. Iron deficient films ($\text{Fe}_{3(1-\delta)}\text{O}_4$) show higher resistivity and lower saturation magnetization compared to stoichiometric crystals [15, 16]. Both changes, in conductivity and magnetization, are assigned to a spin canting angle originating from an alteration of the magnetic interactions. This alteration is due to a decreasing amount of Fe^{2+} , caused by the iron vacancies, weakening the ferromagnetic double exchange. The appearance of a spin canting angle also explains the occurrence of a negative magnetoresistance in Fe_3O_4 thin films [15, 196]. Also antiphase boundaries are observed in epitaxial thin films. They cause perturbations in the magnetic lattice, resulting in a reduced magnetization and conductivity as well as a contribution to the observed magnetoresistance [12, 14, 189, 193, 195–197, 200–203].

Due to its magnetic and electric properties (a ferrimagnetic, half metallic semiconductor), Fe_3O_4 is a promising material for spintronic applications [12, 14]. Nevertheless, using Fe_3O_4 in spintronics is not an easy task. Significant problems are caused by the sensitivity of the properties to stoichiometry (in particular at the interface) and the formation of antiphase boundaries. This is especially pointed out by a huge variation in reported experimental TMR-values in Fe_3O_4 -based magnetic tunnel junctions (Table 2.3).

The substitution of Fe by Zn in Fe_3O_4 gives the possibility of altering the magnetic and electric properties of Fe_3O_4 [15]. $\text{Zn}_x\text{Fe}_{3-x}\text{O}_4$ shows decreasing carrier concentration, conductivity and saturation magnetization with increasing zinc content [15]. Nevertheless, half metallicity is predicted to persist up to rather high zinc concentrations [17].

The changes in properties arise from the changes in the cationic order in the thin films. The Zn^{2+} -cations substitute Fe^{3+} on **A**-sites. This reduces the amount of Fe^{2+} in **B**-sites due to charge neutrality. It also weakens the mean magnetic moment of the **A**-site lattice, which should result in an increased magnetic moment, following the simple Néel-model [17]. This is in contrast to the observed decrease of magnetization with increasing zinc content [15]. The observed decrease is explained by a spin canting angle. This angle between the magnetic moments of iron cations on **B**-sites is the result of alteration of the magnetic interactions by the incorporation of zinc (weakens antiferromagnetic $\text{Fe}_\text{A}^{3+}\text{-O-Fe}_\text{B}^{3+}$) and the resulting decrease of the amount of Fe^{2+} -cations (weakens ferromagnetic $\text{Fe}_\text{B}^{2+}\text{-O-Fe}_\text{B}^{3+}$ and strengthens antiferromagnetic $\text{Fe}_\text{B}^{3+}\text{-O-Fe}_\text{B}^{3+}$). The spin canting angle increases with increasing zinc content and therefore reduces the overall magnetic moment. It also reduces the hopping amplitude of charge carriers. This, in combination with a decreased amount of itinerant charge carriers due to the reduced number of Fe^{2+} -cations, results

in a decrease of conductivity.

The substitution of Fe by Zn also compensates the effects of iron vacancies. Therefore, Zn-substitution can be used to stabilize the properties of thin Fe_3O_4 films [15].

The change in properties of $\text{Zn}_x\text{Fe}_{3-x}\text{O}_4$ thin films is the result of changing the stoichiometry of the films, and not of defects in the crystal structure. The adjustable properties arises from a stable crystalline configuration, which makes it, in combination with its half metallicity, a promising material class for application in spintronics [15, 17].

ZnFe_2O_4 in its bulk structure is an antiferromagnetic insulator [136, 137]. Theoretical calculations show the influence of inversion and oxygen vacancies on the properties of ZnFe_2O_4 [142]. Simple inversion introduces a splitting in the conduction band minima of majority and minority states, and ferrimagnetism due to the arising magnetic coupling in and between the **A** and **B**-sublattices [142]. This makes partially inverse ZnFe_2O_4 interesting for the application as barrier in spin filter tunnel junctions. Oxygen vacancies in partially inverted ZnFe_2O_4 introduce Fe^{2+} -cations into the system, giving rise to spin polarized conductivity [142].

Experiments on thin films show conductivity in samples grown at low substrate temperatures [139]. This is assigned to the presence of Fe^{3+} in former unoccupied **A**-sites due to iron surplus and oxygen vacancies. In both cases, charge neutrality forms Fe^{2+} in **B**-sites, that are responsible for electron conduction. Resistivity of conducting thin films depends on the oxygen pressure during growth [137, 140]. It decreases with decreasing oxygen pressure, stating the influence of oxygen vacancies on the conduction in ZnFe_2O_4 .

Ferrimagnetism in thin ZnFe_2O_4 films is assigned to partial inversion or occupation of former empty **A**-sites by Fe^{3+} -cations due to iron surplus [138]. The formation of Fe^{2+} might also give rise to the ferrimagnetism due to a strengthening of the ferromagnetic double exchange in the **B**-site sublattice.

Properties of ZnFe_2O_4 thin films, namely ferrimagnetism and conductivity, are based on disorder in the cationic system, caused by the growth mechanism and oxygen vacancies. The origin of the mechanism, leading to the observed properties in ZnFe_2O_4 , is not clear yet. In addition to the cationic disorder, the variation of stoichiometry might be important for the reported properties of ZnFe_2O_4 thin films. The stoichiometry of investigated samples shows variations between 1.8 and 2.5 ($x = 0.85$) for the Fe/Zn-ratio [138, 155], making excessive iron a very likely scenario.

Nevertheless, it can be concluded, that magnetic properties of ZnFe_2O_4 arise mainly from disorder in the cationic structure, be it partial inversion due to exchange of Zn^{2+} and Fe^{3+} between **A** and **B**-sites or occupation of **A**-sites by excessive iron. This cationic configuration was confirmed by XANES measurements [138]. Conductivity in ZnFe_2O_4 thin films is linked to the amount of Fe^{2+} on **B**-sites [142, 267]. It seems to be due to charge neutrality rea-

sons caused by excessive iron and oxygen vacancies. All these mechanisms are cross-linked, making it difficult to tell the impact of every single one, and therefore the real reason for the observed properties of ZnFe_2O_4 thin films.

3 Sample preparation and characterization techniques

3.1 Thin film growth and *in-situ* characterization: Pulsed laser deposition and reflection high-energy electron diffraction

The basis for the preparation of $\text{Zn}_x\text{Fe}_{3-x}\text{O}_4$ based magnetic tunnel junctions in the framework of this thesis are thin films of TiN, ZnFe_2O_4 , $\text{Zn}_x\text{Fe}_{3-x}\text{O}_4$, Fe_3O_4 , MgO and Co (see Section 4), grown by pulsed laser deposition (PLD) in the B-chamber of the semiconductor physics group of the Leipzig University. The B-chamber is equipped with a RHEED-system (reflection high-energy electron diffraction), allowing an *in-situ* observation of the thin film growth and a characterization of the surface.

This section will give a brief overview on pulsed laser deposition, RHEED, the used setup (B-chamber) and the principles of thin film growth.

3.1.1 Pulsed laser deposition (PLD)

In this work, pulsed laser deposition was used to grow TiN, ZnFe_2O_4 , $\text{Zn}_x\text{Fe}_{3-x}\text{O}_4$, Fe_3O_4 , MgO and Co thin films. PLD is one of the physical vapor deposition (PVD) techniques. Thin film growth in PLD is due to the condensation of plasma particles on the surface of a heated substrate. The plasma is produced by a high energy laser pulse, focused on the surface of a stoichiometric target. The source material for the growth of thin films by PLD are ceramic pellets called targets. The targets used for oxide thin films consist of powders of the source materials, being mixed in accurately defined amounts to achieve the desired stoichiometry. The mixed powders get ball milled, pressed and sintered in order to produce a solid, ceramic pellet. During deposition, a short laser pulse with a high energy is focused on the target surface in order to ablate the material.

The growth process in PLD can be divided in three major parts: ablation of the target material, plasma expansion and condensation of plasma particles at the substrate surface [270]. The ablation of material is due to the absorption

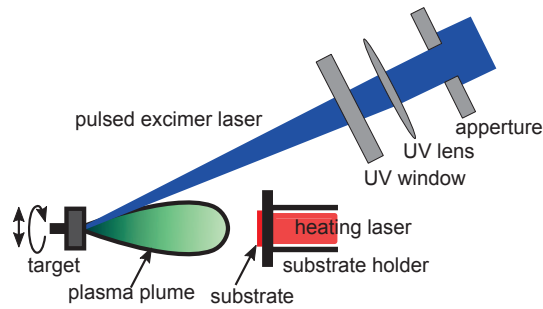


Figure 3.1: Schematic drawing of the pulsed laser deposition process.

of the laser energy at the surface of the target. The material at the surface melts and evaporates. The vaporized target material absorbs parts of the laser energy and forms a plasma in front of the target surface. The plasma expands away from the target surface (plasma plume) and the ablated material inside the plasma plume moves to the substrate surface where it condenses. The condensed material nucleates at the substrate surface and forms the thin film. Thin film formation at the substrate surface is mainly influenced by surface diffusion due to the kinetic energy of the particles (see Section 3.1.3). A schematic of the PLD-process is shown in Figure 3.1.

Using PLD in order to grow different thin films has several advantages. PLD is a flexible method in terms of material choice. Nearly every material, that can be produced as solid pellet, can be used to grow thin films. One only needs to change the targets inside the chamber, usually done without breaking the vacuum by a target carousel. This allows the growth of multilayer structures, containing different materials, in one step [271]. Growth conditions can be easily adjusted by the change of substrate temperature, type of background gas and pressure, target-substrate distance, laser energy density at the target surface and laser pulse repetition frequency. Excellent structural properties of thin films can be achieved by proper adjustment of these variables [271].

One more adjustable property, except of the structural quality, is the stoichiometry of the thin films. PLD is known for its stoichiometric transfer of multielement compounds from a single target [270]. But also exceptions from this general rule are reported [270, 272]. Lorenz [270] reports different concentration transfer factors for dopant elements in ZnO. The achieved stoichiometry of the thin films seems to depend not only on target composition, but on PLD growth parameter such as background pressure, laser energy density at the target surface and substrate temperature. The concentration also shows a huge dependence on the type of dopant. This leads to the assumption, that the stoichiometry of thin films depends on the behavior of the involved elements, including the amount of material evaporated by the laser pulse, the kinetic energy obtained during evaporation, the kinetic behavior in the back-

ground gas (scattering, mean free path) and the desorption (evaporation) at the substrate surface. All this might influence the stoichiometry of thin films and must be adjusted accordingly in order to achieve the desired film composition of multielement compounds.

More details on thin film growth by PLD can be found in [14, 270, 271, 273–275].

3.1.2 Reflection high-energy electron diffraction (RHEED)

The diffraction of high energy electrons in reflecting geometry at the sample surface is a useful tool to characterize the crystalline surface of samples and monitor the growth of thin films *in-situ*. For reflection high-energy electron diffraction, the sample surface gets irradiated by electrons with high kinetic energy ($E \approx 30$ keV) under a small angle ($\theta \approx 2^\circ$). The scattered electrons hit a fluorescent screen (the RHEED-screen), where a diffraction pattern becomes visible. Due to the small incidence angle and the resulting small penetration depth, the electrons are scattered at the two-dimensional surface lattice. The resulting diffraction pattern provides some information about the surface of the sample. Figure 3.2 shows the schematic geometry of RHEED and three experimental RHEED pattern. First, the origin of the RHEED diffraction pattern will be qualitatively discussed based on the kinematic scattering theory, neglecting strong interactions [276]. Then, the provided information on the sample surface will be pointed out.

The accelerated electrons with kinetic energy E have an assigned wavelength λ and a wave vector \vec{k} due to the wave particle duality. Without relativistic corrections (approximately 2% in the used energy range) it is

$$\lambda = \frac{h}{p} = \frac{h}{mv} = \frac{h}{\sqrt{2mE_{\text{kin}}}} \quad \text{and} \quad |\vec{k}| = k = \frac{2\pi}{\lambda} = \frac{\sqrt{2mE_{\text{kin}}}}{\hbar}. \quad (3.1)$$

The wavelength λ for electrons with a kinetic energy of 30 keV is 0.07 Å and therefore smaller than typical lattice constants (≈ 1 to 10 Å).

Due to the small incidence angle and the resulting small penetration depth, the electrons are scattered at a two-dimensional surface lattice. Constructive interference is described by the Laue equation and occurs when the change of the electron wave vector due to scattering is equal to a reciprocal lattice vector \vec{G} of the surface lattice.

$$\Delta\vec{k} = \vec{k}_{\text{out}} - \vec{k}_{\text{in}} = \vec{G} \quad (3.2)$$

The periodicity perpendicular to the surface is missing in a two-dimensional lattice. Therefore, the reciprocal lattice of a two-dimensional surface is described by infinite rods perpendicular to the sample surface (see Figure 3.2 a). The reciprocal lattice vectors define the position of these rods in reciprocal

space and are described as

$$a_1^* = 2\pi \frac{\vec{a}_2 \times \vec{n}}{\vec{a}_1 \circ (\vec{a}_2 \times \vec{n})} \quad a_2^* = 2\pi \frac{\vec{n} \times \vec{a}_1}{\vec{a}_1 \circ (\vec{a}_2 \times \vec{n})}. \quad (3.3)$$

This results in the general form for the reciprocal lattice vector \vec{G} of a two-dimensional lattice

$$\vec{G} = h \cdot \vec{a}_1^* + k \cdot \vec{a}_2^* + l \cdot \vec{n}^* \quad h, k \in \mathbb{N}; \quad l \in \mathbb{R} \quad (3.4)$$

Here, \vec{a}_1 and \vec{a}_2 are the basis vectors of the two-dimensional surface lattice in real space and \vec{n} and \vec{n}^* the normal vectors perpendicular to the sample surface in real and reciprocal space, respectively.

In case of elastic scattering ($|\vec{k}_{\text{in}}| = |\vec{k}_{\text{out}}|$), the Laue condition ($\Delta\vec{k} = \vec{G}$) can be descriptively interpreted by the Ewald sphere. The Ewald sphere has its origin at the scattering point and a radius $r = |\vec{k}_{\text{in}}| = |\vec{k}_{\text{out}}|$. The Laue condition is fulfilled at points, where reciprocal lattice rods intersect the Ewald sphere, as shown in Figure 3.2 a. Since the direction of the electron beam corresponds to the direction of the wave vector \vec{k} , the projections of the intersections are visible at the screen. This results in a diffraction pattern at the RHEED-screen that consists of points arranged in circles. These circles are called Laue circles. The specular spot is labeled (0,0) and is located at the zero Laue circle. All other spots are labeled by (h,k), describing the reciprocal lattice vector \vec{G} , responsible for the change of the wave vector \vec{k} .

The spot position at the RHEED screen allows a determination of the reciprocal lattice vectors parallel and perpendicular to the incident electron beam, g_{\parallel} and g_{\perp} , respectively [277].

$$hg_{\parallel} = |\vec{k}_{\text{in}}| \left[\cos \theta - \frac{1}{\sqrt{(l_h/L)^2 + 1}} \right]$$

$$kg_{\perp} = \frac{|\vec{k}_{\text{in}}|}{\sqrt{(L/l_k)^2 + 1}} \quad (h, k \in \mathbb{N}) \quad (3.5)$$

Here, l_h is the vertical distance and l_k the horizontal distance of the spot from the (0,0) spot at the RHEED-screen. L is the distance between sample and screen. These formulas for g_{\parallel} and g_{\perp} are valid for (h,0) and (0,k) spots, respectively.

Thus, one information provided by the RHEED-pattern is the surface lattice constant perpendicular to the beam direction [277]. It is

$$a_{\perp} = \frac{2\pi}{g_{\perp}} = \frac{2\pi \sqrt{(L/l_n)^2 + 1}}{|\vec{k}_{\text{in}}|}. \quad (3.6)$$

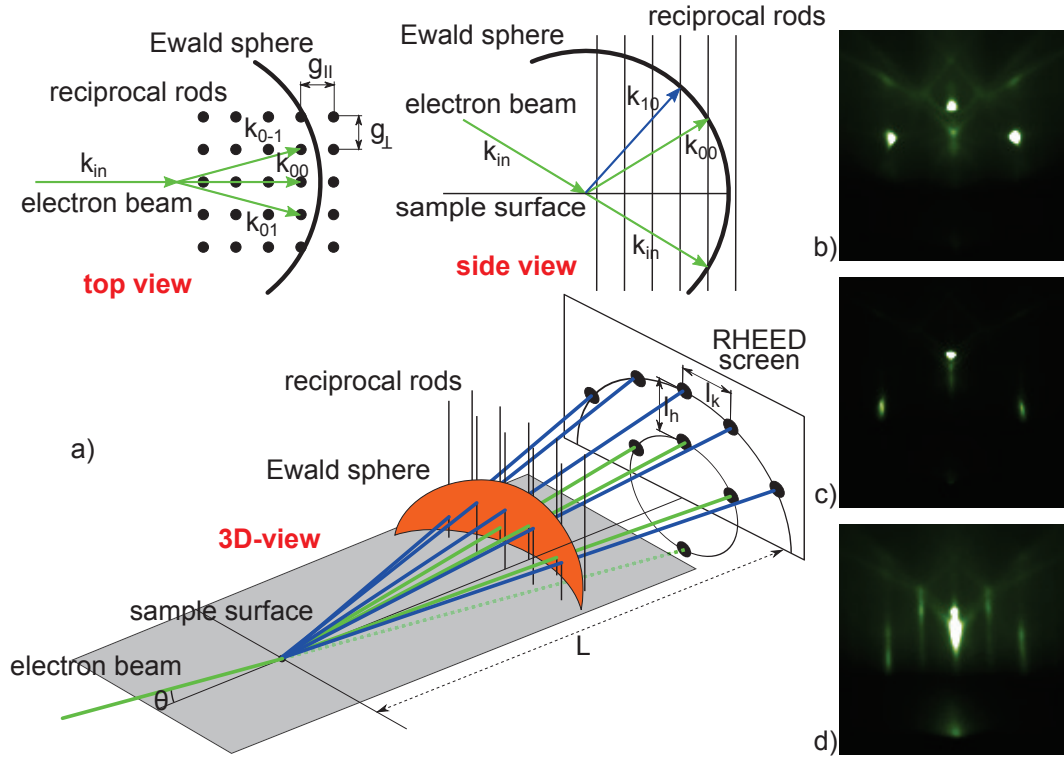


Figure 3.2: a) Geometry of diffraction and origin of RHEED-pattern. (After [277]). Experimental RHEED-pattern in [10]-direction of b) and c) MgO(100) substrates after annealing and d) a $\text{Zn}_x\text{Fe}_{3-x}\text{O}_4$ -thin film after 15000 PLD-pulses. All three pattern show clear Kikuchi lines, indicating a flat, crystalline surface. The substrate in b) shows defined spots and no streak, indicating a perfectly flat surface. c) and d) show streaky spots, indicating a terraced surface. The pattern of the $\text{Zn}_x\text{Fe}_{3-x}\text{O}_4$ -surface shows additional streaks at half the distance of these at MgO. This is due to the doubled lattice constant.

For small perpendicular diffraction angles and $l_n \ll L$ this becomes

$$a_{\perp} = \frac{2\pi L}{|\vec{k}_{\text{in}}| l_n}. \quad (3.7)$$

If the electron beam is parallel to the [10]-direction of a cubic crystal surface, $a_{\perp} = a_{\text{cubic}}$. It can easily be seen that a doubling of the lattice constant a_{cubic} results in a halving of the distance between spots on the RHEED-screen. This can be observed while growing $\text{Zn}_x\text{Fe}_{3-x}\text{O}_4$ on MgO(100)/TiN (see Figure 3.2 c and d).

Information about the surface structure is provided by the form of the spots in the RHEED pattern. A perfectly crystalline and flat surface should show well defined spots located at the Laue circles [278]. Small imperfections like a wavy surface [279] and resulting steps, as well as temperature induced fluctuations

at the surface lead to a broadening of the reciprocal rods [278]. Therefore, the intersections with the Ewald sphere also broaden up. The observed broadening on the RHEED screen is small in horizontal (parallel to the sample surface), and large in vertical (perpendicular to the sample surface) direction. This is due to the angle at which the broadened reciprocal rods intersect the Ewald sphere. The result are streaky pattern as shown in Figure 3.2 c and d. RHEED-pattern of rough surfaces show point-like spots that are not arranged at Laue circles. This pattern are the result of three-dimensional scattering of electrons on crystalline islands on the sample surface [278, 279]. Figure 3.4 h shows an example of a pointy RHEED-pattern of a sample surface with crystalline islands.

Figure 3.2 b and c show the RHEED-pattern of annealed MgO-substrate in [10] direction. The surface in Figure 3.2 b seems to be perfectly flat as indicated by the well defined spots at the zero Laue circle. Figure 3.2 c shows three characteristic streaks due to a rather flat, but wavy crystalline surface with terraces. The lines appearing in the upper part of the picture (diamond shape) are so called Kikuchi lines. They arise from multiple scattering of electrons at the sample surface due to the strong interactions, neglected in the description above [276]. The appearance of Kikuchi lines is an indication for a high quality, flat and crystalline surface [276, 280].

RHEED gives not only information on surface structure and lattice constants. The analysis of the intensity of RHEED spots provides information about the growth mode of the thin film (see Section 3.1.3). If the thin film grows in the layer by layer mode, oscillations can be observed in the intensity of RHEED-spots. The oscillations can be explained by diffuse scattering of electrons on unfinished layers [278]. This mechanism can be compared to the diffuse scattering of light. Light (wavelength $\lambda \approx 0.5 \mu\text{m}$) is diffusely scattered at surface features with dimensions of about $10 \mu\text{m}$. The wavelength of the electrons is about 0.07 \AA and the height of steps on crystalline surfaces is approximately 2 \AA (in case of MgO, TiN and $\text{Zn}_x\text{Fe}_{3-x}\text{O}_4$). Therefore, the ratio of wavelength and feature size is comparable and allows to adopt this ansatz to describe the RHEED-intensity oscillation during thin film growth in layer by layer mode. The density of step edges at the surface defines the amount of diffuse scattered electrons, that do not contribute to the intensity of the RHEED spot. A closed layer has a perfectly flat surface and the amount of diffuse scattered electrons is low. Due to the condensation of atoms on the surface, nucleation centers form. In perfect layer by layer growth, this nucleation centers are monolayer islands, growing with increasing surface coverage Θ . The amount of step edges therefore increases up to a surface coverage of $\Theta = 0.5$ (layer is half closed). Thus, the intensity of the RHEED-spot decreases in the range of $0 \leq \Theta \leq 0.5$. In the range $0.5 \leq \Theta \leq 1$ the amount of step edges decreases and the intensity increases until the layer is completely closed. The situation is schematically shown in Figure 3.3.

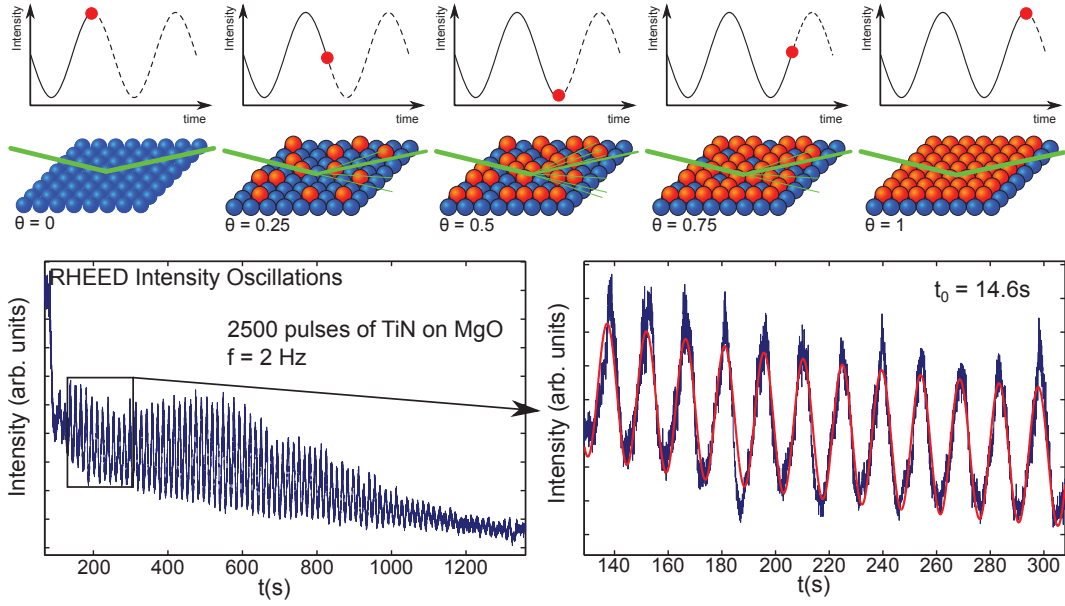


Figure 3.3: Top: RHEED Intensity and arising oscillations in dependence of the surface coverage Θ of the growing layer in two-dimensional growth mode. Bottom: RHEED-intensity oscillation during the pulsed laser deposition of TiN on (100)-MgO. The red line is a fit to a sine based model, that is used to determine the oscillation time t_0 .

The oscillating RHEED-intensity due to the formation of single layers at the surface allows an exact determination of the film thickness. The number of counted maxima during deposition times the (known) thickness of one monolayer results in the thickness of the film. In PLD, also the number of pulses needed to grow exactly one monolayer can be determined. This information is used in interval PLD in order to grow exactly one monolayer after the other and give the surface time in between to rearrange and close the layer [276, 281]. In conventional PLD, the system usually does not have the time to completely rearrange and new layers begin to grow on top of unfinished ones. This is due to a limited surface mobility of atoms, being too small to allow the atoms to reach step edges and fill the first monolayer. This mechanism leads to a decrease of overall intensity and amplitude in the RHEED intensity oscillations [278]. Figure 3.3 shows the RHEED-intensity oscillations during pulsed laser deposition of TiN. The decrease in intensity and amplitude is clearly visible. Detailed information on RHEED, intensity oscillations and theories describing them can be found in [277, 278].

3.1.3 Thin film growth modes

The application of thin films in magnetic tunnel junctions requires atomically flat interfaces. Rough interfaces cause electric field spikes and a concentration of the flowing current in certain spots of the barrier. This results in

the formation of pinholes: small metallic conduction paths across the barrier [282]. Pinholes inside the barrier lower the TMR and limit the performance of MTJs. Another problem occurring with rough interfaces is Néel (or orange peel) coupling between the magnetic layers [283, 284]. It is therefore important to understand and control the growth kinetics of thin films during film deposition, in our case PLD, in order to achieve atomically flat interfaces. The growth of thin films is classified in three different types of growth modes (Figure 3.4) [14, 276, 285]:

- Frank-van-der-Merve (two-dimensional or layer by layer growth)
- Volmer-Weber (three-dimensional or island growth)
- Stranski-Krastanov (combined layer by layer and island growth)

During deposition, small nucleation centers form on the surface due to supersaturation of the vapor phase above the substrate [276, 285]. In principle, the shape of the forming nuclei, and therefore the growth mode, depends on the interactions between depositing atoms (adatoms) and the substrate [14]. If the deposited atoms bond stronger to each other than to the substrate, the nuclei form three-dimensional islands and the film grows in Volmer-Weber mode. Two dimensional layer by layer or Frank-van-der-Merve growth occurs, if the adatoms bind stronger to the substrate than to each other. In this case, the nuclei spread out and form monolayer islands in order to cover the whole surface. Depositing atoms form completely closed layers before growing subsequent layers. With increasing number of layers, the interaction between the newly formed layers and the substrate decreases, until the interaction between surface and new layers reaches the bulk value of the film material. At this point, it is possible, that the growth mode changes and the growth of three dimensional islands is energetically favorable. This combined growth mode (two- to three-dimensional) is known as Stranski-Krastanov growth mode. The interaction between the surface and the depositing atoms is described in thermodynamics by interface energies [276]. The interface energy has three contributions: interface tension between substrate and vacuum γ_s , film and vacuum γ_f and substrate and film γ_{sf} . The shape of the nuclei is derived by minimizing the total interface energy

$$E = \int \gamma_s dA_s + \int \gamma_f dA_f + \int \gamma_{sf} dA_{sf}, \quad (3.8)$$

with A_s , A_f and A_{sf} the areas of substrate-vacuum, film-vacuum and substrate film interface, respectively. This gives in principle two different situations:

- $\gamma_f + \gamma_{sf} < \gamma_s$
The coverage of the surface by the new grown nuclei is favored, resulting in a complete wetting of the surface and the formation of monolayer islands. This results in two-dimensional layer by layer growth.
- $\gamma_f + \gamma_{sf} > \gamma_s$
The formation of the interface between substrate and film is energetically

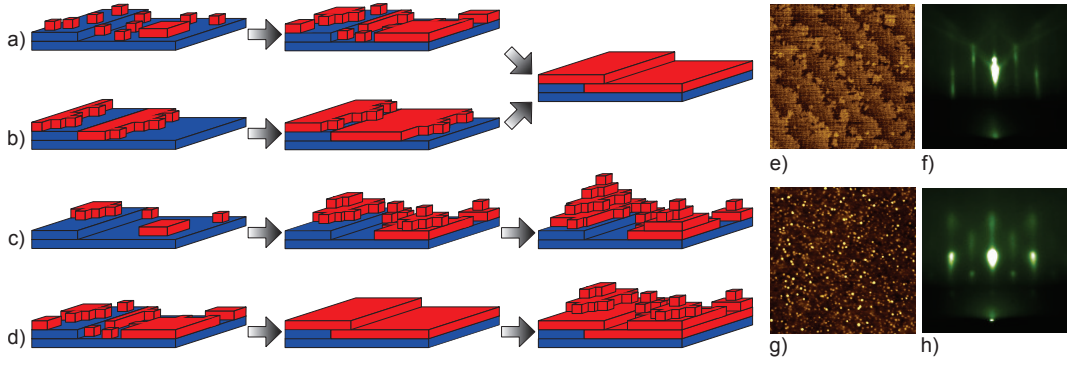


Figure 3.4: Thermodynamic thin film growth modes: a) "Frank-van-der-Merwe" growth (layer by layer or two-dimensional) b) step flow growth c) "Volmer-Weber" growth (island or 3-dimensional) d) "Stranski-Krastanov" growth (combined layer and island) e) AFM scan and f) corresponding RHEED-pattern of a 2D-surface of ZnFe_2O_4 . Step height is 0.2 nm. g) AFM scan and h) corresponding RHEED-pattern of a ZnFe_2O_4 -surface showing small islands. Height of the islands is 2 nm. Scan size of both AFM scans is $2.5 \times 2.5 \mu\text{m}^2$.

unfavored. Three-dimensional islands are formed in order to minimize the interface area. This situation leads to Volmer-Weber growth.

Stranski-Krastanov growth occurs when the interface tensions change during growth and the situation changes from layer by layer growth to island growth. The thermodynamic picture is well oversimplified and neglects the influence of supersaturation and kinetics on thin film growth. It only describes the potential difference between the initial and the final state without taking the processes into account that lead to the formation of the final state. The growth mode in this picture seems to be defined by the choice of material combination and the binding strength between deposited atoms and substrate.

The growth process in pulsed laser deposition is far from equilibrium. In contrast to the description by thermodynamics (process in or near equilibrium), the description of the PLD growth process needs to take the kinetics of surface atoms into account. Usually, a limited surface diffusion in combination with a high supersaturation is the reason for the different observed growth modes. Thin film growth by PLD is a two step process: The first step is nucleation, characterized by a temporary, high supersaturation due to the high particle density inside the plasma plume. The result is the formation of many small nuclei at the surface of the substrate. The second step is the arrangement of the surface atoms and clusters due to surface diffusion. Usually, most clusters formed at the surface do not reach the critical size and are therefore unstable and decompose into single surface atoms (see Figure 3.5). If the size of a cluster reaches the critical size due to agglomeration of mobile surface atoms, the cluster becomes stable and forms an island. The mobility of surface atoms is responsible for a redistribution at the surface and therefore the obtained growth mode in PLD.

Surface diffusion of atoms is described as a hopping process, and the two-dimensional diffusivity D is given by

$$D = \frac{a^2}{4} \Gamma = \frac{\nu a^2}{4} \exp\left(-\frac{E_d}{kT^*}\right) \quad (3.9)$$

with Γ the hopping rate between surface lattice sites, ν the vibration frequency of the atom, E_d the diffusion energy and a the lattice constant of the two dimensional surface lattice [276]. The effective surface diffusion temperature T^* is determined by the substrate temperature and the kinetic energy of the adatoms [286–289]. The characteristic path length x an atom travels at the surface is given by

$$x = \sqrt{D \cdot \tau}. \quad (3.10)$$

The diffusion time τ is usually defined by the laser repetition frequency. The surface atoms diffuse at the surface, until the next pulse of plasma atoms resets the situation. The diffusion of surface atoms is determined by their kinetic energy. Kinetic energy of the surface particles depends on the laser energy density at the target surface, the background gas type and pressure in combination with the target-substrate distance as well as the substrate temperature [270]. Now, the two thermodynamic growth modes have to be considered. Is the formation of islands or layers favored? A high mobility favors the formation of the respective growth mode. The kinetic energy of the system has to be large enough to reach the desired energetic state. If this is not the case, some intermediate states will form. These states are briefly described hereafter.

In case of a thermodynamically favored three-dimensional growth, a high mobility of surface atoms favors the formation of few, large islands. The critical size for the formation of stable clusters is large [276]. Thus, small nuclei decompose and the surface atoms diffuse until they reach a large, stable cluster. These islands grow until they coalesce and a closed film is formed. This growth mode induces the formation of grain boundaries in the thin film and a rough surface. A small surface mobility has compensating effects. Due to their limited range, surface atoms are not able to reach stable islands before the next pulse. Therefore, the chance of forming a stable cluster is enhanced due to the increased amount of surface atoms, being able to form a cluster beyond the critical size. This causes the formation of many small islands, being able to cover the substrate surface more easily. This results in smoother film surfaces compared to growth at high mobility conditions.

More interesting in order to grow smooth films is the case of thermodynamically preferred two-dimensional growth. Well defined layer by layer growth is achieved by a high mobility of surface atoms. Due to their high mobility, surface atoms reach stable sites at step edges where they attach (Figure 3.5). The step edges can be either formed by the substrate miscut (terraces) or by small monolayer islands at the surface. Due to the interaction between depositing atoms and substrate, nuclei formed by the high supersaturation during a

pulse have a small critical size and form monolayer islands [276]. These islands provide step edges for diffusing surface atoms, grow due to attaching surface atoms and close the layer.

The interchange of atoms between layer planes is suppressed by the Ehrlich-Schwöbel barrier [290–292] (Figure 3.5). The energy barrier hinders atoms to jump from a step edge to the lower surface plane and reflects them back onto the upper layer. A high kinetic energy allows the surface atoms to overcome the Ehrlich-Schwöbel barrier at step edges and to diffuse between layers. This allows also surface atoms, deposited on top of a newly forming, and not yet closed layer, to switch to the surface below and attach to the step edge in order to close the actual growing layer [285].

A special case of two-dimensional growth is the so called step flow growth. In step flow growth, the mobility of surface atoms is large enough to reach terrace step edges before they can form small monolayer islands. Therefore, the atoms stick to step edges and the film grows by forward moving steps (Figure 3.4 b). Step flow growth is achieved by high substrate miscut angles (small terrace width) or high substrate temperature (large mobility of adatoms) [293].

A small mobility or a high repetition rate causes the formation of monolayer islands on top of existing ones. Free surface atoms on top of an island, that have not reached a stable site by the time of a new pulse, enhance the chance of forming a stable monolayer cluster. An other effect, supporting the formation of new layers on islands is the Ehrlich-Schwöbel barrier [290–292] (Figure 3.5 c), occurring at step edges. This energy barrier prevents surface atoms from diffusing over the edge and reach the underlying stable site at the step edge. This effect leads to the growth of islands with more than one monolayer [285]. Both effects support the formation of new layers before the underlying layer is closed, and therefore the three-dimensional islands growth at low mobility conditions. This growth mode can be regarded as Stranski-Krastanov mode.

The formation of single layers or three-dimensional features in this growth mode (layer by layer growth is preferred thermodynamically) is due to the mobility (surface and step diffusion) and the binding of surface atoms at step edges and surface defects. Step edges and flat terraces support the formation of smooth films in layer by layer mode. In contrast, surface defects like screw dislocations support the formation of three-dimensional islands [276]. Therefore, a well defined substrate surface with flat terraces, divided by step edges, is crucial for two-dimensional layer by layer growth. This states the importance of substrate pretreatment and the preparation of a high quality surface before film growth.

More information on the theoretical description of thin film growth can be found in [276, 285]

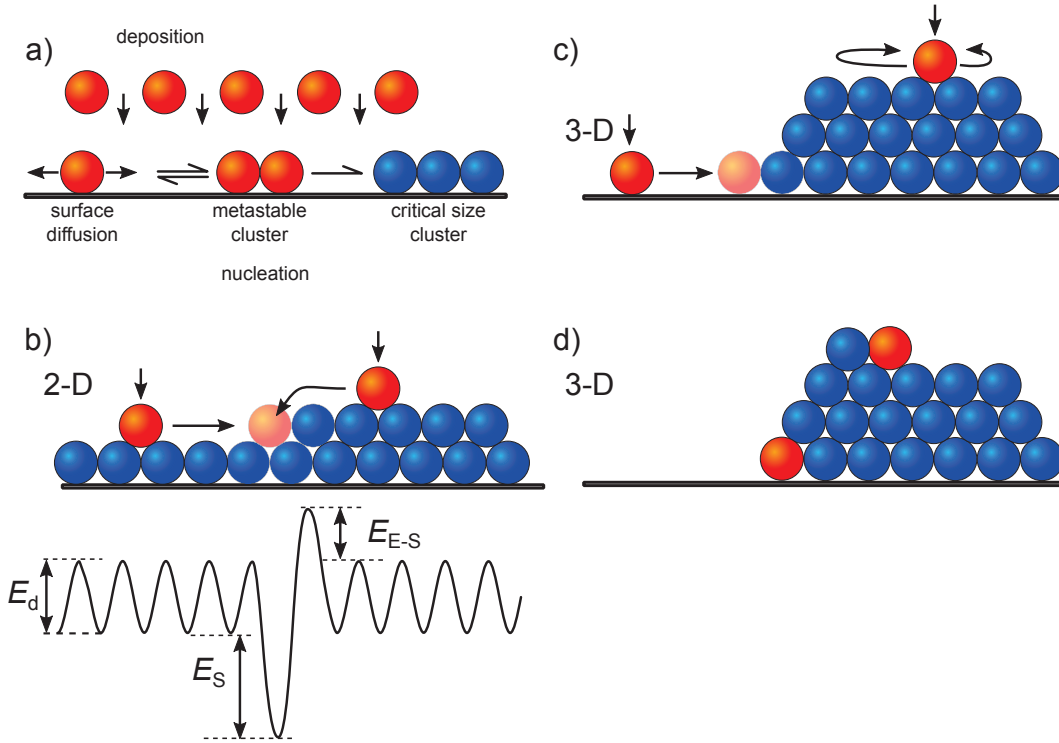


Figure 3.5: a) Nucleation process at the surface during deposition. Depositing atoms form metastable clusters at the surface due to supersaturation. These clusters can decompose and the resulting surface atoms diffuse at the surface. Surface atoms may cluster again. If a cluster reaches the critical size, it gets stable and forms an island on the surface. b) Two dimensional layer by layer growth mode. The stable clusters form monolayer islands. Surface atoms diffuse at the surface and stick to step edges. Due to their high kinetic energy, surface atoms can overcome the Ehrlich-Schwöbel barrier and descent to fill the step edge. The energy landscape describes the diffusion of surface atoms. E_d is the diffusion energy, E_s the step etch binding energy and E_{E-S} the Ehrlich-Schwöbel barrier (after [290]). c) Three-dimensional growth mode. The stable clusters form large islands. Surface atoms diffuse at the surface until they stick to a large island. Atoms on top of an island are reflected at the step edge by the Ehrlich-Schwöbel barrier. d) Formation of three-dimensional islands due to incorporation of surface atoms caused by thermodynamically favored interface energy reduction.

3.1.4 B-Chamber: PLD chamber with CO₂-laser heater and *in-situ* RHEED

Thin film growth in the framework of this thesis was done in the B-chamber of the Semiconductor Physics Group in Leipzig. The B-chamber is a PLD-chamber equipped with a CO₂ laser heater and an *in-situ* high pressure RHEED system. Figure 3.6 shows a schematic drawing and photographs of the chamber. The designation "B"-chamber is the short form of beam-chamber. This is due to the four different beams used at the chamber: The excimer laser, the CO₂ heating laser and the RHEED-electrons. There is also the possibility to attach a spectroscopic ellipsometer to the chamber. A second explanation for "B" is the German term "Beobachtungskammer" (observation chamber) due to the possibility to monitor the thin film growth with different techniques.

The main parts of the PLD-chamber are the high vacuum chamber with motorized target carousel (A), the excimer laser including the laser optics (B), the heating laser (C), the RHEED system (D), the gas supply with pressure regulation system (E) and the vacuum pump system (F) (Figure 3.6).

Pulsed laser deposition is a vacuum process, performed in a well defined and controlled atmosphere. Depending on the deposited material and the desired properties of the thin film, different atmospheres and pressures are used. Films are usually grown in oxidizing (O₂) or inert (Ar, N₂) atmospheres.

The high vacuum chamber is equipped with a pump system consisting of a scroll pump Varian SH-110, providing the prevacuum, and a turbo pump Varian TV 511 Navigator with integrated controller (Figure 3.6 F). During the process, the speed of the turbo pump is set constant. The base pressure of the vacuum chamber is 10⁻⁷ mbar.

Gas supply and pressure control (Figure 3.6 E) in the B-chamber is done in upstream pressure control geometry by a MKS Type 146 vacuum measurement and control system. A vacuum gauge MKS Type 627B Baratron capacitance manometer delivers the actual pressure value. The gas flow, setting the chamber pressure, is regulated by a MKS 248A Flow Control Valve, controlled by the MKS Type 146. This setup can regulate the pressure inside the chamber between 1 and 1 · 10⁻⁴ mbar. Usually, only one type of gas is used (Ar, O₂ or N₂).

Prevacuum is monitored by a MKS Type 722A Baratron absolute capacitance manometer with a range between ambient pressure and 1 mbar, and a Pfeiffer PKR 251 vacuum compact full range gauge monitors the high vacuum inside the chamber between 1 mbar and the base pressure of 10⁻⁷ mbar.

The substrate temperature is a crucial parameter in order to grow high quality thin films by PLD (see Section 3.1.3). In our B-chamber, the substrate is heated by a CO₂ laser heating system, supplied by SURFACE GmbH [294] (Figure 3.6 C). The used CO₂ laser has a maximum output power of $P_0 =$

140 W at a fixed laser wavelength of $\lambda = 10.6 \mu\text{m}$. The initially elliptical laser beam is shaped to a $10 \times 10 \text{ mm}^2$ square by a beam shaper optic. Two adjustable mirrors allow the alignment of the beam along the optical axis of the beam shaper. The beam shaper is rotatable in order to align the square laser spot to the substrate. The laser beam is once again redirected by a beam splitter, before it enters the vacuum chamber through a special ZnSe laser window. ZnSe shows only minimal absorption at $\lambda = 10.6 \mu\text{m}$, making it a suitable window material for the heating laser. The geometry using a beam splitter to direct the laser beam to the substrate allows the use of a pyrometer in order to measure the substrate temperature directly. The temperature is controlled by a PID-controller that compares the actual temperature, provided by the pyrometer, to the target temperature and sets the laser power output accordingly. The laser power output is controlled by a pulse width modulation (PWM) controller, that converts the linear output of the PID-controller into a PWM-signal. A output power of approximately 10% is needed in order to heat a MgO-substrate to 950°C . A fixed temperature change rate of 50 K/min was used for all heating processes.

The use of a CO_2 laser heater has several advantages compared to a conventional, Kantal based resistance heater (as described in [270]). The substrate temperature can be set directly and does not depend on resistance heater power and background gas pressure. Temperature changes are fast and virtually any temperature ramp is possible. The use of a laser heater also minimizes contamination due to evaporated material from the substrate holder by only heating the substrate. The evaporated material can either be directly from the heater and the substrate holder (stainless steel [270]), or originate from previously deposited materials at the substrate holder. This point is important for the growth of TiN in multilayer systems containing oxides. Most metals show a larger enthalpy gain for the formation of oxides than for the formation of the corresponding nitride. Therefore, oxygen supply has to be completely avoided during the growth of nitride thin films. Since the substrate holder is coated by oxides from prior deposition steps, oxygen will desorb from the heated holder during the growth process and oxide instead of nitride is formed. The use of the CO_2 laser heater allows to concentrate the required heater power onto the substrate, which avoids a heating of large, oxygen contaminated areas. This allows the growth of high quality TiN thin films on MgO substrates in pure Ar atmosphere [271][A1]. Another advantage of the CO_2 laser heating system is the lack of serviceable parts inside the growth chamber. Laser, optics and pyrometer are located outside the chamber and are therefore unaffected by deposited material inside the chamber.

The deposition process is started after the desired background gas pressure and substrate temperature is reached. A KrF excimer laser is used to ablate material from the target. The model used at the B-chamber is a Coherent LPX pro 305 with a wavelength of $\lambda = 248 \text{ nm}$ and a pulse duration of $\tau = 25 \text{ ns}$. The

pulse repetition frequency f can be set between 1 and 50 Hz. The maximum pulse energy is 1100 mJ up to 10 Hz and 600 mJ at 50 Hz. Energy stability is 1% and the initial beam dimensions are $30 \times 12 \text{ mm}^2$ with a divergence of maximal $3 \times 1 \text{ rad}$ [295]. Usually, pulse energies of 500 or 600 mJ are used. The dimension of the two interchangeable apertures, located at the outer enclosure of the laser, are 15×4 or $20 \times 8 \text{ mm}^2$. Since the laser is used to run three different PLD-chambers, the laser pulses are deflected at a multilayer mirror in order to guide them into the desired chamber.

An uncoated UV fused silica lens with a focal length of 300 mm is used to focus the laser beam onto the target surface. The lens is moveable in order to change the focus in respect to the target surface and therefore the energy density at the surface. Distance between target and lens is $21 \text{ cm} + L$ ($L(\text{cm})$ is defined by a scale on the rail, the lens is mounted on). The focused beam enters the vacuum chamber through a uncoated UV fused silica window. UV fused silica is used in order to minimize absorption losses. Since the window gets coated during a growth process, causing a decrease of laser energy at the target, it gets cleaned after every process by mechanical polishing. After passing the entrance window, the laser hits the target, ablates material and forms the plasma.

Up to three targets can be mounted on a rotatable plate, the target carousel. This allows an easy change between different materials during the process without opening the chamber. The desired target is simply rotated into the optical path of the excimer laser. During deposition, the targets are rotated and moved up and down in the laser focus in order to obtain a uniform ablation of the target surface. The target movement is driven by two stepper motors. PLD growth of thin films in the B-Chamber is in "on axis" geometry. This means, that the surface normal of the target is parallel to the surface normal of the substrate. In case of the B-chamber, the substrate is located exactly face to face with the target in order to achieve a homogenous layer growth at the whole substrate surface ($10 \times 10 \text{ mm}^2$). This is important since the substrate can not be rotated. The target to substrate distance is set to 60 mm (Figure 3.6 A,B).

RHEED is used in this work to monitor the growth of thin films and to characterize film surfaces. The utilization of RHEED in PLD has some issues due to the rather high background gas pressure during the process. The mean free path of electrons at high background gas pressures is short, making it difficult to use conventional RHEED systems in PLD applications. Another problem at high pressures is the significant lifetime decrease of the electron emitting filament. Therefore, a special two-stage differential pumping system was developed by Rijnders *et al.* [296] in 1996. In order to preserve a good vacuum at the electron gun, they placed it inside a separated vacuum vessel with its own vacuum pump (first pumping stage). The electron gun is connected to the growth chamber by a tube with a small aperture at the end, pointing towards

the substrate. This tube is also evacuated by its own pump (second pumping stage). The electron beam is guided through the aperture, that is located near the sample surface in order to keep the traveling distance of electrons in the high pressure region as short as possible. Also the RHEED-screen has to be located near the sample in order to minimize the electron path in the high pressure region. This setup allows RHEED measurements up to chamber pressures of 0.5 mbar [296].

A more versatile version of a double-differential pumped RHEED system is provided by STAIB Instruments. This system is equipped with two deflection stages. One between electron source and pipe, and the other at the end of the pipe near the aperture. This setup allows the user to adjust the angle, under which the electron beam leaves the pipe through the aperture, and allows a perfect alignment of the electron beam in respect to the surface of a fixed sample.

The B-chamber is equipped with such a STAIB Instruments Double Differential Pumping RHEED system (Figure 3.6 D). Both stages are evacuated by Varian TV 81-M turbo pumps with TV 81AG-NAC controller. The prevacuum is provided by a Varian SH-110 scroll pump. A blocking valve is integrated into the pipe in order to completely separate the electron gun from the chamber during sample change (ambient pressure inside the chamber). Three adjustment screws allow a coarse alignment of the complete RHEED setup in respect to the sample surface. The fine alignment of the beam due to the two deflection units is done by a remote control. Also beam properties (focus and grid) are adjusted by the remote control. The diffraction pattern at the RHEED-screen is recorded by a CCD-camera and analyzed by the KSA400-software (k-space Associates inc.). This software also allows to record the time dependent intensity of RHEED spots. A acceleration voltage of 30 keV and a beam current of 1.4 A is used.

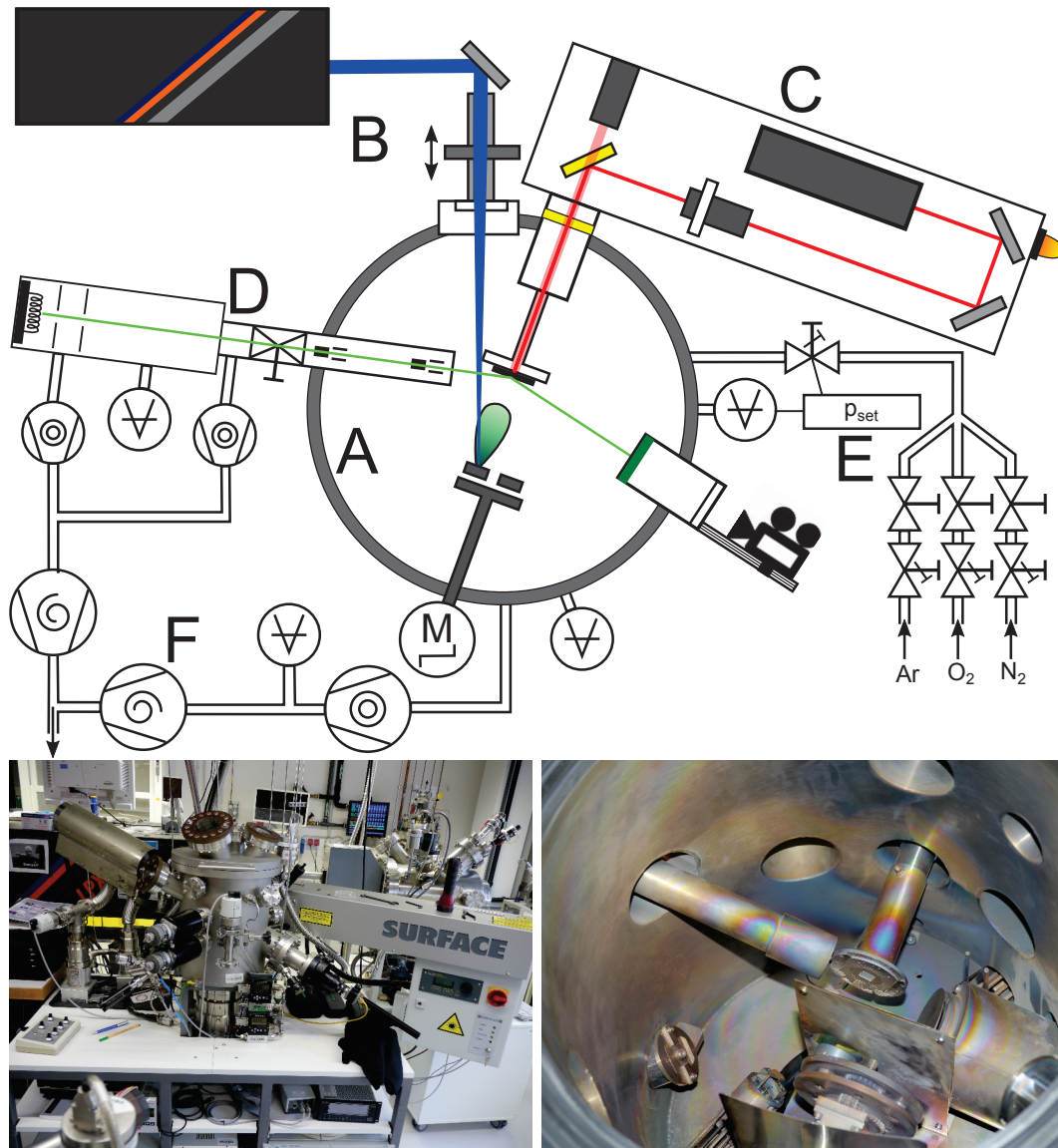
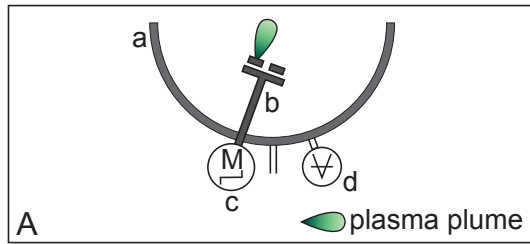
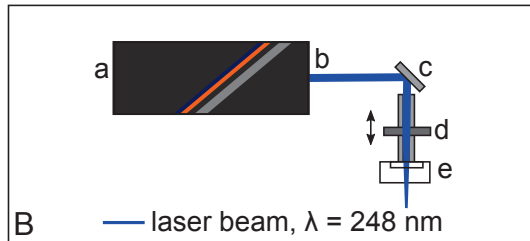


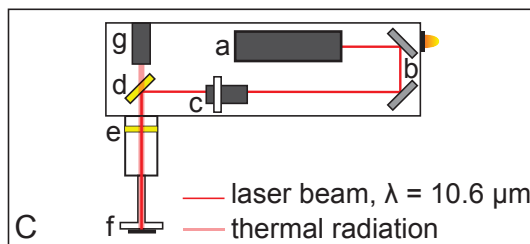
Figure 3.6: Schematic drawing and photographs of the PLD B-chamber. A) Vacuum chamber, B) Excimer laser, C) CO₂-laser heater, D) RHEED system, E) working gas supply and pressure control, F) Vacuum pump system. The single components are listed on the next page.



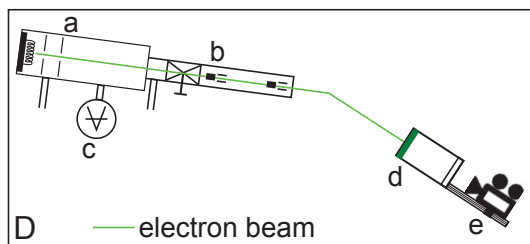
- a) Vacuum vessel
- b) Target carousel
- c) Stepper motors
- d) Vacuum gauge: Pfeiffer PKR 251



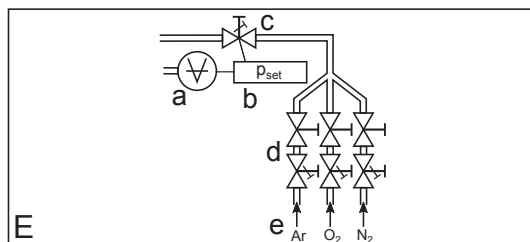
- a) Excimer laser
- b) Aperture
- c) Multi layer mirror
- d) Moveable lens, $f = 30$ cm
- e) Laser entrance window



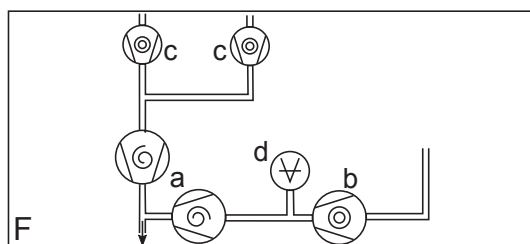
- a) CO₂-laser with pilot laser
- b) Adjustable mirrors
- c) Beam shaper
- d) Beam splitter
- e) ZnSe entrance window
- f) Substrate holder
- g) Pyrometer



- a) Vacuum vessel including filament, acceleration and focus unit
- b) Pipe including blocking valve and deflection units
- c) Vacuum gauge: Pfeiffer PKR 251
- d) Fluorescent screen
- e) CCD camera



- a) Vacuum gauge: MKS Type 627B
- b) Vacuum controller: MKS Type 146
- c) MKS 248A Flow Control Valve
- d) Pressure regulator and blocking valves
- e) Gas supply (Ar, O₂, N₂)



- a) Primary vacuum: scroll pump Varian SH-110
- b) High vacuum: turbo pump Varian TV 551 Navigator
- c) High vacuum: turbo pump Varian TV 81-M
- d) Vacuum gauge: MKS Type 722A

3.2 X-ray diffraction

X-ray diffraction was used to characterize the crystalline structure of the PLD-grown thin films. The investigated sample is illuminated by X-rays (Copper anode, Cu $K_{\alpha 1}$: $\lambda = 1.5406 \text{ \AA}$) under an angle Ω (see Figure 3.7 b). The X-rays are scattered at the three-dimensional lattice of the crystalline film and substrate. Constructive interference, and therefore intensity at the detector, occurs if the Laue condition is fulfilled. The Laue condition states, that the change in the wave vector of the X-ray beam must be exactly one reciprocal lattice vector \vec{G}_{hkl} of the crystalline lattice.

$$\Delta \vec{k} = \vec{k}_{\text{out}} - \vec{k}_{\text{in}} = \vec{G}_{hkl} \quad (3.11)$$

The reciprocal lattice vector \vec{G}_{hkl} is given by

$$\vec{G} = h \cdot \vec{a}_1^* + k \cdot \vec{a}_2^* + l \cdot \vec{a}_3^*, \quad h, k, l \in \mathbb{N} \quad (3.12)$$

with \vec{a}_i^* the basis vectors of the reciprocal lattice. The reciprocal lattice vector \vec{G}_{hkl} is parallel to the normal vector of the corresponding lattice plane with Miller indices (hkl) in real space, and his length is defined by the plane spacing d_{hkl} . It is

$$d_{hkl} = \frac{2\pi}{|\vec{G}_{hkl}|}. \quad (3.13)$$

A geometric interpretation of the Laue condition is the Ewald sphere (see Figure 3.8 a) [297].

Considerations regarding the path difference of X-rays, diffracted at two different lattice planes, yield the well known Bragg equation (Figure 3.7 a)

$$2d_{hkl} \sin \theta = n\lambda \quad (3.14)$$

with $n \in \mathbb{N}$ the diffraction order and θ the angle between crystallographic plane and incident X-ray (Figure 3.7 a). Bragg and Laue condition are equivalent and can be transformed into each other. The geometry of the Laue condition yields

$$\sin \theta = \frac{n|\vec{G}_{hkl}|}{2|\vec{k}|}. \quad (3.15)$$

With

$$|\vec{k}| = \frac{2\pi}{\lambda} \quad \text{and} \quad |\vec{G}_{hkl}| = \frac{2\pi}{d_{hkl}} \quad (3.16)$$

one gets

$$\sin \theta = \frac{n|\vec{G}_{hkl}|}{2|\vec{k}|} = \frac{n\lambda 2\pi}{4\pi d_{hkl}} = \frac{n\lambda}{2d_{hkl}} \quad (3.17)$$

which is exactly the Bragg equation (Equation (3.14)).

The Bragg condition (and then also the Laue condition) is fulfilled and con-

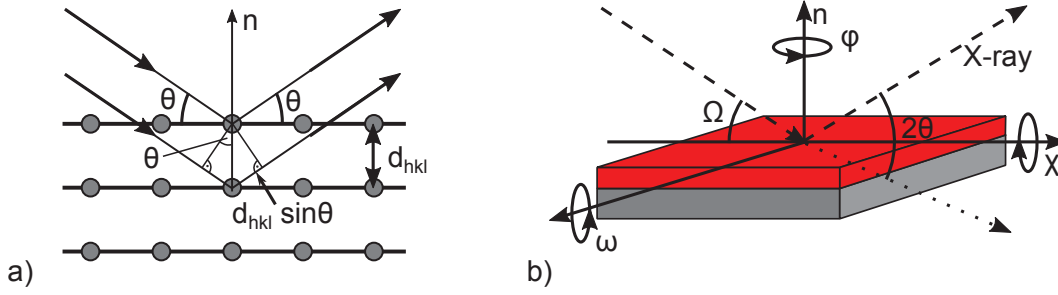


Figure 3.7: a) Geometry describing the Bragg condition. b) Euler angles ω , θ , χ and ϕ , used to access the reciprocal lattice points. Ω is the angle between surface and incident beam.

structive interference, as well as intensity at the detector occurs, when Equation (3.14) is valid and the normal vector of the lattice plane \vec{n} is the angle bisector between incident and diffracted beam, and also part of the diffraction plane (the plane spanned by \vec{k}_{in} and \vec{k}_{out}).

Below, we will assume a fixed X-ray source and a moveable detector. The rotation angle of the sample is ω , and the angle between source and detector is 2θ (Figure 3.7 b). In order to measure a 2θ - ω -scan, the detector (2θ) is rotated with twice the angular speed than the sample (ω). In a symmetric scan, crystal planes parallel to the sample surface are measured. In order to meet the second Bragg condition (the surface normal \vec{n}_{hkl} is angle bisector between incident and diffracted beam and part of the diffraction plane), it is $\omega = \frac{2\theta}{2}$ and $\Omega = \theta$. In order to measure crystal planes, that are not parallel to the sample surface, an asymmetric scan is carried out. Here, the second Bragg condition is fulfilled either by an offset in ω (ω_{off}) or a rotation in χ . Since asymmetric reflexes only appear at $m \in \mathbb{N}$ φ -angles, a φ -scan at fixed 2θ , ω and χ (which should be approximately known for the desired peak) is carried out in order to find the peak position. The number m of peaks and their angular spacing depends on the symmetry of the crystal. For example, a (110) peak in a (100)-oriented, cubic film appears four times with an angular spacing of 90° . The ω -offset ω_{off} is 45° , which is usually not possible to approach ($\omega = \frac{2\theta}{2} + \omega_{off}$ is usually too large). Therefore, the sample is tilted by 45° in χ and a usual "symmetric" scan (skew or pseudo symmetric scan, $\omega = \frac{2\theta}{2}$) is carried out. Different information about the sample can be derived by different measurement modes.

2θ - ω -scan

A 2θ - ω -scan is carried out by rotating the detector twice as fast as the sample. The location of a peak in 2θ is determined by the lattice plane spacing d_{hkl} due to the Bragg equation (Equation (3.14)). Therefore, 2θ - ω -scans are used

to measure the lattice plane spacing d_{hkl} . From d_{hkl} , the lattice constants can be derived. In case of a cubic lattice, it is

$$a = d_{hkl} \cdot \sqrt{h^2 + k^2 + l^2} \quad (3.18)$$

Since the peak position depends on d_{hkl} , small variations Δd_{hkl} lead to a broadening of the corresponding peak. The variations in the lattice spacing are caused by strain or a composition gradient inside the sample. The full width at half maximum (FWHM, $\Delta(2\theta)$) of 2θ - ω -peaks is therefore a quantity to describe the quality of a thin film [297].

Symmetric peaks are also broadened by a finite sample thickness due to a small coherence length. This is described by the Scherrer equation [298].

$$d = \frac{0.9\lambda}{\Delta(2\theta) \cdot \cos \theta} \quad (3.19)$$

Due to the different mechanisms causing a peak broadening, it is difficult to determine the layer thickness from the FWHM of a 2θ - ω -peak.

Another feature appearing in 2θ - ω -scans are thickness fringes. Thickness fringes are intensity oscillations in θ around a Bragg-peak due to the interference of X-rays reflected at the interface and the surface. The spacing $\Delta\theta$ of the fringes allows a direct measurement of the film thickness [299]

$$d = \frac{\lambda}{2\Delta\theta \cdot \cos \theta}. \quad (3.20)$$

Since the refractive index of X-rays is close to one, this method is independent of the film and substrate material and depends only on geometry [299] (see also Section 3.3).

ω -scan

During an ω -scan, the 2θ -angle is kept constant and the sample is rotated around the axis perpendicular to the beam plane (Figure 3.7 b). Such measurements are used to determine the mosaicity of thin films and substrates. Mosaicity describes the spread of the crystal plane orientations inside a film. The result of a ω -scan is a so called Rocking curve. The full width at half maximum (FWHM) of a Rocking curve is a direct measure of the dislocation density and therefore for the crystalline quality of a thin film [297].

Omega scans are also used to determine the miscut angle of substrates [300]. The miscut γ is the angular deviation between surface and crystallographic surface plane. Four ω -scans are recorded every 90° at $\varphi = 0^\circ, 90^\circ, 180^\circ$ and 270° in order to determine the position α of the maximum. From these four positions, the miscut angle is determined by the calculation of two perpendicular

components

$$\begin{aligned}\gamma^{0,180} &= \left| \alpha^{0,180} - \left(\frac{\alpha^0 + \alpha^{180}}{2} \right) \right| \\ \gamma^{90,270} &= \left| \alpha^{90,270} - \left(\frac{\alpha^{90} + \alpha^{270}}{2} \right) \right|.\end{aligned}\tag{3.21}$$

The correlation between miscut γ and the two perpendicular components is

$$\cos \gamma = \cos \gamma^{0,180} \cdot \cos \gamma^{90,270}.\tag{3.22}$$

For small angles γ , this simplifies to

$$\gamma^2 = \left(\gamma^{0,180} \right)^2 + \left(\gamma^{90,270} \right)^2.\tag{3.23}$$

φ -scan

During a φ -scan, the sample is rotated around its surface normal \vec{n} . A φ -scan is carried out in order to determine the in plane component of the normal vector \vec{n}_{hkl} of an asymmetric crystal plane. As described above, if the angles χ , ω and 2θ are set appropriate to detect a peak, the φ -scan shows m peaks, in dependence on the crystal symmetry and domain orientation. Thus, φ -scans allow to determine the in-plane angle between crystallographic directions of the substrate and the film, and therefore the epitaxial relation.

Reciprocal space map (RSM)

A reciprocal space map (RSM) is a two-dimensional scan of the three-dimensional reciprocal space. The two perpendicular scan directions 2θ - ω and ω are used to map the area around a substrate peak.

The position of a film peak in respect to the corresponding substrate peak provides some information about the epitaxial state of the thin film (see Figure 3.8 a and c) [297]. If the film growth is fully epitaxial (pseudomorph, compressive or tensile strain), the reciprocal lattice points of the film are shifted along q_{\perp} in respect to the substrate point. In case of a relaxed film (no strain, film shows bulk lattice constants), the reciprocal lattice points are aligned radially. The shape of a film peak provides additional information on the crystalline quality of the thin film (see Figure 3.8 b). A broadening parallel to q_{\perp} is due to a finite film thickness. A broadening parallel to q_{\parallel} indicates a lateral granularity due to islands and grain boundaries. A peak broadening along the circle with radius $|\vec{G}_{hkl}|$ (the direction of a ω -scan), is due to mosaicity, and a radial broadening (along the direction of a 2θ - ω -scan) indicates a variation in the lattice constants due to relaxation (strain) or composition changes [297].

The coordinates of the reciprocal space (q_{\parallel} and q_{\perp}) are calculated from the

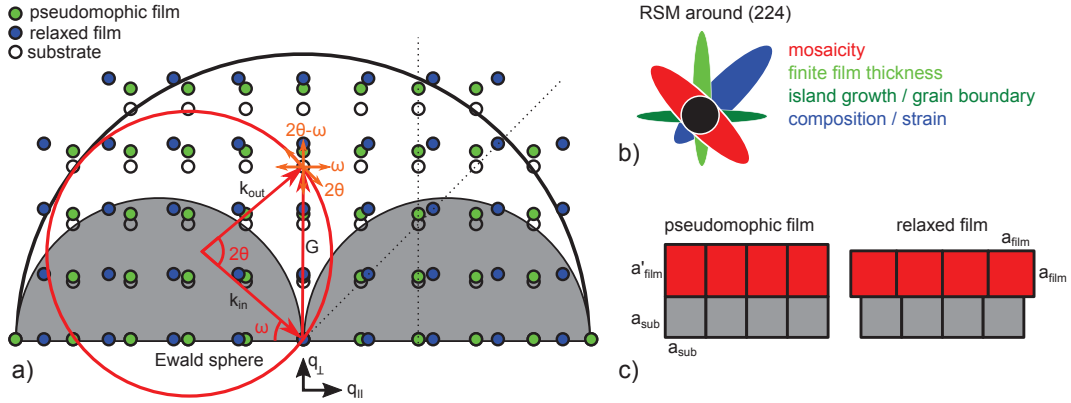


Figure 3.8: a) Reciprocal space map (RSM) of a cubic lattice. Reciprocal lattice points of pseudomorphic films (green) are aligned along q_{\perp} in respect to the substrate points, whereas points of relaxed films are aligned radially (blue). The Ewald sphere with corresponding vectors (\vec{k}_{in} , \vec{k}_{out} , \vec{G}) is marked in red. Orange arrows mark the scan direction of ω , 2θ and $2\theta - \omega$ scans. The outer black sphere marks the maximal addressable region due to the used wavelength ($r = 2|\vec{k}| = \frac{4\pi}{\lambda}$). Gray areas are inaccessible due to geometry (the reflected beam is below the sample surface). b) Peak broadening of a reciprocal lattice spot in a RSM. c) Pseudomorphic and relaxed film growth. After [297].

angles θ and ω the following way

$$q_{\parallel} = R(\cos \omega - \cos(2\theta - \omega)), \quad q_{\perp} = R(\sin \omega + \sin(2\theta - \omega)). \quad (3.24)$$

R is the radius of the Ewald sphere ($|\vec{k}|$) and is set to $R = 1/2$ in this thesis. Therefore, it is $[rlu] = 1$ and a point in the reciprocal space corresponding to crystal planes (hkl) with distance d_{hkl} is spaced $\lambda/2d_{hkl}$ apart from the origin. The two-dimensional plane spanned by q_{\parallel} and q_{\perp} is in principle the diffraction plane and Equation (3.24) is only a coordinate transformation.

In order to plot the measured RSMs appealingly, a program based on the computing environment MatLab was written in the framework of this thesis. Examples are published in [A1,A 3–A5] and [301, 302].

Diffraction systems

Two different setups are used in the framework of this thesis to measure XRD. First is a Philips X'Pert diffractometer with two different diffractometer arms. One arm is located at the line focus site of the X-ray tube and is equipped with a simple wide angle goniometer. Adjustable angles are φ (sample rotation), ω (sample tilting in the beam plane) and 2θ (angle between incident and diffracted beam, see also Figure 3.8 b). This arm provides no monochromator and lines corresponding to $\text{Cu-}K_{\alpha 1}$ and $K_{\alpha 2}$, as well as K_{β} appear in the measurements. Used optics are a crossed slit collimator (divergence of 1°) at the incident beam and a two slit system at the detector site in Bragg-Brentano

geometry. A proportional counter is used as detector. This geometry is used for wide angle 2θ - ω - and φ -scans.

The second diffractometer arm is located at the point focus site of the X-ray tube and is used for high resolution measurements. It is equipped with a 4-bounce monochromator (Barthels monochromator with four Ge (110) crystals, monochromatic radiation $\lambda(\text{Cu } K_{\alpha 1}) = 1.5406 \text{ \AA}$, low divergence of $12''$) and an Eulerian cradle (all four angles are adjustable, θ , ω , φ and χ , see Figure 3.8 b). The detector site provides two options in front of the proportional counter. One is a receiving slit with an acceptance angle between 0.2° and 2° (depends on the used slit), and the other side is a Bonse hart collimator with an acceptance angle of $12''$ (triple axis configuration). This setup is used for high resolution 2θ - ω scans and the determination of the miscut angle of MgO-substrates. 2θ - ω measurements in this work were done with a 0.45 mm receiving slit due to intensity reasons.

The second setup is a Panalytical Pro MRD diffractometer. Here, different optics and detectors can be chosen in order to fit the desired measurement procedure. Reciprocal space maps were measured using the line focus of the X-ray source. The used optics on the incident beam are a divergence slit ($1/8^\circ$), a parabolic mirror, soller slits (0.04°) and a mask (2 mm). At the diffracted beam, only soller slits (0.04°) are positioned before a PIXcel^{3D} detector in receiving slit mode (0.5 mm). The sample stage is a Eulerian cradle with motorized x, y and z positioning system.

3.3 X-ray reflectivity

X-ray reflectivity (XRR) is a non-destructive measurement that allows the determination of thickness and density, as well as surface and interface roughness of thin films. It utilizes the reflection and interference of X-rays at the interfaces of thin films; caused by a change in the electron density.

In XRR, the sample is irradiated by X-rays under a small incident angle $\Omega \leq 5^\circ$. The specular reflection is observed and it is $\Omega = 2\theta/2 = \theta = \omega$, when using a fixed X-ray source (Figure 3.7 b). The reflected intensity is measured in dependence of the incident angle θ . Main features of a reflectivity curve are a abrupt decrease of intensity at the critical angle θ_C and intensity oscillations. The amplitude of the oscillations and the critical angle depend on the density ρ of the thin film, whereas the spacing is defined by the layer thickness. Surface and interface roughness influence the decrease of overall intensity and amplitude, respectively (see Figure 3.9).

The main quantity in the description of reflection phenomena is the refractive index n . The refractive index (without absorption) of a medium for X-rays is defined as

$$n = 1 - \delta. \quad (3.25)$$

Since the interaction of X-rays with matter is rather weak, n is only slightly smaller than one (δ is in the range of 10^{-5} to 10^{-6}) [303]. The value of δ is given by [304]

$$\delta = \frac{e^2 \lambda^2}{2\pi m c^2} N_A \frac{\rho_m (Z + f')}{m_A} = \frac{e^2 \lambda^2}{2\pi m c^2} N_A \rho_e \quad (3.26)$$

Here, Z is the atomic number, m_A is the atomic mass and f' is the real part of the anomalous scattering factor. All these values are average values, determined by the film composition. Further, N_A is the Avogadro number, λ the X-ray wavelength, e the electron charge, m the electron mass and c the speed of light. ρ_m is the mass density while the electron density ρ_e is given by

$$\rho_e = \frac{Z}{m_A} \rho_m. \quad (3.27)$$

The conversion from ρ_m to ρ_e is possible due to $f' \ll Z$ [304]. Therefore, the refractive index can be written as

$$n = 1 - \delta = 1 - A \cdot \rho_m = 1 - A' \cdot \rho_e \quad (3.28)$$

and depends directly on the electron density (ρ_e), from which the mass density (ρ_m) of the film can be calculated. An error source in the determination of the mass density by fitting a simulated curve to a measured one is the composition of the thin film, which determines the average value of Z and m_A .

The principle of XRR and the determination of film properties will be pointed out on the example of a single layer on top of a substrate (see Figure 3.9).

Thin film density

Since the refractive index of the film n ($n = 1 - \delta < 1$) is smaller than the refractive index of air ($n_{\text{air}} = 1$), total reflection occurs at the surface for incident angles below a critical angle θ_C ($\theta < \theta_C$). When θ exceeds θ_C , the X-rays enter the thin film and the total reflected intensity decreases. Snell's law, together with small angle approximations, results in [297]

$$\begin{aligned} n = 1 - \delta = \cos \theta_C &\approx 1 - \frac{\theta_C^2}{2} \\ \Rightarrow \theta_C &\approx \sqrt{2\delta} \end{aligned} \quad (3.29)$$

Due to the density dependence of δ (Equation (3.26) and (3.28)), the critical angle θ_C depends on the density of the thin film. It is

$$\theta_C \propto \sqrt{\rho}. \quad (3.30)$$

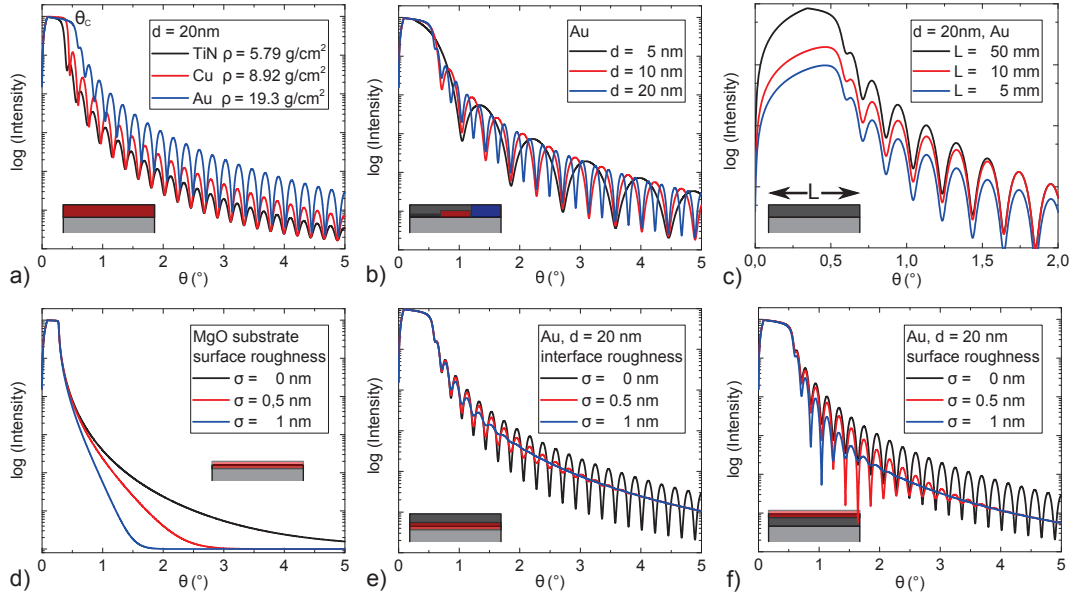


Figure 3.9: Simulated X-ray reflectivity curves of different thin films on top of a MgO substrate ($\rho = 3.58 \text{ g/cm}^3$) for different a) film densities, b) film thicknesses, c) sample lengths parallel to the X-ray beam L , d) surface roughness of the blank substrate, e) roughness of the substrate-film interface and f) surface roughness of the thin film. Simulated by X'pert Reflectivity (Version 1.3a)

Therefore, the film density can be calculated from the critical angle derived from reflectivity measurements by the abrupt decrease of intensity (see Figure 3.9 a). Above the critical angle θ_C ($\theta > \theta_C$), the reflectivity decreases quickly with [304]

$$R \approx \left(\frac{\theta_C}{2\theta} \right)^4. \quad (3.31)$$

The quick decrease of intensity with increasing incident angle θ is clearly visible in the simulated reflectivity curve of a perfectly flat substrate (Figure 3.9 d, black curve with no roughness, $\sigma = 0$).

The refractive index n depends on the film density, and the specular reflectivity at an interface on the difference Δn between film and substrate (Fresnel equations). Therefore, the amplitude of the intensity oscillations, caused by the interference between beams, reflected at the surface and the interface between film and substrate, depends on the density difference $\Delta\rho$ between film and substrate [303]. This correlation is pointed out in Figure 3.9 a. The amplitude of intensity oscillations increases with increasing density difference $\Delta\rho$. Thus, the amplitude of intensity oscillations can be used to determine the layer density by fitting simulated to measured reflectivity curves.

Thin film thickness

Since the difference in the refractive index is small (10^{-6}), the optical path length of X-rays is not affected by the layer material. Therefore, the path difference between the beams reflected at the surface and the interface at a fixed angle θ depends only on the film thickness d . The change in the path difference with increasing incident angle θ causes oscillations in the reflected intensity due to interference. The period of this oscillations depends only on X-ray wavelength and film thickness, allowing a precise determination of the film thickness without being influenced by errors in the determination of the layers X-ray optical properties.

The angular position of the m^{th} ($m \in \mathbb{N}$) interference maxima $\theta_{\text{max}}(m)$ and minima $\theta_{\text{min}}(m)$ is given by

$$\theta_{\text{max}}(m) = \sqrt{\left(\frac{(m + \frac{1}{2})\lambda}{2d}\right)^2 + \theta_{\text{C}}^2} \quad \text{and} \quad \theta_{\text{min}}(m) = \sqrt{\left(\frac{m\lambda}{2d}\right)^2 + \theta_{\text{C}}^2} \quad (3.32)$$

with d the layer thickness, λ the X-ray wavelength and θ_{C} the critical angle [305]. These formulas are valid for a layer density larger than the substrate density. In case of a lower film density, the formulas are exchanged due to the phase shift of $\lambda/2$, caused by the reflection at a denser surface. Plotting $\theta_{\text{max}}^2(m)$ over m^2 (or $(m + 1/2)^2$, respectively) yields a straight line with a slope of $(\lambda/2d)^2$ and an intercept of θ_{C}^2 . This allows a simple and accurate determination of the thickness of a thin film as well as the critical angle. The dependence of the oscillation period (and therefore the slope in the $\theta_{\text{max}}^2(m^2)$ -plot) on the film thickness is pointed out in Figure 3.9 b.

Computer software, like the used X'Pert Reflectivity, allows a fast and exact determination of the layer thickness also by Fourier analysis of the reflectivity curves [305].

Surface and interface roughness

The roughness of a surface, investigated by XRR, can be divided in two types: the macroscopic and the microscopic roughness. Macroscopic roughness or surface waviness (roughness period is large compared to the X-ray wavelength) is described by long waves at the surface. The result of this waves is a local variation of the glancing angle at the film surface. This broadens the specular beam and results in a decreased resolution.

The more interesting roughness in case of XRR is the microscopic roughness. Here, the roughness period is in the order of the X-ray wavelength and results in a diffuse scattering of X-rays in dependence of the incidence angle θ . This leads to a decrease in the reflectivity of the specular beam at the interface.

The microscopic roughness is described by the RMS-roughness σ of the interface (see Section 3.4). The calculation of the reflectivity R at a microscopically

rough surface with RMS-roughness σ yields [304, 306, 307]

$$R = R_F \cdot \exp(-\sigma^2 k_z^2) = R_F \cdot \exp\left(-\sigma^2 \left(\frac{4\pi}{\lambda}\right)^2 \sin^2 \theta\right). \quad (3.33)$$

Here, $k_z = (4\pi/\lambda) \sin \theta$ is the scattering vector and R_F is the ideal surface reflectivity derived by the Fresnel equations.

One can clearly see from this equation, that a microscopic roughness decreases the reflectivity at the surface. The reflectivity drops exponentially with $\sin^2 \theta \approx \theta^2$. The effect of surface roughness is shown in Figure 3.9 d on the example of an uncoated substrate surface.

In case of a thin film on top of the substrate, the interface roughness (between substrate and film) causes a fast decrease of the oscillation amplitude (Figure 3.9 e). This is due to the decreasing amount of X-rays reflected at the interface, contributing to the interference. Figure 3.9 f shows the influence of the film surface roughness on the reflectivity curves. The impact of surface and interface roughness on the reflectivity curves can be used to derive the value of σ by fitting simulated to measured curves.

For simulation and modeling of more than one layer, the considerations made on a single layer are expanded to multiple layer systems. Also absorption is taken into account in order to describe the reflected intensities. Simulation of XRR-intensities and fits to measured curves in this work were done by the program X'Pert reflectivity V.1.3a, provided by PANalytical B.V., Almelo, The Netherlands. The program allows to determine the thin film properties thickness d , density ρ and roughness σ of multilayer systems by fitting simulated curves to measured reflectivity curves. It uses the Parratt-formalism to describe the multilayer systems [308].

The interpretation of X-ray reflectivity curves allows a non-destructive measurement of the film properties d , ρ and σ . Also the determination of the interface roughness in multilayer systems, grown in one step (buried surfaces), is possible without destroying the sample. This makes XRR a versatile tool for the characterization in between preparation steps of electric components.

In the framework of this theses, XRR measurements were done on the Panalytical Pro MRD diffractometer mentioned above. This modular system allows the use of different optics and detectors. The setup used for XRR-measurements is shown in Figure 3.10. This setup allows to measure thin films with a thickness up to 100 nm. Thicker samples (up to 300 nm) can be investigated using a Barthels monochromator in the incident beam path. The use of the monochromator drastically reduces the intensity, and therefore increases the measurement time.

Figure 3.9 c shows the influence of the sample length in parallel to the incident beam. The differences arise from the footprint of the X-ray beam at small incident angles θ . The footprint is $l/\sin \theta$, with l the beam width at the sample at

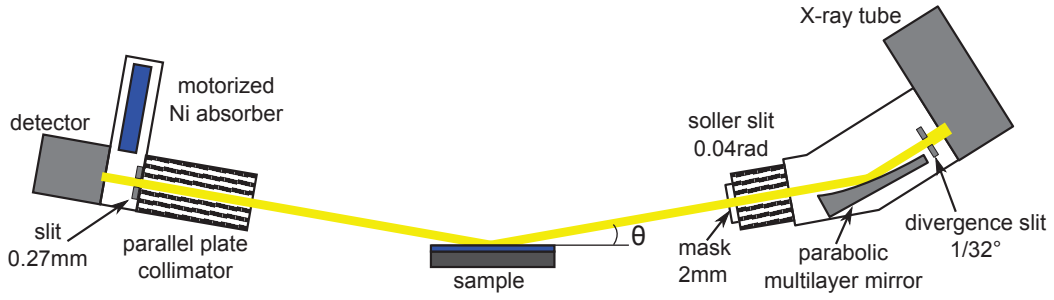


Figure 3.10: Setup of the Panalytical Pro MRD diffractometer used for X-ray reflectivity measurements.

$\theta = 90^\circ$ ($l = 0.3$ mm in our setup without monochromator). At small incident angles θ , the footprint is larger than a small sample and the reflected intensity is low. With increasing angle, the footprint gets smaller and the reflected intensity of a small sample approaches the values of a large one (see Figure 3.9 c). Therefore, a certain minimal sample size is desired for XRR-investigations.

Not all samples are measurable in X-ray reflectivity. Based on the considerations above, there are some demands on sample properties:

- the thin film thickness should be less than 100 nm (300 nm with monochromator, maximum thickness depends on the resolution of the setup)
- the sample should be flat and lateral homogenous
- the RMS-roughness σ should be small ($\sigma < 3$ nm)
- the density contrast should be sufficient to observe oscillations
- the sample length in beam direction should be larger than 5 mm

The measured samples must be aligned perfectly in respect to the incident beam. This is achieved by an automated alignment routine before every measurement.

3.4 Atomic force microscopy

Atomic force microscopy (AFM) is used to measure the surface morphology of substrates and thin films. Measurements in the framework of this thesis were done with an atomic force microscope XE 150 supplied by Park Systems [309]. Nanosensors PPP-NCHR cantilever (non contact) were used. The images were processed by the open source software Gwyddion [310].

Figure 3.11 a) shows a schematic of the AFM-setup. A small silicon tip (typical tip radius is 10 nm), placed at the front of a tiny cantilever (dimensions are in the range of $125 \times 30 \times 4 \mu\text{m}^3$), is guided over the surface of the sample at a small distance (between contact and several nm, depends on the used measurement mode). The interaction between tip and sample surface is used to measure

the morphology of the surface. Main interactions are the the attracting Van-der-Waals force and the electrostatic (Pauli) repulsion between atoms at the surface and the tip (Figure 3.11 b shows the resulting potential). The force acting on the cantilever leads to a deflection (contact mode) or a change in the dynamic behavior of the cantilever (tapping or non-contact mode). Both are measured by a laser beam, that is reflected at the backside of the cantilever and detected at a position sensitive photo detector (PSPD). The height of the cantilever is set by the z-stage, moved by piezo elements that allow an exact height positioning by applying a voltage. The topographic image of the sample surface is recorded by scanning the surface with the tip. Therefore, the sample is moved below the tip by the x-y-stage. The x-y-stage is equipped with piezo elements, allowing an exact movement of the stage by applying a voltage, and strain gauges to determine the exact travel. A picture consists of line scans (e.g. in x-direction) shifted in the perpendicular direction (e.g. y-direction). Since the data evaluation is digital, a picture consists of $M \times N$ pixel with an assigned height value z .

A key figure in order to describe a surface is the root-mean-square roughness (RMS-roughness or σ). It is defined as

$$\sigma = \sqrt{\frac{1}{MN} \sum_{m=1}^M \sum_{n=1}^N (z(x_m, y_n) - \langle z \rangle)^2} \quad (3.34)$$

with $z(x_m, y_n)$ the height at position (m,n) and $\langle z \rangle$ the mean value.

In principle, there are three operation modes in atomic force microscopy: contact, intermittent (or tapping) and non-contact.

Contact mode

In contact mode, the tip is in soft contact with the sample surface. The interaction force is repulsive at small distances between surface and tip due to electrostatic repulsion (green part in Figure 3.11 b). Therefore, the cantilever is bent upwards when the tip approaches the sample surface. The deflection is detected at the PSPD due to the position of the reflected laser beam. As the tip moves across the surface, small changes in the surface morphology change the deflection of the cantilever. This change is detected at the PSPD. There are two operation modes in contact AFM. One is the constant height mode. In this mode, the z-position of the cantilever is kept constant (no movement of the z-stage) and the detected cantilever deflection is directly used to calculate the height differences. In the second mode, called constant force mode, the deflection, and therefore the distance between cantilever fixing point and surface, is kept constant. A feedback loop controls the z-stage and moves the cantilever up or down, in order to keep the deflection constant. The height difference is the travel distance of the z-stage, calculated from the voltage at the piezo element, that is needed to keep the deflection constant.

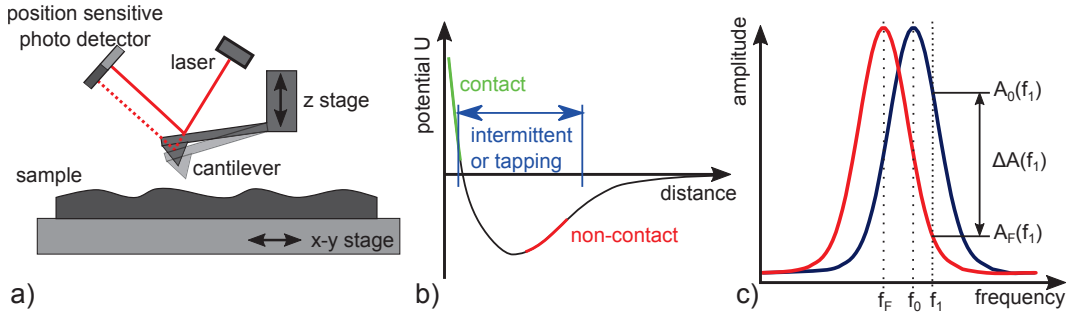


Figure 3.11: a) Schematic of the AFM setup. b) Potential U in dependence of distance, describing the interactions between tip and sample surface. c) Resonance curve of the cantilever and the shift due to the interaction with the sample in non-contact mode.

Non-contact mode

The non-contact mode works at distances, where attractive dipole-dipole interactions (Van-der-Waals) are dominant (red part in Figure 3.11 b). Since these interactions are too weak in order to directly detect a deflection of the cantilever due to a change of the acting forces caused by a distance change, an indirect observation method is used. In non-contact AFM, the change of the resonance frequency of the cantilever due to the acting forces is utilized to keep the tip-sample distance constant. A bimorph is used to mechanically vibrate (frequency f_1) the cantilever near its intrinsic resonance frequency f_0 . The amplitude is detected by the PSPD. The change of the attractive force with changing distance between tip and surface causes a shift in the effective spring constant k_{eff} of the vibrating cantilever. It is

$$k_{\text{eff}} = k_0 - \frac{\partial F}{\partial x} = k_0 - \frac{\partial^2 U}{\partial x^2} < k_0 \quad (3.35)$$

with k_0 the intrinsic spring constant, $F = \partial U / \partial x$ the attractive force between surface and tip and U the van-der-Waals potential (Figure 3.11 b). The resonance frequency of the cantilever is given by

$$f_{\text{res}} = \sqrt{\frac{k_{\text{eff}}}{m^*}} \quad (3.36)$$

with m^* the effective cantilever mass. Since the force gradient $\partial F / \partial x$ is positive, k_{eff} is smaller than k_0 . Thus, the resonance shifts to smaller frequencies when the cantilever approaches the surface. The shift of the resonance frequency causes a shift of the whole resonance curve. This results in a change of the amplitude at the fixed measurement frequency f_1 when changing the tip to sample distance (see Figure 3.11 c). The excitation frequency f_1 is chosen that way, that the resonance curve shows a steep slope at $f = f_1 > f_0$, resulting in a huge amplitude change $\Delta A(f_1)$ with changing distance. The amplitude

decreases with decreasing tip to sample distance and increases with increasing distance.

The non-contact mode utilizes the principle of the constant force mode and a feedback loop controls the z-stage in order to keep the amplitude of the cantilever, and therefore the tip to sample distance, constant. A decreasing amplitude due to a bump (smaller tip to sample distance) at the surface is compensated by retracting the cantilever. Increases the amplitude due to a hole (larger tip to sample distance), the cantilever is lowered towards the surface. The resulting position of the z-stage gives the corresponding height values.

Advantages of non-contact AFM compared to contact mode are a minimization of tip wear and unexpected sample surface manipulation due to the scratching tip.

Intermittent or tapping mode

The intermittent or tapping mode, that is often also referred to as dynamic force microscopy (DFM), is rather similar to the non-contact mode. During the measurement, the tip oscillates at its resonance frequency and the tip to sample distance is regulated by the feedback loop, keeping the oscillation amplitude constant. The difference to the non-contact mode is, that the tip to sample distance and the amplitude are adjusted the way that the tip touches the surface with every oscillation. During the scan, the oscillating tip alternately contacts the surface and lifts off again. The high oscillation energy prevents the tip from sticking to the surface due to meniscus forces caused by e.g. moisture.

The feedback loop, controlling the z-stage in tapping mode, is the same as in non-contact mode. A decrease in amplitude causes the z-stage to retract the tip from the surface. In contrast, the z-stage lowers the cantilever in case of an increasing amplitude.

This is used to measure the topography by tapping mode. Initially, the cantilever oscillates in free space with a excitation frequency $f_1 < f_0$. During the approach to the sample surface, the attractive Van-der-Waals force shifts the resonance frequency to lower values. The amplitude at f_1 increases. This causes the feedback loop to lower the cantilever further until the amplitude $A(f_1)$ gets lowered due to the tapping interaction between tip and surface. At this point, $f_1 = f_{\text{res}}$ and a change in amplitude is mainly caused by the tapping interaction between tip and surface. This interaction acts as damping, decreasing the quality factor Q of the oscillating system. This results in a decrease of the cantilever amplitude ($A = Q \cdot A_0$) with decreasing distance between tip and sample. Therefore, the feedback loop drives the z-stage to retract the cantilever from a bump and and shifts it towards the surface in case of a hole. The position of the z-stage, needed to keep the amplitude constant, is directly the height value of the measured surface point.

Advantages of the tapping mode are a reduced damage at the sample surface compared to contact AFM since the tip is not dragged, but skips across the

sample surface, as well as a reduced chance of tip capture by meniscus forces caused by moisture, as it is often the case in non-contact AFM. Also the resolution is improved compared to non-contact AFM.

Which method yields the best results depends on the measured sample and has to be chosen by the operator accordingly. AFM-topography images shown in this thesis are measured in non-contact or tapping mode, respectively.

3.5 Magnetic properties of thin films: SQUID magnetometry

A SQUID-magnetometer MPMS-7 (Quantum Design) of the division of Superconductivity and Magnetism of the Faculty of Physics and Earth Sciences of the University of Leipzig was used to measure the magnetic properties of $\text{Zn}_x\text{Fe}_{3-x}\text{O}_4$ and Co thin films. Measurements were done by Dipl.-Krist. Annette Setzer.

The MPMS-7 works with a second order gradiometer superconducting detection coil, placed around the sample space in a liquid helium bath. The magnetic moment of the sample, being moved through the coil, is converted to a current in the coil. A change in the sample position causes a change in the flux within the detection coil. This leads to a change of current through the superconducting circuit due to inductance. The gradiometer coil is connected to the SQUID-input coil. A rf-SQUID unit converts the superconducting current inside the gradiometer coil into a voltage signal. The superconducting current and therefore the output voltage depend on the magnetic moment and the position of the sample. The analysis of the voltage signal allows to determine the magnetic moment of the sample [311]. Detailed information on theory and working principle of a (rf-) SQUID magnetometer can be found in [312, 313]. The MPMS-7 SQUID-magnetometer was used to measure the magnetic hysteresis loops of the thin films ($M(H)$ -curves) at different temperatures. The magnetic field is applied in the sample plane for all measurements. The diamagnetic contribution of the substrate (MgO) was eliminated by linear fitting the data at high fields and subtracting the obtained linear contribution from the whole data set. However, it can not be excluded that this procedure also eliminates a non-zero slope at high fields due to spin canting or anti-phase boundaries. Therefore, a blank MgO-substrate was measured and the obtained slope is compared to the subtracted diamagnetic contributions.

In addition, the temperature dependence of magnetization was measured. Therefore, zero field cooled (ZFC), field cooled (FC) and remanence curves were recorded. In order to obtain a ZFC-curve, the sample is heated to 350 K, demagnetized and then cooled to 5 K without an applied field. Then, the desired constant magnetic field is applied and the sample is heated up. The temperature dependent sample magnetization is recorded between 5 and 350 K

in steps of 5 K. Afterwards, a FC-curve is recorded. Therefore, the measurement of temperature dependent magnetization is repeated whilst cooling the sample in the constant magnetic field. Remanent magnetization is measured in the following heating step without applying a magnetic field. The temperature change rate is 5 K/min.

3.6 Dual beam microscope: SEM, EDX and FIB

A dual beam microscope FEI NanoLab Nova 200 was used in this work for secondary electron microscopy (SEM), energy dispersive X-ray analysis (EDX) and sample surface milling by a focused ion beam (FIB). The system is equipped with a EDAX energy dispersive spectroscopy (EDS) detector for EDX analysis (silicon drift detector).

Secondary electron microscopy (SEM)

Secondary electron microscopy (SEM) is used to image the structure of the MTJ-components and to determine thin-film thicknesses. Both methods require a cross section, prepared by a focused ion beam.

In SEM, the surface is scanned by a focused electron beam (acceleration voltage between 5 and 15 kV) and the resulting secondary electrons (SEs) are detected. The brightness of a pixel, and therefore the contrast, is defined by the amount of SEs emitted from the surface. Secondary electrons are ejected from the K-shell of the sample atoms by inelastic scattering interactions with the beam electrons. Only secondary electrons generated near the sample surface escape from the surface, leading to a high spacial resolution when detecting only SEs produced directly by the incident beam. Incident beam electrons are also backscattered by elastic interaction with the sample atoms. These backscattered electrons (BSEs) leave the sample surface in a large area ($\approx 1 \mu\text{m}^2$) around the focus spot and also eject SEs in this area. These secondary electrons contribute to an increased background signal, reduce the contrast and lower the resolution of SEM.

Backscattered and secondary electrons are distinguished by their kinetic energy. Secondary electrons show energies smaller 50 eV, whereas backscattered ones have high energies in the keV-range.

Secondary electrons are detected by two types of detectors. The Everhart-Thornley Detector (ETD) is located close to the sample. It detects all secondary electrons by attracting them to a charged grid. The small kinetic energy of SEs allows to suck all SEs to the detector grid. Behind the grid, the electrons are accelerated towards a scintillator, where they trigger light flashes that are detected by a photomultiplier. The signal is proportional to

the amount of SEs produced by the focused beam at the surface. Advantages of the ETD are a wide field of view (overview scans for orientation at the sample surface) and a good topography contrast. Due to the fact, that the ETD collects all SEs, it shows a high background signal as well as a reduced resolution.

Both, the background signal and the resolution can be improved by excluding the SEs generated by the BSEs from the detected signal and only measure the amount of SEs directly produced by the incident beam. This is achieved by the use of a second detector geometry. The "through the lens" detector (TLD) is placed above the final electron lens. The SEs are collected by the magnetic field of the final lens and guided through the lens to the detector. This geometry allows to suppress the detection of secondary electrons produced by BSEs, resulting in a high spacial resolution and a low background signal. Images taken by a TLD also show a relatively high material contrast.

Backscattered electrons are ignored by both detector types, since they have a much too high kinetic energy to be attracted towards the lens or the grid. They only may reach the detectors through a direct line of sight.

In order to derive an image of the surface, the detector signal is linked to the lateral position of the electron beam spot while scanning the surface. The detector signal is proportional to the amount of SEs produced at the specific spot. This signal is converted to a brightness value of the related image pixel. The topographic contrast observed in SEM-images is based on the dependence of the amount of produced SEs on the incidence angle α of the electron beam at the surface. The yield σ of SEs is [314]

$$\sigma \propto \frac{1}{\cos \alpha}. \quad (3.37)$$

Therefore, facets with different angles show different brightness in the SEM-picture. The topography contrast is superimposed by a element specific contrast (Z -contrast). This contrast arises from the dependence of the yield of SEs on the atomic number Z of the surface material.

Energy dispersive X-ray spectroscopy (EDX)

Energy dispersive X-ray spectroscopy (EDX) was used to determine the stoichiometry of $\text{Zn}_x\text{Fe}_{3-x}\text{O}_4$ -thin films.

The determination of the elemental composition of a sample by EDX is based on the analysis of the characteristic X-ray radiation, produced by the excitation of the sample atoms with the focused electron beam. The high energy (5 to 15 keV) beam electrons remove electrons from the inner shells of the sample atoms. The resulting vacancies are filled by electrons from outer shells and the transition from a high energy (outer shell) to a low energy state (inner shell) requires the radiation of a X-ray photon in order to balance the energy difference. The energies of the emitted X-ray photons are characteristic for

the transition as well as the element [315]. This allows to determine the type and amount of the different elements contained in the sample by analyzing the X-ray spectra emitted from the sample.

Focused ion beam (FIB)

In a FIB system, a beam of gallium ions, produced by a liquid-metal ion source, is focused on the sample surface in order to mill well defined structures. In this work, the ion beam was used for site specific milling in order to cut the sample surface for cross section analysis of thin films by SEM. The focused ions have a high kinetic energy (usually 30 keV) and sputter the sample surface at the beam focus. Due to the small focus, it is possible to mill well defined structures into the sample surface. In order to get clean and well defined cross sections of the thin films, a protective platinum capping is deposited prior to the ion cutting step. The Pt is deposited from an organometallic precursor, injected to the surface by a gas injection system (GIS). The focused electron or ion beam is used to decompose the compound and the Pt is deposited at the surface (ion induced deposition). After deposition of the protective capping, a wedge shaped trench is milled into the sample surface. Prior to SEM investigation, the cross section is polished, using a reduced ion beam current.

A second application of the ion beam was the preparation of holes in the SiN_x passivation layer allowing to top contact the single MTJ-components.

3.7 Sputter Deposition of metal films

Sputter deposition is a physical vapor deposition (PVD) method use for the growth of thin metal films. It utilizes the sputtering of target atoms by plasma ions.

The sample is placed beneath a metal target in an argon atmosphere inside a vacuum chamber. A high voltage is applied between the sample plate (anode) and the target (cathode) in order to ionize the argon atoms and to form a plasma in front of the target. The applied voltage accelerates the plasma ions towards the target surface, where these ions release neutral atoms from the target surface due to collision (sputtering). The released target atoms condense at the sample surface and form the thin film.

Thin metal films were fabricated by dc-magnetron sputtering. This method uses a high constant voltage applied between anode (sample plate) and target (cathode) in order to ionize the Ar-atoms and accelerate the ions towards the target surface. An additional magnetic field at the target enhances the sputter rate by enhancing the Ar-ionization rate. The argon background pressure was set to 0.02 mbar with a flow rate of 100 sccm. Applied sputtering power is either 30 or 60 W, depending on the deposited metal. The sample is not heated during deposition.

3.8 Photolithography

Photolithography is a method that allows to laterally structure thin films in the micrometer range. The sample gets covered by a photo sensitive resist. Usually, the resist is spin coated on the sample surface and fixed by a heat treatment (soft bake). Afterwards, the resist gets exposed by ultraviolet (UV) light through a mask. The mask is a chromium layer on a glass plate, exactly shaped like the desired structure. Only the areas, not covered by the mask layer, are exposed by the UV-light. A bath in a developer patterns the photoresist. In case of a positive resist, the exposed areas dissolve in the developer. Afterwards, the sample gets dried and once again heat treated (hard bake) in order to harden the resist. The resulting resist mask can be used for sample patterning by etching the underlying film or by lift-off. During etching, the resist protects the covered area, allowing a laterally patterning of the underlying thin film. In the lift-off procedure, a new thin film is deposited on top of the resist. The use of an organic solvent and a ultrasonic cleaner allows to remove the resist from the sample. The newly deposited film remains only at areas, where the resist has been dissolved before. This allows the preparation of laterally patterned thin film structures. Below, the photolithography process, used to fabricate the Ti-mask for Ar-ion etching, which define the MTJ-area and to fabricate the top contact pads is described (see Section 4).

Before the samples are covered by the photoresist, they are cleaned in acetone and afterwards in isopropyl alcohol for one minute each, using a ultrasonic bath. The sample is dry blown by nitrogen and dried on a hot plate at 90°C for 60 s in order to obtain a clean surface. The positive resist AZ1514H (Microchemicals GmbH) is spin coated on the sample surface at 6000 rpm for 25 s, resulting in a resist thickness of approximately 1.5 μm . The resist is soft baked at a hot plate (90°C, 90 s). Mask positioning and exposure (contact) are carried out at a SÜSS MJB3 mask aligner. Exposure time is 10 s. Afterwards, the resist is developed in a NaOH-based developer (AZ 351B, diluted 1:4 with purified water) for 40 s under motion, and then rinsed in purified water for 20 s. Subsequently, the sample is spun dry (6000 rpm, 25 s) and hard baked (90°C, 90 s).

Before the sputter deposition (Section 3.7) of the metal layers (Ti or W/Au), the sample is plasma cleaned (Section 3.9) in order to get rid of remaining resist at the developed areas and to enhance layer adhesion. The lift off step is carried out in acetone, using a ultrasonic bath. The time varies between 1 and 5 min, depending on how fast the resist is detached from the sample surface. Afterwards, the sample is cleaned in isopropyl alcohol for one minute in the ultrasonic bath, dry blown by nitrogen and dried on a hot plate at 90°C for 60 s.

3.9 Plasma Cleaning

An Oxford Instruments PlasmaPro NGP 80 ICP is used to clean the sample surface between photolithography and the sputter deposition of Ti or W/Au. A reactive plasma (O_2 , H_2) is applied to the sample surface in order to reactively remove surface contamination. The PlasmaPro is equipped with a ICP-unit (inductively coupled plasma) and the lower electrode (sample plate) is RF-driven. This setup allows a high plasma density, as well as a independent control of the ion energies at the sample surface. This enhances the cleaning efficiency and reduces the damage at the sample surface. The ion energy depends on the RF power at the table, whereas the plasma density depends on the ICP-power.

Three different process steps with different gas mixtures were used to clean the sample surface. The total gas flow rate is set to 100 sccm in all steps.

- An O_2 /Ar mixture is used to remove organic contamination, like remaining photoresist in developed areas. The O_2 plasma is also used to reduce the amount of incorporated H_2 at the surface of PECVD grown SiN_x films (see Section 3.12), in order to enhance the adhesion strength of the tungsten layer. The gas flow rates are set to 75 sccm Ar and 25 sccm O_2 .
- A H_2 /Ar mixture is used to remove surface oxide (produced in the first cleaning step) from the metal thin films. The gas flow rates are set to 75 sccm Ar and 25 sccm H_2 .
- Pure argon (flow rate of 100 sccm) is used in the last step in order to mechanically clean (sputter) the surface without further chemical reactions.

Other process parameter for all three steps are a gas pressure of 20 mTorr (controlled by the angle of a flap valve), an ICP-power of 150 W and a table (RF) power of 50 W. The cleaning was carried out at a table temperature of 15°C.

3.10 Argon Ion Etching inside a SNMS machine

The secondary neutral mass spectrometry (SNMS) is a method to analyze the elemental composition of thin film samples with a high depth resolution. In SNMS, the sample surface material is gradually ablated by Ar-ions. The sputtered neutral atoms are post ionized by electrons in an Ar-plasma, located before the sample, and analyzed in a quadrupole mass filter system. The obtained signal is the time dependent, mass resolved amount of different atoms ablated from the surface. The obtained ion mass can be assigned to

the corresponding element, allowing a element specific analysis of the sample composition. Since the sputter process subsequently removes the surface and forms a sputter crater, the time scale can be recalculated to a depth scale. Therefore, the measurement of a depth profile of the elemental composition is possible.

In this work, a SNMS machine INA-3 (Leibold-Heraeus, now SPECS GmbH) is used. The machine works in the direct bombardment mode (DBM). In this operation mode, the argon ions, ablating the sample surface, originate from the Ar-plasma located in front of the sample (inductively coupled plasma, ICP). They are accelerated towards the sample surface by a voltage V . Insulating samples can be analyzed by using the optional high frequency mode (HFM). In this mode, the acceleration voltage is an AC-voltage in order to avoid surface charging effects by accelerating Ar-ions as well as electrons from the plasma towards the surface. The sputtered sample atoms are post ionized in the Ar-plasma. An ion optics system, including an immersion lens and a 90° spherical deflector, acting as energy filter, guides the ions into a quadrupole mass filter system. The residual ions are detected by a secondary electron multiplier.

The sputtering process during the SNMS inside the INA-3 is used to fabricate the MTJ-pillars (see Section 4) from the closed thin film stack (argon ion etching). The area of the MTJ-element is defined by a titanium mask, produced by photolithography. The mask protects the underlying thin films, whereas the non-protected areas are ablated. This argon ion etching by the SNMS machine results in well defined MTJ-pillars.

Advantages of using the SNMS system for argon ion etching are a uniform depth of the sputter crater (lateral homogenous ablation) over a large area (diameter of 7 mm, defined by the sample aperture) as well as the possibility to stop the etch process at the desired point. This is important for the fabrication of the MTJ-elements, because the TiN-layer, used as back contact, must remain intact. Therefore, the process is stopped once titanium is detected and the Ti-signal rises (the signal from the Ti-mask is neglectable due to the small covered area). An acceleration voltage of $V = 400$ V is used. The INA-3 SNMS machine was operated by Mrs. Gabriele Ramm.

3.11 Laser scanning microscope

A Keyence VK-X200K laser scanning microscope was used to take optical microscope images as well as topography images of sample surfaces. The microscope optics are equivalent to a usual light microscope. In combination with white light illumination and a CCD camera, classical optical microscope images can be taken. In addition, the laser light reflected from the surface is used to obtain high resolution images and topographic information. The laser is focused by the microscope lens and the light reflected by the sample surface is detected. A confocal laser optic allows to detect only laser light reflected at

the focus of the laser. This means, that the laser focus is at the surface of the sample when the detected intensity is at its maximum.

In order to obtain an image, the laser beam focus subsequently scans different focal planes. The reflected intensity is measured at every pixel and the CCD-camera acquires the RGB data (the visible color) of the respective pixel. The information focal plane height (z-coordinate), reflected intensity and RGB-data are stored for every pixel. After obtaining the data for one focal plane height, the objective is moved one step in z-direction and a new scan is started. If the reflected laser intensity at a specific pixel is larger than in the scan before, the data set of the pixel is overridden by the new one. Is it lower, the old data set remains in the memory. This procedure ensures that only information, obtained while the focus is at the surface, remain in the memory.

From this data set, three types of images can be calculated: The visible color image is derived from the RGB-values measured by the CCD camera. It is similar to a digital optical microscope image. The second type is the laser intensity image. It shows the detected intensity of the laser reflection as gray scale. The contrast is due to the dependence of detected intensity on the facet angle at the surface. These images have a rather high resolution, and the overlay with the color image results in a sharp, colored microscope image. The third type is the height image. It provides the topography of the sample surface. The information from the height image can be used e.g. to derive size, height and shape of features at the sample surface.

3.12 Plasma Enhanced Chemical Vapor Deposition (PECVD)

Plasma Enhanced Chemical Vapor Deposition (PECVD) is used to deposit an insulating SiN_x -layer on top of the etched MTJ pillars. The aim of this insulating layer is to separate the conducting TiN (bottom contact) from the gold pad (top contact, see Section 4). The insulating properties of SiN_x are sufficient to constrain the current to the MTJ.

Using PECVD, the layer is formed by a plasma enhanced chemical reaction between precursor gases. The reactant (precursor) gases are filled in a vacuum chamber, where the sample is placed between two parallel electrodes. The lower electrode is grounded, whereas the top electrode is radio-frequency (rf) driven. The induced rf-field ionizes the reactant gases and forms a plasma between the electrodes. The ionized gases react and form the desired film material, which condensates at the sample surface and forms the thin film. A constant flow rate of reactant gases is applied in order to compensate their consumption during deposition.

Advantages of the PECVD method are the possibility to grow uniform, closed films at comparatively low temperatures as well as a conformal coating of the surface. The deposited material also covers side walls uniformly, allowing an

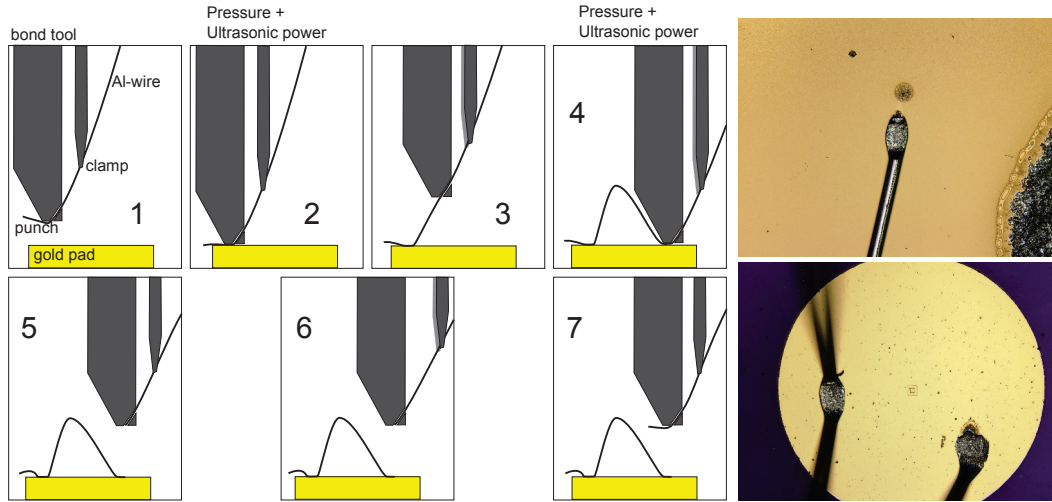


Figure 3.12: Schematic of the working principle of an ultrasonic wedge-wedge wire bonder and optical photographs of bonds.

even insulation also at the edges of a MTJ-pillar. A disadvantage is the incorporation of hydrogen into the SiN_x -layer, leading to a decreased adhesion of subsequent deposited films.

SiN_x layers were deposited in a PECVD system Plasmalab 80 Plus, supplied by Oxford industries. The rf-frequency is 13.56 MHz. Applied rf-power during deposition is 10 W ($20 \frac{\text{mW}}{\text{cm}^2}$). The precursor gases used for the deposition of SiN_x are ammonia (NH_3) and silane (SiH_4). Silane is provided as gas mixture with N_2 (2% SiH_4 in N_2). Flow rate of reactant gases is 28 sccm for NH_3 and 1000 sccm for the SiH_4/N_2 mixture. The injection of the reactant gases is carried out by a "showerhead" gas inlet in the top electrode in order to ensure a homogeneous gas distribution. The gas pressure during deposition is set to 1 Torr ($\approx 1.3 \text{ mbar}$) and regulated by the angle of a flap valve. Substrate temperature during the process is between 80 and 90°C. The achieved growth rate at this settings is approximately $15 \frac{\text{nm}}{\text{min}}$.

The PECVD-system is also used to pretreat the titanium layer on top of the etched MTJ pillars prior to the SiN_x deposition in order to ensure a high adhesion strength of the SiN_x layer (see Section 4). The surface is exposed to a NH_3 plasma in order to remove the oxide layer at the Ti surface and to build a nitride layer. This nitride layer builds Ti-N-Si bonds, enhancing the adhesion strength between Ti and SiN_x . Process parameter for NH_3 plasma treatment are a duration of 60 s, a rf-power of 30 W ($60 \frac{\text{mW}}{\text{cm}^2}$), a chamber pressure of 1 Torr and a NH_3 flow rate of 200 sccm.

3.13 Wire Bonder

A ultrasonic wedge-wedge wire bonder WestBond 5400B is used to contact the single gold pads on top of the finished sample to the contact bridge by aluminum wires (see Section 4). Figure 3.12 shows the working principle of the bonder. An aluminum wire is inserted in a hole inside the bond tool and placed beneath the punch. The wire is held by a clamp. The bond tool gets lowered to the surface of the gold pad and pressure as well as ultrasonic power is applied. Pressure and ultrasonic power lead to the formation of an Al-Au eutectic that forms the bond. The clamp is opened and the bond tool retracted from the pad. This allows the Al-wire to slip through the hole in the bond tool. The tool is placed at the desired spot of the second bond and pressure and ultrasonic power are applied. After completing the second bond, the clamp closes and the tool is retracted. This causes the Al-wire to split at the edge of the bond. Now, the clamp is opened, moved back, closed again and moved forward. This step pushes the Al-wire back into the initial position.

Due to the applied pressure and ultrasonic power, the Au-pad should exhibit a certain thickness in order to protect the layers lying beneath and to ensure a good bond between pad and wire. The thickness of the used gold pads is approximately 800 nm. Used parameter for bonding are a force of 19 g, a ultrasonic power of 400 mW and a pulse duration of 70 ms.

3.14 Electrical Characterization

3.14.1 Resistivity of thin films

Measurements in Van-der-Pauw geometry are used to determine the in-plane resistivity of thin films. The films are contacted at the sample edges by sputtered gold contacts. These contacts are labeled clockwise by A, B, C and D. After Van-der-Pauw [316], the resistivity of a thin film is given by

$$\rho = f \frac{\pi d}{\ln 2} \frac{R_{AB,CD} + R_{BC,AD}}{2} \quad (3.38)$$

with d the film thickness, $f(R_{AB,CD}/R_{BC,AD})$ the correction function (Van-der-Pauw-function), $R_{AB,CD} = U_{CD}/I_{AB}$, $R_{BC,AD} = U_{AD}/I_{BC}$. I_{XY} and U_{XY} ($X, Y = A, B, C, D$) are the applied constant current and the voltage measured between the contacts X and Y, respectively. Therefore, the thin film resistivity can be measured by simply applying a constant current to two neighboring contacts and measure the voltage between the two remaining contacts. The value of ρ is determined as mean value of four measurements (every 90°).

Measurements were done on a self-built Hall-setup. It is equipped with a programmable constant current source Keithley 6221, a Keithley 7001 switch system for changing the contact configuration and a Keithley 2000 multimeter

for voltage detection. Temperature dependent measurements are carried out in a cryostat, cooled by a closed cycle refrigerator system. This system contains of a CTI-cryogenics 8200 compressor and a Model 22 refrigerator cold head. Sample temperature is regulated by counter heating with a resistive heater placed near the sample and controlled by a LakeShore 335 temperature controller. The sample is placed on top of a copper sample holder, thermally connecting it to the refrigerator. The vacuum, used to thermally insulate the cryostat and to get rid of condensates while cooling, is provided by a Pfeiffer Vacuum HiCube 80 eco, equipped with a HiPace 80 turbo pump and a membrane pump MVP 015.

The magnetic field for Hall measurements is produced by a GMW magnet systems Model 5403 electromagnet with a Kepco BOP 25-40 MG current source. The used configuration produces a maximum magnetic field of ≈ 800 mT at the position of the sample. The field is measured by a digital Hall effect teslameter Group3 DTM-133.

3.14.2 I-V measurements at room temperature

Current-voltage (I - V) curves were measured in a Suss MicroTec PA200 wafer prober, connected to an Agilent 4155C semiconductor parameter analyzer. The samples are contacted by tungsten needles placed on top of the gold contact pads. These measurements are performed at room temperature without an applied magnetic field.

3.14.3 TMR measurements: $R(B,T)$, I - $V(B,T)$

In order to measure the magnetotransport properties of the MTJs, a TMR-measurement setup was build in the framework of this thesis. It utilizes the basic components of the Hall-effect setup (cryostat with temperature control and wiring, as well as the magnet with its current source). A source measurement unit (SMU) Keithley Model 2636B is used to measure I - V curves as well as the resistance of the devices in dependence of the applied magnetic field and the temperature. The used setup is schematically shown in Figure 3.13.

During the TMR-measurement, the magnetic field is applied in the sample plane, along the $[010]$ -direction of the MgO substrate (parallel to the sample edges).

In order to measure the TMR, a constant voltage is applied to the magnetic tunnel junctions. To apply a constant voltage instead of a constant current excludes the possibility of shifting the density of states of the magnetic electrodes in respect to each other during the measurement. In case of a constant applied current, the voltage at the MTJ changes by the time the magnetic state changes from the low resistant, parallel state to the high resistant, antiparallel state. The change in voltage shifts the density of states of the magnetic electrodes in respect to each other. This will influence the results, if the density

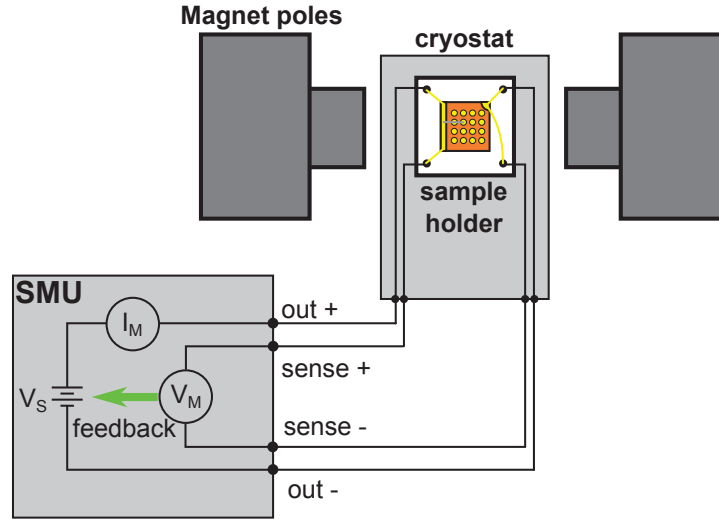


Figure 3.13: Schematic of the source measurement unit (SMU) and the wiring used for TMR-measurements.

of states, and therefore the spin polarization P , are not constant at the Fermi level. Therefore, the constant current source of the Hall setup in combination with the multimeter (in order to determine the applied voltage) is not suitable for TMR-measurements. A source measurement unit (SMU) Keithley Model 2636B is used to apply a constant voltage to the MTJs and to measure the resulting current. The SMU further allows to measure I - V curves.

The SMU is programmed to work in 4-point or remote sense mode (see Figure 3.13). This mode allows a more accurate voltage output compared to local sense mode (2-point mode). The output voltage is forced at the end of the sense leads (connection points of out- and sense-leads) instead of the output terminals of the SMU. This eliminates the errors in the applied voltage due to the lead resistance. In the remote sense mode, the constant voltage is applied by the voltage source (V_S) and monitored by a voltmeter (V_M), providing the actual applied voltage at the end of the sense leads. A feedback loop adjusts the voltage of the source in order to get the desired value at the device under test. The flowing current is measured at the out-leads in series to the voltage source (I_M).

The whole setup is computer controlled and the communication with the devices is by GPIB (General Purpose Interface Bus, IEEE-488). The measurement software is written in MATLAB. The following section describes the measurement routine, used to characterize the magnetic tunnel junction.

First step is to set the magnetic field to the maximal possible value of $\mu_0 H = -800 \text{ mT}$ (-35 A , the parameter set by the program is the coil current), in order to achieve a fully parallel alignment of magnetization between the electrodes of the MTJ. Next step is to set and approach the desired temperature

T . Temperature changes are always carried out in an applied magnetic field of $\mu_0 H = -800$ mT (field cooling conditions). After setting the temperature, an I - V curve is measured in maximum field. This step is optional and can be carried out additionally in any desired field. This gives the opportunity to measure I - V -curves in the parallel and antiparallel state of magnetisation.

In order to measure the TMR at a desired temperature, the magnetic field is changed and a constant voltage V_c is applied to the MTJ. The resulting current flow $I(\mu_0 H, T)$ is measured and the resistance $R(\mu_0 H, T)$ of the MTJ is calculated by $R = V_c / I(\mu_0 H, T)$. The value of the current is determined at a fixed magnetic field over a certain amount of time (survey time is set by the operator, standard is 200 ms and five measurements per point to build the mean value).

During the TMR-measurement, the magnetic field is changed from -800 mT to 800 mT (-35 A to 35 A) and back in small steps. The used resolution is 0.1 A, approximately 2.3 mT.

After finishing the magnetic field loop (back at $\mu_0 H = -800$ mT), the next temperature is approached and another TMR measurement is started.

4 Development of the MTJ-sample layout

In this chapter, the requirements for building magnetic tunnel junctions are discussed. A sample layout was developed in the framework of this thesis in order to meet these requirements. The resulting sample design fulfills the physical requirements, but yields several issues in the manufacturing process. Solutions for these issues are discussed and the resulting evolved sample design is presented.

4.1 First sample layout

This section will give a brief overview on the requirements for MTJ elements and on the sample design resulting from considerations how to match the asked requirements. The resulting first version of the sample layout is shown in Figure 4.1. The sample is designed in the pseudo spin valve geometry (see Page 56). This geometry utilizes the different coercive fields of the two magnetic electrodes in order to achieve parallel and antiparallel alignments of the layer magnetization.

The important layers in a MTJ (or spin valve) are the magnetic bottom electrode, the barrier and the magnetic top electrode (see Page 56). In this work, $\text{Zn}_x\text{Fe}_{3-x}\text{O}_4$ is used as bottom electrode. The barrier is epitaxial MgO and the top electrode is Co. The resulting functional layer stack ($\text{Zn}_x\text{Fe}_{3-x}\text{O}_4$ / MgO / Co) is grown by PLD without breaking the vacuum.

In order to reduce the series resistance of the devices, a highly conductive bottom layer is introduced. Since a successful epitaxial growth of $\text{Zn}_x\text{Fe}_{3-x}\text{O}_4$ on SrTiO_3 -substrates is reported in literature [139, 141], first attempts using conducting, niobium doped SrTiO_3 (STO:Nb) as substrate were made. This attempts failed due to the formation of a Schottky-barrier at the $\text{Zn}_x\text{Fe}_{3-x}\text{O}_4$ / STO:Nb-interface [317, 318]. Therefore, epitaxial TiN was established as conducting bottom layer [46]. The TiN thin films are grown by PLD on (100)-oriented MgO (see Section 5.2).

As discussed on Page 49 ff., the barrier interfaces are essential for the TMR-effect. Therefore, a requirement for the production of working MTJ components are clean barrier interfaces. It is important to avoid contamination due to

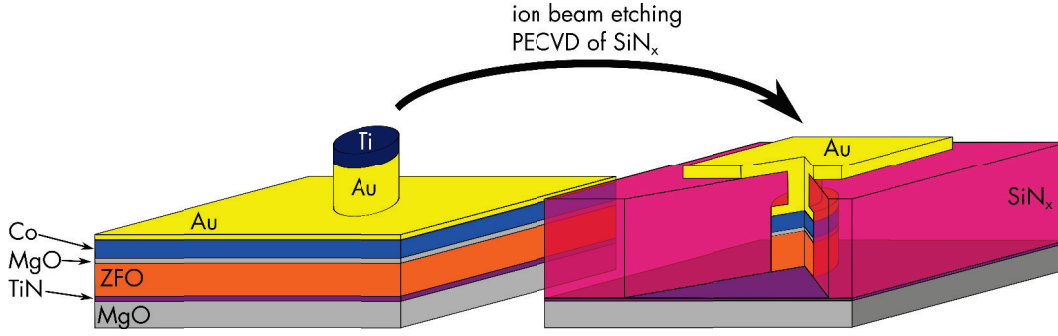


Figure 4.1: First version of the newly developed MTJ-design.

processing steps (photolithography), or simply breaking the vacuum between deposition steps (adsorbates from ambient air). Therefore, the thin film stack $\text{Zn}_x\text{Fe}_{3-x}\text{O}_4/\text{MgO}/\text{Co}$ is grown in one step, without breaking the vacuum. This procedure is possible due to the target carousel at the PLD B-chamber, providing three target places.

Barrier interfaces must be smooth and should not show a large roughness. Problems occurring at rough surfaces are e.g. Néel (or orange peel) coupling between the magnetic layers [283, 284] and the occurrence of voltage spikes, resulting in the formation of pinholes (small metallic conduction paths across the barrier [282]). Also the barrier thickness must be homogenous. Thinner areas carry a over-proportional amount of the tunnel current, leading to the formation of pinholes, too. Therefore, a two dimensional growth of the thin films must be achieved in order to get smooth interfaces and a homogeneous thickness of the thin barrier (only a few nm). To support the two dimensional growth, the MgO-substrates are annealed prior to the deposition of thin films (see Section 5.1). The annealed MgO-substrates show a smooth, terraced surface, providing good conditions for two-dimensional growth. The two dimensional growth of TiN, $\text{Zn}_x\text{Fe}_{3-x}\text{O}_4$ and MgO is verified by RHEED and AFM (Sections 5.2, 5.3 and 5.4).

The Co film is immediately covered by a thin, sputtered gold layer, in order to avoid oxidation.

In order to utilize the effect of TMR, single junctions (MTJs) have to be produced from the thin film stack. The MTJs are fabricated by applying a protective metal mask (small pads, defining the contact area) on top of the layer stack and etch the unprotected areas. The thin films in the unprotected area are removed, except the bottom contact TiN-layer. The result are small pillars with a defined area, connected by the TiN-layer. In order to allow electrical measurements on single MTJs, the junctions are insulated by a SiN_x layer and single MTJs are contacted by an individual top contact pad.

Small Au/Ti-pads, defined by photolithographic lift-off, are produced at the sample surface. These pads protect the underlying films during Ar-ion etching

and define the contact area of the MTJs. Before the deposition of Au/Ti, the sample is plasma cleaned. Ti is used due to its low sputter yield and therefore high resistance against Ar ion etching. The use of Ti as top mask layer reduces the required film thickness by a factor of five, compared to pure Au. The reduced thickness of the film eases the lift-off process and allows the production of well defined pads. The thickness of the Ti layer was chosen such, that the film is completely removed after the etching step and only the Au remains. The required film thickness (or rather the sputter deposition time) is determined by preliminary tests on TiN / $\text{Zn}_x\text{Fe}_{3-x}\text{O}_4$ / MgO / Co / Au-layer stacks and Ti layers. By comparing the sputter times during etching, it is possible to figure out the needed Ti deposition time. This approach is used in order to exclude the possibility of the formation of an insulating titanium oxide layer between the Au-contacting layers. The aim of the Au layer ($\approx 200\text{ nm}$) beneath the Ti is to protect the Co layer from the Ga-ions during the milling of contact holes into the SiN_x layer by FIB.

Argon ion etching is the method of choice to produce the MTJ-pillars due to the complicated wet chemical etching of a layer stack containing Au, Co, MgO and $\text{Zn}_x\text{Fe}_{3-x}\text{O}_4$ ($\text{Zn}_x\text{Fe}_{3-x}\text{O}_4$ is hardly wet chemically etchable). The Ar-ion etching is based on sputtering, and therefore allows to process all types of thin films. Only the etch rate is influenced by the film composition (different sputter rates). The use of the SNMS machine (Section 3.10) has the advantage of a homogenous etch profile over a large area (7 mm in diameter) and the lack of undercutting or lateral etching. This allows the production of well defined pillars from the closed thin film stack. A second advantage is the possibility to monitor the etch process by analyzing the sputtered elements. This gives the opportunity to stop the process exactly at the $\text{Zn}_x\text{Fe}_{3-x}\text{O}_4$ / TiN interface. The MTJ-pillars are passivated by a 300 nm thick SiN_x layer, deposited by PECVD (Section 3.12). The SiN_x layer provides an electrical insulation between the single MTJ-pillars as well as between the bottom contact (TiN-film) and the top Au contact. The flowing current is constrained to the MTJ-pillars by the surrounding SiN_x -matrix. This allows to choose a single MTJ for electrical characterization by contacting the top gold contact of the respective junction. The growth temperature of PECVD- SiN_x is chosen below 100°C in order to avoid interface diffusion at the barrier.

The top contact pads (Au, $750\text{ }\mu\text{m}$ in diameter) are defined by photolithography. In order to electrically contact the top contact pads to the top gold layer of the MTJ-pillar, holes are milled into the SiN_x layer by FIB. Before milling, the resist mask is applied and the sample is covered by a thin, sputtered Au-film in order to avoid charging effects during SEM and FIB-milling. After milling, a second gold layer is sputter deposited in order to form the top contact pad and to contact the MTJ-pillar. Afterwards, the lift-off step is carried out.

The large contact pads with a diameter of $750\text{ }\mu\text{m}$ allow a simple contacting of single MTJ-pillars. First attempts were made by gluing gold wires to the pads

by electrically conductive silver epoxy resin in order to contact the sample to the holder. This procedure has several drawbacks: It is accompanied by a heat treatment of 90°C for 45 min of the whole sample in order to harden the resin. The heating step must be repeated for every contact made. It also is relatively complex and time consuming. In order to avoid this problems, the wire bonder (Section 3.13) is used later on in order to contact the single pads to the sample holder (see Figure 4.3).

4.2 Problems and evolution of the sample design

Some problems occurred by using the simple sample design described above. These problems are an accumulation of gold at the Co / MgO-interface due to diffusion, and the insufficient adhesion between SiN_x and the gold layer on top of the MTJ-pillar, as well as between SiN_x and the top gold contact pad. The occurring problems are discussed in detail in the following section, together with approaches for solutions to them.

Gold diffusion through cobalt

During the Ar-ion etch step, a accumulation of Au at the Co / MgO-interface was observed in the SNMS-spectra (see Figure 4.2 a). The accumulation of Au at the Co / MgO-interface is due to diffusion of gold through the Co layer. The thin Au layer (or the Au/Co alloy) between Co and MgO leads to a decrease or a complete loss of spin polarization at the interface, resulting in a decrease or even loss of TMR. Therefore, gold is not suitable for the desired task of protecting the Co layer from oxidation and providing a pad for top contacting. The use of copper as protecting and contacting layer was figured out to be an appropriate solution. A copper thin film can be easily applied by sputter deposition. It is easily etched by Ar-ions (high sputter yield), is a good conductor and reacts rather slow with atmospheric oxygen (no formation of an insulating oxide layer). The underlying Co film is a good diffusion barrier for Cu [319]. This is confirmed by SNMS spectra, showing a clear interface without any observable diffusion (see Figure 4.2 b). Therefore, a copper layer with a thickness of 300 nm is used instead of the gold layer.

Adhesion of SiN_x on top of gold

Prior to the milling of the contact holes by FIB, the milling depth as well as the positions of the contacts must be obtained in order to set up the script for the AutoFIB-software. The observation of the surface by SEM induces an irradiation of the sample by the electron beam.

During the observation of the SiN_x surface in SEM and the resulting exposure of the surface with electrons, the SiN_x film forms bubbles and is explosively

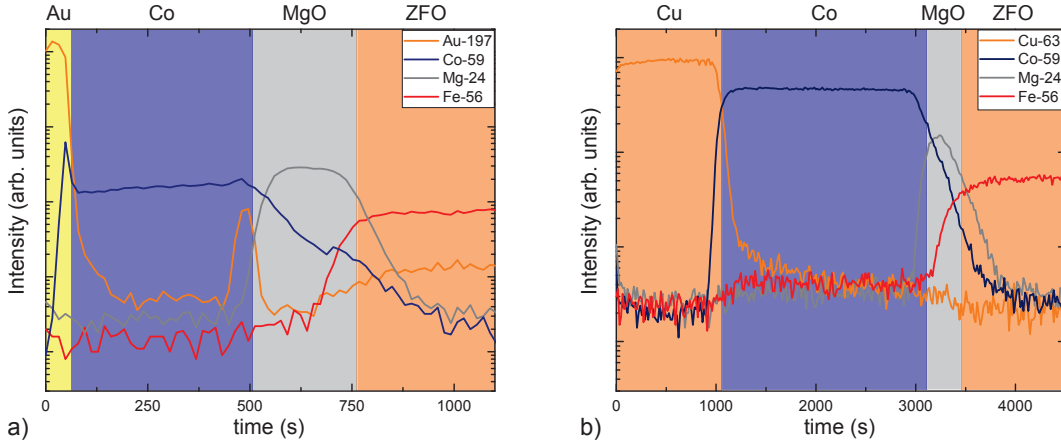


Figure 4.2: SNMS-spectra of thin film stacks of X / Co / MgO / $\text{Zn}_x\text{Fe}_{3-x}\text{O}_4$ / TiN / MgO(substrate) with different cover layers X. a) The cover layer X is Au. A clear accumulation of gold at the Co / MgO-interface is visible. b) The cover layer X is Cu. Clear interfaces without diffusion are observed.

removed from the underlying Au-pad (see Figure 4.3).

Only speculations on the reasons for this effect can be made. The PECVD-grown SiN_x -film contains a large amount of hydrogen, being bond to Si and originating from the precursor gases NH_3 and SiH_4 [320]. Possibly, the electron beam breaks the Si-H bonds and forms H_2 [321]. The forming gas applies a pressure at the interface and removes the SiN_x thin film from the pad. Also catalytic chemical reactions at the gold interface, supported by the electron beam and involving hydrogen, can play a role [322].

In order to avoid the removal of the SiN_x film from the MTJ top contact pad, different metals (Ti, Cu, W, Pt) were tested as contact pads. In addition, the surface is pretreated with an NH_3 -plasma *in-situ* prior to the PECVD deposition of SiN_x in order to clean and chemically passivate the surface by nitridation.

Tests were performed on samples, consisting of the metal pads produced by lift-off on a TiN-layer grown on a MgO substrate. The TiN bottom layer is used as bottom layer in the test samples because TiN is the main surface at the MTJ-samples covered with SiN_x . TiN provides good adhesion for the SiN_x layer and no problems are observed at the TiN / SiN_x interface.

Two samples of every pad metal were produced and one of them pretreated with the NH_3 -plasma. The samples are covered by a 300 nm thick PECVD SiN_x -film.

The areas containing the metal pads were irradiated by the SEM-electron beam for a certain time (≈ 30 s, taking two images) and the number of unaffected pads was counted (out of 20 tested pads on each sample). The best result was obtained for plasma treated Ti-pads.

The possible reason for the good adhesion of SiN_x on NH_3 -plasma treated Ti is depicted in Figure 4.4. The plasma removes the oxide layer at the Ti surface

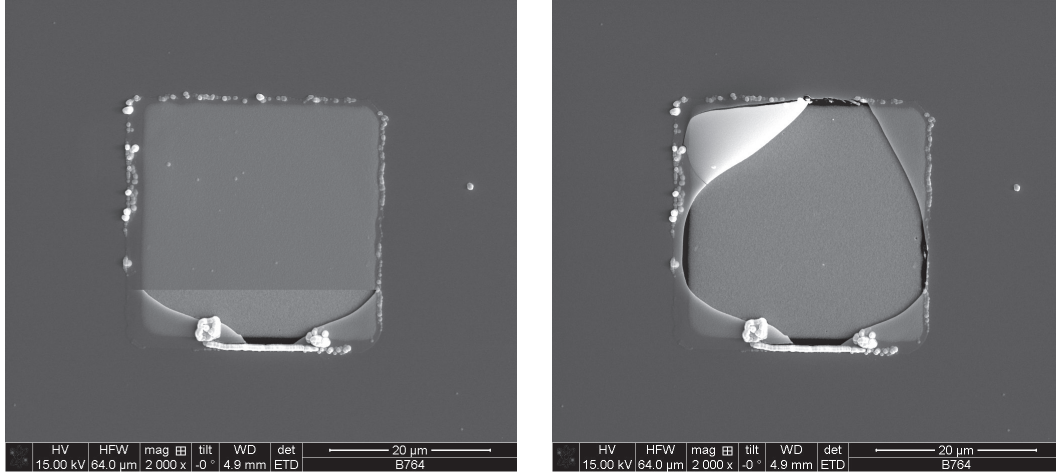


Figure 4.3: SEM images of a SiN_x layer on top of a gold layer (top layer of the MTJ-pillar). The SiN_x layer is removed explosively during electron exposure.

and forms a nitride layer ($\text{TiO} + \text{N}^\bullet + 2\text{H}^\bullet \rightarrow \text{TiN} + \text{H}_2\text{O}$). This nitride layer provides a good adhesion to the SiN_x layer due to Ti-N-Si bonds at the interface. Due to the nitride layer, the Ti-surface is not an active catalyst, which reduces the formation of H_2 . The idea of NH_3 -plasma treatment and the resulting removal of oxide and formation of nitride is based on the treatment of Cu-interconnects, described in [323].

In order to utilize the Ti-layer in the MTJ-structures, a change in the sample design was made. The protective mask, defining the junction area, is now made of Ti only. The thickness of the layer is chosen to be that large, that the Ti layer is not completely removed by the Ar-ion etching step and a layer of approximately 50 nm remains on top of the pillar. This remaining layer provides a good adhesion to the SiN_x layer.

In order to avoid an insulating TiO -layer in the current path, the contact holes, milled by FIB, are cut through the SiN_x - and the Ti-layer. This way, the Cu-layer is directly contacted by the Au-pad on top.

The combination of Cu-layer and Ti mask also reduces the edge defects produced in the Ar-ion etching step, visible in Figure 4.3. A contact, produced by the new method, is shown in Figure 4.11.

Adhesion of gold on top of SiN_x

The third major problem is the insufficient adhesion between the top Au-contacts and the underlying SiN_x . In case of contacting the pads by gluing gold wires with electrically conductive silver epoxy resin, the complete pads detach during electrical measurements. If the pads are contacted by the wire bonder with an Al-wire, which applies some stress to the pad during contacting, the wire tears away the gold at the bonding point and does not stick to the pad.

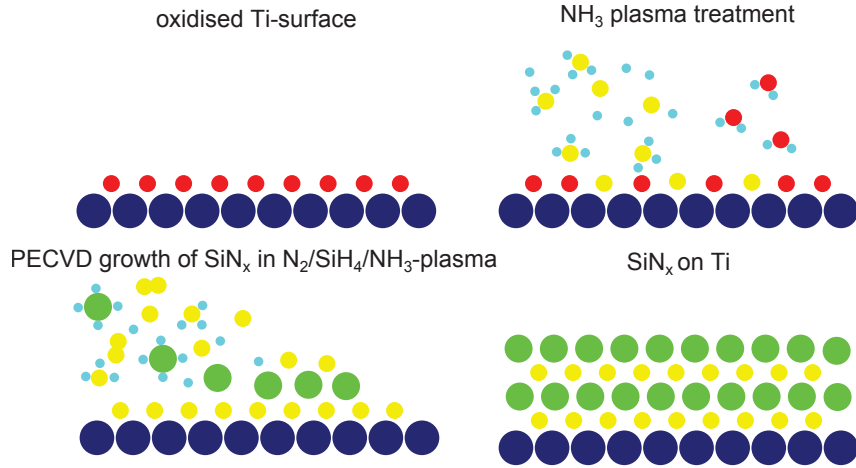


Figure 4.4: Schematic of the NH_3 plasma treatment of the Ti surface and the subsequent PECVD deposition process of SiN_x .

In order to improve the adhesion between SiN_x and the contact pad, different metals (Ti, Cu, W, Pt) were tested as seed layer between SiN_x and Au.

The test samples consist of a TiN (20 nm) / SiN_x (300 nm) film stack with contact pads on top. The contact pads are produced by lift-off and consist of sputtered double layers X / Au (X = Ti, Cu, W, Pt). The film thickness of the seed layer is approximately 100 nm, the Au thickness is 800 nm. The large gold thickness is due to the mechanical load during the wire bonding (pressure and ultrasonic power) and is a prerequisite for successful bonding. The samples are plasma cleaned before the sputter deposition of the metals. Only the Ar/ O_2 and the pure Ar-step are applied in order to reduce the hydrogen content at the surface of the SiN_x .

The pads were contacted with Al-wires using the wire bonder and the percentage of successful bonds on every sample was determined. In addition, a simple pull test is carried out on successful bonds. For that purpose, the sample was simply picked at the bond wire using tweezers and lifted up, utilizing the sample's weight as pulling force.

The tungsten seed layer shows the best results. Almost all bonds are successful and passed the pulling test. Therefore, a 100 nm thick tungsten layer is introduced between the SiN_x and the Au pad in order to provide sufficient adhesion between the layers.

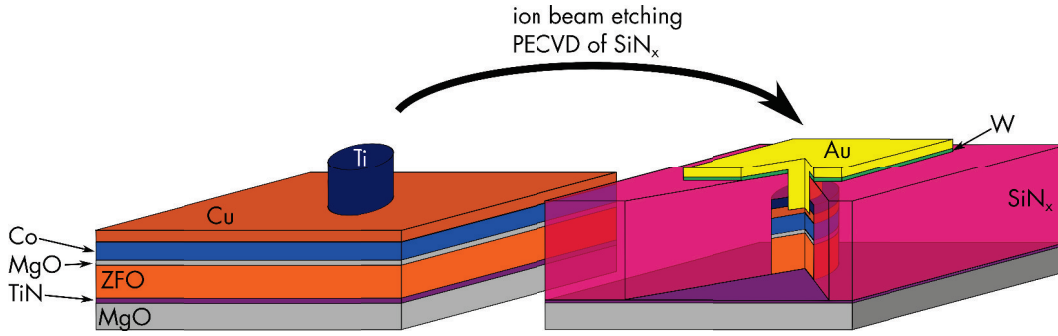


Figure 4.5: Final version of the newly developed MTJ-design.

4.3 The final sample design

The optimized sample design is depicted in Fig. 1.5. Its preparation is described in detail in the present section.

Thin film growth

The basic film stack for the production of MTJs ($\text{TiN} / \text{Zn}_x\text{Fe}_{3-x}\text{O}_4 / \text{MgO} / \text{Co}$) is grown by PLD. In PLD, a ceramic target, consisting of the desired film material, is ablated by an excimer laser in order to deposit the thin film (Section 3.1.1). In this work, targets of ZnFe_2O_4 , MgO , TiN and Co are used. The ZnFe_2O_4 and MgO targets were prepared in our group by Mrs. Gabriele Ramm. The ZnFe_2O_4 -target is prepared by mixing ZnO (purity of 99.997%) and Fe_2O_3 (purity of 99.999%) powders in well defined amounts (stoichiometric target). The MgO -target is produced from pure MgO -powder (purity of 99.998%). All oxide powders are supplied by Alpha Aesar, Berlin. The powders are ball milled, pressed and sintered in ambient air for 6 h at 1500°C (ZnFe_2O_4) and 1650°C (MgO), respectively. The TiN (purity of 99.5%) and Co (purity of 99.9%) targets were supplied by OS-Materials [324].

Prior to the deposition of the thin film stack, the substrate holder is cleaned by sandblasting in order to get rid of prior deposited oxides and to avoid evaporation of oxygen from the substrate holder.

The first step is the annealing of the magnesium oxide substrate. The (100)-oriented substrates ($10 \times 10 \times 1 \text{ mm}^3$ in size) are supplied by ChrysTec [325]. Substrates with a thickness of 1 mm are used to facilitate the adjustment of the RHEED electron beam (the surface of 0.5 mm thick samples matches with the top sample holder plate). The substrates are presorted by their miscut angle. Only substrates with a miscut angle γ smaller than 0.1° are used. The substrates are *in-situ* annealed (CO_2 -laser heater) in vacuum for 2 h at 950°C in order to achieve atomically smooth surfaces with monolayer terraces (see Section 5.1).

Prior to the growth of TiN , the chamber is purged with Ar in order to get rid

Table 4.1: PLD parameter for thin film growth of TiN, $\text{Zn}_x\text{Fe}_{3-x}\text{O}_4$, MgO and Co.

	TiN	$\text{Zn}_x\text{Fe}_{3-x}\text{O}_4$	MgO	Co
Substrate temperature T_{Sub} ($^{\circ}\text{C}$)	600	400	400	RT
Ar pressure $p(\text{Ar})$ (mbar)	$3 \cdot 10^{-2}$	$3 \cdot 10^{-2}$	$3 \cdot 10^{-2}$	$1 \cdot 10^{-3}$
Number of pulses n_{pulses}	2500	15000	300, 500, 700	600000
Laser frequency f_{Laser} (Hz)	2	15	5	10
Laser pulse energy P_{Laser} (mJ)	600	500	500	600
Aperture size A (mm^2)	20×8	15×4	20×8	20×8
Lens position L (cm)	10	10 to 14.5	10	12

of remaining oxygen. The process parameters for TiN growth are summarized in Table 4.1 (see also Section 5.2 for details on TiN growth and properties of the thin films).

After the deposition of TiN, the chamber is opened and the first target is switched from TiN to ZnFe_2O_4 . This step is necessary in order to be able to deposit the $\text{Zn}_x\text{Fe}_{3-x}\text{O}_4$ / MgO / Co stack without breaking the vacuum, since the target carousel only provides three places. $\text{Zn}_x\text{Fe}_{3-x}\text{O}_4$, MgO and Co are deposited in one step, without breaking the vacuum in between. Prior to the deposition of Co, the chamber was completely cooled down (usually over night), in order to avoid three-dimensional growth (see Section 5.5). Also an Ar-purging step is carried out prior to the Co deposition step. The process parameters for PLD growth of the $\text{Zn}_x\text{Fe}_{3-x}\text{O}_4$ / MgO / Co stack are summarized in Table 4.1 and the details on growth and properties of the films are presented in Section 5.

A copper layer is used to protect the Co thin film from oxidation and to provide a sufficiently thick contact layer (protection of the Co-layer during FIB-milling) on top of the MTJ-pillar. The Cu film is deposited by sputtering, using a sputter time of 200 s, a power of 30 W and an Ar flow rate of 100 sccm. The sample is transported to the sputter chamber in ambient air.

Production of the Ti-mask

A titanium mask is applied to the sample surface. The mask consists of small Ti-pads, that define the area of the MTJ-pillars for Ar-ion etching and protect the underlying film stack. The mask is produced by photolithography, using the lift-off technique (see Section 3.8). A schematic of the used photolithog-

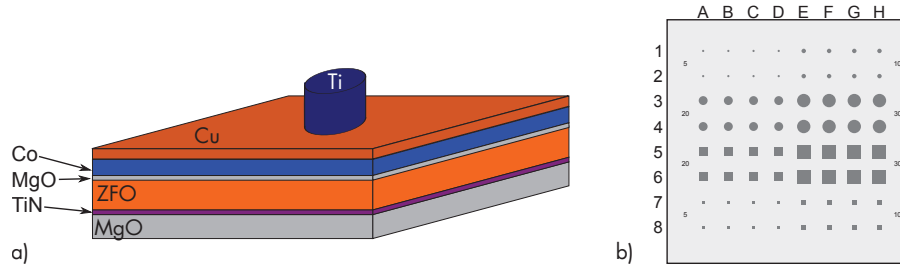


Figure 4.6: Sketch of the sample after lift off preparation of the Ti-mask. The sample consists of the thin film stack grown by PLD (TiN / $\text{Zn}_x\text{Fe}_{3-x}\text{O}_4$ / MgO / Co), the sputtered Cu layer and the Ti-mask, defined by photolithography. b) Schematic of the photolithography-mask used to produce the Ti-pads in order to define the area of the MTJ-pillars.

raphy mask is shown in Figure 4.6 b). The mask defines 64 pads, shaped as squares (edge length is 5, 10, 20 and 30 μm) and circles (diameter of 5, 10, 20 and 30 μm). Pad spacing is 1 mm.

After applying the resist mask, the sample is plasma cleaned (see Section 3.9) in order to get rid of residual resist in the developed pad areas. The O_2/Ar -step removes the residual resist, whereas the H_2/Ar -step is applied in order to remove the oxide layer, probably produced by the first cleaning step [323].

After cleaning, a Ti-film with an approximate thickness of 80 to 100 nm is sputter deposited on top of the resist mask. In order to achieve pure Ti, the target is pre-sputtered for 20 min (60W, 100 sccm Ar) prior to the deposition step. Figure 4.7 shows images of the sputter plasma during the deposition of Ti. Directly after the process is started, the plasma shows a bright white color with a small purple glow, indicating hydrogen and oxygen. After 20 min of sputtering, the plasma color changes to bright blue. This color is due to a pure Ti plasma, that forms after all contamination are removed from the chamber. The residual contamination gases inside the chamber are probably bound in the Ti, that is deposited in the early stage of the process. In order to be able to perform the pre-sputter step and directly afterwards the deposition step (without the need of opening the chamber), a cover for the sample was fitted into the sputter chamber. The cover is a ceramic cup, that is placed above the sample during pre-sputtering. The sample is placed at the sample plate in the way that it can be placed under the cup or the Ti-target by rotating the plate. The cup is visible in Figure 4.7 in the background of the chamber.

After pre-sputtering, the sample is rotated under the target. Ti-deposition parameters are a sputter time of 120 s, a sputter power of 60 W and an Ar-gas flow rate of 100 sccm.

The Ti-pads are formed by lift-off. For this, the resist mask is removed in acetone using a ultrasonic bath. Figure 4.6 a) shows a sketch of the sample at the current state of sample preparation.



Figure 4.7: Images of the plasma in the sputter chamber during the deposition of Ti. The left picture shows the plasma right after the start of the process, the right one after 20 min.

Production of pillars: Ar-ion etching

The MTJ-pillars are produced by Ar-ion etching (Section 3.10). For that purpose, the film stack is removed by sputtering at areas not protected by the Ti-pads. Since it is important for the functionality of the MTJs that the TiN-layer remains intact, the etch process is stopped at the $\text{Zn}_x\text{Fe}_{3-x}\text{O}_4$ / TiN-interface. This is possible due to the observation of sputtered elements in the SNMS-system.

Figure 4.8 a) shows a sketch of a MTJ-pillar after the Ar-etching step. Laser scanning microscope (LSM) topography and optical images (Figure 4.8 b) show well defined contacts with steep edges after Ar-ion etching in the SNMS-machine.

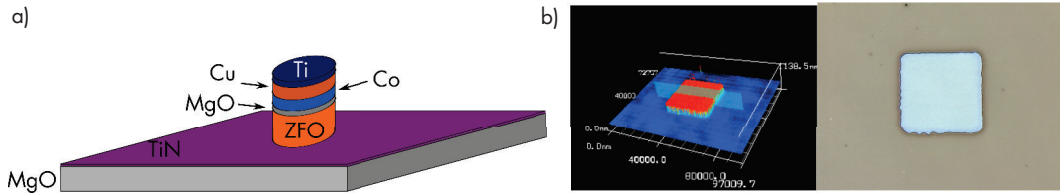


Figure 4.8: a) Sketch of the sample after Ar-ion etching. b) LSM-height image and optical micrograph of a $20 \times 20 \mu\text{m}^2$ sized MTJ-pillar after Ar-ion etching.

PECVD of SiN_x

The remaining, closed TiN thin film and the MTJ-pillars are covered by approximately 300 nm SiN_x using PECVD (Section 3.12). The SiN_x layer should passivate the pillars and constrain the current to single MTJ contacts. This allows electrical measurements on exactly one specific pillar, namely the one connected to the contact bridge (see Figure 4.13). The SiN_x film provides the electrical insulation between the single MTJ-pillars as well as the insulation

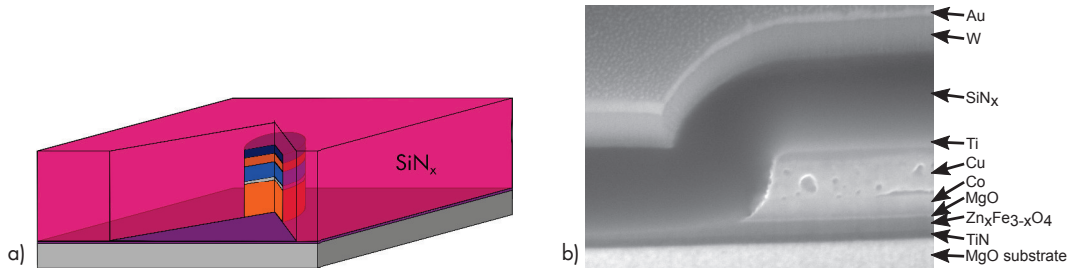


Figure 4.9: Sketch of the sample after the deposition of SiN_x and a SEM-image of a cross section prepared by FIB, showing the conformal coating of the edge of a MTJ-pillar by SiN_x.

between the bottom TiN-layer and the top gold contact.

Prior to the deposition of SiN_x, a NH₃ plasma pretreatment is applied to the sample surface, in order to enhance the adhesion between the Ti layer on top of the MTJ-pillar and the SiN_x-film (Section 4.2). The plasma treatment is ascribed to remove the TiO-surface layer and to form a thin TiN-layer. The TiN-layer provides a good adhesion between Ti and SiN_x due to the formation of Ti-N-Si bonds at the interface (see Section 4.2 and Figure 4.4). The parameters for NH₃ plasma treatment and PECVD of SiN_x are summarized in Section 3.12. Figure 4.9 shows a sketch of the sample after the deposition of SiN_x, as well as a SEM-image of a covered MTJ-edge. The image shows the conformal coating by SiN_x, providing a sufficient insulation even at the edge of a MTJ-pillar.

Top contact resist mask and W/Au-layer

Next step is to apply the resist mask, defining the top contact pads, to the sample. The used photolithography mask is shown schematically in Figure 4.10 b). It consists of 64 contact pads with a diameter of 750 μm. The centers are

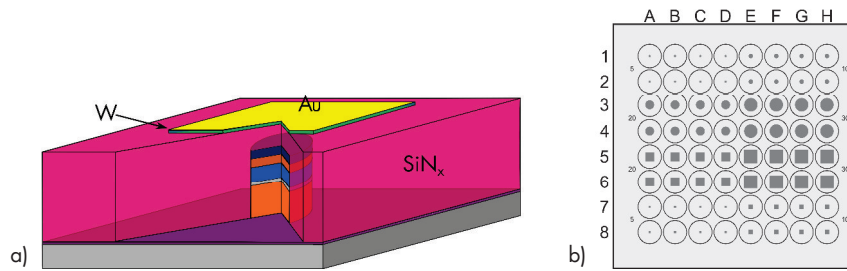


Figure 4.10: a) Sketch of the sample after applying the resist mask and the W/Au-layer (the resist is not shown). b) Schematic of the photolithography mask used to produce the top contact pads. The first mask, defining the MTJ-areas, is also shown.

spaced by 1 mm. The pads are arranged such, that the MTJ-pillars are located at the center of each top contact pad.

The sample with the developed resist mask is plasma cleaned prior to the deposition of the tungsten and gold layers. Only the O_2/Ar and pure Ar steps are applied in order to remove residual resist and to reduce the amount of hydrogen at the SiN_x -surface. The W and Au layers are sputter deposited on top of the resist mask. Sputter parameters are a power of 60 W and an Ar-flow rate of 100 sccm. The sputter time is 60 s for W and 15 s for Au, respectively. There is no lift-off performed at this point. The closed W/Au-films on top of the resist mask were deposited prior to the milling step in order to avoid charging effects during SEM and FIB-milling.

Milling of contact holes by FIB

In order to top contact the MTJ-pillars through the SiN_x -layer, holes are milled into it by FIB (see Section 3.6). The milling depth is adjusted in order to cut through the SiN_x and the Ti layer. The Cu layer on top of the MTJ-pillar is contacted to the top gold layer through this holes.

The first step prior to the milling is the determination of the milling time. Therefore, five small holes ($2 \times 1 \mu m^2$) are milled with different milling times at the top of a sacrificial contact. Afterwards, a cross section is prepared in order to determine the resulting milling depths. The desired milling time, in order to mill through the SiN_x and Ti layers exactly into the Cu layer, is determined by linear regression.

The software Auto-FIB, provided with the dual beam microscope, is used to mill the contact holes automatically. For this, the position, size and nominal depth of the single holes are written into a script. The script is interpreted by the Auto-FIB software that controls the microscope and mills the contact holes fully automatically.

Figure 4.11 shows a sketch of the sample after the milling step as well as SEM-images of a milled contact. The milling stopped directly in the Cu layer (milling depth is ≈ 80 nm in Cu). Therefore, the Co layer is sufficiently protected by the remaining Cu.

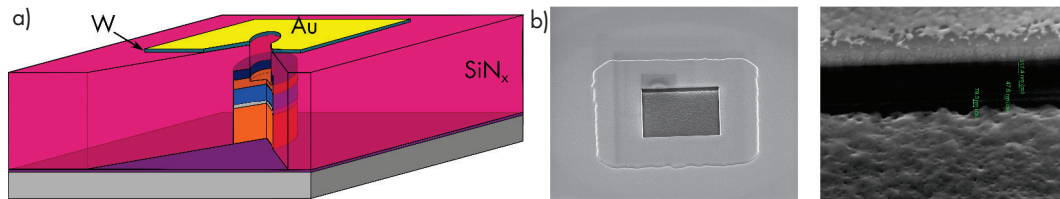


Figure 4.11: a) Sketch of the milling step by FIB. b) SEM-images of a milled contact. Contact size is $20 \times 20 \mu m^2$.

Sputter deposition of the Au-pads and lift-off

After milling the contact holes, the sample is plasma cleaned, using all three cleaning steps (Section 3.9). The thick Au-contact pad ($d \approx 800$ nm) is deposited by sputtering (240 s, 60 W, 100 sccm Ar). Afterwards, the lift-off step is carried out and the resist mask is removed. The Au-contact pads, used for contacting the single MTJs, remain at the surface. Figure 4.13 shows a photograph of a completely processed and contacted sample.

The huge film thickness of the Au-pad is necessary due to the high mechanical load produced by contacting with the wire bonder (Section 3.13). The thick Au-pad provides sufficient material for the formation of the bonding eutectic and protects the underlying SiN_x -film in order to avoid piercing.

Figure 4.12 shows a sketch as well as a SEM-cross section image of a completely processed MTJ.

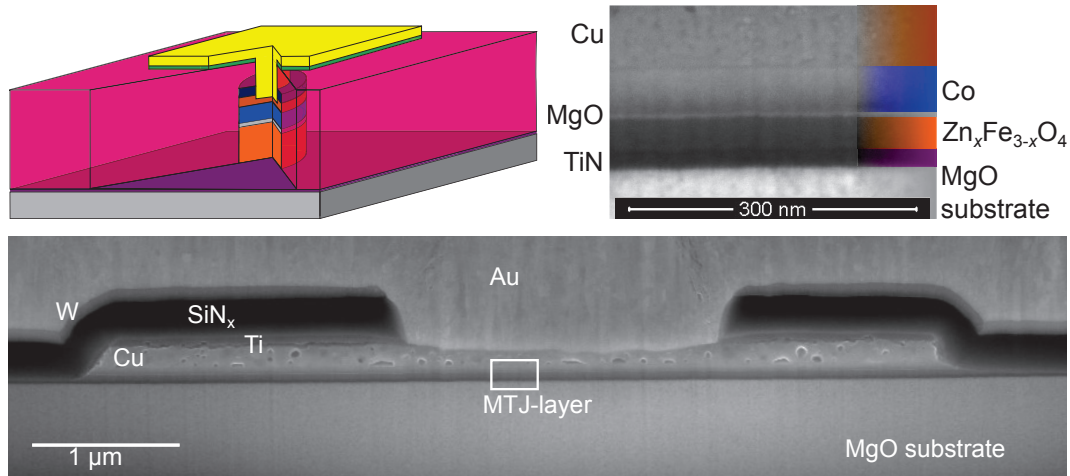


Figure 4.12: Schematic and SEM-cross section image of a completely processed sample.

Sample contacting

The completely processed sample is mounted to a sample holder of the TMR measurement setup (Figure 4.13). In order to be able to measure in 4-point mode (remote sense, see Section 3.14.3), the sample is contacted to four pins. Contact points at the sample are the conductive TiN-layer (back contact) and the top Au-pads of the single MTJ-elements. The mounted sample is shown in Figure 4.13 b).

The TiN-layer is contacted at one sample edge by a gold pad. It is deposited after baring the TiN-film by scratching through the SiN_x layer at one sample edge with a diamond cutter. A shadow mask defines the area of the sputtered Au pad. Sputter parameters are 120 s at 60 W and 100 sccm Ar. The sample is rotated during deposition.

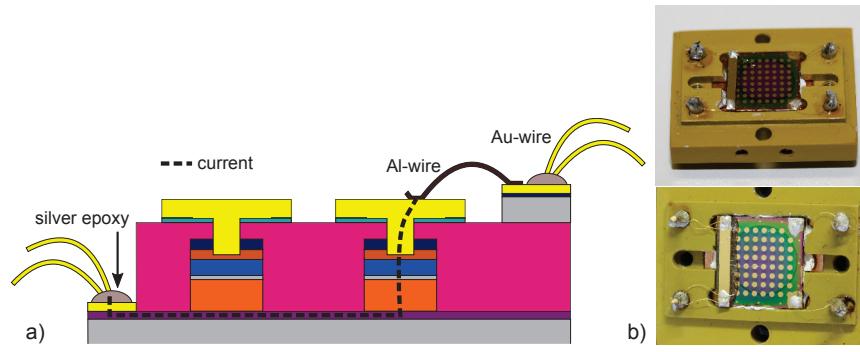


Figure 4.13: a) Schematic cross section of two MTJ-elements. The right one is connected to the contact bridge by an Al-wire, and therefore the one under test. The Au-wires are contacted to the sample holder. b) Photograph of a contacted sample. One contact is connected to the contact bridge (left) by an Al-wire.

The top contact pad of the measured MTJ is contacted with an Al-wire, attached by the wire bonder (Section 3.13). In order to be able to use the wire bonder, a contact bridge is added to the sample. The contact bridge is a 1 mm wide MgO stripe, produced by cleaving a 0.5 mm thick MgO substrate in 1 mm stripes. It is coated with a sputtered Ti / Au contact layer. The Ti-layer is necessary in order to obtain sufficient adhesion between the MgO and the thick Au layer. Sputter parameters for both layers are a power of 60 W and an Ar-flow rate of 100 sccm. Sputter time is 60 s for Ti and 240 s for Au. The large thickness of the gold layer (≈ 800 nm) is required due to the bonding of Al-wires by the wire bonder. The contact bridge is attached to the sample surface by epoxy resin. The Al-wire connects the gold pad of the measured MTJ to the metallization of the bridge.

The gold pad (contacting the TiN-layer) and the contact bridge are connected to the sample holder by four gold wires. Each point is connected to one out- and one sense-lead (see Figure 3.13). The wires are glued to the sample by electrically conductive silver epoxy resin and soldered to the four pins of the sample holder (see Figure 4.13).

All MTJ-pillars are connected to the bottom TiN-layer. In order to measure one specific MTJ-element, this element is contacted to the bridge at its top contact pad by an Al-wire. The use of the contact bridge and the wire bonder allows a fast and simple change of the measured (top-contacted) junction by removing the Al-wire and simply attach a new one in order to connect another pad to the bridge.

Electrical measurements are carried out in 4-point mode (remote sense, see Section 3.14.3). The out- and sense-leads are connected at the contact bridge (bond point of the Al-wire) and at the gold pad, contacting the TiN-layer. Figure 4.13 a) shows the desired current path through the MTJ-sample inside the 4-point geometry. Current flow is through the TiN-layer, the MTJ-pillar,



Figure 4.14: Photographs of the adapter, allowing to contact samples by the wire bonder when they are mounted to the sample holder. The top left image shows the stock sample holder of the wire bonder.

the top metallization (Cu and Au) and the Al-wire, connecting the Au-pad to the contact bridge.

Adapter for the wire bonder

The stock sample holder of the wire bonder provides no possibility to mount the sample holder used in the TMR measurement setup. Since a simple contacting requires the possibility to work with samples mounted to this sample holder, an adapter was developed and manufactured in the mechanical workshop of the Faculty of Physics and Earth Science of the University of Leipzig. This adapter allows to contact samples mounted to the sample holder of the TMR measurement setup. Figure 4.14 shows the stock sample holder and the adapter, as well as a mounted TMR-sample holder.

5 Growth and properties of thin films

This chapter focuses on the growth and the properties of the PLD-grown thin films, used to build the magnetic tunnel junctions (see Section 4).

5.1 MgO-substrate preparation

In Section 4.1, the importance of smooth barrier interfaces was stated. The formation of such interfaces requires the films to grow in the two-dimensional Frank-van-der-Merve or layer by layer growth mode (Section 3.1.3). As discussed, the substrate surface must provide optimal conditions in order to achieve two-dimensional growth of thin films. These optimal conditions are atomically flat, terraced substrate surfaces with monolayer steps. In order to prepare substrate surfaces that meet these requirements, the used MgO substrates are vacuum-annealed *in-situ*, using the CO₂-laser heater.

For the determination of ideal annealing parameters, preliminary tests were carried out on MgO-substrates. Used substrates are (100)-oriented MgO single crystals provided by CrysTec [325]. These crystals are grown by the arc fusion method. The substrate size is $10 \times 10 \times 0.5 \text{ mm}^3$. The single side polished substrates have a miscut angle of $\gamma < 0.5^\circ$. The miscut angle γ of the individual substrates was determined by XRD, performing four XRD ω -scans (see Page 124). Substrates showing a miscut angle $\gamma < 0.25^\circ$ were used for the experiments.

The substrates were annealed at different temperatures (900, 950 and 1000°C) for 2 h, heated by the CO₂-laser. The 2 h are the time the desired temperature is held constant (without the ramping time). Heating and cooling rate are both 50 K/min. Annealing was carried out in vacuum at a pressure of approximately 10^{-6} mbar. In order to generate a reproducible environment, the laser heater was started at a chamber pressure of $5 \cdot 10^{-5}$ mbar, with the turbo pump at full speed.

Figure 5.1 shows AFM topography-images of annealed substrate surfaces. Different morphologies are observed in dependence of the annealing temperature and the substrate miscut angle γ .

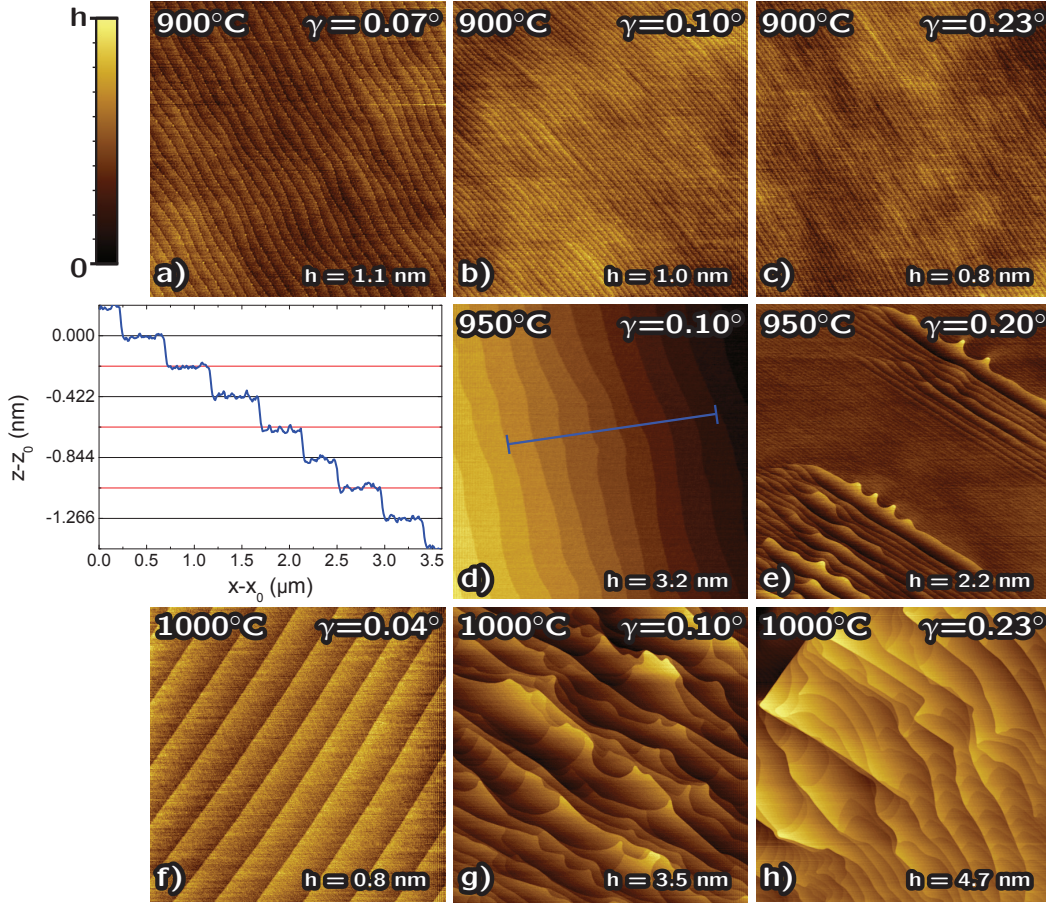


Figure 5.1: AFM topography images ($5 \times 5 \mu\text{m}^2$) of the surface of different MgO substrates after annealing at different temperatures. γ is the miscut angle of the substrates, measured by X-ray diffraction. h denotes the height difference in the AFM images. Figure is published in [A1].

At an annealing temperature of 900°C and large miscut angles of $\gamma > 0.08^\circ$, the surface shows small ripples (Figure 5.1 b, c). For smaller miscut angles ($\gamma < 0.08^\circ$), unsteady terraces with step heights between 1 and 2 \AA appear at the surface (Figure 5.1 a).

The substrates with a miscut angle $\gamma < 0.15^\circ$ annealed at 950°C show atomically flat, terraced surfaces (Figure 5.1 d). The height of the uniform terrace steps is 0.21 nm , which corresponds to half the cubic unit cell of MgO (one atomic layer, see profile in Figure 5.1). The atomically flat terraces show a small RMS-roughness of 0.05 nm . With increased miscut angles ($\gamma > 0.15^\circ$), the monolayer steps grow together and multilayer steps are observed at the surface (Figure 5.1 e).

At temperatures of 1000°C and larger miscut angles ($\gamma > 0.06^\circ$), the surfaces become rather rough and form steps up to a few nm in height (Figure 5.1 g, h). Within these high steps, monolayer steps with a height of 0.21 nm are

also observed. Surfaces of substrates with a small miscut angle ($\gamma < 0.06^\circ$) annealed at 1000°C show no multilayer steps (Figure 5.1 f). Atomically flat, terraced surfaces are observed, similar to those of samples annealed at 950°C ($\gamma < 0.15^\circ$).

Miscut angle and annealing temperature seem to influence the surface morphology of (100)-oriented MgO substrates. Small miscut angles lead to a preferred formation of monolayer steps and terraces (Figure 5.1 d and f), whereas higher angles support the formation of multilayer steps up to several nm in height (Figure 5.1 e, g and h). As discussed in Section 3.1.3, an increase in temperature increases the mobility of surface atoms, allowing them to rearrange the surface. The ripples and unsteady terraces at low temperatures (900°C) may be the result of a rather slow rearrangement of the amorphous substrate surface. The amorphous surface of as-received substrates is caused by polishing. With increasing temperature, the mobility of surface atoms is large enough to rearrange and form a crystalline, stepped surface. At low miscut angles, monolayer terraces form at the surface (Figure 5.1 d and f), whereas at higher angles multilayer steps are formed. The temperature, needed to form multilayer steps, decreases with increasing miscut angle (Figure 5.1 e and g). At high temperatures and miscut angles, even steps with a height of several nm are formed (Figure 5.1 h). The formation of these high steps is probably driven by the energetically favored formation of non-polar $\{010\}$ -facets and the minimization of step edges. Step edges increase the energy of the system due to dangling bonds and unscreened charges. Since the amount of step edges increases with increasing miscut angle, the formation of high steps becomes more favorable at high miscut angles.

Also the absence of oxygen seems to support the formation of monolayer terraces and steps. In contrast to the results presented here, former publications report rectangular sharp edges [326] or intergrown terraces [327, 328] at the surface of MgO crystals annealed at temperatures between 950 and 1050°C in flowing oxygen. The reported step heights are in the range of a few nm. Murugesan *et al.* [326] state, that the absence of oxygen during annealing is probably the reason for the formation of monolayer terraces [326]. The results presented above seem to confirm this assertion.

Concerning these results, an annealing temperature of 950°C for two hours and a maximum miscut angle of 0.15° were chosen for a reproducible preparation of atomically flat, monolayer terraced substrate surfaces. These surfaces provide optimal conditions for the two-dimensional growth of thin films.

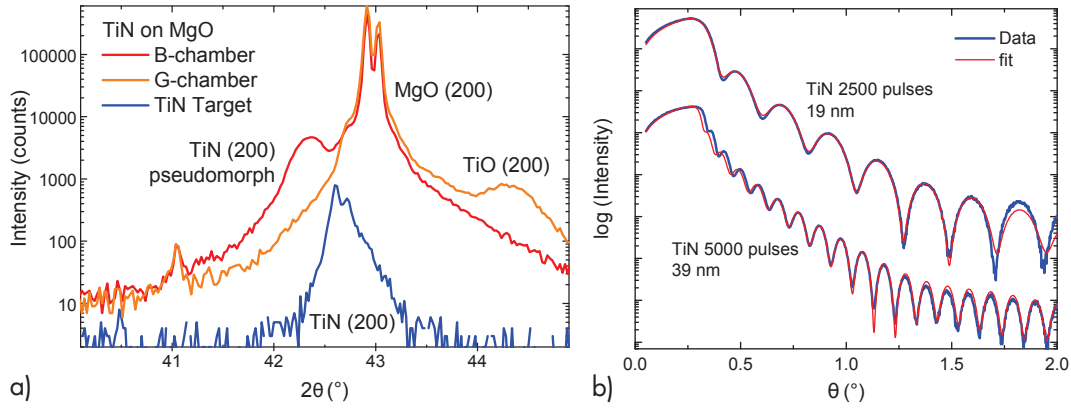


Figure 5.2: a) XRD 2θ - ω -scans of the TiN-target and two different "TiN"-thin films on MgO, grown in different PLD-chambers (G-chamber with Kantal resistance heater, B-chamber with CO₂-laser heater). Both films are deposited using the same TiN-target. b) XRR-curves of two TiN-thin films with different thicknesses.

5.2 TiN-thin films

TiN is used as conductive bottom layer in order to reduce the series resistance of the MTJs (see Section 4.1). It is a highly conducting material ($\sigma \approx 10^6$ S/m [329]), that crystallizes in the rocksalt structure with a lattice constant of $a_{\text{TiN}} = 4.24$ Å. This lattice constant allows an epitaxial growth on top of MgO ($a_{\text{MgO}} = 4.21$ Å, rocksalt structure) with only a small lattice mismatch of 0.7% [327].

The growth of nitrides by PLD in chambers also used to grow oxides has one mayor difficulty. Most metals show a larger enthalpy gain for the formation of oxides than for the formation of the corresponding nitride. Therefore, oxygen supply has to be completely avoided during the growth of nitride thin films. Usually, a Kantal based resistance heater is used to heat the substrate. Consequently, large parts of the chamber are also heated up. Since these chamber parts are coated by oxides from prior deposition steps, oxygen will desorb during the growth process and oxide instead of nitride is formed. The use of the CO₂ laser heater allows to concentrate the required heater power onto the substrate, which avoids the heating of large, oxygen contaminated areas. This allows the growth of high quality TiN thin films on MgO substrates in pure Ar atmosphere in a chamber mainly used for the deposition of oxide materials [271][A1].

Figure 5.2 a) shows 2θ - ω -scans of two different thin films on (100)-oriented MgO, grown from the same TiN-target in different PLD-chambers. The G-chamber is equipped with a Kantal resistance heater, whereas the B-chamber uses a CO₂-laser heater for substrate heating. The resulting film grown in the G-chamber is clearly titanium oxide, although the target was pure TiN. By using the CO₂-laser heater, it is possible to grow phase pure TiN by PLD in a

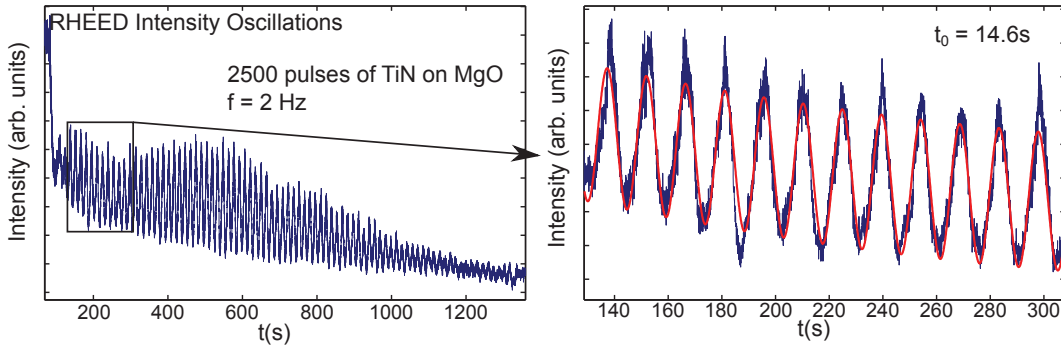


Figure 5.3: RHEED intensity during the growth of an approximately 19 nm thick TiN film on MgO. Oscillations due to the two-dimensional growth mode are clearly visible.

chamber that is also used to deposit oxides.

Before the growth of TiN, the B-chamber is purged with Ar in order to get rid of remaining oxygen. This is done by evacuating the chamber to $1 \cdot 10^{-6}$ mbar and a subsequent filling with 600 mbar Ar. This step is repeated twice before the Ar background pressure for the deposition step is set.

The growth conditions for thin films grown in the B-chamber are summarized in Table 4.1. TiN thin films are grown at a substrate temperature of 600°C and an Ar background pressure of $3 \cdot 10^{-2}$ mbar. An excimer laser repetition frequency of 2 Hz and a laser pulse energy of 600 mJ, as well as a 20×8 mm² laser aperture are used. The lens ($f = 300$ mm) is placed at $L = 10$. The substrate temperature of 600°C was chosen due to the fact, that TiN grows in islands above 650°C [330]. The samples presented in this chapter are grown with different pulse numbers: 2500 ($d \approx 19$ nm), 5000 ($d \approx 39$ nm) and 5750 ($d \approx 43$ nm). The thick samples are used for XRD-investigation due to the higher intensities of the measured peaks.

The TiN thin films grow in two-dimensional layer by layer growth mode on top of the annealed MgO substrates. This is confirmed by RHEED intensity oscillations during growth. Figure 5.3 shows the RHEED intensity during the deposition of a 19 nm thick TiN thin film (2500 laser pulses). One oscillation corresponds to the growth of one monolayer (≈ 0.21 nm). It takes about 29 pulses (14.6 s) to grow one closed monolayer. This yields a growth rate of 0.76 nm per 100 pulses.

The determined growth rate is also confirmed by XRR-measurements. Figure 5.2 b) shows X-ray reflectivity curves of two TiN thin films grown with different numbers of PLD pulses. The thickness of 19 and 40 nm for 2500 and 5000 pulses, respectively, corresponds well to the growth rate determined by RHEED. The shape of the reflectivity curves indicates a smooth interface between substrate and film as well as a smooth surface of the TiN film.

The RHEED pattern of the TiN thin films indicate a smooth, regularly stepped surface (Figure 5.4 d). They show streaky spots at the expected positions for

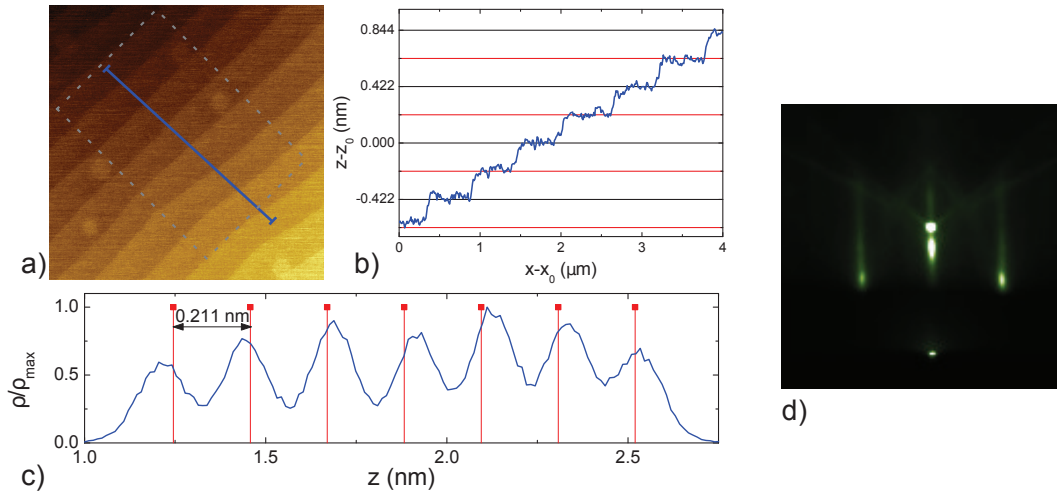


Figure 5.4: (a) AFM-image ($5 \times 5 \text{ nm}^2$, height scale is 0 to 2.4 nm) of the surface of a 43 nm thick TiN thin film grown by PLD on MgO (100). Steps with a height of half the lattice constant (2.11 \AA) are observed also on a line scan (blue line, b). The histogram data (c) is from the area marked by the gray rectangle. Figure is published in [A1]. d) RHEED pattern of a TiN-thin film on (100) oriented MgO. The electron beam is along the [10]-direction.

a cubic lattice with rocksalt structure. Also Kikuchi-lines are observed, indicating a high quality, crystalline surface.

The two dimensional growth mode is also confirmed by AFM topography images (Figure 5.4 a). As implied by the RHEED-pattern, the surface of the TiN thin film is smooth and stepped. The uniform step height is 0.21 nm, determined by line scans and hystographic evaluation of the height data (see Figure 5.4 b and c, respectively). The observed step height is half the lattice constant of TiN (one monolayer) and confirms the assumption of a two dimensional growth in monolayers with a thickness of 0.21 nm. The small area RMS-roughness on the atomically flat terraces is 0.08 nm. Figure 5.4 a) shows the surface of a 43 nm thick (5750 laser pulses) TiN film. The observed atomically flat, monolayer terraced film surface indicates a stable two-dimensional growth mode up to this thickness.

The initial formation of new monolayers at the surface can be observed in the AFM topography image. Clear round spots with the height of the neighboring terrace are visible. These spots might be stable clusters with a thickness of one monolayer, formed at the surface by adatoms after completing the deposition.

Figure 5.5 shows the results of X-ray diffraction measurements on TiN thin films grown on (100)-oriented MgO substrates. High resolution 2θ - ω -scans show strained TiN (Figure 5.5 a). The out-of-plane lattice constant a_{\perp} is slightly larger than that of bulk TiN. The peak position in 2θ gives $a_{\perp} = 4.25 \text{ \AA}$. The presence of intensity fringes indicates an abrupt interface between MgO

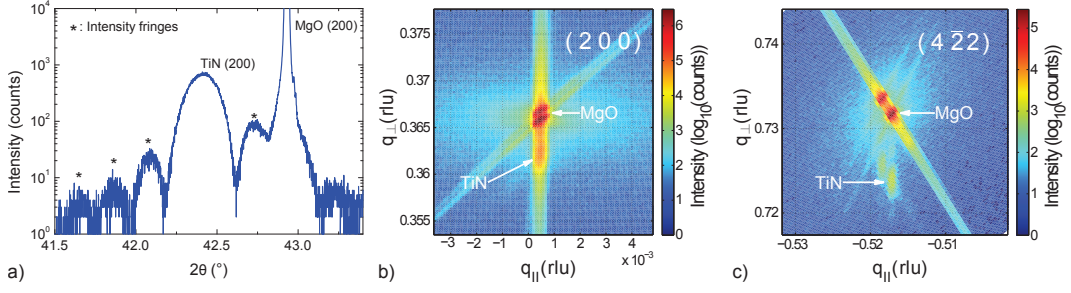


Figure 5.5: (a) High resolution XRD 2θ - ω scan of a TiN thin film grown on (100) MgO. Clearly visible intensity fringes indicate an abrupt interface between TiN and MgO. The spacing in 2θ of the intensity fringes yields a thickness of (44 ± 1) nm. (b) X-ray reciprocal space maps of the (200) and (c) (422) MgO peak. It shows pseudomorphic growth of TiN on MgO. The in-plane strain is -0.7%. Preferential peak broadening only in q_{\perp} -direction due to finite film thickness indicates a high crystalline film quality. The doubled peaks result from the $K_{\alpha 1}$ - $K_{\alpha 2}$ splitting. Figure is published in [A1].

and TiN as well as a good film and surface quality. The 2θ spacing of the intensity fringes corresponds to a TiN film thickness of (44 ± 1) nm (5750 pulses), in accordance with the growth rate obtained by RHEED and XRR. Film thickness is calculated by Equation (3.20).

X-ray diffraction reciprocal space maps around the (200) and (422) reflexes of MgO are shown in Figure 5.5 b) and c), respectively. The TiN reflexes are aligned vertically to those of MgO, indicating strained, pseudomorphical (epitaxial) growth of TiN on MgO. The in-plane compressive strain is $\epsilon_{\parallel} = -0.7\%$. The epitaxial relation is determined by φ -scans on the MgO/TiN (311)-peak (not shown). No additional peaks due to rotational domains is observed. Therefore, the epitaxial relation is $\text{MgO}[100] \parallel \text{TiN}[100]$ for the out-of-plane direction and $\text{MgO}[010] \parallel \text{TiN}[010]$ for the in-plane direction. This means, that TiN grows lattice-matched, cube on cube, on MgO. From the positions of the (200), (420) (not shown) and (422) reflections on the reciprocal space maps, the lattice constants of the TiN film were calculated. The in-plane lattice constant a_{\parallel} and the out-of-plane lattice constant a_{\perp} are determined to be

$$a_{\parallel} = 4.21 \text{ \AA} (\approx a_{\text{MgO}}) \quad \text{and} \quad a_{\perp} = 4.25 \text{ \AA}. \quad (5.1)$$

The fact, that the in-plane lattice constant of the TiN thin film and the MgO substrate are identical, further underlines the strained, pseudomorphical growth of TiN up to a film thickness of 43 nm. The out-of-plane lattice constant matches with the one obtained by high resolution XRD-scans.

A broadening of the TiN spots only in q_{\perp} due to the finite film thickness indicates a high film quality. The narrow width in q_{\parallel} of the TiN spots demonstrates the absence of relaxation or mosaicity in the film and underlines the excellent crystalline quality.

The TiN thin films form an ohmic contact to $\text{Zn}_x\text{Fe}_{3-x}\text{O}_4$ (not shown). Electrical conductivity σ is 1 up to $2 \cdot 10^6 \text{ S/m}$ at room temperature. The films show metallic behavior. The obtained conductivity values match with the reported values for PLD grown TiN in nitrogen atmosphere on silicon [329].

All these properties make the TiN thin films, grown in the framework of this thesis, suitable as conducting back contact layers for $\text{Zn}_x\text{Fe}_{3-x}\text{O}_4$ -based MTJs. Key points are the flat, stepped surfaces, the perfect crystalline structure and the high conductivity. The lattice constant of TiN (almost similar to MgO) allows the epitaxial growth of $\text{Zn}_x\text{Fe}_{3-x}\text{O}_4$. The atomically flat surface with monolayer terraces provides optimal conditions for a two-dimensional growth of $\text{Zn}_x\text{Fe}_{3-x}\text{O}_4$.

5.3 $\text{Zn}_x\text{Fe}_{3-x}\text{O}_4$ thin films

$\text{Zn}_x\text{Fe}_{3-x}\text{O}_4$ ($0 \leq x \leq 1$) is a promising material for spintronic applications (see Section 2). It shows semiconducting behavior as well as ferrimagnetism with a high Curie temperature above room temperature. A high spin polarization (half metallic) is predicted by theoretical calculations.

Therefore, $\text{Zn}_x\text{Fe}_{3-x}\text{O}_4$ is used in this work as magnetic electrode in magnetic tunnel junctions in order to demonstrate the suitability of the material for the application in spintronics. This chapter focuses on the properties of PLD-grown $\text{Zn}_x\text{Fe}_{3-x}\text{O}_4$ thin films, used to build MTJ-structures.

The $\text{Zn}_x\text{Fe}_{3-x}\text{O}_4$ thin films are epitaxially grown by pulsed laser deposition on annealed (100)-oriented MgO substrates (Section 5.1) with a TiN buffer layer (Section 5.2). The thin films used to investigate the film conductivity are grown directly on the annealed MgO substrate. The cubic lattice constants of Fe_3O_4 and ZnFe_2O_4 are $a_{\text{Fe}_3\text{O}_4} = 8.40 \text{ \AA}$ and $a_{\text{ZnFe}_2\text{O}_4} = 8.44 \text{ \AA}$, respectively. The lattice constant increases with increasing Zn content [15] and $a_{\text{Fe}_3\text{O}_4} \leq a_{\text{Zn}_x\text{Fe}_{3-x}\text{O}_4} \leq a_{\text{ZnFe}_2\text{O}_4}$. Therefore, the lattice mismatch between $\text{Zn}_x\text{Fe}_{3-x}\text{O}_4$ and MgO or strained TiN (the in-plane lattice constant is $4.21 \text{ \AA} \approx a_{\text{Zn}_x\text{Fe}_{3-x}\text{O}_4}/2$) is between -0.3% and 0.3%, depending on the Zn content x . The small lattice mismatch allows a pseudomorphical growth of $\text{Zn}_x\text{Fe}_{3-x}\text{O}_4$ on MgO or strained TiN.

The PLD growth parameters of $\text{Zn}_x\text{Fe}_{3-x}\text{O}_4$ are summarized in Table 4.1. The substrate temperature during growth is 400°C and the Ar background pressure is set to $3 \cdot 10^{-2} \text{ mbar}$. Excimer laser pulse energy is 500 mJ with a repetition frequency of 15 Hz. A laser aperture of $15 \times 4 \text{ mm}^2$ is used. The use of the small aperture is due to the occurrence of island growth and the formation of three-dimensional structures when using the large ($20 \times 8 \text{ mm}^2$) one. AFM and RHEED images of $\text{Zn}_x\text{Fe}_{3-x}\text{O}_4$ thin films grown with the small or large

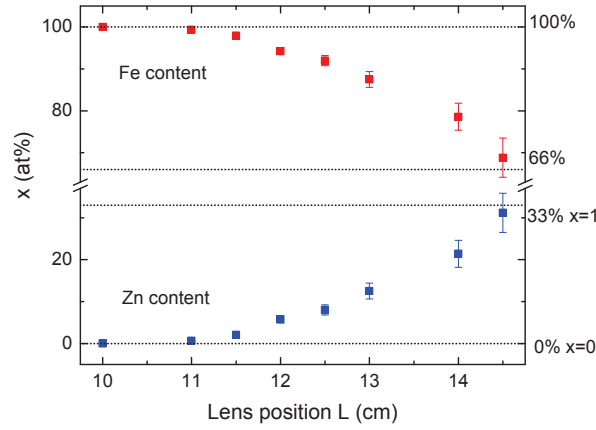


Figure 5.6: Dependence of the composition ($x(\text{at}\%)$), determined by EDX) of $\text{Zn}_x\text{Fe}_{3-x}\text{O}_4$ on the position L of the PLD-lens (laser fluence at the stoichiometric ZnFe_2O_4 -target surface). x values shown here are mean values from two to five different samples. The errors are the standard deviation.

aperture, respectively, are shown in Figure 3.4 e-h. The island growth might be caused by the high supersaturation at the substrate surface, associated with the larger laser spot with identical energy density.

The lens position L is varied between $L = 10$ and $L = 14.5$ in order to achieve different compositions x of the $\text{Zn}_x\text{Fe}_{3-x}\text{O}_4$ -films (Section 5.3.1). The number of PLD pulses is 15000, resulting in film thicknesses between 35 and 50 nm, depending on the lens position L . The thicknesses are determined by X-ray reflectivity measurements (Figure 5.8 a).

5.3.1 Composition x of $\text{Zn}_x\text{Fe}_{3-x}\text{O}_4$ thin films

$\text{Zn}_x\text{Fe}_{3-x}\text{O}_4$ thin films with different Zn contents $0 \leq x \leq 1$ were grown by PLD from a stoichiometric ZnFe_2O_4 -target. The Zn content x is adjusted by the position L of the lens, focusing the excimer laser on the target surface. Figure 5.6 shows the dependence of the Zn content x on the lens position L . The position of the lens changes the laser fluence (laser energy density) at the target surface. The energy density is reduced with increasing distance between target and lens (increasing L , larger spot at the target surface). The energy density at the target surface determines the kinetic energy of the plasma particles. Furthermore, the kinetic energy of adatoms at the substrate surface is determined by the initial kinetic energy of the plasma particles and the type and pressure of the background gas (scattering). Since the Ar background pressure is the same for all processes, the change in laser fluence causes a change in the kinetic energy of the adatoms at the substrate surface. The effective temperature of adatoms T^* (referred to as effective surface diffusion temperature in Section 3.1.3) is determined by the substrate temperature and the kinetic energy of the adatoms [286–289]. Therefore, the effective temper-

ature is reduced with increasing distance between target and lens (increasing L).

Lorenz [270] reports different transfer factors of dopant concentration from the target into the film during PLD. The interesting case is the transfer factor of Fe in ZnO. It is determined to be $1.47 \pm 0.16 > 1$. This means that the iron concentration in the film is increased compared to the concentration in the target. The transfer factor is linked to the evaporation temperature and therefore the vapor pressure of the corresponding element. The element with the lower evaporation temperature may evaporate preferably from the substrate surface, and therefore its concentration in the film is decreased compared to the composition in the target. In contrast, the concentration of the element with a higher evaporation temperature will increase. The evaporation temperature of Zn is 907°C , that of Fe is 2861°C [270]. Therefore, the evaporation of Fe is neglectable and the evaporation rate of Zn determines the film composition. If we apply this considerations to the case of ZnFe_2O_4 , we end up with Zn deficient $\text{Zn}_x\text{Fe}_{3-x}\text{O}_4$ thin films.

The dependence of the Zn concentration x on the lens position L can be explained by the assumption that the effective surface temperature (and not the substrate temperature) is crucial for the evaporation of surface atoms. Therefore, a high kinetic energy of adatoms, caused by a high laser energy density at the target, is responsible for the depletion of Zn. By reducing the energy density at the target, T^* decreases, resulting in a reduced evaporation rate of Zn and an increase of the Zn-amount in the thin films. Therefore, changing the lens position L allows to adjust the Zn ratio in the $\text{Zn}_x\text{Fe}_{3-x}\text{O}_4$ thin films grown by PLD.

5.3.2 Structural properties of $\text{Zn}_x\text{Fe}_{3-x}\text{O}_4$ thin films

Figure 5.7 shows RHEED and AFM-topography images of the surface of a $\text{Zn}_x\text{Fe}_{3-x}\text{O}_4$ thin film. The RHEED pattern (Figure 5.7 a) shows five streaks instead of three in the case of MgO and TiN. The additional streaks, appearing between the (00) and (0 \pm 1) spots of MgO and TiN, are due to the doubling of the lattice constant between the rocksalt structure materials (MgO, TiN) and the spinel $\text{Zn}_x\text{Fe}_{3-x}\text{O}_4$. The length of the reciprocal lattice vectors, and therefore the distance between spots in the RHEED-image, are reciprocally proportional to the cubic lattice constant a (Equation (3.7)). Therefore, a doubling of the cubic lattice constant halves the distance between the spots at the RHEED image. The streaky image indicates a smooth, regularly stepped surface. The observed pattern shows an image produced by an electron beam along the [10]-direction of a cubic lattice as it is the case for the MgO-substrate and the TiN film. Therefore, the [10]-directions (in plane [010]) of MgO, TiN and $\text{Zn}_x\text{Fe}_{3-x}\text{O}_4$ are in parallel. This indicates epitaxial, cube on cube growth of $\text{Zn}_x\text{Fe}_{3-x}\text{O}_4$ on MgO / TiN. The narrow width of the streaks points out the absence of small angle rotational domains.

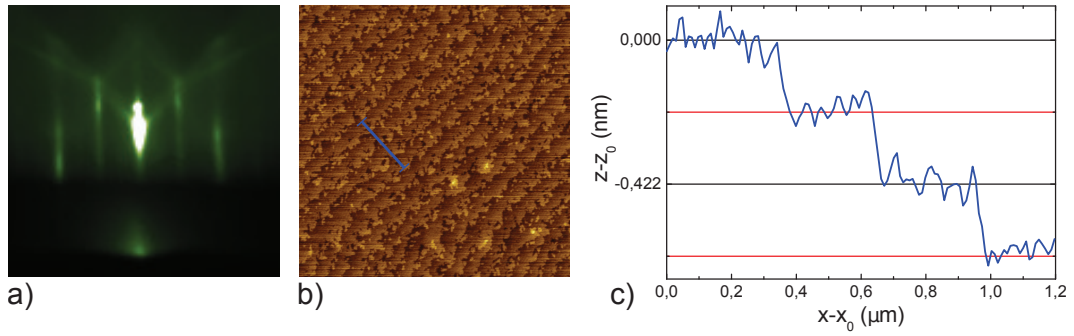


Figure 5.7: Surface of a $\text{Zn}_x\text{Fe}_{3-x}\text{O}_4$ ($x \approx 0.2$) thin film on MgO / TiN. a) RHEED pattern. The electron beam is along the [10]-direction. b) AFM image ($5 \times 5 \mu\text{m}^2$, $h = 0.8 \text{ nm}$). The surface is smooth and terrace steps are clearly visible. Step height is one atomic layer ($\approx 0.21 \text{ nm}$, a quarter lattice constant, see profile c).

The surface morphology, suggested by RHEED, is confirmed by AFM-topography images. Figure 5.7 b) shows a smooth, terraced surface. The uniform step height, determined by extracting height profiles (Figure 5.7 c) is 0.21 nm . This is a quarter lattice constant and corresponds to the distance between two B-site sublattice layers in the spinel structure of $\text{Zn}_x\text{Fe}_{3-x}\text{O}_4$ [331, 332]. Venkateshvaran *et al.* [15] report two-dimensional layer by layer growth of $\text{Zn}_x\text{Fe}_{3-x}\text{O}_4$ in four charge neutral blocks per unit cell (similar to Fe_3O_4 [330]). This corresponds well to the observed surface structure, exhibiting terraces with a step height of 0.21 nm ($= a/4$).

The stepped structure at the surface vanishes for Zn substitution levels $x > 0.4$. Smooth (atomically flat, $\text{RMS} < 0.2 \text{ nm}$), unstructured surfaces are observed for these films. Nevertheless, the RHEED-images remain unchanged, indicating a highly crystalline surface.

No RHEED intensity oscillations were observed during the growth of $\text{Zn}_x\text{Fe}_{3-x}\text{O}_4$. The combination of the smooth, monolayer stepped surface and the lack of RHEED intensity oscillations suggest the two-dimensional step-flow growth mode for the formation of the $\text{Zn}_x\text{Fe}_{3-x}\text{O}_4$ -films.

X-ray reflectivity measurements were used to determine the film thicknesses (an example is shown in Figure 5.8 a). The shape of the reflectivity curves indicates smooth interfaces between substrate and TiN-film, as well as between TiN and $\text{Zn}_x\text{Fe}_{3-x}\text{O}_4$ -film. Also a smooth surface of the $\text{Zn}_x\text{Fe}_{3-x}\text{O}_4$ -film, as confirmed by AFM, is indicated.

Wide angle XRD 2θ - ω -scans show clear peaks of the $\text{Zn}_x\text{Fe}_{3-x}\text{O}_4$ -layers (Figure 5.8 b). The position in 2θ , and therefore the out-of-plane lattice constant, depends on the Zn content x (lens position L). The out-of-plane lattice constant increases with increasing Zn content [15, 17]. A detailed study of the composition dependency of the lattice constant was not possible, since most peaks are overlain by the MgO-substrate peak, making an exact determination of the 2θ position impossible. The Fe_3O_4 film peak ($L = 10$) shows a splitting

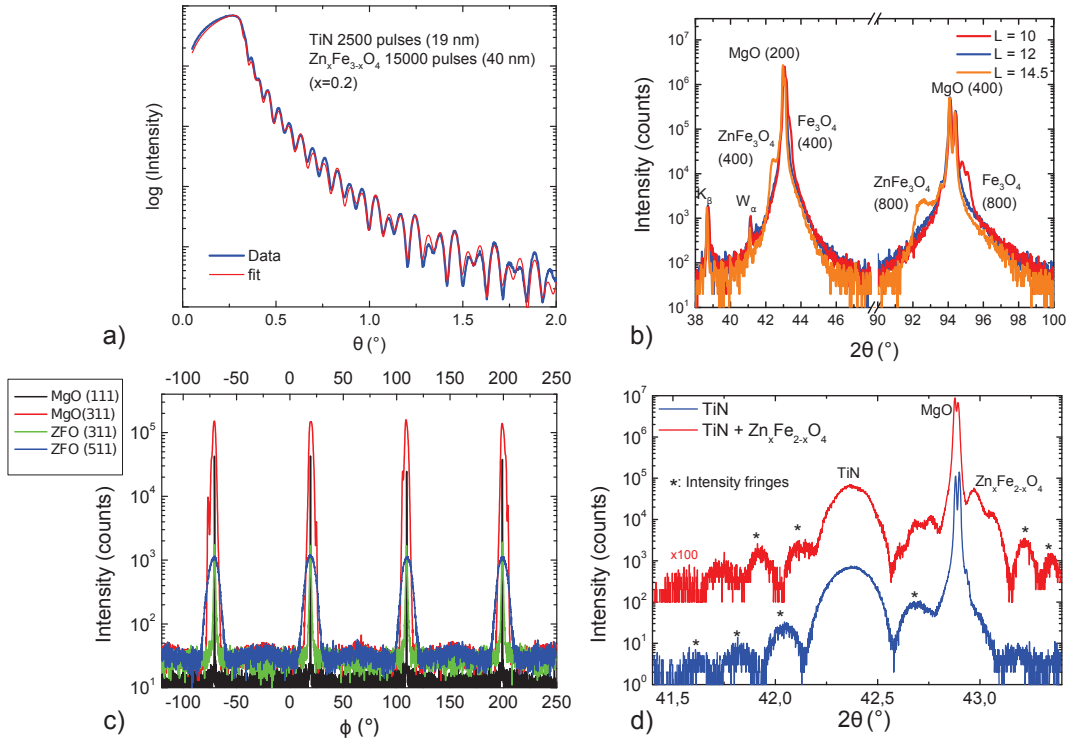


Figure 5.8: a) XRR-curve of a $\text{TiN} / \text{Zn}_x\text{Fe}_{3-x}\text{O}_4$ film stack on MgO ($L = 12$, $x = 0.2$). b) wide angle XRD 2θ - ω -scan of $\text{Zn}_x\text{Fe}_{3-x}\text{O}_4$ thin films on MgO grown at different lens positions L . c) φ -scan of different asymmetric peaks of $\text{Zn}_x\text{Fe}_{3-x}\text{O}_4$ and MgO / TiN. d) High resolution XRD 2θ - ω -scan of a single TiN thin film (blue, see also Figure 5.5 a) and a $\text{TiN} / \text{Zn}_x\text{Fe}_{3-x}\text{O}_4$ double layer (red, lens position $L = 12$). The intensity fringes at the high angle side of the MgO peak are assigned to the $\text{Zn}_x\text{Fe}_{3-x}\text{O}_4$ -layer and yield a thickness of 78 ± 4 nm (30000 pulses).

of $K_{\alpha 1}$ and $K_{\alpha 2}$, indicating a high structural quality of the film. No impurity phases (Fe_2O_3 , ZnO or $\text{Zn}_x\text{Fe}_{3-x}\text{O}_4$ -crystallites with orientations different from (100)) were observed in the wide angle scans.

The epitaxial relation between $\text{Zn}_x\text{Fe}_{3-x}\text{O}_4$ and MgO / TiN was determined by XRD φ -scans (Figure 5.8 c). The asymmetric (311) and (511) peaks of $\text{Zn}_x\text{Fe}_{3-x}\text{O}_4$, as well as the (111) and (311) of MgO / TiN were measured. All four peaks appear at the same φ -angles every 90° , indicating a cube on cube growth of $\text{Zn}_x\text{Fe}_{3-x}\text{O}_4$ on MgO / TiN. Therefore, the epitaxial relation between $\text{Zn}_x\text{Fe}_{3-x}\text{O}_4$ and MgO / TiN is $\text{MgO} / \text{TiN}[100] \parallel \text{Zn}_x\text{Fe}_{3-x}\text{O}_4[100]$ for the out-of-plane direction and $\text{MgO} / \text{TiN}[010] \parallel \text{Zn}_x\text{Fe}_{3-x}\text{O}_4[010]$ for the in-plane direction, as pointed out by the RHEED image.

Figure 5.8 d) shows a high resolution XRD 2θ - ω -scan of a $\text{TiN} / \text{Zn}_x\text{Fe}_{3-x}\text{O}_4$ ($x = 0.2$, $L = 12$) double layer. The scan of the single TiN film is shown for comparison. The $\text{Zn}_x\text{Fe}_{3-x}\text{O}_4$ -peak is located at the high angle side of the MgO-substrate peak, indicating a small lattice constant, in accordance with the small amount of Zn ($x = 0.2$). The intensity fringes at the high angle side of the MgO peak are assigned to the $\text{Zn}_x\text{Fe}_{3-x}\text{O}_4$ -layer. Following Equation (3.20),

the 2θ spacing of the fringes yields a thickness of 78 ± 4 nm (30000 pulses). This is in good agreement with the results of the XRR-analysis. The occurrence of intensity fringes that can be assigned to the $\text{Zn}_x\text{Fe}_{3-x}\text{O}_4$ layer underlines the smooth, abrupt interface between TiN and $\text{Zn}_x\text{Fe}_{3-x}\text{O}_4$, as well as the smooth surface.

The measurements on the structural properties of the $\text{Zn}_x\text{Fe}_{3-x}\text{O}_4$ thin films show a high quality of the films, epitaxially grown on MgO/TiN by PLD. X-ray diffraction confirms the epitaxial growth and indicates a high crystalline quality without any impurity phases or rotational domains. The atomically flat $\text{Zn}_x\text{Fe}_{3-x}\text{O}_4$ surfaces with monolayer terraces should result in optimal interfaces between the magnetic electrode and the MgO tunnel barrier. They also provide optimal conditions for a two-dimensional growth of the thin MgO barrier.

5.3.3 Electrical properties of $\text{Zn}_x\text{Fe}_{3-x}\text{O}_4$ thin films

The film conductivity σ of $\text{Zn}_x\text{Fe}_{3-x}\text{O}_4$ thin films with different Zn content x was measured by the van-der-Pauw method (Section 3.14). These films are directly grown on annealed MgO-substrates without a TiN buffer layer. The individual film thickness was determined by XRR-measurements. Figure 5.9 a) shows the temperature dependent conductivity $\sigma(T)$ of the thin films. A clear linear behavior in the Arrhenius plot indicates the simple thermally activated hopping as transport mechanism (see Equation (2.14)). Therefore, the curves are fitted by

$$\sigma(T) = \sigma_0 \exp\left(-\frac{E_A}{k_B T}\right) \quad (5.2)$$

and the activation energy E_A was determined from the slope. Figure 5.9 b) shows the activation energy E_A in dependence of the Zn concentration x . A clear decrease of E_A with increasing Zn concentration x is observed for $0 \leq x \leq 0.5$. This is in contrast to the results of Venkateshvaran *et al.* [15]. They reported no dependence of $E_A (= 61 - 65 \text{ meV})$ on the composition x of $\text{Zn}_x\text{Fe}_{3-x}\text{O}_4$ thin films grown in Ar.

The obtained activation energies are in the range of $E_A = 46 - 60 \text{ meV}$, which corresponds to values reported in literature. Ziese *et al.* [195] reported $E_A = 52 - 60 \text{ meV}$ in Fe_3O_4 thin films for temperatures above the Verwey temperature. Lorenz *et al.* [139] reported two different activation energies for ZnFe_2O_4 thin films on SrTiO_3 . One is in the range of $E_A = 48 - 55 \text{ meV}$, the other between 70 and 130 meV. This behavior is observed for samples with a room temperature conductivity below 10 S/m. For samples with higher conductivity, the influence of the conduction process with higher activation energy vanishes and the curves become linear in the Arrhenius plot. The slope in this case is due to the small activation energies, as observed in our samples.

The comparison of the temperature dependency of the conductivity in Fe_3O_4 thin films with one activation energy and that in ZnFe_2O_4 thin films on SrTiO_3

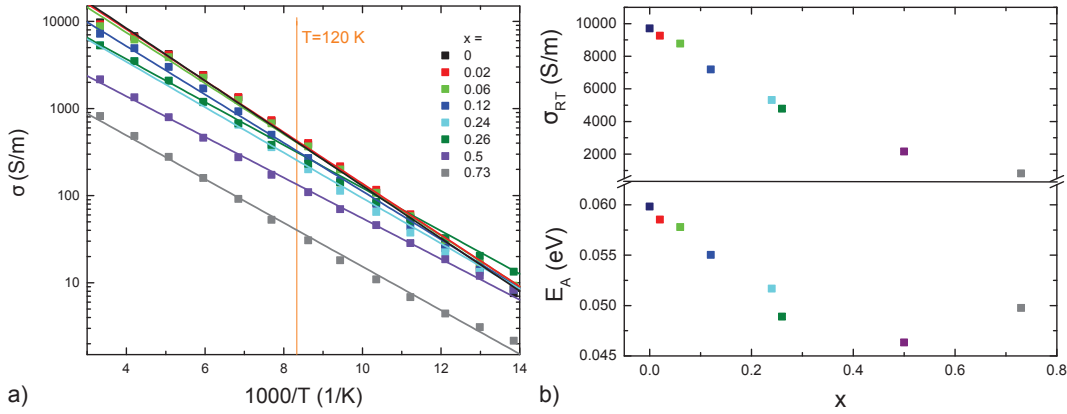


Figure 5.9: a) Arrhenius plot of the thin film conductivity σ vs $1000/T$. Solid lines are fits to Equation (5.2). b) Room temperature conductivity σ_{RT} and activation energy E_A in dependence of the Zn substitution level x .

with two activation energies for samples with low conductivity questions the conclusion of Brachwitz *et al.* [141]. The authors state that the lower activation energies in ZnFe_2O_4 thin films are assigned to hopping conductivity over a single charged oxygen vacancy. Since the lower activation energies are in the range of activation energies observed in Fe_3O_4 , it is more likely that the assigned conduction process is the double exchange mediated hopping between Fe^{2+} and Fe^{3+} on **B**-sites. The process linked to the high activation energies is probably assigned to grain boundary conduction in ZnFe_2O_4 grown on SrTiO_3 (lateral grain size of 150 nm [139]) or MgAl_2O_3 [140].

This considerations might also explain the increase of the activation energy for $x = 0.78$. A closer look shows a curved form of the measured values, which indicates the influence of the process with higher activation energy at higher temperatures. This seems reasonable, since the crystalline quality of thin films decreases at high Zn contents (see Figure 5.8 b, orange line).

The room temperature conductivity σ_{RT} (Figure 5.9 b) decreases with increasing Zn content x , in accordance to the model proposed by Venkateshvaran *et al.* [15] for $\text{Zn}_x\text{Fe}_{3-x}\text{O}_4$ thin films grown in pure Ar (see Section 2.4). The obtained values are comparable to values reported in literature for Fe_3O_4 [195] and $\text{Zn}_x\text{Fe}_{3-x}\text{O}_4$ [15].

The decrease of conductivity with increasing Zn content x is due to the substitution of Fe^{3+} by Zn^{2+} on **A**-sites (see Section 2.4). The substitution of Fe^{3+} by Zn^{2+} on **A**-sites reduces the amount of Fe^{2+} on **B**-sites due to charge neutrality. This reduces the amount of itinerant charge carriers and alters the magnetic interactions inside the **B**-site sublattice. The decrease of Fe^{2+} weakens the ferromagnetic double exchange between Fe^{2+} and Fe^{3+} and strengthens the antiferromagnetic superexchange between Fe^{3+} -cations. The substitution of Fe^{3+} by Zn^{2+} on **A**-sites also weakens the antiferromagnetic superexchange interaction between the **A** and **B**-site lattice due to a dilution of the **A**-site

Fe^{3+} cations. Due to the competition between these interactions, the magnetic moments of **B**-site cations are no longer strictly aligned in parallel. They exhibit a finite spin canting angle, which increases with increasing Zn content x . The dependence of the double exchange hopping amplitude on the angle between **B**-site Fe^{2+} and Fe^{3+} magnetic moments reduces the hopping probability and therefore the conductivity of the system. Both effects, the decrease of itinerant charge carriers and the reduced hopping amplitude due to the finite spin canting angle, result in a decrease of conductivity with increasing Zn content x . The decrease of conductivity with increasing Zn substitution level x indicates the growth of Zn-substituted, Fe_3O_4 without iron vacancies [15]. In contrast to the achieved high conductivity, indicating a good crystalline quality, no Verwey transition is visible in the temperature dependent conductivity measurement of the Fe_3O_4 -sample ($x = 0$). The absence of the Verwey transition indicates structural defects or a deviation from the ideal stoichiometry in the Fe_3O_4 thin film directly grown on MgO (see Section 2.2.2).

5.3.4 Magnetic properties of $\text{Zn}_x\text{Fe}_{3-x}\text{O}_4$ thin films

The magnetic moment is measured in electromagnetic units (emu). In order to be able to compare the measured moments with theoretical calculations, the values are converted to $\mu_B/\text{f.u.}$. The conversion is

$$M(\mu_B/\text{f.u.}) = 10^{-3} \cdot \frac{V_{\text{uc}}}{8 \cdot V_{\text{film}} \cdot \mu_B} M(\text{emu}) \quad (5.3)$$

with the volume of the film V_{film} , the volume of one unit cell V_{uc} and $[M] = 1 \text{ Am}^2 = 10^3 \text{ emu}$. The factor 8 originates from the 8 formula units per unit cell.

Room temperature magnetization

Figure 5.10 a) and b) show the room temperature magnetization M versus applied magnetic field H of $\text{Zn}_x\text{Fe}_{3-x}\text{O}_4$ thin films grown on MgO / TiN. All films show a ferrimagnetic hysteresis loop with a coercive field that decreases with increasing Zn substitution level x (Figure 5.10 d).

The film magnetization does not saturate at an applied field of 1 T and shows a finite slope. This indicates a finite spin canting angle or antiphase boundaries in the films (see Figure 2.2.1 and 2.4).

The film magnetization values at 1 T, as well as the remanent magnetization in dependence of the Zn content x are summarized in Figure 5.10 c). Both values decrease with increasing x , which is in contrast to the descriptive Néel picture [269]. The Néel picture describes the resulting moment of the ferrimagnetic $\text{Zn}_x\text{Fe}_{3-x}\text{O}_4$ as difference between the antiparallel aligned magnetization of the **A** and **B**-site sublattice ($M = |M_{\text{B}}| - |M_{\text{A}}|$). Therefore, the magnetic moment of Fe_3O_4 is calculated to $4\mu_B/\text{f.u.}$, which is the moment of the Fe^{2+} -cation.

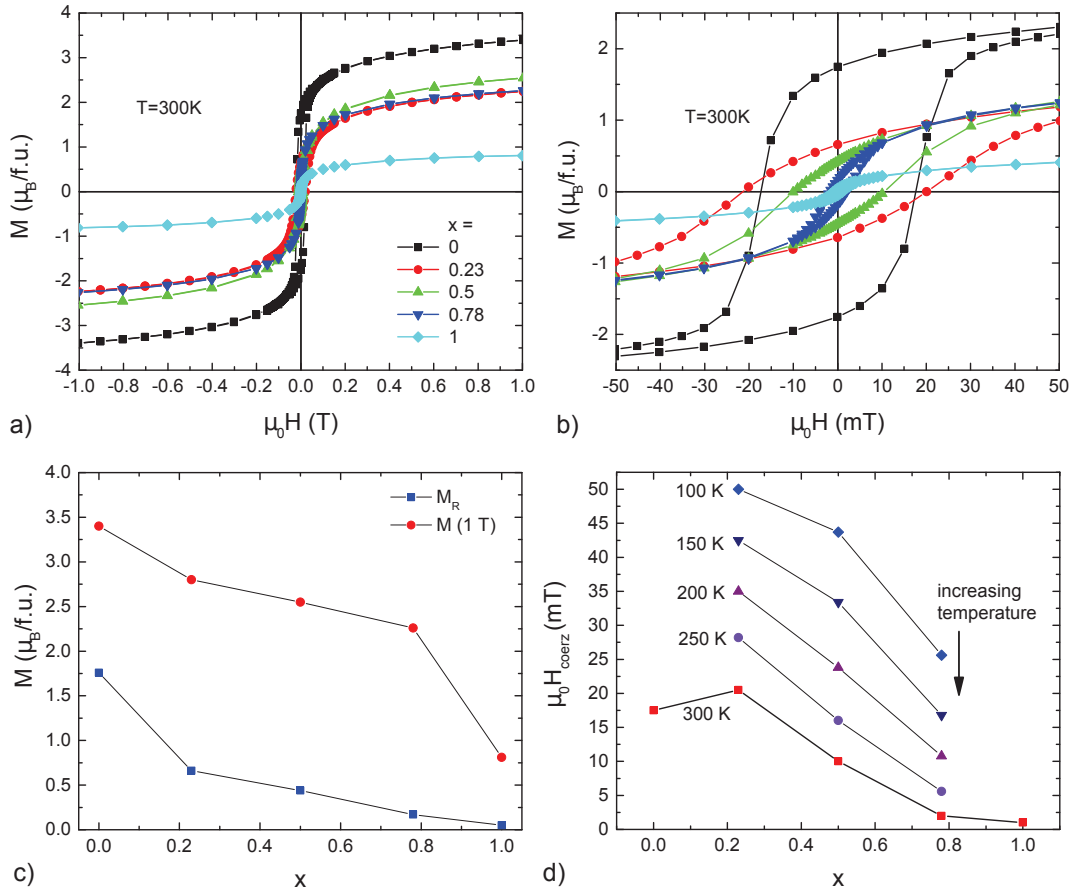


Figure 5.10: a) and b) Room temperature magnetization M of $\text{Zn}_x\text{Fe}_{3-x}\text{O}_4$ thin films versus applied magnetic field H . The magnetic field is applied in-plane, parallel to the $[010]$ -direction. c) Remanent magnetization M_R and magnetization at an applied field of 1 T ($M(1\text{ T})$ is derived from the FC-curve) in dependence of the Zn substitution level x . d) Coercive field in dependence of x and temperature T .

This is due to the complete cancellation of the Fe^{3+} -moments on **A** and **B**-sites. Substitution of **A**-site Fe^{3+} by Zn^{2+} reduces the magnetic moment of the **A**-site lattice by $5\mu_B \cdot x$. Due to charge neutrality, one Fe^{2+} at the **B**-site changes to Fe^{3+} . This increases the moment of the **B**-site by $1\mu_B \cdot x$. This considerations end up in the $(4+6x)$ -rule [269]. This rule states, that the magnetization increases linearly with increasing Zn substitution level x and $M = (4 + 6x)\mu_B/\text{f.u.}$ (see also Section 2.4, page 98).

The Néel picture and the resulting $(4+6x)$ -rule are in contradiction to the experimental results. The magnetization of $\text{Zn}_x\text{Fe}_{3-x}\text{O}_4$ thin films decreases with increasing Zn content x (Figure 5.10 c). These results are in agreement with the experimental findings of Venkateshvaran *et al.* [15] on $\text{Zn}_x\text{Fe}_{3-x}\text{O}_4$ thin films grown in pure Ar. The decreasing magnetization with increasing x can be explained by a finite spin canting angle, caused by the alteration of the magnetic interactions due to the substitution of **B**-site Fe^{3+} by Zn^{2+} , as already pointed out in Section 2.4 and 5.3.3. The substitution with Zn

weakens the antiferromagnetic superexchange interaction between the **A**- and **B**-site sublattice as well as the ferromagnetic double exchange between Fe^{2+} and Fe^{3+} . On the other hand, the antiferromagnetic superexchange between Fe^{3+} on **B**-sites is strengthened. The competition between these interactions leads to a finite angle (spin canting angle) between the magnetic moments of the **B**-site sublattice. This angle increases with increasing Zn substitution level x and strongly decreases the resulting total magnetic moment of $\text{Zn}_x\text{Fe}_{3-x}\text{O}_4$.

Temperature dependency of the magnetization

Figure 5.11 shows temperature dependent magnetization measurements of the different $\text{Zn}_x\text{Fe}_{3-x}\text{O}_4$ -films on MgO / TiN (see Section 3.5). The zero field cooled (ZFC) and field cooled (FC) curves, as well as the remanent magnetization in dependence of the temperature, are shown.

The magnetization of the Fe_3O_4 film, measured at 0.1 and 1 T (Figure 5.11 a and c), shows only a slight temperature dependence, as reported in literature [195]. A hysteresis between FC- and ZFC-curve appears below the Verwey transition. This is probably linked to the structural transition between high and low temperature phase of Fe_3O_4 .

The Fe_3O_4 thin film ($x = 0$) shows a high saturation magnetization of $3.5 \mu_{\text{B}}/\text{f.u.}$ at room temperature and $3.8 \mu_{\text{B}}/\text{f.u.}$ at 120 K, which is rather close to the theoretical value of $4 \mu_{\text{B}}/\text{f.u.}$. The film also exhibits a clear Verwey-transition at $T_{\text{V}} = 117 \text{ K}$ (Figure 5.11 b). Both results state the good quality (stoichiometry and structure) of the Fe_3O_4 thin film grown on MgO / TiN (Figure 2.9).

Due to the complexity of the magnetic interactions and their alterations due to the substitution of Fe by Zn (see Section 2.4), the formation of a spin glass state is expected in $\text{Zn}_x\text{Fe}_{3-x}\text{O}_4$ [140]. In order to figure out the magnetic state in the $\text{Zn}_x\text{Fe}_{3-x}\text{O}_4$ thin films, temperature dependent magnetization measurements were performed (Figure 5.11).

The ZFC- and FC-curves of $\text{Zn}_x\text{Fe}_{3-x}\text{O}_4$ thin films with $x > 0$, measured at an applied field of 1 T, show a linear temperature dependence of the magnetization at temperatures larger than the Verwey temperature ($T > 120 \text{ K}$) (Figure 5.11 c). A hysteresis is observed in the ZFC- and FC-curves measured in an applied magnetic field of 0.1 T (Figure 5.11 a). The temperature, where the FC- and ZFC-curves disconnect (irreversibility, T_{irr}), as well as the position of the maximum in the ZFC-curve (T_{max}), decreases with increasing Zn content x . The hysteresis is absent in an applied field of 1 T. Both features, the linear temperature dependency and the hysteresis at low fields, as well as the shape of the ZFC-curve, can be assigned to spin glass behavior in $\text{Zn}_x\text{Fe}_{3-x}\text{O}_4$ [140, 246].

Another explanation for the hysteresis and the shape of the ZFC-curve are magnetic domain dynamics [140]. The presence of domain walls in ferromagnets leads to a similar behavior. Chen *et al.* [140] report similar hysteresis effects in

the temperature dependent magnetization of ZnFe_2O_4 thin films. They linked the position of the ZFC-curve maximum to the temperature dependency of the coercive field of the ZnFe_2O_4 thin films. This dependency states, that the hysteresis as well as the form of the ZFC-curve is a magnetic domain effect [140]. A similar ansatz can explain the dependence of the ZFC-peak position on the Zn substitution level x . The coercive fields of the $\text{Zn}_x\text{Fe}_{3-x}\text{O}_4$ thin films decrease with increasing Zn content x . They also increase with decreasing temperature (see Figure 5.10 d). Chen *et al.* [140] linked the position of the ZFC-curve maximum (T_{max}) to the temperature dependency of the coercive field. The increase of the coercive field with decreasing temperature is similar for all Zn substitution levels x , but the absolute values of $H_{\text{coerz}}(T)$ increase with decreasing zinc content x . Since the coercive fields $H_{\text{coerz}}(T)$ decrease with increasing x , also the position of the ZFC-curve maximum (T_{max}) shifts to lower temperatures, as observed in our samples. This behavior indicates magnetic domain dynamics [140], and not spin glass behavior, as reason for the observed hysteresis in ZFC- and FC-cooled curves. Also the round shapes of the $M(H)$ -curves and a small coercive squareness (slope at the coercive field H_C) indicate the presence of magnetic domain walls in the $\text{Zn}_x\text{Fe}_{3-x}\text{O}_4$ films.

The linear behavior of the $M(T)$ -curves at an applied field of 1 T is also assigned to spin glass behavior [140]. But this behavior also arises in R-type ferrimagnets [140]. In this materials, the two magnetic sublattices show different internal coupling strengths and therefore different temperature dependencies. Chen *et al.* [140] fitted the Néel-model for antiferromagnets to the temperature dependent magnetization of ZnFe_2O_4 and observed a rather good agreement between experiment and theory. This result states the antiferromagnetic nature of ZnFe_2O_4 as reason for the linear temperature dependence of magnetization.

A further hint, confirming the ferrimagnetic nature of $\text{Zn}_x\text{Fe}_{3-x}\text{O}_4$ is given by Venkateshvaran *et al.* [15]. They observed an upward hump in the remanent magnetization and assigned this behavior to two sublattices with different strength and temperature dependence (see Section 2.4). A similar behavior is observed in our $\text{Zn}_x\text{Fe}_{3-x}\text{O}_4$ -samples. The remanent magnetization of the sample with $x = 0.23$ shows a slight hump at a temperature of approximately 220 K, which can be explained by the temperature dependency of the two sublattices (see Figure 5.11 b). Both explanations of the temperature dependency of the magnetization are based on the Néel-model of antiferromagnets. This states, that the linear temperature dependency of the magnetization arises from the ferrimagnetic nature of $\text{Zn}_x\text{Fe}_{3-x}\text{O}_4$.

Nevertheless, these findings can not completely rule out the possibility of spin glass behavior and complementary measurements have to be performed to gain clarity on the magnetic state in $\text{Zn}_x\text{Fe}_{3-x}\text{O}_4$.

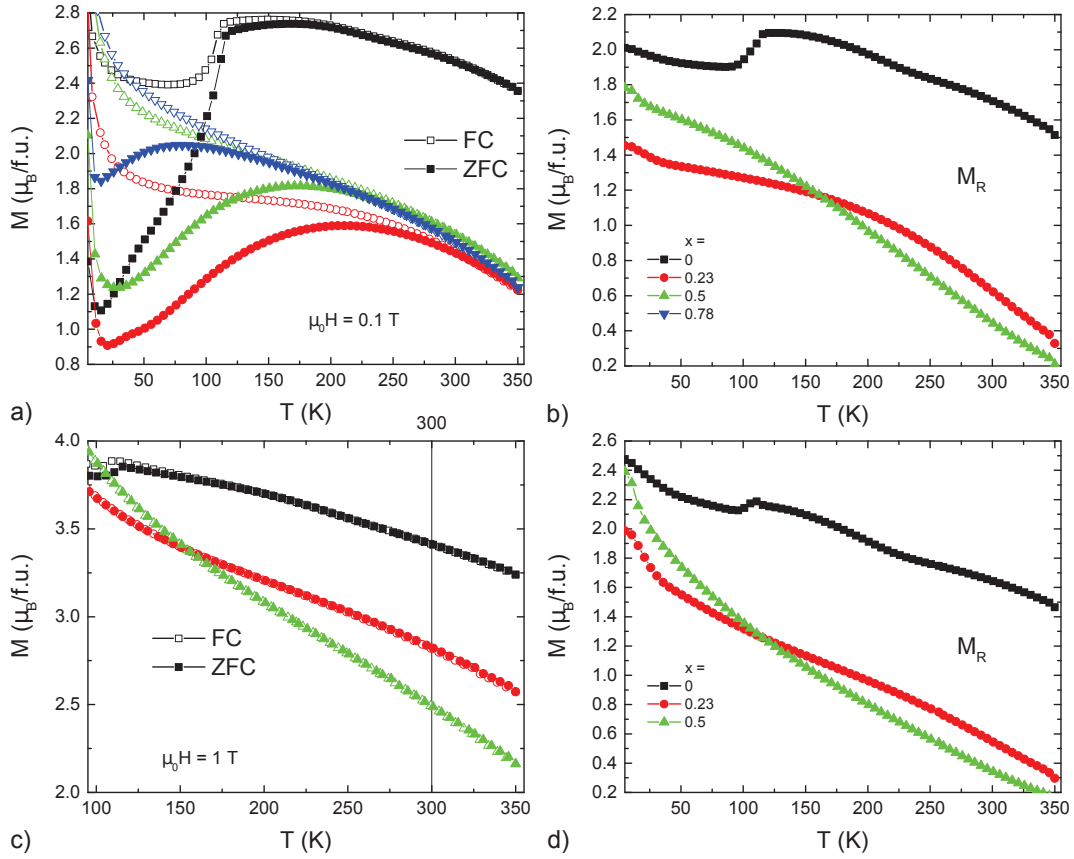


Figure 5.11: Zero field cooled curves (ZFC), field cooled curves (FC) and remanent magnetization (M_R) of $\text{Zn}_x\text{Fe}_{3-x}\text{O}_4$ -thin films at $\mu_0 H = 0.1 \text{ T}$ (a,b) and 1 T (c,d). The Fe_3O_4 ($x = 0$) film shows a clear Verwey-transition at 117 K.

5.4 MgO barrier

Epitaxial MgO is used as barrier material in the MTJs prepared in the framework of this thesis. MgO is an insulator with a band gap of 7.8 eV, giving an expected barrier height of 3.9 eV [333]. MgO is used successfully as barrier material in magnetic tunnel junctions (see Section 1.1.4) and huge TMR-values are predicted due to symmetry filtering of tunneling electrons (Figure 1.2.5). Even though MgO barriers are implemented successfully into MTJ-elements, the observed barrier heights are one order of magnitude smaller than expected [333]. This is assigned to defect states inside the barrier.

Nevertheless, significant TMR-values have been obtained in Fe_3O_4 -based MTJs with a MgO-barrier, showing the potential of this material combination (see Section 2.2.3, [233, 234, 237, 238]). On the other hand, also huge problems with MgO-barriers in Fe_3O_4 -based MTJs are reported [229, 235, 236]. These problems are assigned to the $\text{Fe}_3\text{O}_4/\text{MgO}$ -barrier interface (Section 2.2.3).

Due to the high expected TMR-values and the possibility to grow MgO epitaxially on $\text{Zn}_x\text{Fe}_{3-x}\text{O}_4$, MgO is used as barrier material in this work.

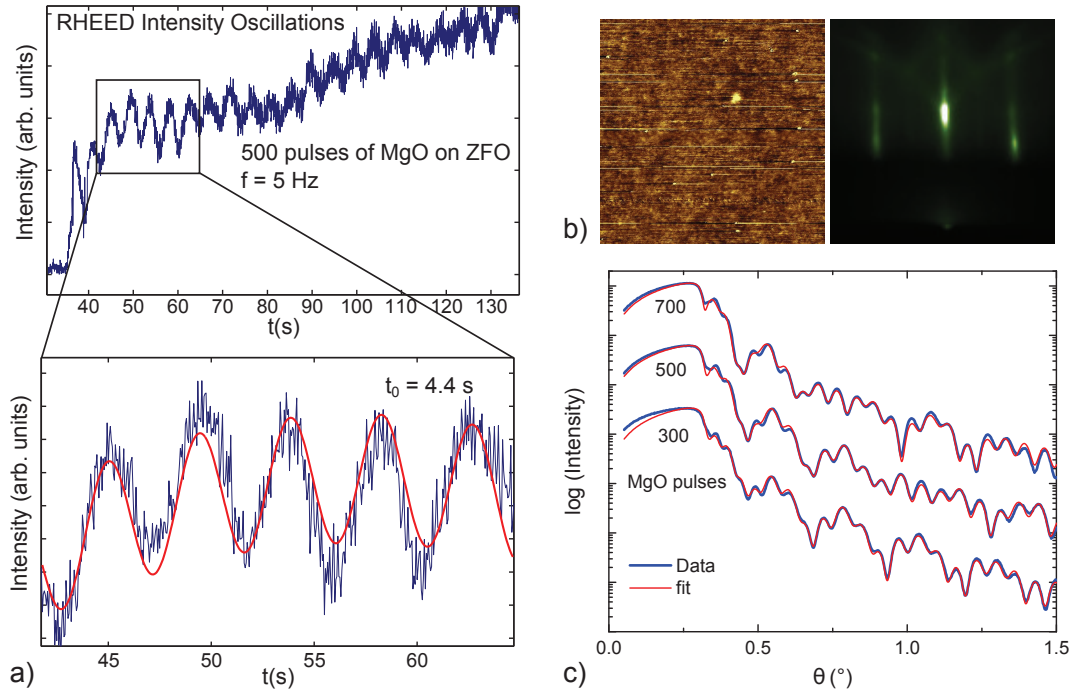


Figure 5.12: a) RHEED intensity during the deposition of the MgO-barrier. Clear intensity oscillations are visible. The period time yields a growth rate of 0.95 nm per 100 pulses. b) AFM topography ($5 \times 5 \mu\text{m}^2$, $h = 1 \text{ nm}$) and RHEED image of a MgO-barrier surface. The electron beam is along the $[10]$ -direction. c) X-ray reflectivity (XRR) curves of the test samples for MgO thickness determination. The obtained thicknesses are summarized in Table 5.1.

The thin MgO films are grown by PLD on top of the $\text{Zn}_x\text{Fe}_{3-x}\text{O}_4$ -layer. PLD parameters are summarized in Table 4.1. Substrate temperature during deposition is 400°C and the argon background pressure is set to $3 \cdot 10^{-2} \text{ mbar}$. Excimer laser pulse energy is 500 mJ with a repetition frequency of 5 Hz. The $20 \times 8 \text{ mm}^2$ laser aperture is used and the lens position is $L = 10$. MgO-barriers are produced with different thicknesses, defined by the number of laser pulses. Used pulse numbers are 300, 500 and 700 pulses.

5.4.1 Growth and structural properties

The tunneling barrier in MTJs must provide a homogenous thickness and a smooth surface. This is achieved by a two-dimensional layer by layer growth mode of the MgO thin film. The growth of the MgO film is monitored by RHEED (Figure 5.12 a) and intensity oscillations due to the layer by layer growth are observed. The growth rate is determined to be 0.95 nm per 100 pulses by the periodicity of the intensity oscillations ($t_0 = 4.4 \text{ s}$, the thickness of one monolayer is $0.21 \text{ nm} = a_{\text{MgO}}/2$).

Table 5.1: Thin film thicknesses determined by XRR and RHEED intensity oscillation analysis. The MgO thickness is also determined by fitting I - V -curves to the BDR formula (Equation (5.4)).

	pulses	XRR	RHEED	BDR-fit
TiN	2500	19 nm	19 nm	
$\text{Zn}_x\text{Fe}_{3-x}\text{O}_4$	10000	27 nm		
MgO	300	2.7 nm	2.9 nm	1.3 nm
	500	4.5 nm	4.8 nm	1.8 nm
	700	6.2 nm	6.7 nm	2.7 nm
$\text{Zn}_x\text{Fe}_{3-x}\text{O}_4$	5000	14 nm		

The RHEED-images of the MgO-surfaces of thin films grown on $\text{Zn}_x\text{Fe}_{3-x}\text{O}_4$ show well defined streaks assigned to the cubic structure of MgO and a smooth surface (Figure 5.12 b). The narrow streaks indicate the absence of small angle rotational domains and therefore epitaxial growth of MgO on $\text{Zn}_x\text{Fe}_{3-x}\text{O}_4$. The epitaxial relations are $\text{MgO} / \text{TiN} / \text{Zn}_x\text{Fe}_{3-x}\text{O}_4[100] \parallel \text{MgO}[100]$ for the out-of-plane direction and $\text{MgO} / \text{TiN} / \text{Zn}_x\text{Fe}_{3-x}\text{O}_4[010] \parallel \text{MgO}[010]$ for the in-plane direction. Kikuchi lines are visible in the RHEED images, indicating a high crystalline quality of the MgO-surface. The AFM-topography images show a smooth, unstructured surface of the MgO layer (Figure 5.12 b).

In order to confirm the growth rate obtained by RHEED, X-ray reflectivity measurements (XRR) were carried out on different test samples (Figure 5.12 c). The test samples are layer stacks of $\text{MgO}(\text{substrate}) / \text{TiN} / \text{Zn}_x\text{Fe}_{3-x}\text{O}_4 / \text{MgO} / \text{Zn}_x\text{Fe}_{3-x}\text{O}_4$. Lens position for $\text{Zn}_x\text{Fe}_{3-x}\text{O}_4$ is $L = 12$ ($x \approx 0.2$). The derived film thicknesses are summarized in Table 5.1. The different values of the MgO-barrier thickness derived by XRR and RHEED are in good agreement. In the following analysis of I - V -curves, MgO-barrier thicknesses of 2.8 nm (300 pulses), 4.7 nm (500 pulses) and 6.5 nm (700 pulses) are used as fixed thickness values of the MgO barriers grown with the different pulse numbers.

5.4.2 I-V-measurements and barrier parameter

In order to determine the quality and the tunneling barrier parameter thickness d and mean barrier height Φ of the MgO barriers grown by pulsed laser deposition, electrical measurements (I - V -curves) were performed on different tunneling structures. Room temperature I - V -curves without magnetic field are measured on test samples with a gold top contact. The samples are simply the usual layer stack $\text{MgO}(\text{substrate}) / \text{TiN} / \text{Zn}_x\text{Fe}_{3-x}\text{O}_4$ ($L=12$) / MgO with gold contact pads on top. The contact pads are defined by a shadow mask and produced by thermal evaporation of Au. The contact shape is circular with diameters of 225, 340 and 390 μm , respectively. Electrical measurements are carried out in the Suss MicroTec PA200 wafer prober. Completely structured

MTJ-elements are used for temperature dependent measurements. The lens position for the $\text{Zn}_x\text{Fe}_{3-x}\text{O}_4$ film is $L = 12$ ($x \approx 0.2$). The I - V -curves are measured in the parallel magnetization state in an applied magnetic field of 800 mT. The current is normalized to the contact area A ($j = I/A$, current density). The BDR-model (Equation (1.38)) is fitted to the j - V -curves in order to determine the barrier parameter thickness d and mean barrier height Φ (the mean barrier thickness is denoted as $\bar{\Phi}$ and not as Φ in this chapter). The BDR-model is used due to the expected asymmetric barriers caused by the different electrode materials.

To achieve high TMR-values, the conduction through the barrier must be dominated by tunneling. A possibility to identify the nature of the current through a barrier is the use of the Rowell criteria, developed for superconducting tunneling [334]. Åkerman *et al.* [335, 336] adopt these criteria to the case of normal metal / insulator-tunneling. The criteria for tunneling as dominant conduction mechanism are:

1. A non-linear j - V -curve that is well fitted by the BDR-model.
2. An exponential thickness dependence of the conductance ($G(0)$) or resistance (RA).
3. An insulator-like temperature dependence of the conductance or resistance.
4. A slight temperature dependence of the barrier parameter determined by the BDR-model. The thickness d decreases and the mean barrier height Φ increases with decreasing temperature.

Åkerman *et al.* further state that the presence of small metallic conduction paths (pinholes) changes the temperature dependence of the observed barrier parameter thickness d and mean barrier height Φ . The thickness d increases and the mean barrier height Φ decreases with decreasing temperature in the presence of pinholes.

It is important to note that the apparent barrier parameter determined by fitting the BDR-model to the j - V -curves are just fitting parameter without any real physical significance [335]. They do not reflect the real barrier properties since they are influenced by many parameters neglected in the BDR-model. These influences are e.g. thickness fluctuations over the contact area, pinholes and defect states inside the barrier.

Room temperature barrier parameter

The apparent tunneling barrier parameter d and Φ are determined by fitting the BDR-model Equation (1.38) to the measured j - V -curves. The used fitting

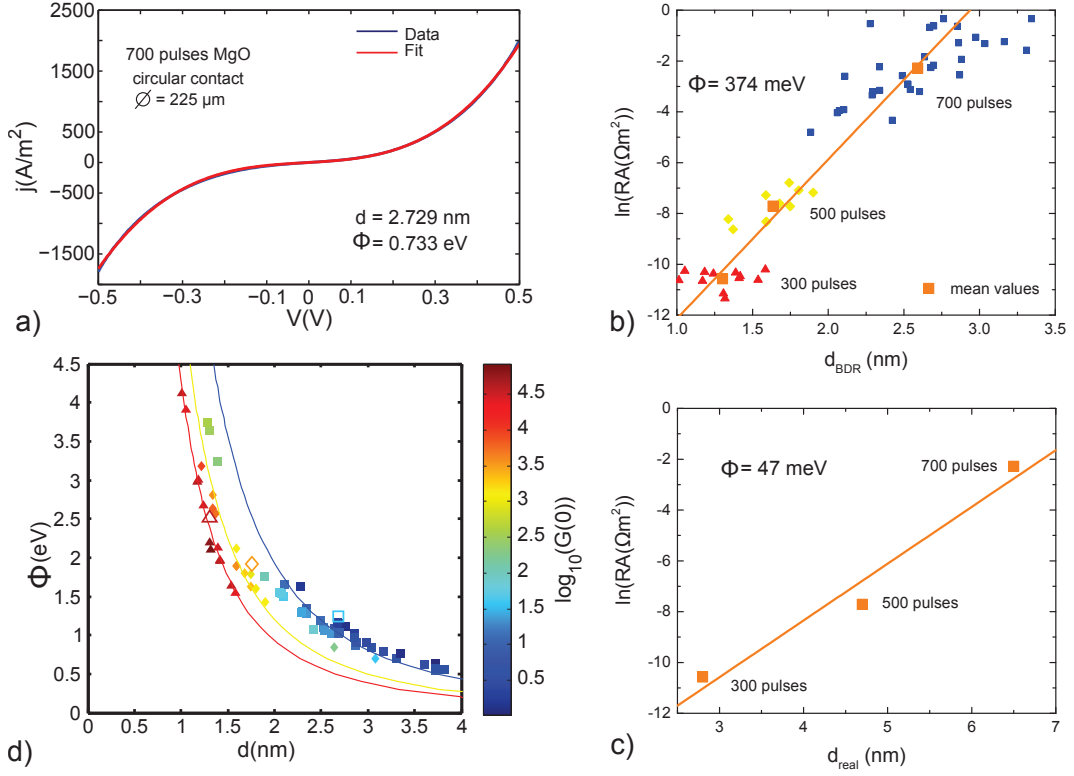


Figure 5.13: a) j - V curve of a MgO barrier grown with 700 PLD-pulses. The fit is to Equation (5.4). b) Area-resistance ($RA = 1/G(0)$) values of different contacts over the MgO barrier thickness, obtained by fitting Equation (5.4) to the j - V -curves. The slope gives a barrier height of 374 meV (Equation (5.5)). c) Area-resistance (RA) mean values of different contacts over the MgO barrier thickness, obtained by RHEED and XRR (Table 5.1). The slope gives a barrier height of 47 meV. d) Barrier height over barrier thickness obtained by fitting Equation (5.4) to the j - V -curves. The color code shows the $G(0)$ -value of the respective contact. The large open symbols are the mean values over the different samples (different MgO-pulse number). The lines are plots of Equation (5.6) for different values of $G(0)$.

formula for the current density is Equation (1.38):

$$\begin{aligned}
 j(V) &= \int_{j(0)=0} G(V) dV = \\
 &= G(0) \left[V - \left(\frac{e\sqrt{2m}}{24\hbar} \frac{d\Delta\Phi}{\Phi^{\frac{3}{2}}} \right) \cdot V^2 + \left(\frac{e^2 m}{12\hbar^2} \frac{d^2}{\Phi} \right) \cdot V^3 \right] \quad (5.4)
 \end{aligned}$$

with the conductance at $V = 0$ V

$$G(0) = \frac{e^2 \sqrt{2m} \sqrt{\Phi}}{4\pi^2 \hbar^2 d} \cdot \exp \left(-\frac{2\sqrt{2m}}{\hbar} d \sqrt{\Phi} \right). \quad (5.5)$$

An example j - V -curve and the corresponding fit is shown in Figure 5.13 a). The BDR-model fits well to most measured j - V -curves with a goodness of fit of $R^2 > 0.95$. Therefore, the fits are also in the 10% range that is given as error for the BDR-model [95]. The fits to the BDR-model used to obtain the apparent barrier parameter are all inside this range, values obtained by fits outside this range were excluded from the following considerations.

In conclusion, the BDR-model fits well to the measured j - V -curves and the first criterion for tunneling as dominant conduction mechanism is fulfilled for the PLD-grown MgO-barriers.

The values determined from the j - V -curves by fitting the BDR-model are the barrier parameter thickness d and mean barrier height Φ . The values of $G(0)$ and RA are simply determined from the slope of the j - V -curve at $V = 0$ V.

Figure 5.13 b) and c) show the dependence of the resistance-area product ($RA = 1/G(0)$) on the barrier thickness d . The mean values of RA -products of the junctions with different barrier thickness are $2.6 \cdot 10^{-5} \Omega\text{m}^2$ for 300 pulses, $5.3 \cdot 10^{-4} \Omega\text{m}^2$ for 500 pulses and $2.0 \cdot 10^{-1} \Omega\text{m}^2$ for 700 pulses of MgO, respectively. The thickness values are obtained by BDR-fits (d_{BDR} , Figure 5.13 b) and XRR / RHEED (d_{real} , see Table 5.1, Figure 5.13 c). Both plots show an exponential dependency of the RA -value on the barrier thickness. The solid red lines are fits to Equation (5.5). The barrier height is determined from the slope. It is $\Phi = 374 \text{ meV}$ in case of the thickness values derived by the BDR-model (d_{BDR}). This is in good agreement with literature values for MgO barriers [333]. The small values (compared to the expected 3.9 eV) are explained by defects (oxygen vacancies) inside the barrier. The barrier height determined using the structural thicknesses (d_{real} , Figure 5.13 c) is one order of magnitude smaller ($\Phi = 47 \text{ meV}$). This might be explained by thickness variations inside the barrier. Since an overproportional amount of the tunnel current flows through thinner areas, the effective tunneling thickness is smaller than the structural thickness obtained by XRR and RHEED. This behavior decreases the slope of the $RA(d)$ -curve and therefore the obtained barrier height Φ .

Due to the observed exponential dependency of RA on d , the second criterion for tunneling as dominant conduction mechanism is fulfilled.

The determination of the barrier thickness d by fitting the BDR-model to the j - V -curves is not reliable in our case. It can not be determined individually from the barrier height due to defects inside the barrier, as shown in the next paragraph. Therefore, the obtained thickness values can not be used to determine a reliable barrier height Φ from the $RA(d)$ -curve. Nevertheless, the exponential behavior is reproduced and the determined barrier height is comparable to values reported in literature [333], which might be surprising.

The barrier parameters obtained by fitting the BDR-model to j - V -curves of tunnel junctions with different nominal barrier thickness, defined by 300 (rect-

angles), 500 (diamond) and 700 (squares) PLD-pulses during MgO-growth, are summarized in Figure 5.13 d). A clear correlation between the apparent barrier parameters is observed.

In the BDR-model, the barrier thickness d and the barrier height Φ are connected by $G(0)$ (Equation (5.5)). Rearranging and solving for d yields:

$$d(\Phi) = \frac{\text{lambertW}\left(\frac{A^2 B \Phi}{G(0)}\right)}{8em}, \quad A = \frac{2\sqrt{2m}}{\hbar}, \quad B = \frac{e^2}{8\pi^2 \hbar}. \quad (5.6)$$

LambertW is the inverse function of $x \cdot \exp(x)$. The solid lines in Figure 5.13 d) are plots to Equation (5.6) with different values of $G(0)$. The used values are the mean values of $G(0)$ obtained in j - V -curves of tunnel junctions with the same nominal thickness. The plots after Equation (5.6) describe the observed dependence of d and Φ very well. This states a problem of the BDR-model, namely the strong correlation of the parameters d and Φ , making it impossible to determine the parameters independently. This might explain the discrepancies in barrier parameters obtained from the j - V -curves of different tunnel junctions [337].

In order to achieve more reliable values of the barrier height, and to get rid of the dependence between d and Φ , barrier thickness variations are taken into account. Therefore, the thickness of the MgO-barrier is approximately described by a normal (Gaussian) distribution

$$P(d) = \frac{1}{\sigma_d \sqrt{2\pi}} \cdot \exp\left(-\frac{1}{2} \left(\frac{\bar{d} - d}{\sigma_d}\right)^2\right) \quad (5.7)$$

with the mean barrier thickness \bar{d} and the standard deviation σ_d .

The basis of this approach is the BDR-model and the resulting fit function is

$$j(\sigma_d, \Phi, \Delta\Phi, V) = \int_a^b P(d, \sigma_d) F(d, \Phi, \Delta\Phi, V) dd. \quad (5.8)$$

With $F(d)$ the BDR-current density (Equation (5.4)) and the integration limits $a, b = \bar{d} \pm 10\sigma_d$, respectively. The fit parameters are now σ_d , Φ and $\Delta\Phi$. The mean barrier thickness \bar{d} is fixed to the value obtained by XRR and RHEED (Table 5.1), namely 2.8 nm (300 MgO-pulses), 4.7 nm (500 pulses) and 6.5 nm (700 pulses).

This model was developed in collaboration with M.Sc. Daniel Splith and is based on the work of Werner and Güttler [338] on inhomogeneities in Schottky-barriers. Fitting was done with a MATLAB-based software written by M.Sc. Daniel Splith.

The results are presented in Figure 5.14. The standard deviations of the thickness are determined to be 0.4 nm (300 pulses), 0.65 nm (500 pulses) and 6.5 nm (700 pulses). This is approximately $0.14 \cdot \bar{d}$ and in the range of roughness values

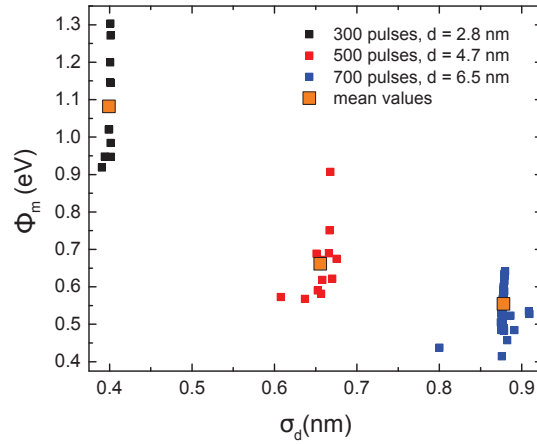


Figure 5.14: Barrier parameters σ_d and Φ , derived by fitting the j - V -characteristics of different tunnel junctions by the expanded BDR-model (Equation (5.8))

obtained by XRR-measurements. The mean barrier heights Φ are determined to be 1.08 eV, 0.66 eV and 0.55 eV (mean values), respectively. Since these values are only fit parameters also in the expanded BDR-model, the values do not reflect the real barrier height. But a conclusion can be drawn from the trend of Φ . The decreasing barrier height with increasing thickness indicates the presence of barrier defects, caused by the growth process. In PLD, these defects are droplets. Droplets are small crystallites that are ejected from the target surface by the excimer laser and deposited at the sample surface. The AFM-topography images of MgO barriers show clear hints for the formation of small droplets (Figure 5.12 b). The droplet density increases with increasing number of PLD-pulses. Since the droplets can provide a metallic conduction path through the barrier, they can be regarded as pinholes. The increasing amount of pinholes due to droplets decreases the observed value of the barrier height with increasing number of PLD-pulses.

Temperature dependency of the barrier parameter

Temperature dependent j - V -measurements were carried out on MTJs. In order to characterize the MgO-barriers, the resistance at $V = 0$ V and the barrier parameter d and Φ are determined in dependence of the temperature. The barrier parameters are determined by fitting the stock BDR-model to the j - V -curves.

Figure 5.15 a) shows the temperature dependence of the resistance of two MTJs with a barrier thickness of approximately 2.8 nm (300 pulses) and a $\text{Zn}_x\text{Fe}_{3-x}\text{O}_4$ / Co-contact without a MgO-barrier. The resistance of the $\text{Zn}_x\text{Fe}_{3-x}\text{O}_4$ / Co-contact shows a neglectable temperature dependence, whereas the MTJs show a clear insulator like temperature dependence. Therefore the observed de-

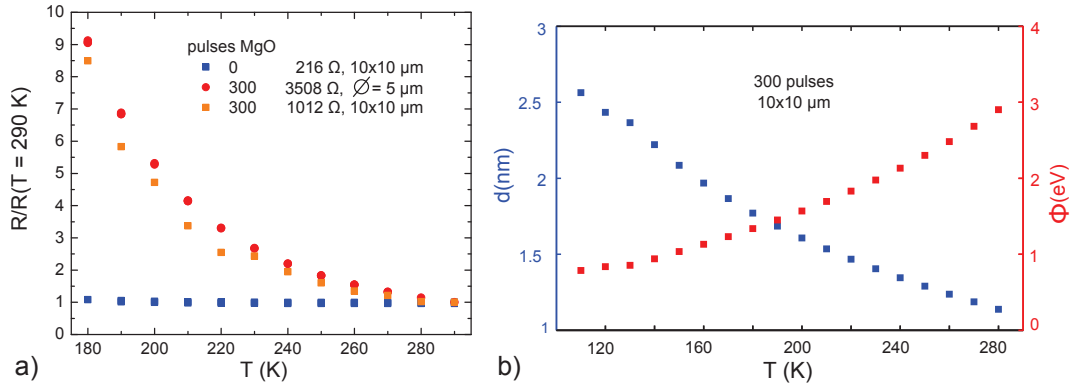


Figure 5.15: a) Temperature dependence of the resistance of two MTJs with a barrier thickness of approximately 2.8 nm (300 pulses) and a $\text{Zn}_x\text{Fe}_{3-x}\text{O}_4$ / Co-contact (without MgO-barrier, zero pulses). The given resistance values are obtained at room temperature ($R(T=290\text{ K})$). b) Temperature dependence of barrier parameters d and Φ , obtained by fitting the BDR-model to j - V -curves obtained at different temperatures.

pendance can be attributed to the tunnel barrier. The observed temperature dependence is huge compared to the temperature dependence reported in [335, 336]. Åkerman *et al.* report an increase of resistance by a factor of two when cooling down to 4 K and state that this kind of behavior indicates tunneling as dominant conduction mechanism. The resistance of our tunnel contacts increases by a factor of nine when cooled down to 180 K. A similar behavior is reported by Reisinger [339] on Fe_3O_4 / MgO / Co tunnel junctions containing PLD-grown barriers. He states that this behavior is linked to barrier defects like oxygen vacancies or impurities, allowing tunneling over thermally activated states inside the barrier. This leads to a decrease of resistance at higher temperatures and a quick increase with decreasing temperature. Nevertheless, the Rowell criterion on insulating temperature dependence is also fulfilled in this case, since the transport seems to be dominated by tunneling over thermally activated states, and not by ballistic transport.

The temperature dependency of the apparent barrier parameter d and Φ of a MTJ, obtained by the BDR-model, is shown exemplary in Figure 5.15 b). The barrier thickness d increases with decreasing temperature, whereas the height Φ decreases. Åkerman *et al.* [335, 336] stated that this kind of behavior is linked to the presence of pinholes in the barrier.

Therefore, the temperature dependency of the apparent barrier parameter support the conclusion drawn from the thickness dependency of the barrier height obtained by fits to the expanded BDR-model.

The MgO-barriers grown by PLD on $\text{Zn}_x\text{Fe}_{3-x}\text{O}_4$ fulfill the first three criteria showing that tunneling is the dominant conduction mechanism through the

barrier. Therefore, the barriers should be suitable for the application in MTJs in order to observe TMR in $\text{Zn}_x\text{Fe}_{3-x}\text{O}_4$.

Nevertheless, the analysis of the j - V -characteristics and the apparent barrier parameter gives hints for the presence of pinholes in the barrier, caused by droplets formed by the PLD-film deposition. The presence of pinholes provides a spin-independent conduction path through the barrier and therefore will decrease the observed TMR-values.

A second spin-independent conduction path is possibly present in the processes contacts consisting of ion beam etched pillars. The measured resistances of the complete MTJs with a Co-top electrode and a MgO-barrier grown by 300 PLD-pulses result in a mean RA-product of $\text{RA} \approx 10^{-7} \Omega\text{m}^2$. This is two orders of magnitude smaller than the RA-product of the large test contacts with an evaporated Au top electrode. This reduction of resistance is an indication of an additional conduction path, probably caused by redeposited material at the contact edges during the etch process. This conduction channel might also additionally contribute to the temperature dependence of the apparent barrier parameter described by the fourth Rowell criterion.

As shown above, the barrier parameter d and Φ obtained by fitting the BDR-model to the j - V -curves of our tunnel junctions only results in apparent barrier parameter that do not reflect the real properties of the MgO barrier. A certain dependence between the parameter was observed. The main reason for this behavior might be the fact that the BDR-model assumes perfect barriers. Our barriers are far from perfect since they seem to contain several defects like oxygen vacancies, droplets, edge conduction and thickness inhomogeneities. All these defects make it hardly possible to extract reliable barrier parameter by fitting the BDR-model to measures j - V -curves. Nevertheless, some conclusions about the nature of the defects can be made, as demonstrated above.

5.5 Co thin films

Cobalt is used as top magnetic electrode in the prepared MTJ-structures. The Co thin film is also grown by PLD. This gives the possibility to grow the whole layer stack ($\text{Zn}_x\text{Fe}_{3-x}\text{O}_4 / \text{MgO} / \text{Co}$) in one step, without exposing the barrier to ambient air due to the transport into another chamber. The growth of Co by PLD on top of the MgO-barrier creates some problems. Three dimensional island growth seems to be the thermodynamically preferred growth mode (Section 3.1.3). In high mobility conditions (large energy density at the target surface and a growth temperature of 400°C), the films grow in large islands and no closed thin films are formed. Figure 5.16 a) shows a SEM-cross section of such a film. Adjusting the growth conditions in order to decrease the mobility of adatoms allows to grow closed Co thin films on top of MgO. A SEM-cross section of a smooth, closed thin film is shown in Figure 5.16 b). The optimized PLD growth parameter are summarized in Table 4.1. The

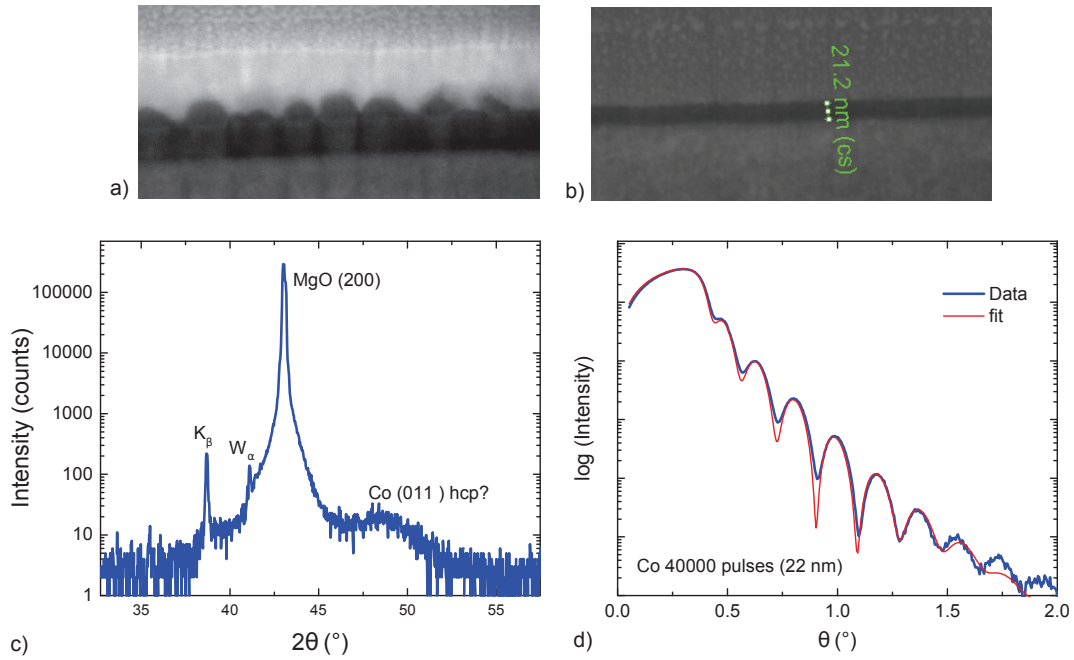


Figure 5.16: SEM images of Co thin films. a) Co thin film grown in three dimensional island growth mode (on top of the MgO-barrier of a MTJ-structure). b) closed Co thin film on (100)-oriented MgO after adjusting the PLD growth parameter and corresponding c) XRD-scan and d) XRR-curve.

Co films used in the MTJ-structures are grown at room temperature with an Ar-background pressure of $1 \cdot 10^{-3}$ mbar. The laser pulse energy is 600 mJ at a repetition frequency of 10 Hz. The $20 \times 8 \text{ mm}^2$ sized aperture is used and the lens position is $L = 12$. Number of PLD pulses is 40000 ($d \approx 22 \text{ nm}$) and 60000 ($d \approx 33 \text{ nm}$). Test samples are grown directly on (100)-oriented MgO substrates.

The XRD-scans of a Co layers grown on (100)-MgO show one additional peak (see Figure 5.16 c). This peak can be assigned to the (011)-planes of hcp-Co. The occurrence of this peak indicates polycrystalline and oriented growth of hcp-Co on top of the MgO-barrier.

The XRR-curve of a Co thin film grown with 40000 pulses is shown in Figure 5.16 d). The period of the intensity oscillations gives a film thickness of 22 nm, as observed in the SEM-cross section. The shape of the curve indicates a smooth interface and an increased surface roughness compared to the epitaxial layers (TiN, $\text{Zn}_x\text{Fe}_{3-x}\text{O}_4$ and MgO).

The magnetization curve $M(H)$ of a Co film is shown in Figure 5.17. The thin films show a coercive field of 3 mT at room temperature and 10 mT at 200 K. A high saturation magnetization of 1480 emu/cm^3 is observed, which is in good agreement with literature values [340].

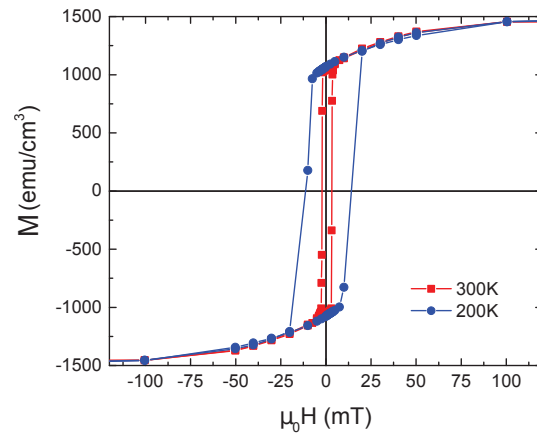


Figure 5.17: Magnetization curves $M(H)$ of a Co thin film at room temperature and 200 K.

6 Magnetic properties and TMR of $\text{Zn}_x\text{Fe}_{3-x}\text{O}_4$ -based MTJs

This chapter focuses on the magnetic properties of the MTJ-multilayer and the observed TMR-effect on samples prepared in the framework of this thesis. Measurements presented here are carried out on samples containing $\text{Zn}_x\text{Fe}_{3-x}\text{O}_4$ thin films grown with a lens position of $L=12$ (zinc content $x \approx 0.2$). The MgO-barriers are grown by 300 PLD-pulses, resulting in a barrier thickness of 2.8 nm.

Magnetic properties of $\text{Zn}_x\text{Fe}_{3-x}\text{O}_4$ -based MTJs

Magnetization measurements are carried out on multilayer samples of MgO (substrate) / TiN / $\text{Zn}_x\text{Fe}_{3-x}\text{O}_4$ / MgO / Co / Cu. The samples consist of the closed, unpatterned thin film stack on top of the substrate.

In order to obtain a TMR-effect in MTJs based on the pseudo spin valve geometry, the magnetic layers must exhibit different coercive fields. The coercivity contrast allows to obtain an antiparallel configuration of the layer magnetization and a change between parallel and antiparallel alignment during the sweep of the applied magnetic field (see Equation 1.2.5).

Figure 6.1 a) and b) show the magnetic moment of a multilayer sample in dependence of the applied magnetic field. The $M(H)$ -curves show a clear step like structure, indicating an independent switching of the magnetization direction of the $\text{Zn}_x\text{Fe}_{3-x}\text{O}_4$ and Co layers.

The small switching (coercive) field is assigned to the $\text{Zn}_x\text{Fe}_{3-x}\text{O}_4$ -layer due to the smaller magnetic moment (height of the step in the $M(H)$ -curve) and coercive squareness of the $\text{Zn}_x\text{Fe}_{3-x}\text{O}_4$ -film compared to Co. The larger coercive field, assigned to the Co layer, is significantly increased in comparison to the coercive field of a single Co layer (see Section 5.5). This effect might be caused by grain boundary diffusion of Cu into Co. Pellerin *et al.* [341] report an increase of the room temperature coercive field of a Co-thin film capped by a Cu layer. This effect is assigned to a reduced magnetostatic and intergranular exchange coupling due to the the incorporation of Cu in Co grain boundaries. The reported change in the coercive field is in the same range as observed in the samples described in this thesis.

The coercive fields increase with decreasing temperature, as measured on the

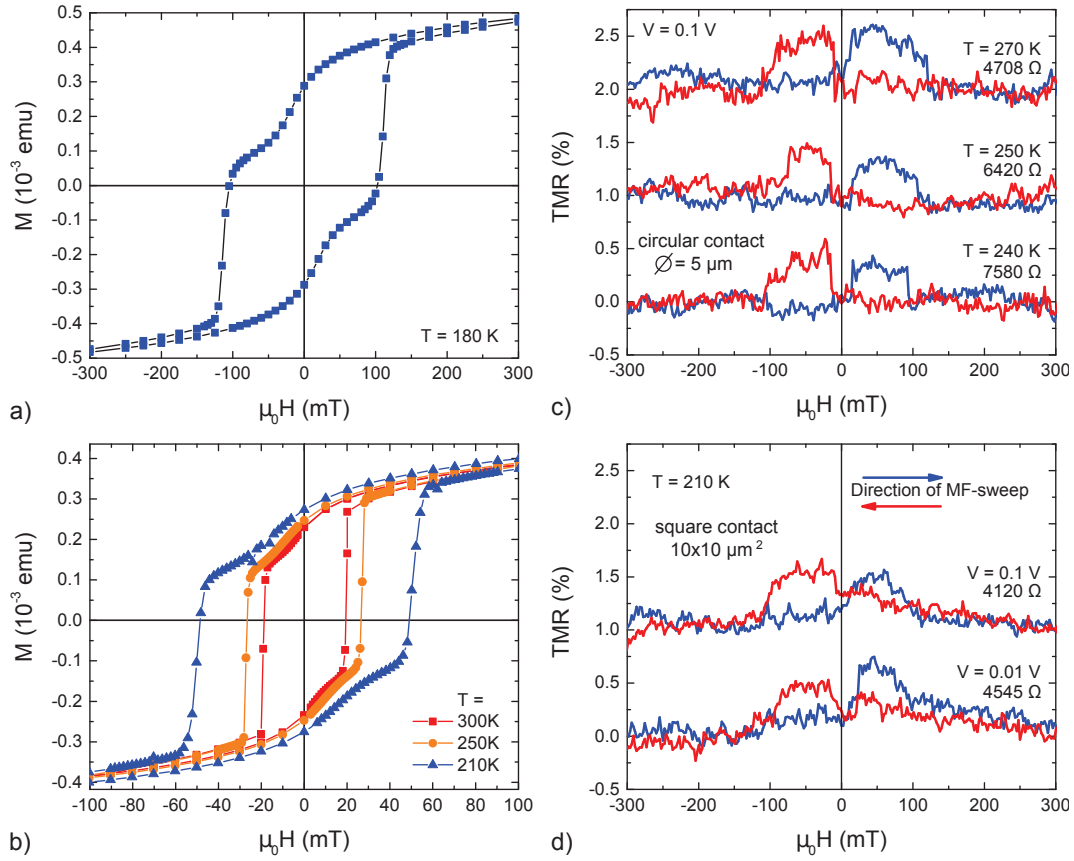


Figure 6.1: a) and b) Magnetization curves $M(H)$ of a $\text{MgO}(\text{substrate})/\text{TiN}/\text{Zn}_x\text{Fe}_{3-x}\text{O}_4/\text{MgO}/\text{Co}/\text{Cu}$ multilayer at different temperatures. c) and d) TMR-curves of two different $\text{Zn}_x\text{Fe}_{3-x}\text{O}_4/\text{MgO}/\text{Co}$ MTJs from the same sample. The Zn content is $x \approx 0.2$ and the barrier thickness is $d \approx 2.8$ nm (300 pulses MgO). The curves are shifted for clarity.

single layer samples (Section 5.3.4 and 5.5). The observed coercivity contrast should be sufficient to achieve an antiparallel alignment of the layer magnetization during resistance measurements in dependence of the applied magnetic field (TMR-measurements).

TMR measurements on $\text{Zn}_x\text{Fe}_{3-x}\text{O}_4$ -based MTJs

Figure 6.1 c) and d) show the result of TMR-measurements (see Section 3.14.3) on two different tunnel junctions at different temperatures and applied voltages. The MTJ-elements show a clear switching of the resistance at well defined magnetic fields. These switching fields do not correspond to the ones observed in the SQUID measurements.

The tunnel magnetoresistance TMR is defined as (Equation (1.7) and (1.68))

$$\text{TMR} = \frac{R_{\uparrow\downarrow} - R_{\uparrow\uparrow}}{R_{\uparrow\uparrow}} = \frac{G_{\uparrow\uparrow} - G_{\uparrow\downarrow}}{G_{\uparrow\downarrow}} = \frac{2P_1P_2}{1 - P_1P_2}. \quad (6.1)$$

A positive TMR of approximately 0.5% is obtained in our samples.

The observed positive TMR of 0.5% is in contradiction to the expected high negative spin polarization of $\text{Zn}_x\text{Fe}_{3-x}\text{O}_4$. Similar results are reported in literature for Fe_3O_4 -based MTJs with a MgO barrier [229, 236]. The small and positive TMR is likely caused by the Fe_3O_4 / MgO-interface. Van der Zaag *et al.* [236] assigned this behavior to a magnetically dead layer at the Fe_3O_4 / MgO-interface [244]. The dead layer is likely caused by spin canting of the magnetic moments at the interface. Different measurements on ferrite nanoparticles prove this behavior [342, 343]. The spin canting and the resulting random spin directions at the Fe_3O_4 -surface lead to spin mixing and thus a drastic change of the interface spin polarization [236].

Li *et al.* [235] proposed the formation of a reduced iron oxide at the interface that alters the spin polarization. This effect was also reported by Park *et al.* [231] on Fe_3O_4 -based MTJs with an AlO_x -barrier.

The diffusion of MgO into the Fe_3O_4 -layer is an additional effect suggested in literature and leads to an alteration of the spin polarization at the interface [238]. The effect is demonstrated by annealing experiments on Fe_3O_4 / MgO-based MTJs. Annealing of the tunnel junctions subsequently reduces the obtained negative TMR and switches it to positive values. Marnitz *et al.* [238] linked this behavior to changes in the spin polarization due to the diffusion of Mg into Fe_3O_4 . Another explanation might be the formation of a reduced iron oxide at the interface due to the annealing steps.

Kado *et al.* [233, 234] report TMR-values of -26 to +18% in Fe_3O_4 / MgO-tunnel junctions. A clear correlation between the resistance area (RA)-value and the TMR was found. The authors assign this behavior to the quality of the MgO-barrier. The negative TMR is considered to be intrinsic, whereas the positive one is caused by electron transport via barrier imperfections. Thus, the quality of the barrier seems to drastically influence the observed TMR in Fe_3O_4 / MgO-based MTJs.

The results on Fe_3O_4 / MgO-based MTJs reported in literature can be applied to our results. The diffusion of Mg into $\text{Zn}_x\text{Fe}_{3-x}\text{O}_4$ is very likely due to the growth by PLD. The effective surface temperature of adatoms is much larger than the substrate temperature due to the high kinetic energy of plasma particles. This might induce a diffusion of MgO into $\text{Zn}_x\text{Fe}_{3-x}\text{O}_4$ and alter the spin structure at the interface significantly.

Also the formation of a reduced (zinc-)iron oxide at the barrier interface and the resulting alteration of the spin polarization may play a role in our samples. The MgO-barrier is grown in a pure Ar-atmosphere and MgO is known

to detract oxide from adjacent layers [344]. This might induce the observed positive TMR [231].

Another possible reason for the observed positive TMR are defects in the barrier, as suggested by Kado *et al.* [233, 234]. The electrical characterization of our MgO-barriers implies a certain amount of defect states inside the barriers (Section 5.4.2). Also the presence of pinholes formed by droplets results in a decrease of the observed TMR. This is due to the spin-independent, parallel current flowing through these pinholes.

Moreover, the contribution of the MgO / Co interface to the observed TMR is not clear (see Section 2.2.3 and page 49). Thus, it is unclear which mechanism is exactly responsible for the observed TMR in our $\text{Zn}_x\text{Fe}_{3-x}\text{O}_4$ / MgO / Co-based magnetic tunnel junctions. Further studies have to be carried out in order to clarify the responsible mechanisms.

In order to explain the results, namely the discrepancy between the switching fields and the observed small MR-effect, it should be taken into account that the observed magnetoresistive effect might be tunneling anisotropic magnetoresistance (TAMR) [345] instead of tunnel magnetoresistance (TMR). $\text{Zn}_x\text{Fe}_{3-x}\text{O}_4$ shows crystalline anisotropy with an easy axis along the [111]-direction [263] and the magnetic field was applied in [100]-direction during all measurements presented in this work. Therefore, it is possible that the TAMR-effect mimics spin valve behavior in our devices. A deeper investigation of this point was not possible in the framework of this thesis due to a limited measurement equipment.

Another problem occurring with our MTJ-samples is a bad reproducibility of the magnetoresistive effect. Only two working junctions (from 30 prepared and measured ones) are obtained in the framework of this thesis and the effect is only obtained in a small temperature range (one sample between 240 and 270 K, the other at 210 K).

Similar results are reported by van der Zaag *et al.* [236] on MBE grown, Fe_3O_4 / MgO / Fe_3O_4 -based junctions. The authors assign the low yield of tunnel junctions showing an identifiable switching behavior to barrier defects, either located in the area (defects induced by the growth process, like droplets in our PLD-grown samples) or at the edge (produced by the microfabrication process, ion milling) of the junction.

In order to achieve a better yield of working devices, the production process of our tunnel junctions has to be further evolved. Nevertheless, the results of this work show the potential of $\text{Zn}_x\text{Fe}_{3-x}\text{O}_4$ -based magnetic tunnel junctions.

Summary

The present thesis focused on the preparation and characterization of magnetic tunnel junctions (MTJs) based on the spinel oxide $\text{Zn}_x\text{Fe}_{3-x}\text{O}_4$. $\text{Zn}_x\text{Fe}_{3-x}\text{O}_4$ is reported to be half metallic [15–17] and is therefore a promising material for spintronic applications.

To demonstrate the potential of $\text{Zn}_x\text{Fe}_{3-x}\text{O}_4$ in spintronic applications, a new MTJ-sample design based on the pseudo spin valve geometry was developed in order to achieve a reasonable TMR-effect in $\text{Zn}_x\text{Fe}_{3-x}\text{O}_4$ -based MTJs. Further, a TMR-measurement setup was developed and assembled in the framework of this thesis in order to measure the desired TMR-effect. A TMR of 0.5% was obtained on our MTJ-samples.

The design of the magnetic tunnel junctions is based on thin film stacks of MgO (substrate) / TiN / $\text{Zn}_x\text{Fe}_{3-x}\text{O}_4$ / MgO / Co grown by pulsed laser deposition. The TiN layer is used as conducting back contact in order to reduce the series resistance of the devices. The $\text{Zn}_x\text{Fe}_{3-x}\text{O}_4$ -thin films act as bottom magnetic electrode and a thin MgO-layer with a thickness of 2.8 nm is used as barrier layer. The top magnetic electrode consists of Co.

Since a high crystalline quality and smooth barrier interfaces are a prerequisite for working MTJ-devices, the PLD-parameters were adjusted in order to obtain a two-dimensional growth of the thin films. In order to provide perfect conditions for two-dimensional thin film growth, an annealing procedure for the MgO-substrates was established. *In-situ* annealing of the MgO-substrates by the CO_2 -laser heater at 950°C for 2 h resulted in smooth, terraced surfaces with monolayer steps [A1].

The growth of the thin films was monitored by RHEED and clear intensity oscillations, indicating two-dimensional layer by layer growth, were observed during the deposition of TiN and MgO. The absence of oscillations during the growth of $\text{Zn}_x\text{Fe}_{3-x}\text{O}_4$ and smooth, monolayer stepped surfaces measured by AFM indicate step-flow growth. RHEED patterns show a high crystalline quality and smooth surface of the TiN, $\text{Zn}_x\text{Fe}_{3-x}\text{O}_4$ and MgO layers. The AFM topography images of TiN and $\text{Zn}_x\text{Fe}_{3-x}\text{O}_4$ show smooth, monolayer stepped surfaces, whereas the MgO-surfaces are smooth but unstructured. XRR-measurements also indicate smooth interfaces between all layers. The high crystalline quality of the thin films is confirmed by XRD measurements.

They also prove an epitaxial growth of the complete layer stack, except for the Co top electrode.

It was possible to deposit $\text{Zn}_x\text{Fe}_{3-x}\text{O}_4$ -thin films with different zinc concentrations x from a stoichiometric target by changing the laser energy density at the target surface. The zinc content x shows a clear dependence on the position of the lens focusing the excimer laser beam.

The thin $\text{Zn}_x\text{Fe}_{3-x}\text{O}_4$ films were investigated for their electrical and magnetic properties. The magnetization as well as the conductivity show a clear dependence on the zinc content x . This dependence can be assigned to spin canting, resulting from the alteration of the magnetic interactions in $\text{Zn}_x\text{Fe}_{3-x}\text{O}_4$ due to the substitution of Fe by Zn [15]. The high observed room temperature conductivity and magnetization values indicate a high quality of the $\text{Zn}_x\text{Fe}_{3-x}\text{O}_4$ thin films. The activation energy observed in temperature dependent conductivity measurements can be assigned to electron hopping between **B**-site iron cations. Temperature dependent magnetization measurements show features of spin glass behavior [246]. These features could also be explained by magnetic domain effects [140]. A final explanation of the origin of the observed features was not possible in the framework of this thesis.

The structural thickness of the MgO-barrier layer was determined by the analysis of RHEED intensity oscillations and XRR. The tunneling properties of the MgO-barriers were investigated by fitting the BDR-model [95] to j - V -curves of the junctions. Determined parameters are the apparent barrier thickness d and energetic height Φ . The apparent thickness is considerably lower than the structural thickness, which can be assigned to inhomogeneities of the barrier thickness. A strong correlation between the two apparent barrier parameters d and Φ was found. This correlation seems to be based on the model itself. The description of the barrier thickness by a normal distribution with the standard deviation σ_d was included into the model in order to get rid of the correlation between the fitting parameters. The analysis of the j - V -curves using the new model reveals the presence of growth related barrier defects such as droplets. The presence of pinholes probably caused by droplets is stated by the temperature dependence of the apparent barrier parameter obtained by using the BDR-model. Nevertheless, the barriers fulfill all other Rowell criteria [334] indicating tunneling as dominant conduction mechanism [335, 336].

A MR of 0.5% was measured in our tunnel junctions. It could not be figured out finally if the observed MR-effect is due to TMR or TAMR and further investigation is necessary in order to clarify this point.

A successful demonstration of MR in $\text{Zn}_x\text{Fe}_{3-x}\text{O}_4$ based MTJs is presented in this work. The effect was measured on samples developed and processed in the framework of this thesis. This is also a proof of the functionality of the MR-measurement setup developed and assembled in the framework of this thesis.

In order to improve the observed effect and to enhance the reproducibility, further improvements in the sample preparation have to be made. The focus should lie on the $\text{Zn}_x\text{Fe}_{3-x}\text{O}_4$ / barrier interface as well as on the barrier itself. Appropriate solution approaches are for example the growth of the MgO-barrier by eclipse or off-axis PLD in order to reduce the formation of droplets and the interface diffusion of Mg. Also investigations on magnetic anisotropy effects and an improvement on the sample design is necessary to figure out the effect of TAMR in these junctions.

Bibliography

- [1] M. N. BAIBICH, J. M. BROTO, A. FERT, F. N. VAN DAU, F. PETROFF: *Giant Magnetoresistance of (001)Fe/(001)Cr Magnetic Superlattices*, Physical Review Letters **61**, 2472 (1988)
- [2] G. BINASCH, P. GRÜNBERG, F. SAURENBACH, W. ZINN: *Enhanced magnetoresistance in layered magnetic structures with antiferromagnetic inter-layer exchange*, Physical Review B **39**, 4828 (1989)
- [3] A. FERT: *Nobel Lecture: Origin, development, and future of spintronics*, Reviews of Modern Physics **80**, 1517 (2008)
- [4] P. GRUNBERG: *From spinwaves to Giant Magnetoresistance (GMR) and beyond*, Nobel Lecture p. 92–108 (2007)
- [5] J.-G. ZHU, C. PARK: *Magnetic tunnel junctions*, Materials Today **9**, 36 (2006)
- [6] S. S. P. PARKIN, K. P. ROCHE, M. G. SAMANT, P. M. RICE, R. B. BEYERS, R. E. SCHEUERLEIN, E. J. O’SULLIVAN, S. L. BROWN, J. BUCCHIGANO, D. W. ABRAHAM, Y. LU, M. ROOKS, P. L. TROUILLOUD, R. A. WANNER, W. J. GALLAGHER: *Exchange-biased magnetic tunnel junctions and application to nonvolatile magnetic random access memory (invited)*, Journal of Applied Physics **85**, 5828 (1999)
- [7] J.-G. ZHU: *Magnetoresistive Random Access Memory: The Path to Competitiveness and Scalability*, Proceedings of the IEEE **96**, 1786 (2008)
- [8] EVERS PIN TECHNOLOGIES INC.: *Everspin technologies - The MRAM company: MRAM replaces DRAM*, <http://www.everspin.com/mram-replaces-dram>, accessed on Sept. 28 (2015)
- [9] C. SEALY: *Winning the memory race*, Materials Today **11**, 16 (2008)
- [10] J. KIM, A. PAUL, P. A. CROWELL, S. J. KOESTER, S. S. SAPATNEKAR, JIAN-PING WANG, C. H. KIM: *Spin-Based Computing: Device Concepts, Current Status, and a Case Study on a High-Performance Microprocessor*, Proceedings of the IEEE **103**, 106 (2015)

- [11] M. JULLIERE: *Tunneling between ferromagnetic films*, Physics Letters A **54A**, 225 (1975)
- [12] J.-B. MOUSSY: *From epitaxial growth of ferrite thin films to spin-polarized tunnelling*, Journal of Physics D: Applied Physics **46**, 143001 (2013)
- [13] M. BIBES, A. BARTHÉLÉMY: *Oxide spintronics*, IEEE Transactions on Electron Devices **54**, 1003 (2007)
- [14] M. OPEL: *Spintronic oxides grown by laser-MBE*, Journal of Physics D: Applied Physics **45**, 033001 (2012)
- [15] D. VENKATESHVARAN, M. ALTHAMMER, A. NIELSEN, S. GEPRÄGS, M. RAMACHANDRA RAO, S. T. B. GOENNENWEIN, M. OPEL, R. GROSS: *Epitaxial $\text{Zn}_x\text{Fe}_{3-x}\text{O}_4$ thin films: A spintronic material with tunable electrical and magnetic properties*, Physical Review B **79**, 134405 (2009)
- [16] P. WANG, Z. KAKOL, M. WITTENAUER, J. M. HONIG: *Electrical properties of zinc ferrites $\text{Fe}_{3-x}\text{Zn}_x\text{O}_4$ with $0 < x < 0.3$* , Physical Review B **42**, 4553 (1990)
- [17] J. TAKAOBUSHI, H. TANAKA, T. KAWAI, S. UEDA, J.-J. KIM, M. KOBATA, E. IKENAGA, M. YABASHI, K. KOBAYASHI, Y. NISHINO, D. MIWA, K. TAMASAKU, T. ISHIKAWA: *$\text{Fe}_{3-x}\text{Zn}_x\text{O}_4$ thin film as tunable high Curie temperature ferromagnetic semiconductor*, Applied Physics Letters **89**, 242507 (2006)
- [18] S. A. WOLF, D. D. AWSCHALOM, R. A. BUHRMAN, J. M. DAUGHTON, S. VON MOLNÁR, M. L. ROUKES, A. Y. CHTCHELKANOVA, D. M. TREGER: *Spintronics: a spin-based electronics vision for the future.*, Science (New York, N.Y.) **294**, 1488 (2001)
- [19] P. P. FREITAS: *Spin-Valve and Spin-Tunneling Devices: Read Heads, MRAMs, Field Sensors*, in: *Spin Eletronics*, M. ZIESE, M. J. THORNTON, Ed. (Springer Berlin Heidelberg, 2001), p. 464–488
- [20] S. PARKIN, C. KAISER, A. PANCHULA, K. ROCHE, M. SAMANT: *Magnetically engineered spintronic sensors and memory*, Proceedings of the IEEE **91**, 661 (2003)
- [21] E. GROCHOWSKI, T. COUGHLIN: *The Perennial Hard Disk Drive Storage Industry " Workhorse", SNIA data storage innovation conference, April 7-9, 2015 in Santa Clara CA* (2015)

- [22] K. ZHANG: *International Solid-State Circuits Conference ISSCC 2013, Februar 17-21 2013, in San Francisco, CA*, <http://www.maltiel-consulting.com/ISSCC-2013-Memory-trends-Flash-NAND-DRAM.html> (2013)
- [23] G. A. PRINZ: *Magnetoelectronics*, Science **282**, 1660 (1998)
- [24] J. M. SLAUGHTER, N. D. RIZZO, F. B. MANCOFF, R. WHIG, K. SMITH, S. AGGARWAL, S. TEHRANI: *Toggle and Spin-Torque MRAM : Status and Outlook*, Journal of the Magnetic Society of Japan **5**, 171 (2010)
- [25] EVERSPIN TECHNOLOGIES INC.: *Everspin technologies - The MRAM company: MRAM Technology Attributes*, <http://www.everspin.com/mram-technology-attributes>, accessed on Sept. 28 (2015)
- [26] D. APALKOV, A. ONG, A. DRISKILL-SMITH, M. KROUNBI, A. KHVALKOVSKIY, S. WATTS, V. NIKITIN, X. TANG, D. LOTTIS, K. MOON, X. LUO, E. CHEN: *Spin-transfer torque magnetic random access memory (STT-MRAM)*, ACM Journal on Emerging Technologies in Computing Systems **9**, 1 (2013)
- [27] J. SLONCZEWSKI: *Current-driven excitation of magnetic multilayers*, Journal of Magnetism and Magnetic Materials **159**, L1 (1996)
- [28] TOSHIBA CORPORATION: *Development of a nonvolatile memory circuit for high-performance processors using new types of magnetic memory elements*, http://www.toshiba.co.jp/rdc/rd/detail_e/e1503_01.html, accessed on Sept. 24 (2015)
- [29] EVERSPIN TECHNOLOGIES INC.: *Everspin technologies - The MRAM company: Automotive*, <http://www.everspin.com/automotive>, accessed on Sept. 28 (2015)
- [30] Y. HUAI: *Spin-Transfer Torque MRAM (STT-MRAM): Challenges and Prospects*, AAPPS bulletin **18**, 33 (2008)
- [31] D. BOHM: *The Classical Limit of Quantum Theory. The WKB Approximation*, in: *Quantum theory* (Dover Publications, New York, 1989), Chap. 12, p. 264–295
- [32] J. SLONCZEWSKI: *Conductance and exchange coupling of two ferromagnets separated by a tunneling barrier*, Physical Review B **39**, 6995 (1989)
- [33] C. FELSER, G. H. FECHER: *Spintronics* (Springer Netherlands, Dordrecht, 2013)
- [34] J. MATHON: *Giant Magnetoresistance*, in: *Spin Eletronics*, M. ZIESE, M. THORNTON, Ed. (Springer Berlin Heidelberg, 2001), p. 71–88

- [35] N. F. MOTT: *The electrical conductivity of transition metals*, Proc. R. Soc. A **153**, 699 (1936)
- [36] N. MOTT: *Electrons in transition metals*, Advances in Physics **13**, 325 (1964)
- [37] D. EDWARDS, J. MATHON, R. MUNIZ, S. PARKIN: *Dependence of the giant magnetoresistance in Co/Cu multilayers on layer thickness*, Journal of Magnetism and Magnetic Materials **114**, 252 (1992)
- [38] B. DIENY, V. S. SPERIOSU, S. S. P. PARKIN, B. A. GURNEY, D. R. WILHOIT, D. MAURI: *Giant magnetoresistive in soft ferromagnetic multilayers*, Physical Review B **43**, 1297 (1991)
- [39] IBM: *The Application of Spintronics*, <http://www-03.ibm.com/ibm/history/ibm100/us/en/icons/spintronics/>, accessed on Okt. 10 (2015)
- [40] S. S. P. PARKIN, Z. G. LI, D. J. SMITH: *Giant magnetoresistance in antiferromagnetic Co/Cu multilayers*, Applied Physics Letters **58**, 2710 (1991)
- [41] W. F. EGELHOFF, P. J. CHEN, C. J. POWELL, M. D. STILES, R. D. MCMICHAEL, C.-L. LIN, J. M. SIVERTSEN, J. H. JUDY, K. TAKANO, A. E. BERKOWITZ, T. C. ANTHONY, J. A. BRUG: *Optimizing the giant magnetoresistance of symmetric and bottom spin valves (invited)*, Journal of Applied Physics **79**, 5277 (1996)
- [42] R. MESERVEY, P. M. TEDROW, P. FULDE: *Magnetic field splitting of the quasiparticle states in superconducting aluminum films*, Physical Review Letters **25**, 1270 (1970)
- [43] P. M. TEDROW, R. MESERVEY: *Spin-Dependent Tunneling into Ferromagnetic Nickel*, Physical Review Letters **26**, 192 (1971)
- [44] P. M. TEDROW, R. MESERVEY: *Spin polarization of electrons tunneling from films of Fe, Co, Ni, and Gd*, Physical Review B **7**, 318 (1973)
- [45] R. MESERVEY, P. TEDROW: *Spin-polarized electron tunneling*, Physics Reports **238**, 173 (1994)
- [46] M. OPEL, S. GEPRÄGS, E. P. MENZEL, A. NIELSEN, D. REISINGER, K.-W. NIELSEN, A. BRANDLMAIER, F. D. CZESCHKA, M. ALTHAMMER, M. WEILER, S. T. B. GOENNENWEIN, J. SIMON, M. SVETE, W. YU, S.-M. HÜHNE, W. MADER, R. GROSS: *Novel multifunctional materials based on oxide thin films and artificial heteroepitaxial multilayers*, Physica Status Solidi (a) **208**, 232 (2011)

- [47] S. S. P. PARKIN, M. HAYASHI, L. THOMAS: *Magnetic Domain-Wall Racetrack Memory*, Science **320**, 190 (2008)
- [48] J. MATHON, A. UMERSEKI: *Theory of tunneling magnetoresistance of an epitaxial Fe/MgO/Fe(001) junction*, Physical Review B **63**, 220403 (2001)
- [49] T. MIYAZAKI, T. YAOI, S. ISHIO: *Large magnetoresistance effect in 82Ni-Fe/Al-Al₂O₃/Co magnetic tunneling junction*, Journal of Magnetism and Magnetic Materials **98**, L7 (1991)
- [50] J. S. MOODERA, L. R. KINDER, T. M. WONG, R. MESERVEY: *Large Magnetoresistance at Room Temperature in Ferromagnetic Thin Film Tunnel Junctions*, Physical Review Letters **74**, 3273 (1995)
- [51] T. MIYAZAKI, N. TEZUKA: *Giant magnetic tunneling effect in Fe/Al₂O₃/Fe junction*, Journal of Magnetism and Magnetic Materials **139**, L231 (1995)
- [52] D. WANG, C. NORDMAN, J. M. DAUGHTON, Z. QIAN, J. FINK: *70% TMR at room temperature for SDT sandwich junctions with CoFeB as free and reference layers*, IEEE Transactions on Magnetics **40**, 2269 (2004)
- [53] W. H. BUTLER, X.-G. ZHANG, T. C. SCHULTHESS, J. M. MACLAREN: *Spin-dependent tunneling conductance of Fe/MgO/Fe sandwiches*, Physical Review B **63**, 054416 (2001)
- [54] S. YUASA, A. FUKUSHIMA, T. NAGAHAMA, K. ANDO, Y. SUZUKI: *High tunnel magnetoresistance at room temperature in fully epitaxial Fe/MgO/Fe tunnel junctions due to coherent spin-polarized tunneling*, Japanese Journal of Applied Physics, Part 2: Letters **43**, 41 (2004)
- [55] M. BOWEN, V. CROS, F. PETROFF, A. FERT, C. MARTÍNEZ BOUBETA, J. L. COSTA-KRÄMER, J. V. ANGUITA, A. CEBOLLADA, F. BRIONES, J. M. DE TERESA, L. MORELLÓN, M. R. IBARRA, F. GÜELL, F. PEIRÓ, A. CORNET: *Large magnetoresistance in Fe/MgO/FeCo(001) epitaxial tunnel junctions on GaAs(001)*, Applied Physics Letters **79**, 1655 (2001)
- [56] S. IKEDA, J. HAYAKAWA, Y. M. LEE, R. SASAKI, T. MEGURO, F. MATSUKURA, H. OHNO: *Dependence of tunnel magnetoresistance in MgO based magnetic tunnel junctions on Ar pressure during MgO sputtering*, Japanese Journal of Applied Physics, Part 2: Letters **44**, L1442 (2005)
- [57] S. YUASA, A. FUKUSHIMA, H. KUBOTA, Y. SUZUKI, K. ANDO: *Giant tunneling magnetoresistance up to 410% at room temperature in fully epitaxial Co/MgO/Co magnetic tunnel junctions with bcc Co(001) electrodes*, Applied Physics Letters **89**, 042505 (2006)

- [58] Y. M. LEE, J. HAYAKAWA, S. IKEDA, F. MATSUKURA, H. OHNO: *Effect of electrode composition on the tunnel magnetoresistance of pseudo-spin-valve magnetic tunnel junction with a MgO tunnel barrier*, Applied Physics Letters **90**, 212507 (2007)
- [59] S. IKEDA, J. HAYAKAWA, Y. ASHIZAWA, Y. M. LEE, K. MIURA, H. HASEGAWA, M. TSUNODA, F. MATSUKURA, H. OHNO: *Tunnel magnetoresistance of 604% at 300 K by suppression of Ta diffusion in CoFeB/MgO/CoFeB pseudo-spin-valves annealed at high temperature*, Applied Physics Letters **93**, 082508 (2008)
- [60] S. DATTA, B. DAS: *Electronic analog of the electro-optic modulator*, Applied Physics Letters **56**, 665 (1990)
- [61] N. LOCATELLI, V. CROS, J. GROLLIER: *Spin-torque building blocks*, Nature Materials **13**, 11 (2013)
- [62] M. BIBES, J. E. VILLEGAS, A. BARTHÉLÉMY: *Ultrathin oxide films and interfaces for electronics and spintronics*, Advances in Physics **60**, 5 (2011)
- [63] M. BIBES, A. BARTHÉLÉMY: *Multiferroics: Towards a magnetoelectric memory*, Nature materials **7** (2008)
- [64] W. E. PICKETT, J. S. MOODERA: *Half Metallic Magnets*, Physics Today **54**, 39 (2001)
- [65] J. S. MOODERA, J. NASSAR, G. MATHON: *Spin-Tunneling in Ferromagnetic Junctions*, Annual Review of Materials Science **29**, 381 (1999)
- [66] M. C. PRESTGARD, G. P. SIEGEL, A. TIWARI: *Oxides for spintronics: A review of engineered materials for spin injection*, Advanced Materials Letters **5**, 242 (2014)
- [67] M. JOHNSON, P. LEMMENS: *Crystallography and Chemistry of Perovskites*, in: *Handbook of Magnetism and Advanced Magnetic Materials*, H. KRONMÜLLER, S. S. PARKIN, Ed. (John Wiley & Sons, Ltd, Chichester, UK, 2007)
- [68] M. BOWEN, M. BIBES, A. BARTHÉLÉMY, J.-P. CONTOUR, A. ANANE, Y. LEMAÎTRE, A. FERT: *Nearly total spin polarization in La₂/3Sr₁/3MnO₃ from tunneling experiments*, Applied Physics Letters **82**, 233 (2003)
- [69] V. GARCIA, M. BIBES, A. BARTHÉLÉMY, M. BOWEN, E. JACQUET, J.-P. CONTOUR, A. FERT: *Temperature dependence of the interfacial spin polarization of La₂/3Sr₁/3MnO₃*, Physical Review B **69**, 052403 (2004)

- [70] U. LÜDERS, M. BIBES, K. BOUZEHOUE, E. JACQUET, J.-P. CONTOUR, S. FUSIL, J.-F. BOBO, J. FONTCUBERTA, A. BARTHÉLÉMY, A. FERT: *Spin filtering through ferrimagnetic NiFe₂O₄ tunnel barriers*, Applied Physics Letters **88**, 082505 (2006)
- [71] U. LÜDERS, A. BARTHÉLÉMY, M. BIBES, K. BOUZEHOUE, S. FUSIL, E. JACQUET, J.-P. CONTOUR, J.-F. BOBO, J. FONTCUBERTA, A. FERT: *NiFe₂O₄: A Versatile Spinel Material Brings New Opportunities for Spintronics*, Advanced Materials **18**, 1733 (2006)
- [72] U. LÜDERS, G. HERRANZ, M. BIBES, K. BOUZEHOUE, E. JACQUET, J.-P. CONTOUR, S. FUSIL, J.-F. BOBO, J. FONTCUBERTA, A. BARTHÉLÉMY, A. FERT: *Hybrid perovskite-spinel magnetic tunnel junctions based on conductive ferrimagnetic NiFe₂O₄*, Journal of Applied Physics **99**, 08K301 (2006)
- [73] C. A. FERNANDES VAZ, U. STAUB: *Artificial multiferroic heterostructures*, Journal of Materials Chemistry C **1**, 6731 (2013)
- [74] J.-B. MOUSSY: *Ultimate magnetism: Oxides in spintronics*, Clefs du CEA (2008)
- [75] Y.-H. CHU, L. W. MARTIN, M. B. HOLCOMB, M. GAJEK, S.-J. HAN, Q. HE, N. BALKE, C.-H. YANG, D. LEE, W. HU, Q. ZHAN, P.-L. YANG, A. FRAILE-RODRÍGUEZ, A. SCHOLL, S. X. WANG, R. RAMESH: *Electric-field control of local ferromagnetism using a magnetoelectric multiferroic*, Nature Materials **7**, 478 (2008)
- [76] S. M. WU, S. A. CYBART, P. YU, M. D. ROSSELL, J. X. ZHANG, R. RAMESH, R. C. DYNES: *Reversible electric control of exchange bias in a multiferroic field-effect device*, Nature Materials **9**, 756 (2010)
- [77] S. M. WU, S. A. CYBART, D. YI, J. M. PARKER, R. RAMESH, R. C. DYNES: *Full Electric Control of Exchange Bias*, Physical Review Letters **110**, 067202 (2013)
- [78] H. BÉA, M. BIBES, S. CHERIFI, F. NOLTING, B. WAROT-FONROSE, S. FUSIL, G. HERRANZ, C. DERANLOT, E. JACQUET, K. BOUZEHOUE, A. BARTHÉLÉMY: *Tunnel magnetoresistance and robust room temperature exchange bias with multiferroic BiFeO₃ epitaxial thin films*, Applied Physics Letters **89**, 242114 (2006)
- [79] J. ALLIBE, S. FUSIL, K. BOUZEHOUE, C. DAUMONT, D. SANDO, E. JACQUET, C. DERANLOT, M. BIBES, A. BARTHÉLÉMY: *Room temperature electrical manipulation of giant magnetoresistance in spin valves exchange-biased with BiFeO₃*, Nano letters **12**, 1141 (2012)

- [80] E. I. RASHBA: *Theory of electrical spin injection: Tunnel contacts as a solution of the conductivity mismatch problem*, Physical Review B - Condensed Matter and Materials Physics **62**, 267 (2000)
- [81] B. BEHIN-AEIN, D. DATTA, S. SALAHUDDIN, S. DATTA: *Proposal for an all-spin logic device with built-in memory*, Nature Nanotechnology **5**, 266 (2010)
- [82] I. ŽUTIĆ, S. DAS SARMA: *Spintronics: Fundamentals and applications*, Reviews of Modern Physics **76**, 323 (2004)
- [83] M. G. CHAPLINE, S. X. WANG: *Room-temperature spin filtering in a $\text{CoFe}_2\text{O}_4/\text{MgAl}_2\text{O}_4/\text{Fe}_3\text{O}_4$ magnetic tunnel barrier*, Physical Review B **74**, 014418 (2006)
- [84] C. KITTEL: *Einführung in die Festkörperphysik* (Oldenbourg, 2005)
- [85] H. C. KANDPAL, G. H. FECHER, C. FELSER, H. C. K. PAL: *Calculated electronic and magnetic properties of the half-metallic, transition metal based Heusler compounds*, Journal of Physics D: Applied Physics **40**, 1507 (2007)
- [86] R. A. DE GROOT, F. M. MUELLER, P. G. V. ENGEN, K. H. J. BUSCHOW: *New class of materials: Half-metallic ferromagnets*, Physical Review Letters **50**, 2024 (1983)
- [87] N. LAKSHMI, V. SEBASTIAN, K. VENUGOPALAN: *Clustering in Heusler Alloys*, in: *Advances in Nanoscale Magnetism*, 1 (Springer, 2008), Chap. 2, S. 330
- [88] K. INOMATA, S. OKAMURA, A. MIYAZAKI, M. KIKUCHI, N. TEZUKA, M. WOJCIK, E. JEDRYKA: *Structural and magnetic properties and tunnel magnetoresistance for $\text{Co}_2(\text{Cr,Fe})\text{Al}$ and Co_2FeSi full-Heusler alloys*, Journal of Physics D: Applied Physics **39**, 816 (2006)
- [89] N. TEZUKA, N. IKEDA, S. SUGIMOTO, K. INOMATA: *175% tunnel magnetoresistance at room temperature and high thermal stability using $\text{Co}_2\text{FeAl}_{0.5}\text{Si}_{0.5}$ full-Heusler alloy electrodes*, Applied Physics Letters **89**, 252508 (2006)
- [90] K. INOMATA, N. IKEDA, N. TEZUKA, R. GOTO, S. SUGIMOTO, M. WOJCIK, E. JEDRYKA: *Highly spin-polarized materials and devices for spintronics*, Science and Technology of Advanced Materials **9**, 014101 (2008)
- [91] B. H. BRANSDEN: *Quantum mechanics* (Prentice Hall, Harlow, England; New York, 2000)
- [92] D. R. BES: *Quantum Mechanics- A Modern and Concise Introductory Course* (Springer, Berlin New York, 2007)

- [93] B. SWIRLES JEFFREYS: *The Asymptotic Approximation (AA) Method*, in: *Quantum theory*, D. BATES, Ed. (Academic Press, New York, London, 1961), Chap. 7, p. 229–249
- [94] J. G. SIMMONS: *Generalized Formula for the Electric Tunnel Effect between Similar Electrodes Separated by a Thin Insulating Film*, Journal of Applied Physics **34**, 1793 (1963)
- [95] W. F. BRINKMAN, R. DYNES, J. M. ROWELL: *Tunneling Conductance of Asymmetrical Barriers*, Journal of Applied Physics **41**, 1915 (1970)
- [96] W. A. HARRISON: *Tunneling from an Independent-Particle Point of View*, Physical Review **123**, 85 (1961)
- [97] G.-L. INGOLD, Y. V. NAZAROV: *Charge Tunneling Rates in Ultrasmall Junctions*, in: *Single Charge Tunneling*, Vol. 294, H. GRABERT, M. DEVORET, Ed. (Plenum Press, New York, 1992), Chap. 2, p. 21–107
- [98] P. K. MUDULI: *Spin-polarized transport in planar structures and tunnel junctions of perovskite oxides*, Dissertation, Indian Institute of Technology, Kanpur (2009)
- [99] R. H. FOWLER, L. NORDHEIM: *Electron Emission in Intense Electric Fields*, Proceedings of the Royal Society A: Mathematical, Physical and Engineering Sciences **119**, 173 (1928)
- [100] M. LENZLINGER, E. SNOW: *Fowler-Nordheim Tunneling into Thermally Grown SiO₂*, Journal of Applied Physics **40**, 278 (1969)
- [101] N. M. RAVINDRA, J. ZHAO: *Fowler-Nordheim tunneling in thin SiO₂ films*, Smart Materials and Structures **1**, 197 (1992)
- [102] J. G. SIMMONS: *Electric Tunnel Effect between Dissimilar Electrodes Separated by a Thin Insulating Film*, Journal of Applied Physics **34**, 2581 (1963)
- [103] T. E. HARTMAN: *Tunneling Through Asymmetric Barriers*, Journal of Applied Physics **35**, 3283 (1964)
- [104] R. STRATTON: *Volt-current characteristics for tunneling through insulating films*, Journal of Physics and Chemistry of Solids **23**, 1177 (1962)
- [105] J. G. SIMMONS: *Generalized Thermal J-V Characteristic for the Electric Tunnel Effect*, Journal of Applied Physics **35**, 2655 (1964)
- [106] T. E. HARTMAN, J. S. CHIVIAN: *Electron Tunneling Through Thin Aluminum Oxide Films*, Physical Review **134**, A1094 (1964)

- [107] J. BARDEEN, L. N. COOPER, J. R. SCHRIEFFER: *Theory of superconductivity*, Physical Review **108**, 1175 (1957)
- [108] J. MACLAREN, X.-G. ZHANG, W. BUTLER: *Validity of the Julliere model of spin-dependent tunneling*, Physical Review B **56**, 11827 (1997)
- [109] A. BRATKOVSKY: *Tunneling of electrons in conventional and half-metallic systems: Towards very large magnetoresistance*, Physical Review B **56**, 2344 (1997)
- [110] S. YUASA, D. D. DJAYAPRAWIRA: *Giant tunnel magnetoresistance in magnetic tunnel junctions with a crystalline MgO(0 0 1) barrier*, Journal of Physics D: Applied Physics **40**, R337 (2007)
- [111] X.-G. ZHANG, W. H. BUTLER: *Large magnetoresistance in bcc Co/MgO/Co and FeCo/MgO/FeCo tunnel junctions*, Physical Review B **70**, 172407 (2004)
- [112] Y. LU, X. LI, G. GONG, G. XIAO, A. GUPTA, P. LECOEUR, J. SUN, Y. WANG, V. DRAVID: *Large magnetotunneling effect at low magnetic fields in micrometer-scale epitaxial La_{0.67}Sr_{0.33}MnO₃ tunnel junctions*, Physical Review B **54**, R8357 (1996)
- [113] M. VIRET, M. DROUET, J. NASSAR, J. P. CONTOUR, C. FERMON, A. FERT: *Low-field colossal magnetoresistance in manganite tunnel spin valves*, Europhysics Letters (EPL) **39**, 545 (1997)
- [114] J. Z. SUN, W. J. GALLAGHER, P. R. DUNCOMBE, L. KRUSIN-ELBAUM, R. A. ALTMAN, A. GUPTA, Y. LU, G. Q. GONG, G. XIAO: *Observation of large low-field magnetoresistance in trilayer perpendicular transport devices made using doped manganate perovskites*, Applied Physics Letters **69**, 3266 (1996)
- [115] J. Z. SUN, L. KRUSIN-ELBAUM, P. R. DUNCOMBE, A. GUPTA, R. B. LAIBOWITZ: *Temperature dependent, non-ohmic magnetoresistance in doped perovskite manganate trilayer junctions*, Applied Physics Letters **70**, 1769 (1997)
- [116] M. BOWEN, A. BARTHÉLÉMY, V. BELLINI, M. BIBES, P. SENEOR, E. JACQUET, J.-P. CONTOUR, P. H. DEDERICHs: *Observation of Fowler-Nordheim hole tunneling across an electron tunnel junction due to total symmetry filtering*, Physical Review B **73**, 140408 (2006)
- [117] J. VELEV, K. BELASHCHENKO, D. STEWART, M. VAN SCHILFGAARDE, S. JASWAL, E. TSYMBAL: *Negative Spin Polarization and Large Tunneling Magnetoresistance in Epitaxial Co/SrTiO₃/Co Magnetic Tunnel Junctions*, Physical Review Letters **95**, 216601 (2005)

- [118] Y. ANDO, T. MIYAKOSHI, M. OOGANE, T. MIYAZAKI, H. KUBOTA, K. ANDO, S. YUASA: *Spin-dependent tunneling spectroscopy in single-crystal Fe/MgO/Fe tunnel junctions*, Applied Physics Letters **87**, 1 (2005)
- [119] J. M. DE TERESA: *Role of Metal-Oxide Interface in Determining the Spin Polarization of Magnetic Tunnel Junctions*, Science **286**, 507 (1999)
- [120] J. DE TERESA, A. BARTHÉLÉMY, A. FERT, J. CONTOUR, R. LYONNET, F. MONTAIGNE, P. SENEOR, A. VAURÈS: *Inverse Tunnel Magnetoresistance in Co/SrTiO₃/La_{0.7}Sr_{0.3}MnO₃: New Ideas on Spin-Polarized Tunneling*, Physical Review Letters **82**, 4288 (1999)
- [121] J. DE TERESA, A. BARTHÉLÉMY, J. CONTOUR, A. FERT: *Manganite-based magnetic tunnel junctions: new ideas on spin-polarised tunnelling*, Journal of Magnetism and Magnetic Materials **211**, 160 (2000)
- [122] X.-G. ZHANG, W. H. BUTLER, A. BANDYOPADHYAY: *Effects of the iron-oxide layer in Fe-FeO-MgO-Fe tunneling junctions*, Physical Review B **68**, 092402 (2003)
- [123] C. TUSCHE, H. MEYERHEIM, N. JEDRECY, G. RENAUD, A. ERNST, J. HENK, P. BRUNO, J. KIRSCHNER: *Oxygen-Induced Symmetrization and Structural Coherency in Fe/MgO/Fe(001) Magnetic Tunnel Junctions*, Physical Review Letters **95**, 176101 (2005)
- [124] M. SHARMA, S. X. WANG, J. H. NICKEL: *Inversion of Spin Polarization and Tunneling Magnetoresistance in Spin-Dependent Tunneling Junctions*, Physical Review Letters **82**, 616 (1999)
- [125] S. ZHANG, P. LEVY, A. MARLEY, S. PARKIN: *Quenching of Magnetoresistance by Hot Electrons in Magnetic Tunnel Junctions*, Physical Review Letters **79**, 3744 (1997)
- [126] I. I. OLEINIK, E. Y. TSYMBAL, D. G. PETTIFOR: *Structural and electronic properties of Co/Al₂O₃/Co magnetic tunnel junction from first principles*, Phys. Rev. B. **62**, 3952 (2000)
- [127] I. I. OLEINIK, E. Y. TSYMBAL, D. G. PETTIFOR: *Atomic and electronic structure of Co/SrTiO₃/Co magnetic tunnel junctions*, Physical Review B **65**, 020401 (2001)
- [128] OLEYNIK I, E. Y. TSYMBAL: *Atomic, electronic, and magnetic properties of magnetic tunnel junctions*, Journal of Applied Physics **93**, 6429 (2003)
- [129] C. SHANG, J. NOWAK, R. JANSEN, J. MOODERA: *Temperature dependence of magnetoresistance and surface magnetization in ferromagnetic tunnel junctions*, Physical Review B **58**, R2917 (1998)

- [130] C. HÖFENER, J. B. PHILIPP, J. KLEIN, L. ALFF, A. MARX, B. BÜCHNER, R. GROSS: *Voltage and temperature dependence of the grain boundary tunneling magnetoresistance in manganites*, Europhysics Letters (EPL) **50**, 681 (2000)
- [131] L. I. GLAZMAN, K. A. MATVEEV: *Inelastic tunneling across thin amorphous films*, Zh. Eksp. Teor. Fiz **94**, 343 (1988)
- [132] R. GROSS, A. MARX: *Lecture on Spinelectronics* (Technical University, Munich, 2004)
- [133] X.-G. ZHANG, W. H. BUTLER: *Band structure, evanescent states, and transport in spin tunnel junctions*, Journal of Physics: Condensed Matter **15**, R1603 (2003)
- [134] M. ZIESE: *Extrinsic magnetotransport phenomena in ferromagnetic oxides*, Reports on Progress in Physics **65**, 143 (2002)
- [135] H.-J. MEYER: *Festkörperchemie*, in: *Moderne Anorganische Chemie*, H.-J. MEYER, Ed. (De Gruyter, 2012), Chap. 2., p. 171–391
- [136] J. M. HASTINGS, L. M. CORLISS: *An Antiferromagnetic Transition in Zinc Ferrite*, Physical Review **102**, 1460 (1956)
- [137] A. MARCU, T. YANAGIDA, K. NAGASHIMA, H. TANAKA, T. KAWAI: *Transport properties of ZnFe_2O_4 - δ thin films*, Journal of Applied Physics **102**, 023713 (2007)
- [138] C. E. RODRÍGUEZ TORRES, F. GOLMAR, M. ZIESE, P. ESQUINAZI, S. P. HELUANI: *Evidence of defect-induced ferromagnetism in ZnFe_2O_4 thin films*, Physical Review B **84**, 064404 (2011)
- [139] M. LORENZ, M. BRANDT, K. MEXNER, K. BRACHWITZ, M. ZIESE, P. ESQUINAZI, H. HOCHMUTH, M. GRUNDMANN: *Ferrimagnetic ZnFe_2O_4 thin films on SrTiO_3 single crystals with highly tunable electrical conductivity*, physica status solidi (RRL) - Rapid Research Letters **5**, 438 (2011)
- [140] Y. F. CHEN, D. SPODDIG, M. ZIESE: *Epitaxial thin film ZnFe_2O_4 : a semi-transparent magnetic semiconductor with high Curie temperature*, Journal of Physics D: Applied Physics **41**, 205004 (2008)
- [141] K. BRACHWITZ, T. BÖNTGEN, M. LORENZ, M. GRUNDMANN: *On the transition point of thermally activated conduction of spinel-type MFe_2O_4 ferrite thin films ($M = \text{Zn}, \text{Co}, \text{Ni}$)*, Applied Physics Letters **102**, 172104 (2013)

- [142] C. JIN, P. LI, W. MI, H. BAI: *Structure, magnetic, and transport properties of epitaxial ZnFe₂O₄ films: An experimental and first-principles study*, Journal of Applied Physics **115**, 213908 (2014)
- [143] M. BOHRA, S. PRASAD, N. KUMAR, D. S. MISRA, S. C. SAHOO, N. VENKATARAMANI, R. KRISHNAN: *Large room temperature magnetization in nanocrystalline zinc ferrite thin films*, Applied Physics Letters **88**, 262506 (2006)
- [144] B. DARUKA PRASAD, H. NAGABHUSHANA, K. THYAGARAJAN, B. NAGABHUSHANA, D. JNANESHWARA, S. SHARMA, C. SHIVAKUMARA, N. GOPAL, S.-C. KE, R. CHAKRADHAR: *Temperature dependent magnetic ordering and electrical transport behavior of nano zinc ferrite from 20 to 800K*, Journal of Alloys and Compounds **590**, 184 (2014)
- [145] N. PONPANDIAN, A. NARAYANASAMY: *Influence of grain size and structural changes on the electrical properties of nanocrystalline zinc ferrite*, Journal of Applied Physics **92**, 2770 (2002)
- [146] K. E. SICKAFUS, J. M. WILLS, N. W. GRIMES: *Structure of Spinel*, Journal of the American Ceramic Society **82**, 3279 (1999)
- [147] A. F. HOLLEMAN, E. WIEBERG: *Lehrbuch der anorganischen Chemie, 101. Auflage* (DeGruiter, Berlin, 1995), 34. Ed.
- [148] S.-D. MO, W. CHING: *Electronic structure of normal, inverse, and partially inverse spinels in the MgAl₂O₄ system*, Physical Review B **54**, 16555 (1996)
- [149] H. S. T. C. NEILL: *Temperature dependence of the cation distribution in zinc ferrite (ZnFe₂O₄) from powder XRD structural refinements*, European Journal of Mineralogy **4**, 571 (1992)
- [150] J. WU, N. LI, J. XU, Y. JIANG, Z.-G. YE, Z. XIE, L. ZHENG: *Partially inverse spinel ZnFe₂O₄ with high saturation magnetization synthesized via a molten salt route*, Applied Physics Letters **99**, 202505 (2011)
- [151] Z. Ž. LAZAREVIĆ, Č. JOVALEKIĆ, V. N. IVANOVSKI, A. REČNIK, A. MILUTINOVIĆ, B. CEKIĆ, N. Ž. ROMČEVIĆ: *Characterization of partially inverse spinel ZnFe₂O₄ with high saturation magnetization synthesized via soft mechanochemically assisted route*, Journal of Physics and Chemistry of Solids **75**, 869 (2014)
- [152] E. J. VERWEY, P. W. HAAYMAN, F. C. ROMEIJN: *Physical Properties and Cation Arrangement of Oxides with Spinel Structures II. Electronic Conductivity*, The Journal of Chemical Physics **15**, 181 (1947)

- [153] A. ROSENCWAIG: *Double Exchange and the Metal-Nonmetal Transition in Magnetite*, Physical Review **181**, 946 (1969)
- [154] Z. ZHANG, S. SATPATHY: *Electron states, magnetism, and the Verwey transition in magnetite*, Physical Review B **44**, 13319 (1991)
- [155] K. BRACHWITZ: *Defekt-induzierte Leitungsmechanismen und magnetische Eigenschaften spinellartiger Ferrite*, Dissertation, Universität Leipzig (2013)
- [156] L. NÉEL: *Proprietes Magnetiques des Ferrites - Ferrimagnetisme et Antiferromagnetisme*, Annales de Physique **3**, 137 (1948)
- [157] J. S. SMART: *The Néel Theory of Ferrimagnetism*, American Journal of Physics **23**, 356 (1955)
- [158] C. E. RODRÍGUEZ-TORRES, F. GOLMAR, M. ZIESE, P. ESQUINAZI, S. P. HELUANI: *Magnetic Thin Films*, Brazilian Synchrotron Light Laboratory: Activity Report 2011 **12** (2011)
- [159] J. B. GOODENOUGH, A. L. LOEB: *Theory of ionic ordering, crystal distortion, and magnetic exchange due to covalent forces in spinels*, Physical Review **98**, 391 (1955)
- [160] P. W. ANDERSON: *Antiferromagnetism. Theory of Superexchange Interaction*, Physical Review **79**, 350 (1950)
- [161] J. B. GOODENOUGH: *Theory of the role of covalence in the perovskite-type manganites $[La, M(II)]MnO_3$* , Physical Review **100**, 564 (1955)
- [162] JOHN B. GOODENOUGH: *Magnetism and the Chemical Bond* (Interscience Publishers. New York, London, 1963)
- [163] J. KANAMORI: *Superexchange interaction and symmetry properties of electron orbitals*, Journal of Physics and Chemistry of Solids **10**, 87 (1959)
- [164] J. GOODENOUGH: *Goodenough-Kanamori rule*, Scholarpedia **3**, 7382 (2008)
- [165] C. ZENER: *Interaction between the d-shells in the transition metals. II. Ferromagnetic compounds of manganese with Perovskite structure*, Physical Review **82**, 403 (1951)
- [166] P. W. ANDERSON, H. HASEGAWA: *Considerations on double exchange*, Physical Review **100**, 675 (1955)
- [167] P. G. DE GENNES: *Effects of double exchange in magnetic crystals*, Physical Review **118**, 141 (1960)

- [168] J. LOOS, P. NOVÁK: *Double exchange and superexchange in a ferromagnetic half-metal*, Physical Review B **66**, 1 (2002)
- [169] Y. YAFET, C. KITTEL: *Antiferromagnetic Arrangements in Ferrites*, Physical Review **87**, 290 (1952)
- [170] A. YANASE, K. SIRATORI: *Band Structure in the High Temperature Phase of Fe_3O_4* (1984)
- [171] M. FONIN, R. PENTCHEVA, Y. S. DEDKOV, M. SPERLICH, D. V. VYALIKH, M. SCHEFFLER, U. RÜDIGER, G. GÜNTHERODT: *Surface electronic structure of the $Fe_3O_4(100)$: Evidence of a half-metal to metal transition*, Physical Review B - Condensed Matter and Materials Physics **72**, 1 (2005)
- [172] L. ZHU, K. L. YAO, Z. L. LIU: *First-principles study of the polar (111) surface of Fe_3O_4* , Physical Review B **74**, 035409 (2006)
- [173] X. YU, C.-F. HUO, Y.-W. LI, J. WANG, H. JIAO: *Fe_3O_4 surface electronic structures and stability from GGA+U*, Surface Science **606**, 872 (2012)
- [174] M. FONIN, Y. S. DEDKOV, R. PENTCHEVA, U. RÜDIGER, G. GÜNTHERODT: *Magnetite: a search for the half-metallic state*, Journal of Physics: Condensed Matter **19**, 315217 (2007)
- [175] D. J. HUANG, C. F. CHANG, J. CHEN, L. H. TJENG, A. D. RATA, W. P. WU, S. C. CHUNG, H. J. LIN, T. HIBMA, C. T. CHEN: *Spin-resolved photoemission studies of epitaxial $Fe_3O_4(100)$ thin films*, Journal of Magnetism and Magnetic Materials **239**, 261 (2002)
- [176] Y. S. DEDKOV, U. RÜDIGER, G. GÜNTHERODT: *Evidence for the half-metallic ferromagnetic state of Fe_3O_4 by spin-resolved photoelectron spectroscopy*, Physical Review B **65**, 064417 (2002)
- [177] J. G. TOBIN, S. A. MORTON, S. W. YU, G. D. WADDILL, I. K. SCHULLER, S. A. CHAMBERS: *Spin resolved photoelectron spectroscopy of Fe_3O_4 : the case against half-metallicity.*, Journal of physics. Condensed matter : an Institute of Physics journal **19**, 315218 (2007)
- [178] M. FONIN, Y. S. DEDKOV, R. PENTCHEVA, U. RÜDIGER, G. GÜNTHERODT: *Spin-resolved photoelectron spectroscopy of Fe_3O_4 -revisited*, Journal of Physics: Condensed Matter **20**, 142201 (2008)
- [179] D. MARGULIES, F. PARKER, F. SPADA, R. GOLDMAN, J. LI, R. SINCLAIR, A. BERKOWITZ: *Anomalous moment and anisotropy behavior in Fe_3O_4 films*, Physical Review B **53**, 9175 (1996)

- [180] R. MANTOVAN, A. LAMPERTI, M. GEORGIEVA, G. TALLARIDA, M. FANCIULLI: *CVD synthesis of polycrystalline magnetite thin films: structural, magnetic and magnetotransport properties*, Journal of Physics D: Applied Physics **43**, 065002 (2010)
- [181] S. VANGELISTA, R. MANTOVAN, S. COCCO, A. LAMPERTI, O. SALICIO, M. FANCIULLI: *Chemical vapor deposition growth of Fe_3O_4 thin films and Fe/Fe_3O_4 bi-layers for their integration in magnetic tunnel junctions*, Thin Solid Films **520**, 4617 (2012)
- [182] F. VOOGT, T. HIBMA, G. ZHANG, M. HOEFMAN, L. NIESEN: *Growth and characterization of non-stoichiometric magnetite $Fe_{3-\delta}O_4$ thin films*, Surface Science **331-333**, 1508 (1995)
- [183] F. VOOGT, T. HIBMA, P. SMULDERS, L. NIESEN: *Composition of MBE-grown iron oxide films*, Journal of Crystal Growth **174**, 440 (1997)
- [184] F. C. VOOGT, T. FUJII, P. J. M. SMULDERS, L. NIESEN, M. A. JAMES, T. HIBMA: *NO_2 -assisted molecular-beam epitaxy of Fe_3O_4 , $Fe_{3-\delta}O_4$, and γ - Fe_2O_3 thin films on $MgO(100)$* , Physical Review B **60**, 11193 (1999)
- [185] S. A. CHAMBERS: *Epitaxial growth and properties of thin film oxides*, Surface Science Reports **39**, 105 (2000)
- [186] G. Q. GONG, A. GUPTA, G. XIAO, W. QIAN, V. P. DRAVID: *Magnetoresistance and magnetic properties of epitaxial magnetite thin films*, Physical Review B **56**, 5096 (1997)
- [187] S. KALE, S. M. BHAGAT, S. E. LOFLAND, T. SCABAROZI, S. B. OGALE, A. OROZCO, S. R. SHINDE, T. VENKATESAN, B. HANNOYER, B. MERCEY, W. PRELLIER: *Film thickness and temperature dependence of the magnetic properties of pulsed-laser-deposited Fe_3O_4 films on different substrates*, Physical Review B **64**, 205413 (2001)
- [188] Y. SUZUKI: *Epitaxial spinel ferrite thin films*, Annual Review of Materials Research **31**, 265 (2001)
- [189] J. ORNA, P. A. ALGARABEL, L. MORELLÓN, J. A. PARDO, J. M. DE TERESA, R. LÓPEZ ANTÓN, F. BARTOLOMÉ, L. M. GARCÍA, J. BARTOLOMÉ, J. C. CEZAR, A. WILDES: *Origin of the giant magnetic moment in epitaxial Fe_3O_4 thin film*, Physical Review B **81**, 144420 (2010)
- [190] A. BOLLERO, M. ZIESE, R. HÖHNE, H. SEMMELHACK, U. KÖHLER, A. SETZER, P. ESQUINAZI: *Influence of thickness on microstructural and magnetic properties in Fe_3O_4 thin films produced by PLD*, Journal of Magnetism and Magnetic Materials **285**, 279 (2005)

- [191] M. ZIESE: *Spontaneous resistivity anisotropy and band structure of LCMO and FeO films*, Physical Review B **62**, 1044 (2000)
- [192] P. KUIPER, B. G. SEARLE, L. C. DUDA, R. M. WOLF, P. J. VANDERZAAG: *Fe L_{2,3} linear and circular magnetic dichroism of Fe₃O₄*, J. Electron Spectrosc. Relat. Phenom. **86**, 107 (1997)
- [193] D. T. MARGULIES, F. T. PARKER, M. L. RUDEE, F. E. SPADA, J. N. CHAPMAN, P. R. AITCHISON, A. E. BERKOWITZ: *Origin of the anomalous magnetic behaviour in single crystal Fe₃O₄ films*, Physical Review Letters **79**, 5162 (1997)
- [194] J. M. D. COEY, A. E. BERKOWITZ, L. BALCELLS, F. F. PUTRIS, F. T. PARKER: *Magnetoresistance of magnetite*, Applied Physics Letters **72**, 734 (1998)
- [195] M. ZIESE, H. J. BLYTHE: *Magnetoresistance of magnetite*, Journal of Physics: Condensed Matter **12**, 13 (2000)
- [196] A. FERNÁNDEZ-PACHECO, J. ORNA, J. M. DE TERESA, P. A. ALGARABEL, L. MORELLON, J. A. PARDO, M. R. IBARRA, E. KAMPERT, U. ZEITLER: *High-field Hall effect and magnetoresistance in Fe₃O₄ epitaxial thin films up to 30 Tesla*, Applied Physics Letters **95**, 28 (2009)
- [197] W. EERENSTEIN, T. T. M. PALSTRA, T. HIBMA, S. CELOTTO: *Origin of the increased resistivity in epitaxial Fe₃O₄ films*, Physical Review B **66**, 201101 (2002)
- [198] X. W. LI, A. GUPTA, G. XIAO, G. Q. GONG: *Transport and magnetic properties of epitaxial and polycrystalline magnetite thin films*, J. Appl. Phys. **83**, 7049 (1998)
- [199] R. ARRAS, L. CALMELS, B. WAROT-FONROSE: *Electronic structure near an antiphase boundary in magnetite*, Physical Review B - Condensed Matter and Materials Physics **81**, 1 (2010)
- [200] S. CELOTTO, W. EERENSTEIN, T. HIBMA: *Characterization of anti-phase boundaries in epitaxial magnetite films*, European Physical Journal B **36**, 271 (2003)
- [201] T. HIBMA, F. C. VOOGT, L. NIESEN, P. A. A. VAN DER HEIJDEN, W. J. M. DE JONGE, J. J. T. M. DONKERS, P. J. VAN DER ZAAG: *Anti-phase domains and magnetism in epitaxial magnetite layers*, Journal of Applied Physics **85**, 5291 (1999)
- [202] W. EERENSTEIN, T. T. M. PALSTRA, S. S. SAXENA, T. HIBMA: *Spin-polarized transport across sharp antiferromagnetic boundaries.*, Physical review letters **88**, 247204 (2002)

- [203] A. V. RAMOS, J. B. MOUSSY, M. J. GUITTET, A. M. BATAILLE, M. GAUTIER-SOYER, M. VIRET, C. GATEL, P. BAYLE-GUILLEMAUD, E. SNOECK: *Magnetotransport properties of Fe_3O_4 epitaxial thin films: Thickness effects driven by antiphase boundaries*, Journal of Applied Physics **100** (2006)
- [204] S. TODO, K. SIRATORI, S. KIMURA: *Transport Properties of the High Temperature Phase of Fe_3O_4* , Journal of the Physical Society of Japan **64**, 2118 (1995)
- [205] C. BOEKEMA, R. L. LICHTI, K. C. B. CHAN, V. A. M. BRABERS, A. B. DENISON, D. W. COOKE, R. H. HEFFNER, R. L. HUTSON, M. E. SCHILLACI: *Experimental evidence for a Mott-Wigner glass phase of magnetite above the Verwey temperature*, Physical Review B **33**, 210 (1986)
- [206] D. IHLE, B. LORENZ: *Theory of the verwey transition in the mixed valence compound Eu_3S_4* , Physica Status Solidi (B) **116**, 539 (1983)
- [207] D. IHLE, B. LORENZ: *Small-polaron conduction and short-range order in Fe_3O_4* , J. Phys. C: Solid State Phys. **19**, 5239 (1986)
- [208] F. WALZ: *The Verwey transition - a topical review*, Journal of Physics: Condensed Matter **14**, R285 (2002)
- [209] J. GARCÍA, G. SUBÍAS: *The Verwey transition-a new perspective*, Journal of Physics: Condensed Matter **16**, R145 (2004)
- [210] S. OGALE, K. GHOSH, R. SHARMA: *Magnetotransport anisotropy effects in epitaxial magnetite (Fe_3O_4) thin films*, Physical Review B **57**, 7823 (1998)
- [211] E. J. W. VERWEY: *Electronic Conduction of Magnetite (Fe_3O_4) and its Transition Point at Low Temperatures*, Nature **144**, 327 (1939)
- [212] E. J. W. VERWEY, P. W. HAAYMAN: *Electronic conductivity and transition point of magnetite (" Fe_3O_4 ")*, Physical Review B **8**, 979 (1941)
- [213] M. IIZUMI, T. F. KOETZLE, G. SHIRANE, S. CHIKAZUMI, M. MATSUI, S. TODO: *Structure of magnetite (Fe_3O_4) below the Verwey transition temperature*, Acta Crystallographica Section B Structural Crystallography and Crystal Chemistry **38**, 2121 (1982)
- [214] J. P. SHEPHERD, J. W. KOENITZER, R. ARAGÓN, J. SPAL/EK, J. M. HONIG: *Heat capacity and entropy of nonstoichiometric magnetite $Fe_3(1-\delta)O_4$: The thermodynamic nature of the Verwey transition*, Physical Review B **43**, 8461 (1991)

- [215] J. P. SHEPHERD, R. ARAGÓN, J. W. KOENITZER, J. M. HONIG: *Changes in the nature of the Verwey transition in nonstoichiometric magnetite (Fe_3O_4)*, Physical Review B **32**, 1818 (1985)
- [216] S. P. SENA, R. A. LINDLEY, H. J. BLYTHE, C. SAUER, M. AL-KAFARJI, G. A. GEHRING: *Investigation of magnetite thin films produced by pulsed laser deposition*, J. Magn. Magn. Mater. **176**, 111 (1997)
- [217] P. MILES, W. WESTPHAL, A. VON HIPPEL: *Dielectric Spectroscopy of Ferromagnetic Semiconductors*, Reviews of Modern Physics **29**, 279 (1957)
- [218] J. DRABBLE, T. WHYTE, R. HOOPER: *Electrical conductivity of magnetite at low temperatures*, Solid State Communications **9**, 275 (1971)
- [219] N. F. MOTT: *Metal-Insulator Transitions* (Taylor and Francis, London, 1990), 2. Ed.
- [220] N. F. MOTT: *Conduction in non-crystalline materials*, Philosophical Magazine **19**, 835 (1969)
- [221] J. P. WRIGHT, J. P. ATTFIELD, P. G. RADAELLI: *Charge ordered structure of magnetite Fe_3O_4 below the Verwey transition*, Physical Review B **66**, 214422 (2002)
- [222] P. NOVÁK, V. A. M. BRABERS: *NMR in magnetite below and around the Verwey transition*, Physical Review B **61**, 1256 (2000)
- [223] J. GARCÍA, G. SUBÍAS, M. G. PROIETTI, J. BLASCO, H. RENEVIER, J. L. HODEAU, Y. JOLY: *Absence of charge ordering below the Verwey transition temperature in magnetite*, Physical Review B **63**, 54110 (2001)
- [224] P. SENEOR, A. FERT, J.-L. MAURICE, F. MONTAIGNE, F. PETROFF, A. VAURÈS: *Large magnetoresistance in tunnel junctions with an iron oxide electrode*, Appl. Phys. Lett. **74**, 4017 (1999)
- [225] H. MATSUDA, M. TAKEUCHI, H. ADACHI, M. HIRAMOTO, N. MATSUKAWA, A. ODAGAWA, K. SETSUNE, H. SAKAKIMA: *Fabrication and magnetoresistance properties of spin-dependent tunnel junctions using an epitaxial Fe_3O_4 film*, Japanese Journal of Applied Physics, Part 2: Letters **41**, 1 (2002)
- [226] K. I. AOSHIMA, S. X. WANG: *Fe_3O_4 and its magnetic tunneling junctions grown by ion beam deposition*, Journal of Applied Physics **93**, 7954 (2003)
- [227] CHANDO PARK, YIMING SHI, YINGGUO PENG, K. BARMAN, JIANGANG ZHU, D. LAUGHLIN, R. WHITE: *Interfacial composition and microstructure of Fe_3O_4 magnetic tunnel junctions*, IEEE Transactions on Magnetics **39**, 2806 (2003)

- [228] A. M. BATAILLE, R. MATTANA, P. SENEOR, A. TAGLIAFERRI, S. GOTA, K. BOUZEHOUE, C. DERANLOT, M. J. GUITTET, J. B. MOUSSY, C. DE NADAÏ, N. B. BROOKES, F. PETROFF, M. GAUTIER-SOYER: *On the spin polarization at the $\text{Fe}_3\text{O}_4/\gamma\text{-Al}_2\text{O}_3$ interface probed by spin-resolved photoemission and spin-dependent tunneling*, Journal of Magnetism and Magnetic Materials **316**, 963 (2007)
- [229] D. REISINGER, P. MAJEWSKI, M. OPEL, L. ALFF, R. GROSS: *Room temperature tunneling magnetoresistance in magnetite based junctions: Influence of tunneling barrier*, ArXiv p. 1–7 (2004)
- [230] K. S. YOON, J. H. KOO, Y. H. DO, K. W. KIM, C. O. KIM, J. P. HONG: *Performance of $\text{Fe}_3\text{O}_4/\text{AlOx}/\text{CoFe}$ magnetic tunnel junctions based on half-metallic Fe_3O_4 electrodes*, Journal of Magnetism and Magnetic Materials **285**, 125 (2005)
- [231] C. PARK, D. E. LAUGHLIN, R. M. WHITE: *Inverse magnetoresistance in magnetic tunnel junction with an Fe_3O_4 electrode*, IEEE Transactions on Magnetics **41**, 2691 (2005)
- [232] T. NAGAHAMA, Y. MATSUDA, K. TATE, S. HIRATANI, Y. WATANABE, T. YANASE, T. SHIMADA: *Magnetic properties of epitaxial Fe_3O_4 films with various crystal orientations and TMR effect in room temperature*, arXiv preprint arXiv: 1406.1296 **4**, 1 (2014)
- [233] T. KADO: *Large room-temperature inverse magnetoresistance in tunnel junctions with a Fe_3O_4 electrode*, Applied Physics Letters **92**, 1 (2008)
- [234] T. KADO, H. SAITO, K. ANDO: *Room-temperature magnetoresistance in magnetic tunnel junctions with Fe_3O_4 electrode*, Journal of Applied Physics **101**, 09J511 (2007)
- [235] X. W. LI, A. GUPTA, G. XIAO, W. QIAN, V. P. DRAVID: *Fabrication and properties of heteroepitaxial magnetite (Fe_3O_4) tunnel junctions*, Applied Physics Letters **73**, 3282 (1998)
- [236] P. J. V. D. ZAAG, P. J. H. BLOEMEN, J. M. GAINES, R. M. WOLF, P. A. A. V. D. HEIJDEN, R. J. M. V. D. VEERDONK, W. J. M. D. JONGE: *On the construction of an Fe O -based all-oxide spin valve*, Journal of Magnetism and Magnetic Materials **211**, 301 (2000)
- [237] F. GREULLET, E. SNOECK, C. TIUSAN, M. HEHN, D. LACOUR, O. LENOBLE, C. MAGEN, L. CALMELS: *Large inverse magnetoresistance in fully epitaxial $\text{Fe}/\text{Fe}_3\text{O}_4/\text{MgO}/\text{Co}$ magnetic tunnel junctions*, Applied Physics Letters **92**, 053508 (2008)
- [238] L. MARNITZ, K. ROTT, S. NIEHÖRSTER, C. KLEWE, D. MEIER, S. FABRETTI, M. WITZIOK, A. KRAMPF, O. KUSCHEL, T. SCHEMME,

- K. KUEPPER, J. WOLLSCHLÄGER, A. THOMAS, G. REISS, T. KUSCHEL: *Sign change in the tunnel magnetoresistance of Fe₃O₄/MgO/Co-Fe-B magnetic tunnel junctions depending on the annealing temperature and the interface treatment*, AIP Advances **5** (2015)
- [239] G. HU, Y. SUZUKI: *Negative Spin Polarization of Fe₃O₄ in Magnetite/Manganite-Based Junctions*, Physical Review Letters **89**, 276601 (2002)
- [240] L. M. B. ALLDREDGE, R. V. CHOPDEKAR, B. B. NELSON-CHEESEMAN, Y. SUZUKI: *Spin-polarized conduction in oxide magnetic tunnel junctions with magnetic and nonmagnetic insulating barrier layers*, Applied Physics Letters **89**, 30 (2006)
- [241] A. M. BATAILLE, A. TAGLIAFERRI, S. GOTA, C. DE NADAÏ, J.-B. MOUSSY, M.-J. GUITTET, K. BOUZEHOUE, F. PETROFF, M. GAUTIER-SOYER, N. B. BROOKES: *Negative spin polarization of the Fe₃O₄/γ-Al₂O₃ interface measured by spin-resolved photoemission*, Physical Review B **73**, 172201 (2006)
- [242] M. BETH STEARNS: *Simple explanation of tunneling spin-polarization of Fe, Co, Ni and its alloys*, Journal of Magnetism and Magnetic Materials **5**, 167 (1977)
- [243] Y. PENG, C. PARK, J. G. ZHU, R. M. WHITE, D. E. LAUGHLIN: *Characterization of interfacial reactions in magnetite tunnel junctions with transmission electron microscopy*, Journal of Applied Physics **95**, 6798 (2004)
- [244] P. A. A. VAN DER HEIJDEN, P. J. H. BLOEMEN, J. M. GAINES, J. T. W. M. VAN EEMEREN, R. M. WOLF, P. J. VAN DER ZAAG, W. J. M. DE JONGE: *Magnetic interface anisotropy of MBE-grown ultra-thin (001) Fe₃O₄ layers*, Journal of Magnetism and Magnetic Materials **159**, 293 (1996)
- [245] J. A. GOMES, G. M. AZEVEDO, J. DEPEYROT, J. MESTNIK-FILHO, G. J. DA SILVA, F. A. TOURINHO, R. PERZYNSKI: *ZnFe₂O₄ nanoparticles for ferrofluids: A combined XANES and XRD study*, Journal of Magnetism and Magnetic Materials **323**, 1203 (2011)
- [246] S. NAKASHIMA, K. FUJITA, K. TANAKA, K. HIRAO: *High magnetization and the high-temperature superparamagnetic transition with inter-cluster interaction in disordered zinc ferrite thin film.*, Journal of physics. Condensed matter : an Institute of Physics journal **17**, 137 (2005)
- [247] S. R. SHANNIGRAHI, K. P. PRAMODA, F. A. A. NUGROHO: *Synthesis and characterizations of microwave sintered ferrite powders and their com-*

- posite films for practical applications*, Journal of Magnetism and Magnetic Materials **324**, 140 (2012)
- [248] I. SHARIFI, H. SHOKROLLAHI, S. AMIRI: *Ferrite-based magnetic nanofluids used in hyperthermia applications*, Journal of Magnetism and Magnetic Materials **324**, 903 (2012)
- [249] A. SUTKA, K. . ARLIS, A. GROSS: *Spinel ferrite oxide semiconductor gas sensors*, Sensors and Actuators B **222**, 95 (2016)
- [250] V. JESEENTHARANI, M. GEORGE, B. JEYARAJ, A. DAYALAN, & K. S. NAGARAJA, K. S. NAGARAJA: *Synthesis of metal ferrite (MFe_2O_4 , $M = Co, Cu, Mg, Ni, Zn$) nanoparticles as humidity sensor materials*, Journal of Experimental Nanoscience **8**, 358 (2013)
- [251] I. CHICINAS: *Soft magnetic nanocrystalline powders produced by mechanical alloying routes*, Journal of Optoelectronics and Advanced Materials **8**, 439 (2006)
- [252] A. SUTKA, G. MEZINSKIS: *Sol-gel auto-combustion synthesis of spinel-type ferrite nanomaterials*, Frontiers of Materials Science **6**, 128 (2012)
- [253] S. AYYAPPAN, S. P. RAJA, C. VENKATESWARAN, J. PHILIP, B. RAJ: *Room temperature ferromagnetism in vacuum annealed $ZnFe_2O_4$ nanoparticles*, Applied Physics Letters **96**, 143106 (2010)
- [254] F. S. LI, L. WANG, J. B. WANG, Q. G. ZHOU, X. Z. ZHOU, H. P. KUNKEL, G. WILLIAMS: *Site preference of Fe in nanoparticles of $ZnFe_2O_4$* , Journal of Magnetism and Magnetic Materials **268**, 332 (2004)
- [255] S. NAKASHIMA, K. FUJITA, K. TANAKA, K. HIRAO, T. YAMAMOTO, I. TANAKA: *First-principles XANES simulations of spinel zinc ferrite with a disordered cation distribution*, Physical Review B - Condensed Matter and Materials Physics **75**, 2 (2007)
- [256] S. NAKASHIMA, K. FUJITA, K. TANAKA, K. HIRAO, T. YAMAMOTO, I. TANAKA: *Thermal annealing effect on magnetism and cation distribution in disordered $ZnFe_2O_4$ thin films deposited on glass substrates*, Journal of Magnetism and Magnetic Materials **310**, 2543 (2007)
- [257] M. SULTAN, R. SINGH: *Magnetic and optical properties of rf-sputtered zinc ferrite thin films*, Journal of Applied Physics **105**, 18 (2009)
- [258] C. N. CHINNASAMY, A. NARAYANASAMY, N. PONPANDIAN, K. CHATTOPADHYAY, H. GUÉRAULT, J.-M. GRENECHE: *Magnetic properties of nanostructured ferrimagnetic zinc ferrite*, Journal of Physics: Condensed Matter **12**, 7795 (2000)

- [259] G. GOYA, H. RECHENBERG: *Ionic disorder and Néel temperature in ZnFe_2O_4 nanoparticles*, Journal of Magnetism and Magnetic Materials **196-197**, 191 (1999)
- [260] D. ZHANG, Y. DU: *Structure and giant magnetoresistance in zinc ferrite*, Journal Wuhan University of Technology, Materials Science Edition **21**, 113 (2006)
- [261] D. YOU-WEI, C. PENG, Z. JIAN-MIN, X. DING-YU: *Giant magnetoresistance in nanostructured $\text{Zn}_x\text{Fe}_{3-x}\text{O}_4$ polycrystalline material*, Acta Physica Sinica **50**, 2275 (2001)
- [262] P. SHENG, B. ABELES, Y. ARIE: *Hopping conductivity in granular metals*, Physical Review Letters **31**, 44 (1973)
- [263] A. A. TIMOPHEEV, A. M. AZEVEDO, N. A. SOBOLEV, K. BRACHWITZ, M. LORENZ, M. ZIESE, P. ESQUINAZI, M. GRUNDMANN: *Magnetic anisotropy of epitaxial zinc ferrite thin films grown by pulsed laser deposition*, Thin Solid Films **527**, 273 (2013)
- [264] C. CHENG, C.-S. LIU: *Effects of cation distribution in ZnFe_2O_4 and CdFe_2O_4 : ab initio studies*, Journal of Physics: Conference Series **145**, 012028 (2009)
- [265] V. G. HARRIS, N. C. KOON, C. M. WILLIAMS, Q. ZHANG, M. ABE, J. P. KIRKLAND: *Cation distribution in NiZn -ferrite films via extended x-ray absorption fine structure*, Applied Physics Letters **68**, 2082 (1996)
- [266] J.-H. KIM, H.-I. YOO, H. L. TULLER: *Electrical Properties and Phase Stability of a Zinc Ferrite*, Journal of the American Ceramic Society **73**, 258 (1990)
- [267] V. ZVIAGIN, P. RICHTER, T. BÖNTGEN, M. LORENZ, M. ZIESE, D. R. T. ZAHN, G. SALVAN, M. GRUNDMANN, R. SCHMIDT-GRUND: *Comparative study of optical and magneto-optical properties of normal, disordered, and inverse spinel-type oxides*, Physica Status Solidi (B) Basic Research **8**, 1 (2015)
- [268] Q. TIAN, Q. WANG, Q. XIE, J. LI: *Aqueous Solution Preparation, Structure, and Magnetic Properties of Nano-Granular $\text{Zn}_x\text{Fe}_{3-x}\text{O}_4$ Ferrite Films*, Nanoscale Research Letters **5**, 1518 (2010)
- [269] Y. H. CHENG, L. Y. LI, W. H. WANG, H. LIU, S. W. REN, X. Y. CUI, R. K. ZHENG: *Tunable electrical and magnetic properties of half-metallic $\text{Zn}_x\text{Fe}_{3-x}\text{O}_4$ from first principles*, Physical Chemistry Chemical Physics **13**, 21243 (2011)

- [270] M. LORENZ: *Pulsed Laser Deposition of ZnO-Based Thin Films*, in: *Transparent Conductive Zinc Oxide*, K. ELLMER, A. KLEIN, B. RECH, Ed. (Springer Berlin Heidelberg, Berlin-Heidelberg, 2008), Chap. 7, p. 303–357, 1. Ed.
- [271] M. LORENZ, H. HOCHMUTH, M. KNEISS, M. BONHOLZER, M. JENDERKA, M. GRUNDMANN: *From high-T_c superconductors to highly correlated Mott insulators- 25 years of pulsed laser deposition of functional oxides in Leipzig*, Semiconductor Science and Technology **30**, 024003 (2015)
- [272] C. B. ARNOLD, M. J. AZIZ: *Stoichiometry issues in pulsed-laser deposition of alloys grown from multicomponent targets*, Applied Physics A: Materials Science and Processing **69** (1999)
- [273] M. LORENZ: *Gepulste Laser-Plasmaabscheidung (PLD) von oxidischen Dünnsfilm- und Nanostrukturen*, Habilitationsschrift, Universität Leipzig (2008)
- [274] D. B. CHRISLEY, G. K. HUBLER (Ed.): *Pulsed Laser Deposition of Thin Films* (Viley-Interscience, New York, 1994), 1. Ed.
- [275] M. LORENZ, M. S. RAMACHANDRA RAO: *25 Years of Pulsed Laser Deposition*, Journal of Physics D: Applied Physics **47**, 030301 (2014)
- [276] J. ZIPPEL: *Gepulste Laserabscheidung und Charakterisierung funktionaler oxidischer Dünnsfilme und Heterostrukturen*, Dissertation, Universität Leipzig (2012)
- [277] J. KLEIN: *Epitaktische Heterostrukturen aus dotierten Manganaten*, Dissertation, Universität Köln (2001)
- [278] J. ORTON, T. FOXON: *Molecular Beam Epitaxy* (Oxford University Press, 2015)
- [279] ZHONG LIN WANG: *Reflection Electron Microscopy and Spectroscopy for Surface Analysis* (Cambridge University Press, Cambridge, 1996), 1. Ed.
- [280] R. EASON (Ed.): *Pulsed Laser Deposition of Thin Films* (John Wiley and Sons, Hoboken, New Jersey, 2007)
- [281] J. ZIPPEL, M. LORENZ, G. BENNDORF, M. GRUNDMANN: *Persistent layer-by-layer growth for pulsed-laser homoepitaxy of (000 -1) ZnO*, physica status solidi (RRL) - Rapid Research Letters **6**, 433 (2012)
- [282] J. M. TEIXEIRA, J. VENTURA, F. CARPINTEIRO, J. P. ARAUJO, J. B. SOUSA, P. WISNIOWSKI, P. P. FREITAS: *The effect of pinhole formation/growth on the tunnel magnetoresistance of MgO-based magnetic tunnel junctions*, Journal of Applied Physics **106**, 073707 (2009)

- [283] B. D. SCHRAG, A. ANGUELOUCH, S. INGVARSSON, G. XIAO, Y. LU, P. L. TROUILLOUD, A. GUPTA, R. A. WANNER, W. J. GALLAGHER, P. M. RICE, S. S. P. PARKIN: *Néel "orange-peel" coupling in magnetic tunneling junction devices*, Applied Physics Letters **77**, 2373 (2000)
- [284] S. TEGEN, I. MÖNCH, J. SCHUMANN, H. VINZELBERG, C. M. SCHNEIDER: *Effect of Néel coupling on magnetic tunnel junctions*, Journal of Applied Physics **89**, 8169 (2001)
- [285] T. MICHELY, J. KRUG: *Islands, Mounds and Atoms, Springer Series in Surface Sciences*, Vol. 42 (Springer, Berlin, Heidelberg, 2004)
- [286] S. ROSSNAGEL, R. ROBINSON, H. KAUFMAN: *Impact enhanced surface diffusion during impurity induced sputter cone formation*, Surface Science **123**, 89 (1982)
- [287] J. Y. CAVAILLÉ, M. DRECHSLER: *Surface self-diffusion by ion impact*, Surface Science **75**, 342 (1978)
- [288] M. A. MAKEEV, A.-L. BARABÁSI: *Ion-induced effective surface diffusion in ion sputtering*, Applied Physics Letters **71**, 2800 (1997)
- [289] L. WANG, K. FU, X. TIAN, B. TANG, P. CHU: *Influence of temperature and ion kinetic energy on surface morphology of CeO₂ films prepared by dual plasma deposition*, Materials Science and Engineering: A **336**, 75 (2002)
- [290] R. L. SCHWOEBEL, E. J. SHIPSEY: *Step motion on crystal surfaces*, Journal of Applied Physics **37**, 3682 (1966)
- [291] G. EHRLICH, F. G. HUDDA: *Atomic View of Surface Self-Diffusion: Tungsten on Tungsten*, The Journal of Chemical Physics **44**, 1039 (1966)
- [292] R. L. SCHWOEBEL: *Step Motion on Crystal Surfaces. II*, Journal of Applied Physics **40**, 614 (1969)
- [293] M. LIPPMAN, N. NAKAGAWA, M. KAWASAKI, S. OHASHI, H. KOINUMA: *Growth mode mapping of SrTiO₃ epitaxy*, Applied Physics Letters **76**, 2439 (2000)
- [294] SURFACE GmbH, *Laser Heater for Substrates*, <http://www.surface-tec.com/pldlaserheater.php>, accessed on Feb. 25 (2016)
- [295] COHERENT: *LPXpro Series Data sheet* (2012)
- [296] G. J. H. M. RIJNDERS, G. KOSTER, D. H. A. BLANK, H. ROGALLA: *In situ monitoring during pulsed laser deposition of complex oxides using reflection high energy electron diffraction under high oxygen pressure*, Applied Physics Letters **70**, 1888 (1997)

- [297] L. SPIESS, R. SCHWARZER, H. BEHNKEN, G. TEICHERT: *Moderne Röntgenbeugung* (B. G. Teubner, Wiesbaden, 2005)
- [298] Y. WASEDA, E. MATSUBARA, K. SHINODA: *X-Ray Diffraction Crystallography* (Springer Berlin Heidelberg, Berlin, Heidelberg, 2011)
- [299] D. K. BOWEN, B. K. TANNER: *High Resolution X-ray Diffractometry and Topography* (CRC Press by Taylor and Francis Group, Boca Raton, FL, 1998)
- [300] J. SASS, K. MAZUR, B. SURMA, F. EICHHORN, D. LITWIN, J. GALAS, S. SITAREK: *X-ray studies of ultra-thin Si wafers for mirror application*, Nuclear Instruments and Methods in Physics Research Section B: Beam Interactions with Materials and Atoms **253**, 236 (2006)
- [301] M. LORENZ, G. WAGNER, V. LAZENKA, P. SCHWINKENDORF, H. MODARRESI, M. J. VAN BAEI, A. VANTOMME, K. TEMST, O. OECKLER, M. GRUNDMANN: *Correlation of magnetoelectric coupling in multiferroic BaTiO₃-BiFeO₃ superlattices with oxygen vacancies and antiphase octahedral rotations*, Applied Physics Letters **106**, 012905 (2015)
- [302] H. WEI, M. JENDERKA, M. GRUNDMANN, M. LORENZ: *LaNiO₃ films with tunable out-of-plane lattice parameter and their strain-related electrical properties*, Physica Status Solidi (a) **212**, 1925 (2015)
- [303] M. YASAKA: *X-ray thin-film measurement techniques*, V. X-ray reflectivity measurement. The Rigaku Journal **26**, 1 (2010)
- [304] M. F. TONEY, C. THOMPSON: *X-ray reflectivity on perfluoropolyether polymer molecules on amorphous carbon*, J. Chem. Phys. **92**, 3781 (1990)
- [305] K. SAKURAI, M. MIZUSAWA: *Significance of Frequency Analysis in X-ray Reflectivity: Towards analysis which does not depend too much on models*, Transaction of the Materials Research Society of Japan **33**, 523 (2008)
- [306] N. I. CHKHALOV, M. V. FEDORCHENKO, E. P. KRUGLYAKOV, A. I. VOLOKHOV, K. S. BARABOSHKIN, V. F. KOMAROV, S. I. KOSTYUKOV, E. A. PETROV: *Ultradispersed diamond powders of detonation nature for polishing X-ray mirrors*, Nuclear Inst. and Methods in Physics Research, A **359**, 155 (1995)
- [307] Y. FUJII: *Comparison of Surface Roughness Estimations by X-ray Reflectivity Measurements and TEM observations*, IOP Conference Series: Materials Science and Engineering **24**, 012008 (2011)
- [308] L. G. PARRATT: *Surface studies of solids by total reflection of x-rays*, Physical Review **95**, 359 (1954)

- [309] PARK SYSTEMS CORPORATION: *XE-150 User's Manual, Version 1.8.2* (2009)
- [310] D. NEČAS, P. Klapetek: *Gwyddion: an open-source software for SPM data analysis*, Open Physics **10**, 181 (2012)
- [311] M. McElfresh: *Fundamentals of Magnetism and Magnetic Measurements* (Quantum Design, 1994)
- [312] J. CLARKE, A. I. BRAGINSKI (Ed.): *The SQUID Handbook. Vol. I: Fundamentals and Technology of SQUIDs and SQUID systems* (Wiley-VCH, Weinheim, 2004)
- [313] J. CLARKE, A. I. BRAGINSKI (Ed.): *SQUID Handbook. Vol. II: Applications of SQUIDs and SQUID systems* (Wiley-VCH, Weinheim, 2005)
- [314] R. A. SHATAS, J. F. MARSHALL, M. A. POMERANTZ: *Dependence of Secondary Electron Emission upon Angle of Incidence of 1.3-MeV Primaries*, Physical Review **102**, 682 (1956)
- [315] H. BETHGE: *Electron microscopy in solid state physics* (Elsevier, Amsterdam, 1987)
- [316] L. J. VAN-DER PAUW: *A method of measuring the resistivity and Hall coefficient on lamellae of arbitrary shape*, Philips Technical Review **20**, 220 (1958)
- [317] M. ZIESE, U. KOHLER, R. HOHNE, A. BOLLERO, P. ESQUINAZI: *Schottky barrier formation at the Fe₃O₄/Nb:SrTiO₃ interface*, Journal of Magnetism and Magnetic Materials **290**, 1116 (2005)
- [318] M. ZIESE, U. KÖHLER, A. BOLLERO, R. HÖHNE, P. ESQUINAZI: *Schottky barrier and spin polarization at the Fe₃O₄-Nb:SrTiO₃ interface*, Physical Review B **71**, 180406 (2005)
- [319] K. CHOW, W. NG, L. YEUNG: *Interdiffusion of Cu substrate/electrodeposits for Cu/Co, Cu/Co-W, Cu/Co/Ni and Cu/Co-W/Ni systems*, Surface and Coatings Technology **99**, 161 (1998)
- [320] G. SUCHANECK, V. NORKUS, G. GERLACH: *Low-temperature PECVD-deposited silicon nitride thin films for sensor applications*, Surface and Coatings Technology **142-144**, 808 (2001)
- [321] M. L. REED, J. D. PLUMMER: *Chemistry of Si-SiO₂ interface trap annealing*, Journal of Applied Physics **63**, 5776 (1988)
- [322] C. KARTUSCH, J. A. BOKHOVEN: *Hydrogenation over gold catalysts: The interaction of gold with hydrogen*, Gold Bulletin **42**, 343 (2009)

- [323] Y.-M. CHANG, J. LEU, B.-H. LIN, Y.-L. WANG, Y.-L. CHENG: *Comparison of H₂ and NH₃ Treatments for Copper Interconnects*, Advances in Materials Science and Engineering **2013**, 1 (2013)
- [324] Osnabruegge GmbH & Co. KG, Maedachaeckerweg 39, D-75181 Pforzheim, Germany, www.os-materials.com
- [325] CrysTec GmbH, Köpenicker Str. 325, D-12555 Berlin, Germany, www.crystec.de
- [326] M. MURUGESAN, H. OBARA, Y. NAKAGAWA, S. KOSAKA, H. YAMASAKI: *Influence of MgO substrate annealing on the microwave properties of laser ablated YBa₂Cu₃O₇ thin films*, Superconductor Science and Technology **17**, 113 (2004)
- [327] K. INUMARU, T. OHARA, S. YAMANAKA: *Pulsed laser deposition of epitaxial titanium nitride on MgO(001) monitored by RHEED oscillation*, Applied Surface Science **158**, 375 (2000)
- [328] A. DE LUCA, A. DÉGARDIN, F. ABBOTT, F. HOUZÉ, A. KREISLER: *Influence of microstructure on electrical and microwave properties of YBaCuO thin films*, Physica C: Superconductivity **372-376**, 578 (2002)
- [329] M. LEE, M. KAWASAKI, M. YOSHIMOTO, M. KUMAGAI, H. KOINUMA: *Epitaxial growth of highly crystalline and conductive nitride films by pulsed laser deposition*, Japanese Journal of Applied Physics **33**, 6308 (1994)
- [330] D. REISINGER, M. SCHONECKE, T. BRENNINGER, M. OPEL, A. ERB, L. ALFF, R. GROSS: *Epitaxy of Fe₃O₄ on Si(001) by pulsed laser deposition using a TiN/MgO buffer layer*, Journal of Applied Physics **94**, 1857 (2003)
- [331] B. STANKA, W. HEBENSTREIT, U. DIEBOLD, S. CHAMBERS: *Surface reconstruction of Fe₃O₄(001)*, Surface Science **448**, 49 (2000)
- [332] G. S. PARKINSON, Z. NOVOTNÝ, P. JACOBSON, M. SCHMID, U. DIEBOLD: *A metastable Fe(A) termination at the Fe₃O₄(001) surface*, Surface Science **605**, L42 (2011)
- [333] F. SCHLEICHER, U. HALISDEMIR, D. LACOUR, M. GALLART, S. BOUKARI, G. SCHMERBER, V. DAVESNE, P. PANISSOD, D. HALLEY, H. MAJJAD, Y. HENRY, B. LECONTE, A. BOULARD, D. SPOR, N. BEYER, C. KIEBER, E. STERNITZKY, O. CREGUT, M. ZIEGLER, F. MONTAIGNE, E. BEAUREPAIRE, P. GILLIOT, M. HEHN, M. BOWEN: *Localized states in advanced dielectrics from the vantage of spin- and symmetry-polarized tunnelling across MgO.*, Nature communications **5**, 4547 (2014)

- [334] J. M. ROWELL: *Tunneling Density of States-Experiment*, in: *Tunneling phenomena in Solids*, E. BURSTEIN, S. LUNDQVIST, Ed. (Springer US, Boston, MA, 1969), Chap. 20, S. 273
- [335] J. J. AKERMAN, J. M. SLAUGHTER, R. W. DAVE, I. K. SCHULLER: *Tunneling criteria for magnetic-insulator-magnetic structures*, Applied Physics Letters **79**, 3104 (2001)
- [336] J. J. AKERMAN, R. ESCUDERO, C. LEIGHTON, S. KIM, D. RABSON, R. W. DAVE, J. SLAUGHTER, I. K. SCHULLER: *Criteria for ferromagnetic-insulator-ferromagnetic tunneling*, Journal of Magnetism and Magnetic Materials **240**, 86 (2002)
- [337] N. A. TUAN, P. L. MINH, T. T. DUNG: *Determination of the barrier parameters of Al₂O₃ layer in MTJs by Simmons' and Brinkman's models*, Communication in Physics **16**, 7 (2006)
- [338] J. H. WERNER, H. H. GÜTTLER: *Barrier inhomogeneities at Schottky contacts*, Journal of Applied Physics **69**, 1522 (1991)
- [339] D. REISINGER: *Magnetit in ultradünnen epitaktischen Schichtsystemen für die Spinelektronik*, Dissertation, Technische Universität München (2004)
- [340] R. PAUTHENET: *Experimental verification of spin-wave theory in high fields (invited)*, Journal of Applied Physics **53**, 8187 (1982)
- [341] J. G. PELLERIN, S. G. H. ANDERSON, P. S. HO, C. WOOTEN, K. R. COFFEY, J. K. HOWARD, K. BARMAK: *Grain boundary diffusion and its effects on the magnetic properties of Co/Cu and Co/Cr thin film bilayers*, Journal of Applied Physics **75**, 5052 (1994)
- [342] J. M. D. COEY: *Noncollinear Spin Arrangement in Ultrafine Ferrimagnetic Crystallites*, Physical Review Letters **27**, 1140 (1971)
- [343] R. H. KODAMA, A. E. BERKOWITZ, E. J. MCNIFF, S. FONER: *Surface spin disorder in ferrite nanoparticles (invited)*, Journal of Applied Physics **81**, 5552 (1997)
- [344] D. TELESKA, B. SINKOVIC, S. H. YANG, S. S. P. PARKIN: *X-ray studies of interface Fe-oxide in annealed MgO based magnetic tunneling junctions*, Journal of Electron Spectroscopy and Related Phenomena **185**, 133 (2012)
- [345] M. GRÜNEWALD, N. HOMONNAY, J. KLEINLEIN, G. SCHMIDT: *Voltage-controlled oxide barriers in organic/hybrid spin valves based on tunneling anisotropic magnetoresistance*, Physical Review B **90**, 205208 (2014)

List of Figures

1.1	Spintronics in data storage applications	7
1.2	Schematic of the exchange splitting in the density of states. . . .	9
1.3	Principles of the giant magneto resistance	12
1.4	Overview on magnetic tunnel junctions	14
1.5	Calculated density of states of Fe, Co, Ni and Cu.	20
1.6	Potential landscape of a tunnel junction and the Fermi function.	24
1.7	Barrier geometries for the Simmons-Model	27
1.8	Barrier geometries for the BDR-Model	30
1.9	The zero conductance $G(0)$ in dependence of barrier thickness d and barrier height Φ	31
1.10	Calculated $j(V)$ and $G(V)$ curves based on the Simmons- and BDR-model	32
1.11	Temperature dependency of the tunnel current.	36
1.12	Theory of the superconducting tunneling spectroscopy.	38
1.13	Illustrative presentation the Julliere model.	42
1.14	Effective spin polarization after Slonczewski.	45
1.15	Conductance ratio after MacLaren.	46
1.16	Correlation between the TMR effect, the polarization of tunnel current obtained by STS measurements and the spin polariza- tion in the bulk of an electrode.	47
1.17	Band dispersion of bcc-Fe and bcc-Co and symmetry filtering in amorphous and epitaxial barriers.	48
1.18	Dependency of the tunnel current on the band structure of Δ_1 electrons.	50
1.19	Influence of the barrier material on the TMR-effect.	51
1.20	Dependence of the TMR on the density of states of the magnetic electrodes.	52
1.21	Principle of the pseudo spin valve.	56
2.1	Sketch of the spinel structure.	61
2.2	Sketch of the energetic splitting in an octahedral and tetrahedral ligand field.	63
2.3	Principle of superexchange and double exchange.	68
2.4	Sketch of the spin configuration in $\text{Zn}_x\text{Fe}_{3-x}\text{O}_4$	70

2.5	Calculated density of states (DOS) for Fe_3O_4	73
2.6	Electric properties of Fe_3O_4 thin films.	74
2.7	Antiphase boundaries in Fe_3O_4	75
2.8	Theory of the impact of antiphase boundaries in Fe_3O_4	76
2.9	The Verwey transition in Fe_3O_4	79
2.10	TMR(V) of a Fe_3O_4 / MgO / Co-MTJ at two different temperatures.	82
2.11	Room temperature magnetization measurements of nanocrystalline ZnFe_2O_4	85
2.12	Electric properties of ZnFe_2O_4 thin films.	88
2.13	Magnetic properties of ZnFe_2O_4 thin films.	91
2.14	Magnetoresistance and spin canting in ZnFe_2O_4	92
2.15	Calculated density of states for partial inverse ZnFe_2O_4 including oxygen vacancies.	93
2.16	Properties of $\text{Zn}_x\text{Fe}_{3-x}\text{O}_4$ thin films.	96
2.17	Calculated density of states of $\text{Zn}_x\text{Fe}_{3-x}\text{O}_4$ at different zinc concentrations x	98
3.1	Schematic drawing of the pulsed laser deposition process.	104
3.2	Principle of RHEED.	107
3.3	Origin of RHEED intensity oscillations.	109
3.4	Thermodynamic thin film growth modes:	111
3.5	Sketches of the nucleation process at the surface during deposition and different growth modes.	114
3.6	Schematic drawing and photographs of the PLD B-chamber.	119
3.7	Geometry of X-ray diffraction.	122
3.8	Principle description of reciprocal space maps.	125
3.9	Simulated X-ray reflectivity curves.	128
3.10	Setup of the Panalytical Pro MRD diffractometer used for X-ray reflectivity measurements.	131
3.11	Principles of atomic force microscopy.	133
3.12	Working principle of the wire bonder.	143
3.13	Schematic of the source measurement unit (SMU) and the wiring used for TMR-measurements.	146
4.1	First version of the newly developed MTJ-design.	150
4.2	SNMS-spectra of thin film stacks for the production of MTJs.	153
4.3	SEM-images of a detached SiN_x layer.	154
4.4	Schematic of the NH_3 plasma treatment of the Ti surface and the subsequent PECVD deposition process of SiN_x	155
4.5	Final version of the newly developed MTJ-design.	156
4.6	Sketch of the sample after lift off preparation of the Ti-mask.	158
4.7	Images of the plasma in the sputter chamber during the deposition of Ti.	159

4.8	Sketch of the sample after Ar-ion etching and LSM-images of a MTJ-pillar.	159
4.9	Sketch of the sample after the deposition of SiN_x and a SEM-image of a cross section prepared by FIB.	160
4.10	Sketch of the sample after applying the resist mask and the W/Au-layer as well as the used photolithography mask.	160
4.11	Sketch of the sample after contact hole milling and SEM-images of milled contact.	161
4.12	Schematic and SEM-cross section image of a completely processed sample.	162
4.13	Schematic of the current path through the MTJ-sample and image of a contacted sample.	163
4.14	Images of the adapter developed for the wire bonder.	164
5.1	AFM topography images of the surface of annealed MgO- substrates.	166
5.2	XRD 2Θ - ω -scans of the TiN-target and two different "TiN"-thin films on MgO, grown in different PLD-chambers and XRR-curves.	168
5.3	RHEED intensity oscillations during PLD-growth of TiN.	169
5.4	AFM topography and RHEED images of a TiN-surface.	170
5.5	X-ray diffraction measurements on TiN-thin films.	171
5.6	Dependence of the composition $x(\text{at}\%)$ of $\text{Zn}_x\text{Fe}_{3-x}\text{O}_4$ on the position L of the PLD-lens.	173
5.7	Surface of a $\text{Zn}_x\text{Fe}_{3-x}\text{O}_4$ ($x \approx 0.2$) thin film on MgO / TiN.	175
5.8	X-ray measurements on $\text{Zn}_x\text{Fe}_{3-x}\text{O}_4$ thin films.	176
5.9	Electric properties of $\text{Zn}_x\text{Fe}_{3-x}\text{O}_4$ thin films.	178
5.10	Room temperature magnetic properties of $\text{Zn}_x\text{Fe}_{3-x}\text{O}_4$ thin films.	180
5.11	Temperature dependent properties of $\text{Zn}_x\text{Fe}_{3-x}\text{O}_4$ thin films.	183
5.12	Thickness determination of MgO-barriers.	184
5.13	Results of the analysis of j - V curve by the BDR-model.	187
5.14	Barrier parameters obtained by the expanded BDR-model.	190
5.15	Temperature dependence of resistance and barrier parameters.	191
5.16	Structure of Co thin films grown by PLD.	193
5.17	Magnetic properties of Co thin films grown by PLD.	194
6.1	Magnetization and TMR-curves of $\text{Zn}_x\text{Fe}_{3-x}\text{O}_4$ -based MTJs.	196

List of Tables

1.1	Spin polarization of transition metals and alloys	19
1.2	TMR values of Heusler-based MTJs	21
2.1	Crystal field stabilization energy (CFSE) for tetrahedral and octahedral ligand field geometry and the resulting octahedral site preference energy (OSPE).	62
2.2	Magnetic interactions in spinel ferrite.	67
2.3	TMR-values with assigned temperature (TMR (@ T)) and room temperature TMR-values of Fe_3O_4 based magnetic tunnel junctions	80
4.1	PLD parameter for thin film growth of TiN, $\text{Zn}_x\text{Fe}_{3-x}\text{O}_4$, MgO and Co.	157
5.1	MgO barrier thickness determined by XRR, RHEED and BDR-fit	185

List of own and contributed Articles

- [A1] M. BONHOLZER, M. LORENZ, M. GRUNDMANN: *Layer-by-layer growth of TiN by pulsed laser deposition on in-situ annealed (100) MgO substrates*, physica status solidi (a) **211**, 2621 (2014)
- [A2] S. BITTER, P. SCHLUPP, M. BONHOLZER, H. VON WENCKSTERN, M. GRUNDMANN: *Influence of the Cation Ratio on Optical and Electrical Properties of Amorphous Zinc-Tin-Oxide Thin Films Grown by Pulsed Laser Deposition*, ACS Combinatorial Science **18**, 188 (2016)
- [A3] M. LORENZ, G. WAGNER, V. LAZENKA, P. SCHWINKENDORF, M. BONHOLZER, M. J. V. BAEI, A. VANTOMME, K. TEMST, O. OECKLER, M. GRUNDMANN: *Correlation of High Magnetoelectric Coupling with Oxygen Vacancy Superstructure in Epitaxial Multiferroic BaTiO₃-BiFeO₃ Composite Thin Films*, Materials **9**, accepted (2016)
- [A4] V. LAZENKA, M. LORENZ, H. MODARRESI, M. BISHT, R. RÜFFER, M. BONHOLZER, M. GRUNDMANN, M. J. VAN BAEI, A. VANTOMME, K. TEMST: *Magnetic spin structure and magnetoelectric coupling in BiFeO₃-BaTiO₃ multilayer*, Applied Physics Letters **106**, 082904 (2015)
- [A5] H. WEI, M. JENDERKA, M. BONHOLZER, M. GRUNDMANN, M. LORENZ: *Modeling the conductivity around the dimensionality-controlled metal-insulator transition in LaNiO₃/LaAlO₃ (100) superlattices*, Applied Physics Letters **106**, 042103 (2015)
- [A6] M. LORENZ, H. HOCHMUTH, M. KNEISS, M. BONHOLZER, M. JENDERKA, M. GRUNDMANN: *From high-T_c superconductors to highly correlated Mott insulators- 25 years of pulsed laser deposition of functional oxides in Leipzig*, Semiconductor Science and Technology **30**, 24003 (2015)
- [A7] R. SCHMIDT-GRUND, H. KRAUSS, C. KRANERT, M. BONHOLZER, M. GRUNDMANN: *Temperature dependence of the dielectric function in*

the spectral range (0.5-8.5) eV of an In₂O₃ thin film, Applied Physics Letters **105**, 111906 (2014)

- [A8] M. BRANDT, M. BONHOLZER, M. STÖLZEL, G. BENNDORF, D. SPEMANN, M. LORENZ, M. GRUNDMANN: *Electrical transport in strained Mg_xZn_{1-x}O:P thin films grown by pulsed laser deposition on ZnO(000-1)*, Physica Status Solidi (B) **249**, 82 (2012)

List of own and contributed Conference Talks and Posters

- Michael Bonholzer, Kerstin Brachwitz, Katja Mexner, Jan Zippel, Michael Lorenz and Marius Grundmann: *Preparation of magnetic tunnel junctions based on zinc ferrite and cobalt* (Poster), DPG-Frühjahrstagung 2011, Dresden (2011)
- K. Brachwitz, K. Mexner, M. Bonholzer, M. Lorenz, N. Sobolev, M. Ziese, P. Esquinazi, M. Grundmann: *Electrical and magnetic properties of zinc ferrite thin films* (Talk), 4th BuildMoNa Workshop 2011, Dresden, Germany (2011)
- M. Bonholzer, K. Brachwitz, J. Zippel, A. Setzer, P. Esquinazi, M. Lorenz and M. Grundmann: *Magnetic tunnel junctions based on zinc ferrite and cobalt* (Talk), DPG-Frühjahrstagung 2012, Berlin (2012)
- M. Bonholzer, K. Brachwitz, J. Zippel, A. Setzer, P. Esquinazi, M. Lorenz and M. Grundmann: *Magnetic tunnel junctions based on zinc ferrite and cobalt* (Poster), 5th Scientific Symposium of BuildMoNa 2012, Leipzig, Germany (2012)
- M. Bonholzer, K. Brachwitz, J. Zippel, A. Setzer, P. Esquinazi, M. Lorenz and M. Grundmann: *Magnetic tunnel junctions based on zinc ferrite and cobalt* (Poster), Intermag IEEE International Magnetism Conference, Vancouver, Canada (2012)
- K. Brachwitz, M. Bonholzer, M. Lorenz, M. Ziese, P. Esquinazi, M. Grundmann: *Zinc ferrite - Magnetic thin films with highly tunable conductivity* (Poster), Intermag IEEE International Magnetism Conference, Vancouver, Canada (2012)
- M. Bonholzer, K. Brachwitz, J. Zippel, A. Setzer, P. Esquinazi, M. Lorenz and M. Grundmann: *Magnetic tunnel junctions based on zinc ferrite and cobalt* (Poster), Spintronic Workshop 2012 des SFB 689, Regensburg, Germany (2012)

- M. Bonholzer, K. Brachwitz, J. Lenzner, A. Setzer, P. Esquinazi, M. Lorenz and M. Grundmann: *Magnetic tunnel junctions based on zinc ferrite and cobalt* (Talk), 5th BuildMoNa Workshop 2012, Burgstädt, Germany (2012)
- M. Bonholzer, K. Brachwitz, J. Zippel, A. Setzer, P. Esquinazi, M. Lorenz and M. Grundmann: *Magnetic tunnel junctions based on zinc ferrite and cobalt* (Poster), MRS Fall Meeting 2012, Boston, Massachusetts, USA (2012)
- M. Bonholzer: *Resonant Magnetic tunnel junctions* (Poster), Minisymposium Quantum Coherence in Nanostructures, Leipzig, Germany (2012)
- M. Bonholzer, K. Brachwitz, M. Lorenz, A. Setzer, M. Ziese, P. Esquinazi and M. Grundmann: *Zinc ferrite, an oxide for spintronics?* (Poster), Annual Conference of BuildMoNa 2013, Leipzig, Germany (2013)
- M. Bonholzer, K. Brachwitz, M. Lorenz, A. Setzer, M. Ziese, P. Esquinazi and M. Grundmann: *Zinc ferrite, an oxide for spintronics?* (Poster), DPG-Frühjahrstagung 2013, Regensburg, Germany (2013)
- M. Bonholzer, K. Brachwitz, M. Lorenz, A. Setzer, M. Ziese, P. Esquinazi and M. Grundmann: *Zinc ferrite, an oxide for spintronics?* (Poster), International School for Oxide Electronics ISOE 2013, Cargèse/Korsika, Germany (2013)
- M. Bonholzer, M. Lorenz and M. Grundmann: *Bottom electrode for zinc ferrite based magnetic tunnel junctions* (Poster), Annual Conference of BuildMoNa 2014, Leipzig, Germany (2014)
- M. Bonholzer, M. Lorenz and M. Grundmann: *High quality TiN as bottom electrode for zinc ferrite based magnetic tunnel junctions grown by pulsed laser deposition* (Poster), DPG-Frühjahrstagung 2014, Dresden, Germany (2014)
- M. Bonholzer, M. Lorenz and M. Grundmann: *Bottom electrode for zinc ferrite based magnetic tunnel junctions*, (Poster), Internationaler SFB-Workshop Kloster Irsee, Irsee, Germany (2014)
- M. Bonholzer: *Präparation von FIB-Lamellen am FEI NanoLab Nova 200* (Talk), 2. Sächsisches TEM-Präparatorentreffen, Leipzig, Germany (2014)
- M. Bonholzer, M. Lorenz and M. Grundmann: *Bottom electrode for zinc ferrite based magnetic tunnel junctions* (Poster), Transparent Conductive Oxides- Fundamentals and Applications TCO 2014, Leipzig, Germany (2014)

- M. Bonholzer, M. Lorenz and M. Grundmann: *Zinc ferrite based magnetic tunnel junctions* (Poster), DPG-Frühjahrstagung 2015, Berlin, Germany (2015)
- R. Schmidt-Grund, C. Sturm, C. Kranert, V. Zviagin, H. Krauß, H. von Wenckstern, M. Bonholzer, J. Lenzner, and M. Grundmann: *NIR-VUV dielectric function of $(Al,In,Ga)_2O_3$ thin films* (Poster), DPG-Frühjahrstagung 2015, Berlin, Germany (2015)
- R. Schmidt-Grund, C. Sturm, C. Kranert, H. Krauß, H. von Wenckstern, M. Bonholzer, J. Lenzner and M. Grundmann: *NIR-VUV dielectric function of $(Al,In,Ga)_2O_3$ thin films* (Poster), 9th Workshop Ellipsometry at the University of Twente, Enschede, the Netherlands (2015)

Danksagung

An dieser Stelle möchte ich mich bei allen bedanken, die mich bei der Erstellung der vorliegenden Arbeit unterstützt haben. Mein Dank gilt

- Prof. Dr. Marius Grundmann für die Möglichkeit, diese Arbeit im Rahmen der von ihm geführten Arbeitsgruppe zu schreiben, sowie für das mir entgegengebrachte Vertrauen, die vielen Freiheiten und die große Unterstützung, die es mir ermöglicht haben diese Arbeit zu erstellen.
- Prof. Dr. Michael Lorenz für seine Unterstützung in vielen physikalischen Fragen, insbesondere der PLD und der Röntgendiffraktometrie.
- Dr. Holger von Wenckstern für viele zielführende Diskussionen zu allen Facetten der elektrischen Probencharakterisierung und der zugehörigen theoretischen Auswertung.
- Dr. Heiko Frenzel für die Unterstützung an der PECVD und der Plasmaätzenanlage.
- Dr. Kerstin Brachwitz, Dr. Jan Zippel, Dr. Matthias Brandt, Dr. Matthias Schmidt und Tammo Böntgen für die Einführung in wissenschaftliches Arbeiten sowie die Betreuung im Anfangsstadium meiner Arbeit.
- Daniel Splith für das von ihm entwickelte, sehr vielseitige, MATLAB-basierte Datenanalyseprogramm sowie die damit durchgeführte Anpassung der j-V-Kennlinien an das erweiterte BDR-Modell.
- dem Sekretariats-Team Anja Heck und Birgit Wendisch für die Hilfe bei allen organisatorischen Fragen.
- Jörg Lenzner für ein immer offenes Ohr bei allen technischen Problemen, die Unterstützung am Dual-Beam Mikroskop sowie die Durchführung und Auswertung vieler EDX-Messungen.
- Holger Hochmuth für die Unterstützung an der PLD.
- den beiden PhyTA-Azubis Maik Hoffmann und Sascha Bader für die Unterstützung beim Auffinden von Lösungen diverser technischer Probleme.

- Monika Hahn für ihre Hilfe bei der Probenpräparation.
- Gabriele Ramm für die Präparation der PLD-Targets sowie die Durchführung der SNMS-Messungen.
- Marcus Jenderka, Dr. Fabian Klüpfel und Daniel Splith für die Unterstützung beim MATLAB-Programmieren.
- Francis Bern, Annette Setzer und Dr. José Luis Barzola Quiquia für SQUID-Messungen und tiefgreifende Diskussionen zum Thema Magnetismus.
- meinem Korrektorenteam Dr. Holger von Wenckstern, Dr. Christian Kranert, Peter Schlupp, Daniel Splith, Sofie Bitter und Tjadina Klein für viele Korrekturvorschläge für die vorliegende Arbeit.
- den Zimmerkollegen aus TA ($100 \cdot \pi$) für viele spannende Diskussionen, Motivation und einfach für die gemeinsame Zeit. Vergessen werden darf natürlich auch nicht das leckere, selbstermachte Eis, mit dem Dr. Christian Kranert regelmäßig die Kaffeepause versüßt hat.
- dem gesamten HLP-Team für sehr viele spannende Diskussionen, die gute Zusammenarbeit sowie eine sehr angenehme und freundschaftliche Arbeitsatmosphäre.
- der Graduiertenschule BuildMoNa für die Möglichkeit zur Teilnahme an wissenschaftlichen Modulen sowie für Tagungen und Konferenzen in einem sehr familiären Rahmen.
- meinen Freunden und meiner Familie für deren Unterstützung, Verständnis und Motivation in allen Lebenslagen.

Für finanzielle Unterstützung durch ein Landesinnovationspromotionsstipendium bedanke ich mich beim Europäischen Sozialfonds ESF und dem Freistaat Sachsen. Desweiteren sei noch die finanzielle Unterstützung durch die Deutsche Forschungsgemeinschaft DFG im Rahmen des SFB 762 "Functionality of oxide interfaces" dankend erwähnt.



Selbstständigkeitserklärung

Hiermit versichere ich,

- dass die vorliegende Arbeit ohne unzulässige Hilfe und ohne Benutzung anderer als der angegebenen Hilfsmittel angefertigt wurde, und dass die aus fremden Quellen direkt oder indirekt übernommenen Gedanken in der Arbeit als solche kenntlich gemacht wurden;
- dass alle Personen in der Dissertation genannt wurden, von denen ich bei der Auswahl und Auswertung des Materials sowie bei der Herstellung des Manuskripts Unterstützungsleistung erhalten habe;
- dass keine weiteren Personen bei der geistigen Herstellung der vorliegenden Arbeit beteiligt waren;
- dass dritte Personen weder unmittelbar noch mittelbar geldwerte Leistungen für Arbeiten erhielten, die im Zusammenhang mit dem Inhalt der vorgelegten Dissertation stehen;
- dass die vorgelegte Arbeit weder im Inland noch im Ausland in gleicher oder in ähnlicher Form einer anderen Prüfungsbehörde zum Zwecke einer Promotion oder eines anderen Prüfungsverfahrens vorgelegt und in ihrer Gesamtheit noch nicht veröffentlicht wurde;
- dass keine früheren erfolglosen Promotionsversuche stattgefunden haben.

Leipzig, 31.03.2016
Ort, Datum

Michael Bonholzer

Erklärung über die Anerkennung der Promotionsordnung

Mit meiner Unterschrift erkläre ich, dass ich die Promotionsordnung der Fakultät für Physik und Geowissenschaften der Universität Leipzig, in der Fassung vom 23. März 2010, anerkenne.

Leipzig, 31.03.2016
Ort, Datum

Michael Bonholzer